

Application of Time Domain Reflectometry and Heat Pulse Methods for Quantifying Phase Change,
Water Flow and Heat Transport in Frozen Soils

by

Hailong He

A thesis submitted in partial fulfillment of the requirements for the degree of

Doctor of Philosophy

Water and Land Resources

Department of Renewable Resources
University of Alberta

© Hailong He, 2015

Abstract

Understanding water flow and heat transport processes in frozen/freezing soils is limited by methodologies for simultaneous, automated measurement of soil properties affecting soil water and heat flux. The major objective of this dissertation was to develop and evaluate time domain reflectometry (TDR) and heat pulse (HP) methodologies to measure soil liquid-water and ice content and soil thermal properties in order to better understand the physics of water flow and heat transport in frozen soils. Extensive lab work was performed and datasets from published work and soil moisture monitoring stations were used to validate and apply these methodologies. The main results are: (1) two multiphase dielectric mixing models that can be parameterized with unfrozen soil and implemented in frozen soils to accurately estimate liquid-water and ice content simultaneously with TDR method alone; (2) application of the developed TDR method to field data facilitates the understanding of soil freeze-thaw processes and snowmelt infiltration under natural boundary conditions despite the assumption of constant soil water content; (3) the dual probe HP method in combination with the TDR method can be used to quantify HP-induced ice melting and correct HP-measured specific heat capacity at high subfreezing temperatures; and (4) the soil freezing-thawing curve (SFTC) measured with these methods can be used explain the hysteresis, freeze-thaw processes, snowmelt infiltration and ice melting resulted from HP method. The application of these methodologies will advance the understanding of mass and energy transport in frozen soils and will spur the development of more innovative methodologies.

Preface

Chapter 2 of this dissertation has been published as H. He and M. Dyck, 2013, “Application of Multiphase Dielectric Mixing Models for Understanding the Effective Dielectric Permittivity of Frozen Soils”, *Vadoze Zone Journal*. I was responsible for the data collection and analysis as well the manuscript composition. M. Dyck was the supervisory author.

Dedication

To my parents, Kaishu Huang and Kaiguo He and to my wife Yang Liu for their unwavering support and encouragement.

Acknowledgements

Sincerely thanks go to my supervisor, Prof. Dr. Miles Dyck. It has been a privilege to work with and study under his direction. This enriching experience has fundamentally shaped my scientific understanding. I wish to thank Miles for his guidance, encouragement, instruction, and friendship during my time at the University of Alberta. He has been an excellent mentor and friend.

I am indebted to my committee members: Prof. Dr. Carl Mendoza and Prof. Dr. Uldis Silins for their feedback and encouragement, the time they dedicated to review and edit this dissertation. Special thanks go to Prof. Dr. Bingcheng Si and Prof. Dr. David Olefeldt for agreeing to be the external examiners.

I wish to extend my appreciation to Prof. Dr. Gang Liu and Prof. Dr. Bingcheng Si for their introduction to construction of heat pulse devices. I am also thankful for Prof. Dr. Kunio Watanabe for providing their dataset for the second chapter and Ralph Wright at the Agriculture and Rural Development (Alberta) and Dick Puurveen at the Ellerslie farm of University of Alberta for providing datasets of the Drought Monitoring Network weather station data.

Special thanks go to André Christensen, Amanuel Weldevohannes, and Syed Mostafa for their technical support.

Funding for this study was provided in part by China Scholarship Council (CSC), Natural Science and Engineering Research Council of Canada (NSERC), and the University of Alberta.

Table of Contents

Chapter 1 General Introduction	1
1.1. Background	1
1.2. Soil freezing/thawing processes and snowmelt infiltration	2
1.3. Fundamentals of TDR methods	5
1.4. Fundamentals of HP methods	6
1.5. Objectives and outline of this dissertation	10
Chapter 2 Application of Multiphase Dielectric Mixing Models for Understanding the Effective Dielectric Permittivity of Frozen Soils	14
2.1. Abstract	14
2.2. Introduction	16
2.3. Theory	19
2.3.1. Physically-based dielectric mixing models	19
2.3.2. Randomly distributed discrete ellipsoids in a homogenous background (isotropic)	20
2.3.3. Randomly distributed confocal ellipsoids in a homogeneous background (isotropic)	21
2.3.4. Choice of geometry and self-consistency with physically-based dielectric mixing models	23
2.3.5. Bound water in frozen soils	24
2.3.6. Temperature-dependent modified <i>Friedman</i> [1998] & <i>Or and Wraith</i> [1999] approach	24
2.3.7. Temperature-dependent linear function based on <i>Robinson et al.</i> [2002]	27
2.4. Materials and Methods	28
2.4.1. Published data sets	28
2.4.2. Calculation and optimization in frozen soils	29
2.4.3. Additional measurement on local soil samples	30
2.4.4. Additional freeze-thaw cycles	31

2.5 Results	32
2.5.1. Sensitivity of effective permittivity-water content function to aspect and self-consistency parameters of discrete and confocal ellipsoid mixing models for unfrozen, 3-phase soils	32
2.5.2. Simulation of effective permittivity in frozen soils with 4-phase discrete and concentric spheres	33
2.5.3. Performance of three phase discrete and confocal ellipsoid models for describing measured $\epsilon_{eff}(\theta)$ relationships in the literature	34
2.5.3.1. Unfrozen soils.....	34
2.5.3.2. Frozen soils.....	35
2.5.4. Measurement of $\epsilon_{eff}(T)$ during soil freezing and thawing.....	36
2.6. Discussion	37
2.6.1. Physical significance of mixing model parameters.....	37
2.6.2. Consistency of 3-phase and 4-phase mixing model parameters	38
2.6.3. Bound water	38
2.6.4. Hysteresis in soil freezing and thawing curves	40
2.7. Conclusions	41
Chapter 3 Soil Freezing-Thawing Characteristics and Snowmelt Infiltration under Natural Boundary Conditions at Breton Plots, Alberta, Canada	61
3.1. Abstract	61
3.2. Introduction	62
3.3. Material and Methods.....	64
3.3.1. Site description.....	64
3.3.2. Instrumentation	65
3.3.3. TDR calibration.....	66
3.3.4. Estimation of unfrozen water and ice content with TDR-measured permittivity	66
3.3.5. Estimation of soil water storage.....	67
3.3.6. Groundwater.....	68
3.3.7. Additional lab experiments on collected soils from Breton Plots site for the measurement of soil freezing-thawing curves (SFTCs)	69
3.4. Results and Discussion.....	69

3.4.1. Overview of 5-year record	69
3.4.2. Soil freezing and thawing phenomena	72
3.4.2.1. Initial soil freezing, snowpack accumulation and maximum depth of soil frost	72
3.4.2.2. Mid-winter freeze-thaw cycles and snowpack depth dynamics	76
3.4.2.3. Soil thawing and snowmelt infiltration	79
3.5. Conclusion.....	83
Chapter 4 Evaluation of TDR Method for Quantifying Ice Melting Caused by the Heat Pulse	
Method in Frozen Soils	107
4.1. Abstract	107
4.2. Introduction	110
4.3. Theory	111
4.4. Material and Methods.....	114
4.4.1. Probe design and construction of thermo-TDR and conventional TDR.....	114
4.4.2. Experimental procedure	115
4.4.3. Specific heat capacity of soil solids	117
4.4.4. Specific heat capacity of water and ice	117
4.4.5. Calibration of Thermo-TDR and conventional TDR.....	117
4.5. Results and Discussion.....	119
4.5.1. Specific heat capacity of soil solids	119
4.5.2. Evidence of ice melting using TDR waveforms	119
4.5.3. Quantification of ice melting by comparing TDR-estimated C_v before HP and	
HP-estimated C_a during HP period	122
4.5.3.1. Comparison of TDR part of thermo-TDR to conventional TDR	122
4.5.3.2. Interpretation of HP and conventional TDR data.....	124
4.5.3.3. Comparison of TDR-estimated C_v and HP-estimated C_a	124
4.5.3.4. Ice melting.....	127
4.6. Conclusion.....	129
Chapter 5 General Discussion and Conclusion	147
5.1. Summary and contribution of this PhD work	147
5.2. Future research	148
References	149

List of Tables

Table 2-1.	Description of six local soils used to measure freezing and thawing curves	42
Table 2-2.	Best fit parameters and goodness of fit for each published unfrozen soil data to predict permittivity (ϵ_{eff}) using discrete and confocal models of a SWA configuration with water permittivity calculated using Friedman 1998 model (Eq. [2-7]) and $\epsilon_w = 80$	43
Table 2-3.	Best fit parameters and goodness of fit for each local unfrozen soil data to predict permittivity (ϵ_{eff}) using discrete and confocal models with constant water permittivity ($\epsilon_w = 88$). ϵ_{eff} of each initial water content θ_{init} was averaged from data ≥ 5 °C	45
Table 2-4.	Best fit parameters and goodness of fit for published frozen soil data to predict permittivity (ϵ_{eff}) using discrete and confocal models for different water permittivity (ϵ_w) scenarios. $\epsilon_w =$ modified using ϵ_w calculated with Friedman-Or-Wraith (FOW) approach (Fig. 2-2, Eqs. [2-7] & [2-8]), $\epsilon_w(T)$ using Eq. [2-9], and $\epsilon_w =$ linear using Eqs. [2-10] & [2-11].....	46
Table 3-1.	Selected soil characteristics.....	85
Table 3-2.	TDR calibration, model parameters, and goodness of fit of Breton Plots site	86
Table 3-3.	Comparison of air and soil temperatures(value in parenthesis is standard error) and dates of soil freezing and thawing.....	87
Table 3-4.	Precipitation and snowpack depth and SWE (average and maximum).....	88
Table 3-5.	Selected characteristics.....	90
Table 4-1.	Experiment design.....	131
Table 4-2.	The best fit parameters and goodness of fit for the estimation of liquid unfrozen water content and ice content with dielectric confocal model for TDR calibration of thermo-TDR and conventional TDR.....	132

List of Figures

Fig. 1-1. TDR principles - relationship of TDR probe parts (top) to wave form features (bottom) for moist sand.....	11
Fig. 1-2. Schematic of dual probe heat pulse probe	12
Fig. 1-3. Comparison of instantaneous heat pulse (Eq.[1-6]) and short duration heat pulse (Eq.[1-7])	13
Fig. 2-1. Simplified discrete ellipsoid (A, dimension: a, b, c) and confocal ellipsoid (B, dimension: a, b = c, c is not shown) conceptual diagrams for a multiphase mixture. One of the constituents acts as the host matrix (ϵ_0 , usually air), and the other components (ϵ_K , ϵ_{K-1} , and ϵ_{K-2}) are embedded as discrete or confocal inclusions in it.....	47
Fig. 2-2. The temperature-dependent effective water permittivity (ϵ_w) as a function of water film thickness based on modified <i>Friedman</i> [1998] and <i>Or and Wraith</i> [1999] models (Eqs. [2-7] & [2-8]).....	48
Fig. 2-3. Influence of particle shape (aspect) on $\epsilon_{eff}(\theta)$ for the discrete ellipsoid model with self-consistency coefficient $\nu = 1$ (A) and confocal ellipsoid model with $\nu = 0$ (B) with solid-water-air configuration	49
Fig. 2-4. Influence of self-consistency (ν) on discrete and confocal models with spherical inclusions (aspect = 1 or a = b = c) in a solid-water-air (SWA) configuration	50
Fig. 2-5. Influence of configuration of mixture inclusions (SWA versus ASW) for the discrete and confocal models with spherical inclusions and two levels of self-consistency	51
Fig. 2-6. Simulation of freezing for discrete spherical inclusions (aspect = 1) of a solid-water-ice-air (SWIA) configuration with (A) $\nu = 0$, (B) $\nu = 1$ and (C) $\nu = 2$. Total porosity of the soil was assumed to be $0.5 \text{ cm}^3 \text{ cm}^{-3}$, $\epsilon_w = 81$, $\epsilon_s = 5$, $\epsilon_g = 1$, and $\epsilon_{ice} = 3.2$ for 4-phase model	52

Fig. 2-7. Simulation of freezing for concentric sphere inclusions (confocal model with aspect = 1) of a solid-water-ice-air (SWIA) configuration with (A) $\nu = 0$, (B) $\nu = 1$ and (C) $\nu = 2$, and solid-ice-water-air (SIWA) configuration with (D) $\nu = 0$, (E) $\nu = 1$ and (F) $\nu = 2$. Total porosity of the soil was assumed to be $0.5 \text{ cm}^3 \text{ cm}^{-3}$, $\epsilon_w = 81$, $\epsilon_s = 5$, $\epsilon_g = 1$, and $\epsilon_{ice} = 3.2$ for 4-phase model53

Fig. 2-8. Miyamoto and Friedman soils with *Friedman* [1998] water permittivity model $\lambda = 10^{10}$ (see Table 2-2 for the parameters and goodness of fit).....54

Fig. 2-9. Unfrozen data from six western Canadian soils with discrete and confocal models for constant water permittivity (see Table 2-3 for the parameters and goodness of fit).....55

Fig. 2-10. Comparison of modeled and measured effective permittivity at different temperatures with the discrete model for $\epsilon_w = 88$56

Fig. 2-11. Comparison of modeled and measured effective permittivity at different temperatures with the confocal model for $\epsilon_w = 88$ (see Table 2-4 for the parameters and goodness of fit)57

Fig. 2-12. Comparison of the measured and modeled liquid-water content for $\epsilon_w = 88$ with best fitted discrete or confocal model from prediction of permittivity58

Fig. 2-13. Soil freezing and thawing curves showing hysteresis measured on Malmo silty loam (described in Table 2-1) with two different initial water contents. A&C are measured permittivity and B&D are the estimated liquid-water content. Liquid-water content is estimated by the discrete model (parameters in Table 2-3).....59

Fig. 2-14. Soil freezing and thawing curves showing hysteresis measured on Mundare loamy sand (described in Table 2-1) with two different initial water contents. A&C are measured permittivity and B&D are the estimated liquid-water content using the confocal model (parameters in Table 2-3).....60

Fig. 3-1. TDR calibration curves for the estimation of liquid-water content and ice content for soil at 5 cm (A&B), 20 and 50 cm (share the same calibration, C&D), and 100 cm (E&F)....91

Fig. 3-2. Time series of 5-year (Nov. 2008 - Oct. 2013) daily air temperature (A), precipitation, cumulative precipitation (calculated from Nov. 1st - Oct. 31st each year), depth of snowpack (B) and volumetric moisture content and soil temperature for 5 cm (C), 20 cm (D), 50 cm (E), and 100 cm (F) depths92

Fig. 3-3. Time series of 5-year (Nov. 2008 - Oct. 2013) daily air temperature (A), precipitation, cumulative precipitation (calculated from Nov. 1st - Oct. 31st), depth of snowpack (B) and soil temperature at 5 cm and total soil water storage for top 50 and 100 cm (C)93

Fig. 3-4. Time series of hourly air temperature (A), precipitation, daily snow depth (B) and hourly permittivity, liquid-water content (expressed in %), and soil temperature for 5 cm (C), 20 cm (D), and 50 cm (E) between Oct. 1st, 2008 and Apr. 30th, 200994

Fig. 3-5. Time series of hourly air temperature (A), precipitation, daily snow depth (B) and hourly permittivity, liquid-water content (expressed in %), and soil temperature for 5 cm (C) and 20 cm (D) between Oct. 1st, 2009 and Apr. 30th, 201095

Fig. 3-6. Time series of hourly air temperature (A), precipitation, daily snow depth (B) and hourly permittivity, liquid-water content (expressed in %), and soil temperature for 5 cm (C) and 20 cm (D) between Oct. 1st, 2010 and Apr. 30th, 201196

Fig. 3-7. Time series of hourly air temperature (A), precipitation, daily snow depth (B) and hourly permittivity, liquid-water content (expressed in %), and soil temperature for 5 cm (C), 20 cm (D), and 50 cm (E) between Oct. 1st, 2011 and Apr. 30th, 201297

Fig. 3-8. Time series of hourly air temperature (A), precipitation, daily snow depth (B) and hourly permittivity, liquid-water content (expressed in %), and soil temperature for 5 cm (C) and 20 cm (D) between Oct. 1st, 2012 and Apr. 30th, 201398

Fig. 3-9. Daily permittivity (A&C) and the interpreted liquid-water content (B&D) at 5 cm depth as a function of temperature during the period over Nov. 1st - Apr. 30th for years 2008/2009 and 2011/2012. Zoom in graphs for temeprature between -4 and 0 °C each year are showed in E and F, respectively. Arrows are used to show the direction of each freezing/thawing segments99

Fig. 3-10. Daily permittivity (A&B) and the interpreted liquid-water content (C&D) at 5 cm depth as a function of temperature during the period over Nov. 1st - Apr. 30th for years 2010/2011 and 2012/2013. Arrows are used to show the direction of each freezing/thawing segments 100

Fig. 3-11. Soil freezing and thawing curves (SFTCs) measured under lab conditions on soils collected from Breton Plots 101

Fig. 3-12. Soil freezing characteristic (SFC) shaped soil freezing and thawing curves (SFTCs, Feb. 9th - Mar. 29th, 2011, daily permittivity vs temperature) at 5 cm depth during the winter 2010/2011 102

Fig. 3-13. Soil freezing characteristic (SFC) shaped soil freezing and thawing curves (SFTCs, Nov. 1st - Apr. 30th, 2012, daily permittivity vs temperature) at 20 cm depth during the winter 2011/2012 103

Fig. 3-14. Soil freezing and thawing curves (SFTCs, Jan. 20th - Apr. 30th, 2012, daily permittivity vs temperature) at 50 cm depth during the winter 2011/2012..... 104

Fig. 3-15. Storage change of top 100 cm plotted against air filled porosity at 5 cm depth at the onset of freezing 105

Fig. 3-16. Storage change of top 100 cm and storage of top 30 cm prior to soil freezing 106

Fig. 4-1. Schematic of thermo-TDR probe..... 133

Fig. 4-2. TDR waveform at above zero temperature (A&B, 1 °C) and at subzero temperatures (C&D, -3.5 °C, evidence of ice melting) recorded from experiment one. t_1 and t_2 are usually used to calculate the travel time of electromagnetic waveform in soil along probe and can be converted to permittivity and then soil water content..... 134

Fig. 4-3. Changes of TDR traces logged at different subfreezing temperatures on the thawing curve (-30 °C for A-1 ~ D-1, -10 °C for A-2 ~ D-2, -3.5 °C for A-3 ~ D-3, and -1 °C for A-4 ~ D-4) for measurements with heat pulse duration of 8 s (probe #2, A-1 ~ A-4), 15 s (probe #3, B-1 ~ B-4), 30 s (probe #4, C-1 ~ C-4), and 60 s (probe #5, D-1 ~ D-4) in experiment two.), TDR 100 was used for the measurement and a CR1000 was programmed for logging waveform..... 135

Fig. 4-4. Thermal properties of water as a function of temperature (water is officially considered as ice when temperature ≤ 0 °C, specific heat capacity is calculated from Eqs. [4-11] and [4-12], thermal conductivity is from handbook of chemistry and physics [p.6-12, <i>Haynes and Lide, 2011</i>])	136
Fig. 4-5. Comparison of measurements made by conventional TDR (line) and thermo-TDR (points)	137
Fig. 4-6. Calibration curves for estimation of liquid-water and ice content for conventional TDR and thermo-TDR (initial water content = $0.25 \text{ cm}^3 \text{ cm}^{-3}$).....	138
Fig. 4-7. Temperature change as a function of time, $T(t)$ for soil at different temperatures (probe #6, heat strength 48.51 W m^{-1} , heat duration 8 s), see Table 4-1 for more details	139
Fig. 4-8. TDR-calculated C_v (conventional 3-needle TDR) and HP-estimated C_a using the SPM during soil thawing (-35 to 25 °C) with 4 heat pulse duration (A-8 s, B-15 s, C-30 s, and D-60 s, strength is $\sim 36 \text{ W m}^{-1}$) and three heat strength treatments (A- 35.57 W m^{-1} , E- 48.51 W m^{-1} , and F- 57.53 W m^{-1} , heat pulse duration is 8 s), see Table 4-1 for more details	140
Fig. 4-9. $(C_a - C_v)/C_v$ as a function of temperature during soil thawing (-35 to 25 °C) and freezing (25 to -35 °C) with 4 heat pulse duration (8 s, 15 s, 30 s, and 60 s, strength is $\sim 36 \text{ W m}^{-1}$) and three heat strength treatments (35.57 W m^{-1} , 48.51 W m^{-1} , and 57.53 W m^{-1} , heat pulse duration is 8 s), see Table 4-1 for more details	141
Fig. 4-10. Maximum temperature rise ΔT_m and time t_m needed to get ΔT_m across all temperatures for columns #2 ~ #7 with 8 - 60 s of heat pulse.....	142
Fig. 4-11. TDR-calculated C_v (conventional 3-needle TDR) and HP-estimated C_a using the SPM during soil freezing (25 to -35 °C) with 4 heat pulse duration (A-8 s, B-15 s, C-30 s, and D-60 s, strength is $\sim 36 \text{ W m}^{-1}$) and three heat strength treatments (A- 35.57 W m^{-1} , E- 48.51 W m^{-1} , and F- 57.53 W m^{-1} , heat pulse duration is 8 s). The spike in C is $30 \text{ MJ m}^{-3} \text{ }^\circ\text{C}^{-1}$ and is not shown completely.....	143
Fig. 4-12. Ice melting for probe of different heat strength and duration at subfreezing temperatures (SPM).....	144

Fig. 4-13. Simulated temperature distribution cross-section of the heater in a homogeneous and isotropic soil..... 145

Fig. 4-14. Relationship between TDR- C_v , HP- C_a and energy input. 146

List of Symbols

α	Parameter of dielectric mixing model, -1 ~ 1
ϵ_{eff}	Composite dielectric permittivity
ϵ	Parameter for calculation in the heat pulse method
ϵ_g	Dielectric permittivity of soil air
ϵ_w	Dielectric permittivity of unfrozen liquid-water
ϵ_i	Dielectric permittivity of ice
ϵ_s	Dielectric permittivity of soil solids
θ_i	Ice content, $\text{m}^3 \text{m}^{-3}$ or $\text{cm}^3 \text{cm}^{-3}$
θ_{init}	Initial water content or total water content before freezing, $\text{m}^3 \text{m}^{-3}$ or $\text{cm}^3 \text{cm}^{-3}$
θ_l	Liquid-water content, $\text{m}^3 \text{m}^{-3}$ or $\text{cm}^3 \text{cm}^{-3}$
θ_t	Total water content including liquid-water and ice, $\text{m}^3 \text{m}^{-3}$ or $\text{cm}^3 \text{cm}^{-3}$
κ	Thermal diffusivity, $\text{m}^2 \text{s}^{-1}$
λ	Thermal conductivity, $\text{W m}^{-1} \text{°C}^{-1}$
π	Pi Constant, 3.141
ρ_b	Bulk density (dry), kg m^{-3}
ρ_g	Density of air, 1.225 kg m^{-3}
ρ_i	Density of ice, 961.7 kg m^{-3}
ρ_s	Particle density, kg m^{-3}
ρ_w	Density of water, 1000 kg m^{-3}

τ	A parameter proportional to the rate of increase of ϵ_w between minimum and maximum ϵ_w
ϕ	Porosity, $\text{m}^3 \text{m}^{-3}$ or $\text{cm}^3 \text{cm}^{-3}$
A_n	The depolarization factors for the de Looer model ($n = 1 \dots 3, \sum A_n = 1$)
a_0, a_1	Parameters for Theta probe calibration
c	Velocity of the electromagnetic wave in free space, $3 \times 10^8 \text{ m s}^{-1}$
C_a	Apparent heat capacity calculated by HP method, $\text{J m}^{-3} \text{ }^\circ\text{C}^{-1}$
c_g	Specific heat capacity of soil air, $\text{J kg}^{-1} \text{ }^\circ\text{C}^{-1}$
c_i	Specific heat capacity of ice, $\text{J kg}^{-1} \text{ }^\circ\text{C}^{-1}$
c_l	Specific heat capacity of unfrozen liquid-water, $\text{J kg}^{-1} \text{ }^\circ\text{C}^{-1}$
c_s	Specific heat capacity of soil solid, $\text{J kg}^{-1} \text{ }^\circ\text{C}^{-1}$
C_v	Volumetric heat capacity, $\text{J m}^{-3} \text{ }^\circ\text{C}^{-1}$
$E_1(x)$	Exponential integral
$exp(x)$	Exponential function
L	Length of probe, m or mm
L_a	The distance between reflections at the beginning and the end of the TDR probe
Q	Strength of heat source (heater of thermo-TDR), $\text{m}^2 \text{ }^\circ\text{C}$
q	Heat input per unit length of the line source, J m^{-1}
R_{htr}	Resistance of heater, Ω
R_{ref}	Resistance of reference resistor, Ω
r	Probe spacing of thermo-TDR or distance from heater, m or mm
S	Soil storage, m or mm
t	Time, s
t_0	The duration of heat pulse release, s

t_m	The time at which the maximum change of temperature (ΔT_m) is reached, s
$T(r, t)$	Temperature change at time t , r away from the heater, °C
$T(t)$	Temperature-time data
ΔT_m	The maximum change of temperature, °C
ν	Coefficient of self-consistency for the dielectric mixing model
v_p	Ratio of the velocity of propagation in a coaxial cable to that in free space, 0.99
V_{drop}	Voltage drop across the heater circuit, volt

List of Abbreviations

ASW	Discrete and confocal models in a air-solid-water configuration
Avg-Dev	Average deviations
DPHP	Dual probe heat pulse
DSC	Differential scanning calorimetry
FOW	Friedman-Or-Wraith
HP	Heat pulse
IPCC	International panel on climate change
NMR	Nuclear magnetic resonance
NS-Eff	Nash-Sutcliffe Efficiency
RMSE	Root mean square error
SFC	Soil freezing characteristic
SFTC	Soil freezing and thawing curve
SIWA	Discrete and confocal models in a solid-ice-water-air configuration
SMRC	Soil moisture retention curve
SWA	Discrete and confocal models in a solid-water-air configuration
SWE	Snow water equivalent
SWIA	Discrete and confocal models in a solid-water-ice-air configuration
TDR	Time domain reflectometry
Thermo-TDR	Combination of HP and TDR probes and methods
TRFCs	Thawing and refreezing cycles

Chapter 1 General Introduction

1.1. Background

Frozen soil processes are critical components of arctic and boreal forest ecosystem mass and energy balances in dry, cold environments such as the Canadian Prairies. During spring snowmelt events, for example, snowmelt may contribute to the recharge of soil moisture reservoirs, which provide water to crops, trees and rangeland plant communities and affect microbial activities in soils (seasonally frozen soils and permafrost). Significant deep drainage (groundwater recharge) may also occur because of the low evapotranspirational demand during these periods. Snowmelt infiltration may also be re-frozen or aid in soil thawing depending on its heat content. Snowmelt, however, may become runoff if soil infiltration capacity is inhibited by ice lenses, ice-filled pores or ice on the soil surface [Kane, 1980; Miller, 1980; Cade-Menun *et al.*, 2013]. Snowmelt runoff likely erodes fertile surface soil (e.g., [Zuzel *et al.*, 1982; Groffman *et al.*, 2001; Cade-Menun *et al.*, 2013]), contributes to spring flooding of catchments (e.g., [Shanley and Chalmers, 1999; Janowicz *et al.*, 2002; Hall *et al.*, 2012]), and influences downstream aquatic nutrient cycling (e.g., [Agren *et al.*, 2008; Amon *et al.*, 2012; Olefeldt and Roulet, 2014]). Recent reports from the Intergovernmental Panel on Climate Change (IPCC) predict significant changes in amount, timing, and phase (i.e., snow or rain) of precipitation on the Canadian Prairies [IPCC, 2007]. Winter precipitation is predicted to increase by up to 10%, but the amount of snow is expected to decrease and the amount of rain is expected to increase. Growing season precipitation is predicted to decrease or remain similar to current levels. The winter soil thermal regime is extremely sensitive to the timing and duration of seasonal snow cover and the wetness of soil prior to freezing. Late establishment of snowpack, dry fall soil or shorter duration of snow cover on the ground may result in increased depth of soil frost in cold regions; conversely, wet fall soil conditions and early, deep snowpack may result in shallow frost (e.g., [Goodrich, 1982; Ling and Zhang, 2003; Zhang, 2005]). Furthermore, changes or variability in the soil water balance over time may affect agricultural and forestry productivity, surface water flows and recharge of groundwater and surface water reservoirs. Therefore, understanding the complex interactions between and the influence of these water and heat

transport processes on soil water and energy balances is required to assess the impact of climate change and climate variability on the soil water balance.

Currently, few methodologies are available for simultaneous, automated measurement of soil properties that affect soil water flow and heat transport in frozen/freezing soils. At present, methods for measuring soil water content, soil thermal properties and soil water flux such as time domain reflectometry (TDR) [Topp *et al.*, 1980; Roth *et al.*, 1990], heat pulse (HP) and thermo-TDR methods [Campbell *et al.*, 1991; Bristow *et al.*, 1993, 1994b; Kluitenberg *et al.*, 1993, 1995; Mori *et al.*, 2003, 2005] have primarily been developed and tested in unfrozen soils and do not directly estimate soil unfrozen/liquid-water content (θ_l), ice content (θ_i), and thermal properties in frozen soils. Previous studies [Patterson and Smith, 1980; Smith *et al.*, 1988; Seyfried and Murdock, 1996; Spaans and Baker, 1996] have calibrated TDR to measure soil θ_l in frozen soils but cannot simultaneously estimate both θ_l and θ_i . The use of composite dielectric mixing models has the potential to calibrate TDR for simultaneous measurement of θ_l and θ_i [Seyfried and Murdock, 1996; Watanabe and Wake, 2009]. For the HP method, its application in frozen soil is confounded by the fact that it may induce phase change which alters the thermal properties that are being measured [Putkonen, 2003; Liu and Si, 2008; Ochsner and Baker, 2008]. This issue, however, may be mitigated by controlling ice melting through optimized heat application or quantifying the influence of the melt on measured thermal properties [Zhang *et al.*, 2011]. Both TDR and HP methods, therefore, have the potential to be used in frozen soils and new methodologies have been developed and tested in the research presented in this dissertation.

In this chapter, a brief review of literature relevant to the soil freezing/thawing processes and snowmelt infiltration, fundamentals of TDR and HP methods is given, followed by a statement of objectives and outlines of this dissertation. The relevant literature has been grouped into the following categories: (1) soil freezing/thawing processes and snowmelt infiltration; (2) fundamentals of TDR methods; and (3) fundamentals of HP methods.

1.2. Soil freezing/thawing processes and snowmelt infiltration

Phase change from water to ice when soil temperature drops below 0 °C is termed soil freezing, and the opposite processes is called soil thawing [Stahli, 2005]. Freezing of soil is associated with solidification of soil water as polycrystalline ice. Phase change of soil water to ice does not

take place at a specific temperature; instead it occurs over a range of temperatures several degrees below 0 °C [Stahli, 2005]. It has been a widely accepted fact for many years that ice and unfrozen liquid-water coexist in frozen soils [Bouyoucos, 1917; Anderson and Tice, 1971; Ishizaki et al., 1996], thus frozen soils are really only partially frozen. Supercooling of soil water may also occur during the freezing processes in the lab (see Chapter 2 of this dissertation) and in situ (Chapter 3). The θ_i in soil with ice present is dependent on temperature, pressure, and solute concentration [Lewis and Randall, 1961; Black, 1994; Marion, 1995; Watanabe and Mizoguchi, 2002], soil texture (surface area) and structure, and the shape of the soil moisture retention curve (SMRC, also called soil moisture characteristic in literature) [Cary and Mayland, 1972]. Generally, the soil freezing characteristic (SFC) is used to describe the relationship between θ_i and temperature, at thermal equilibrium and constant total water content (θ_t) [Miller, 1965; Koopmans and Miller, 1966]. Comparisons between the SMRC and SFC are made because they both represent the replacement of soil water with another phase. For example, the drying process in an unfrozen soil involves the replacement of water with air and the freezing process involves the replacement of water with ice, and hysteresis is found to exist in both SMRC and SFC [Spaans and Baker, 1996; Suzuki et al., 2002; He and Dyck, 2013].

Soil freezing and thawing processes are a result of the balance of sensible heat flux (change in soil temperature mainly through heat conduction) and latent heat flux (phase change from liquid-water to ice or the opposite) that are manifested as the soil thermal regime, which is sensitive to the timing of snow establishment, snowpack depth and duration, and soil moisture content prior to freezing as alluded to earlier [Goodrich, 1982; Ling and Zhang, 2003; Zhang, 2005]. Soil freezes from the ground surface downward, but thaws from both top and bottom [Christensen et al., 2013], resulting in a temporary frozen layer some depth below the soil surface. This frozen layer may or may not impede infiltration of the snowmelt depending on its air-filled pore spaces and pore connectivity (i.e., hydraulic conductivity).

Thermal equilibrium and constant θ_t may not always meet in the field or lab environment. For example, during freezing in moist soil, water moves from warmer subsoil into the upper freezing zones, which is called “freezing induced water redistribution”. Frost-induced water redistribution likely changes θ_t , θ_i , θ_l , soil thermal properties and infiltration capacity. The magnitude of water redistribution is governed by the soil hydraulic properties (which are a

function of θ_l) and imposed temperature gradient. Upward water movement increases soil moisture content at the freezing zone and ice lenses may grow parallel to the freezing front in incompressible soils under favorable conditions (e.g., fine textured soil, adequate water supply and low surface temperatures) [Miller, 1980; Stahli, 2005]. Frost heaving may or may not occur during soil freezing. Ice-filled pores or ice lenses can effectively impede or reduce infiltration. In addition, ice in soil pores tends to form as a pure phase and exclude solutes to soil water at the vicinity of the freezing front. Similarly, thawing in field most often occurs at transient state and is accompanied by snowmelt infiltration. Infiltrating snowmelt may facilitate soil thawing or refreezing depending on its heat content. Therefore, snowmelt infiltration into frozen ground is a very complicated process and many manipulated experiments have been conducted to understand the snowpack and soil moisture content on snowmelt infiltration [e.g., Kane and Stein, 1983b; Decker et al., 2003; Iwata et al., 2010; Christensen et al., 2013; Fouli et al., 2013; Watanabe et al., 2013], but few were conducted under natural boundary conditions. Thus snowmelt infiltration studies from site to catchment to continental scales require more attention.

Soil freezing-thawing and snowmelt infiltration are processes of coupled water and heat flow which can be described by the heat conduction equation with latent heat and water flux terms [Fuchs et al., 1978; Ochsner and Baker, 2008]

$$\frac{\partial(C_v T)}{\partial t} = -L_f \rho_l \left(\frac{\partial \theta_l}{\partial t} + \frac{\partial J_l}{\partial z} \right) + \frac{\partial}{\partial z} \left(\lambda \frac{\partial T}{\partial z} \right) - J_l C_l \frac{\partial T}{\partial z} \quad [1-1]$$

where C_v is soil volumetric heat capacity ($\text{J m}^{-3} \text{ }^\circ\text{C}^{-1}$), subscript l represents liquid-water, T is temperature ($^\circ\text{C}$ or K), t is time (s), L_f is the latent heat of fusion for water (J Kg^{-1}), z is depth (m), λ is thermal conductivity ($\text{W m}^{-1} \text{ }^\circ\text{C}^{-1}$), and J is water flux ($\text{m}^3 \text{ m}^{-2} \text{ s}^{-1}$). Equation [1-1] is essentially a “conductive convective/advective” equation with a sink, the first term at the right accounts for the latent heat flux including phase change of soil water and bypass water flow, the second term is conduction, and the third is convective heat transport as part of the water flux. Conduction is the dominant process of heat transfer in winter [Hinkel et al., 2001], but latent heat and convection play significant roles affecting heat transfer and soil thermal regime. Convection in frozen soils is complex since water flux is subject to Darcy’s law, water potential gradients, and the hydraulic properties are functions of temperature which is constantly changing due to conduction.

1.3. Fundamentals of TDR methods

The TDR method is based on the measurement of the travel time of an electromagnetic wave generated by a TDR cable tester through a wave guide (also called a probe) inserted into the soil [e.g., *Topp et al.*, 1980; *Smith and Tice*, 1988; *Evet*, 2000]. A TDR cable tester consists of an electromagnetic wave generator and a sampling oscilloscope. The electromagnetic wave generator generates a high frequency, broadband (0.5 - 1.5 GHz) electromagnetic wave that travels through the wave guide (i.e., soil probe). As the electromagnetic wave travels through the waveguide its voltage or amplitude is sampled at every point along the waveguide by the oscilloscope and displayed on the screen of the cable tester as a function of time. The travel time (t), of the wave through the waveguide and the soil is a function of the composite/bulk/effective soil permittivity (ϵ_{eff}). The ϵ_{eff} of the soil is a function of the permittivity of the individual constituents in the soil (i.e., air, water, solids, and ice), their volumetric fractions, and geometric arrangement. The relative dielectric permittivity of soil solids (ϵ_s) falls in the range of 3.9 to 10 [Roth et al., 1990; Dirksen and Dasberg, 1993; Seyfried and Murdock, 1996; Friedman, 1998; Robinson and Friedman, 2003; Miyamoto et al., 2005]. For ice and air, $\epsilon_i = 3.2$ and $\epsilon_g = 1$, respectively. Water permittivity (ϵ_w) is a function of temperature (i.e., ϵ_w varying from 96 at -20 °C to 88 at 0 °C and to 80 at 20 °C). Since ϵ_w is much higher than ϵ_s , ϵ_g and ϵ_i , it allows the measurement of soil water content by a calibration relationship between ϵ_c of a soil and its volumetric water content. The ϵ_{eff} measured by TDR methods can be estimated with

$$\epsilon_{eff} = \left(\frac{ct}{2L}\right)^2 = \left(\frac{L_a}{V_p L}\right)^2 \quad [1-2]$$

where c is velocity of the electromagnetic wave in free space, 3×10^8 m s⁻¹; t is the time for a round trip of the wave through the wave guide (s); L is the length of wave guide or TDR probe (m); L_a is the distance between reflections at the beginning and the end of the probe (see Fig. 1-1); and V_p is ratio of the velocity of propagation in a coaxial cable to that in free space. *Noborio et al.* [2001] and *Robinson et al.* [2003] provide detailed information about TDR methods.

Currently only *Smith and Tice* [1988], *Spaans and Baker* [1995], and *Watanabe and Wake* [2009] have attempted to calibrate TDR in frozen soils by relating TDR-measured permittivity, ϵ_{eff} to independently measured θ_i . *Smith and Tice* [1988] presented a third order polynomial TDR calibration equation for saturated frozen soils with independent measurements of unfrozen

water content using nuclear magnetic resonance (NMR). Their calibration relationship, however, underestimated θ_l in unsaturated frozen soils since less ice exists in unsaturated soil, resulting in a lower ϵ_{eff} in frozen, unsaturated soil than frozen, saturated soil at the same unfrozen liquid-water content. The equations developed by *Spaans and Baker* [1995] were obtained in unsaturated frozen soils with a few different initial total water contents but are only valid for one soil. The polynomial equations presented by *Smith and Tice* [1988] and *Spaans and Baker* [1995] have no physical relevance to the frozen soil system. The mixing model presented by *Watanabe and Wake* to estimate θ_l is somewhat physically based but it requires additional knowledge of soil properties (e.g., soil specific surface area). There is no such calibration equation or calibration method for wide application in frozen soils and only θ_l can be accurately estimated by TDR in unfrozen soils so far. To directly measure both θ_l and θ_i independent of TDR, an additional instrument (e.g., gas dilatometer, neutron meter or NMR) is usually required [*Smith et al.*, 1988; *Spaans and Baker*, 1995; *Watanabe and Wake*, 2009]. In the second chapter of this dissertation, I explore the use of composite dielectric mixing models that relate the ϵ_{eff} to the permittivity and volume fraction of soil components to predict the amount of θ_l and θ_i with TDR alone. Since the composite dielectric mixing models are based on the assumption of constant total water content (θ_{init}) measured prior to soil freezing, its application may be challenged in field conditions where frost-induced water redistribution and snowmelt infiltration may change the total soil water content. Thus the third chapter evaluates this method for in situ use and to understand the soil freezing-thawing processes and snowmelt infiltration under natural boundary conditions.

1.4. Fundamentals of HP methods

Two common techniques, steady-state (e.g., axial rod [*Powell and Tye*, 1960] and guarded hot plate [*Pham and Smith*, 1986]) and transient methods (e.g., probe method [*de Vries and Peck*, 1958]), have been described in the literature to measure soil thermal properties. The steady-state method is based on the theory of steady-state heat flow, which requires maintenance of a constant temperature gradient across the soil sample being tested. The transport of heat in unsaturated soil is, however, usually accompanied by distillation of water vapor [*de Vries*, 1952] and appreciable moisture migration [*de Vries and Peck*, 1958; *Farouki*, 1981]. This method thus may create conditions that alter the thermal properties being measured [*Farouki*, 1981; *Bristow*

et al., 1994a]. The transient methods using small temperature gradients, on the other hand, can reduce phase changes and convective heat transport. They cause much less water redistribution compared to steady-state methods [*de Vries*, 1952; *Farouki*, 1981; *Shiozawa and Campbell*, 1990]. This transient method, widely used in recent literature, is called the heat pulse (HP) method. Essentially, the HP method involves monitoring the soil temperature response “downstream” of a pulsed heat source. It is based on the linear-heat-source theory [*Carslaw and Jaeger*, 1959], including single-probe-heat-pulse (SPHP) and dual-probe-heat-pulse (DPHP) methods. Heater and temperature sensors are mounted together for SPHP method and a relatively long duration heat pulse is used (e.g., 90s [*Shiozawa and Campbell*, 1990] and 180s [*de Vries and Peck*, 1958]). Heater and temperature sensors are separated into different probes for the DPHP method and a short duration of heat pulse is used (e.g., 8s [*Campbell et al.*, 1991; *Bristow et al.*, 1994b]). Introduction of the SPHP method can be traced back to the late 19th century [*Winkelmann*, 1875]. *Stalhane and Pyk* [1931] first presented the mathematical model of line-heat source method, and then SPHP was developed for measuring heat conductivity of liquids by *Weishaupt* [1940] and *Van der Held and Van Drunen* [1949], and of soils by *Hooper and Lepper* [1950]. *Merrill* [1968] first separated the temperature sensor from the heater probe (2 mm apart) and took advantage of the instantaneous line heat source theory. Later *Campbell et al.* [1991] developed the DPHP for soil measurements and HP method entered another era. See Fig. 1-2 for an example of DPHP probe. The basics of HP method are described below.

In semi-infinite, homogenous, isotropic, and isothermal medium (e.g., soil) without water flow and latent heat, C_v , λ in Eq. [1-1] may be taken out of the derivative provided they are constant with space and time. The radial heat conduction (in cylindrical coordinates system) becomes [*Carslaw and Jaeger*, 1959; *Farouki*, 1981]

$$C_v \frac{\partial T}{\partial t} = \lambda \left(\frac{\partial^2 T}{\partial r^2} + \frac{1}{r} \frac{\partial T}{\partial r} \right) \quad [1-3]$$

This particular solution to Eq. [1-3] with a line heat source is [*de Vries*, 1952; *Carslaw and Jaeger*, 1959]

$$T(r, t) = \frac{-Q}{4\pi\kappa t} E_i \left(\frac{-r^2}{4\kappa t} \right) \quad [1-4]$$

where $-E_i(-x)$ is the exponential integral; $T(r, t)$ is temperature at a radial distance, r (m) from the line heat source at time, t (s) after heat is released; Q , the strength of heat source ($\text{m}^2 \text{ }^\circ\text{C}$), is the quantity of heat input per unit length of the line source, q (J m^{-1}), divided by C_v , $Q = q/C_v$. Heat input q can be calculated using Joule's law

$$q = \left(\frac{V_{drop}}{R_{ref}} \right)^2 \frac{R_{htr}}{L} t_0 \quad [1-5]$$

where V_{drop} is voltage drop (volt) across the heater circuit; R_{htr} is the resistance of the heater (ohm); R_{ref} is the resistance of the reference resistor (ohm); L is the probe length (m); t_0 is the heat pulse duration (s). Boundary conditions of the HP method are as follows: $T = 0$ (thermal equilibrium) for $t = 0$ and $r \geq 0$; $T = 0$ (no heat flow far from the heat source) for $t > 0$ and $r \rightarrow \infty$; $-2\pi r \lambda (\partial T / \partial t) = q$ for $t > 0$ and $r \rightarrow 0$. $T(r, t)$ is directly related to Q and inversely related to C_v and κ of soil. The greater the κ , the faster the heat pulse dissipates into the surrounding soil and thus the shorter the time lag between the initial heat pulse and the peak of the thermal wave at distance r . The greater the C_v , the more energy is required to raise a unit temperature of the soil and therefore decreases the maximum temperature rise.

Differentiation of Eq. [1-4] with respect to time lead to the instantaneous line source theory (i.e., instantaneous release of heat pulse from an infinite line source) assuming small changes in time [Merrill, 1968; Campbell *et al.* 1991]:

$$\Delta T(r, t) = \frac{Q}{4\pi\kappa t} \exp\left(\frac{-r^2}{4\kappa t}\right) \quad [1-6]$$

In practice, however, it is not possible to meet the theoretical requirements of an instantaneous line source of infinite length. Therefore, a cylindrical heat source of finite length is used to approximate an infinite line source and a short-duration heat pulse to approximate an instantaneous release of heat [Bristow *et al.*, 1994b]. The short duration heat pulse causes a significant delay in the time (t_m) to get the maximum temperature rise (ΔT_m), but has very little effect on ΔT_m (see Fig. 1-3) [Kluitenberg *et al.*, 1993; Bristow *et al.*, 1994b]. Therefore, it is possible to obtain accurate C_v via Eq. [1-1] with heat pulses of short duration [Campbell *et al.*, 1991; Kluitenberg *et al.*, 1993; Bristow *et al.*, 1993, 1994b]. The solution to Eq. [1-1] for the conditions described above is [de Vries, 1952]:

$$\Delta T(r, t) = \begin{cases} -\frac{Q}{4\pi\kappa t_0} E_i\left(\frac{-r^2}{4\kappa t}\right) & 0 < t \leq t_0 \\ \frac{Q}{4\pi\kappa t_0} \left[E_i\left(\frac{-r^2}{4\kappa(t-t_0)}\right) - E_i\left(\frac{-r^2}{4\kappa t}\right) \right] & t > t_0 \end{cases} \quad [1-7]$$

This solution to the heat equation predicts the temperature change at distance r as a function of time when a heat pulse is liberated at $t = 0$ and terminated at $t = t_0$. Thereby, the solution includes two sections, the heating period ($0 < t \leq t_0$) and the cooling period ($t > t_0$). The temperature-time, $T(t)$, data can be analyzed either by the single point method (SPM) [Bristow *et al.*, 1994b] or non-linear model fit (NMF) method [Bristow *et al.*, 1995] to extract soil thermal properties.

Besides soil thermal properties, the combination of TDR and HP probes and methodology have led to the thermo-TDR method which allows the simultaneous measurement of other properties in unfrozen and/or frozen soils. For example, it can determine water content and electric conductivity [Campbell *et al.*, 1991; Bristow *et al.*, 1993, 1994b; Kluitenberg *et al.*, 1993, 1995; Mori *et al.*, 2003, 2005], soil water flux and soil pore water velocity [Ren *et al.*, 2000; Wang *et al.*, 2002; Mori *et al.*, 2005; Kluitenberg *et al.*, 2007; Kamai *et al.*, 2008], soil bulk density [Ochsner *et al.*, 2001; Ren *et al.*, 2003b; Liu *et al.*, 2008], snow density [Liu and Si, 2008], and potentially ice content and unfrozen water content under certain conditions [Liu and Si, 2011a; Zhang *et al.*, 2011] etc. Thermo-TDR is ideal for comparison of water contents between HP and TDR methods because the probe makes both measurements on nearly the same soil volume [Ren *et al.*, 2005]. The weakness of this method in frozen soils is that the release of the heat pulse may melt ice and change thermal properties that are being measured. But if the amount of ice melted is greater than the measurement error of TDR, a composite dielectric mixing model may be utilized to quantify the ice melting. Once the ice melting is quantified, the HP method may be modified to accurately estimate frozen soil thermal properties (e.g., heat capacity, thermal conductivity, and thermal diffusivity) and provides parameters for a variety of modelling purposes. Advantages of the HP method would be in its cost-effectiveness and straightforward design and the ability to have continuous, automated data collection with minimal disturbance compared with coring techniques. Chapter 4 of this dissertation will evaluate the TDR method to quantify HP-induced ice melting and propose a method to correct the estimation of frozen soil heat capacity.

1.5. Objectives and outline of this dissertation

The research presented in this dissertation deals with development and evaluation of TDR and HP methodologies to understand the water flow and heat transport in frozen soils. The objectives of this work include: (1) develop and test the TDR method for simultaneous estimation of soil liquid-water and ice content of frozen soil; (2) evaluate the method developed in objective 1 for field application and to understand freezing and thawing processes and snowmelt infiltration under natural boundary conditions; and (3) evaluate the TDR method to quantify HP-induced ice melting.

This dissertation is organized accordingly into three main chapters (chapters 2 - 4) describing the objectives and results of this research. Chapter 2 provides a detailed description of two four-phase composite dielectric mixing models based TDR methods for estimation of liquid-water content and ice content in frozen soils. Published datasets of a wide range of soils around the world and self-measured data on local soils in Canada are used to test, modify, and evaluate the two models for frozen soil purposes. Chapter 3 is the application and evaluation of the mixing model with field data and to understand the soil freezing and thawing characteristics and snowmelt infiltration under natural boundary conditions. Chapter 4 evaluates the TDR method for quantifying ice melting caused by heat pulse method in frozen soils. Results are provided at the end of every chapter and they are also summarized in chapter 5, the general conclusions.

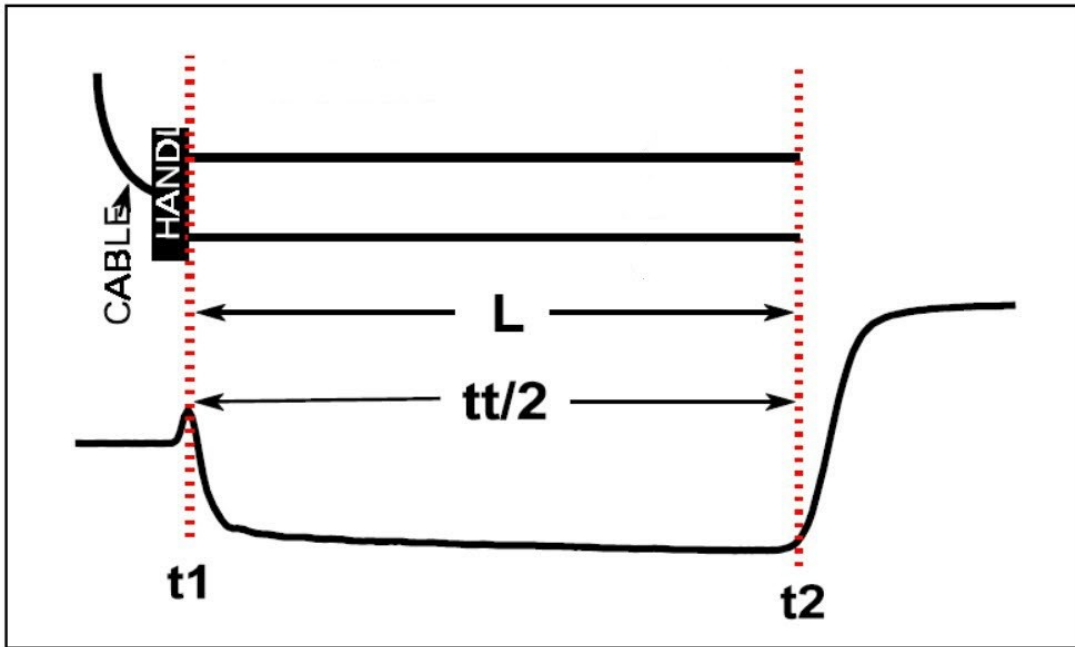


Fig. 1-1. TDR principles - relationship of TDR probe parts (top) to TDR cable tester recorded wave form features (bottom) for moist sand (from Ch. 7 in TACQ users guide [Evelt, 2000]). The units are voltage and time for y- and x-axis, respectively of the waveform. S - rod spacing, L - rod length, $tt/2$ - one way travel time, t_1 - the time when the step pulse exits and the probe handle, and t_2 - time when pulse reaches the rod end and is reflected back).

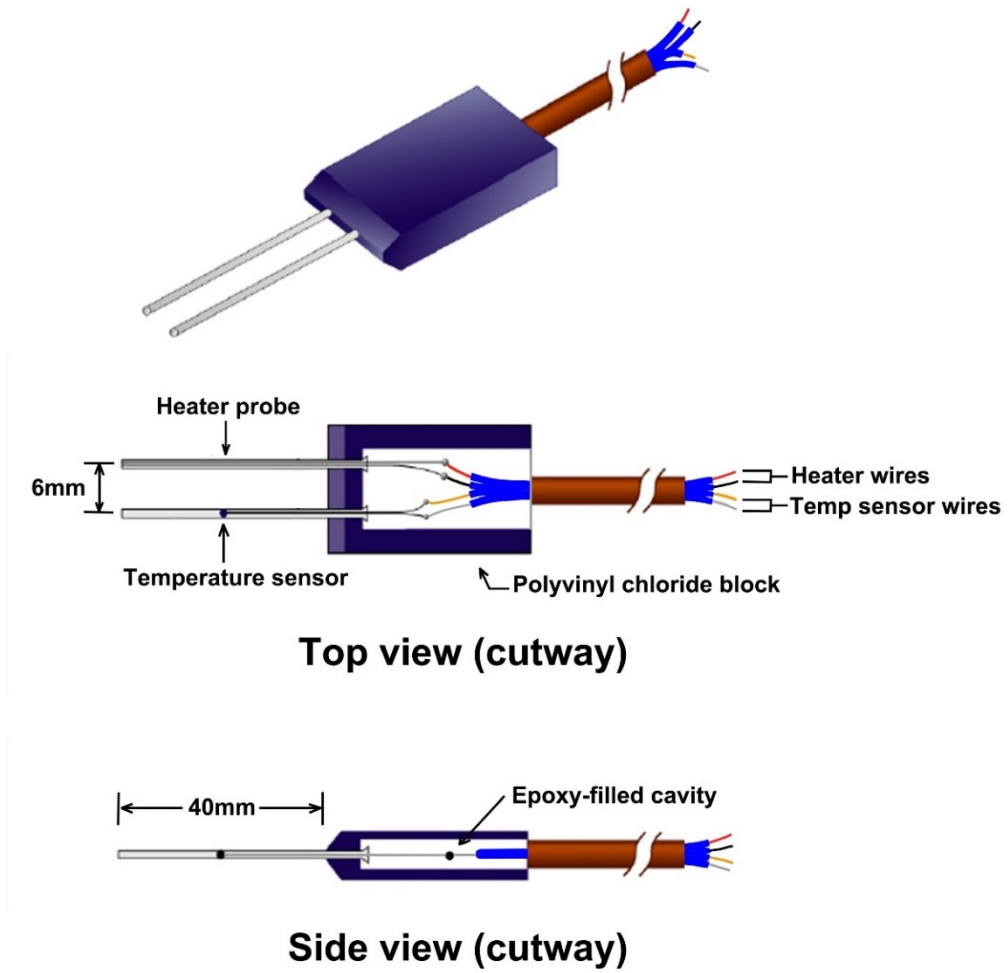


Fig. 1-2. Schematic of dual probe heat pulse probe (after *Heitman et al.* [2003]).

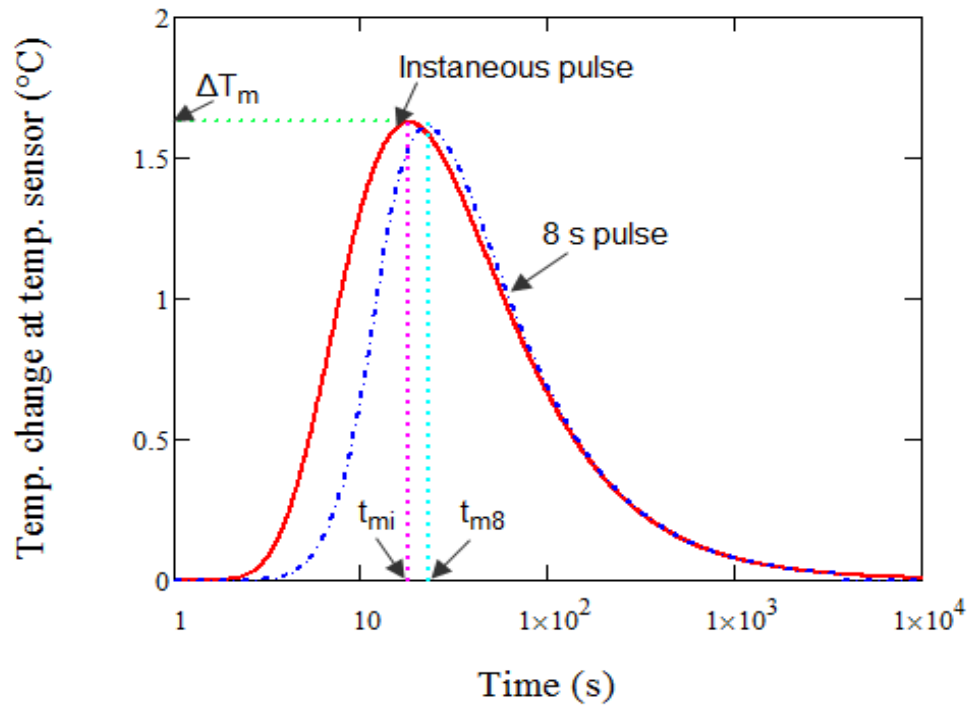


Fig. 1-3. Comparison of instantaneous heat pulse (Eq. [1-6]) and short duration heat pulse (Eq. [1-7]) (modified from *Bristow et al.* [1994]).

Chapter 2 Application of Multiphase Dielectric Mixing Models for Understanding the Effective Dielectric Permittivity of Frozen Soils

*[A version of this chapter has been published. He, H. & M. Dyck. 2013. *Vadose Zone J.* doi:10.2136/vzj2012.0060]

2.1. Abstract

The TDR-measured effective permittivity in frozen soil conditions is affected by many complex factors including bound water effects on soil water permittivity, phase changes, soil microstructure and relative positions of soil constituents with respect to each other. The objective of this chapter was to improve understanding of some of the factors affecting the effective permittivity of frozen soils through the use of dielectric mixing models. Published datasets and frozen and unfrozen soil data measured on western Canadian soils were investigated with multi-phase discrete and confocal ellipsoid models available in the literature. The results revealed that adjusting model parameters allowed the mixing models to describe the frozen soil permittivity equally well when bound water effects and temperature-dependent water permittivity effects were included or not included. Measurement of freezing and thawing curves on western Canadian soils showed significant hysteresis and some mechanisms for this observed hysteresis and its influence on the interpretation of published datasets are discussed. When independent measurements of liquid-water, ice and effective permittivity are available, it is possible to find one set of model parameters that reasonably predicts effective permittivity for both frozen and unfrozen conditions.

List of symbols and acronyms:

α	Parameter of dielectric mixing model, -1 ~ 1
ϵ_{eff}	Composite dielectric permittivity
ϵ_g	Dielectric permittivity of soil air
ϵ_w	Dielectric permittivity of unfrozen liquid-water

ϵ_i	Dielectric permittivity of ice
ϵ_s	Dielectric permittivity of soil solids
θ_i	Ice content, $\text{m}^3 \text{m}^{-3}$ or $\text{cm}^3 \text{cm}^{-3}$
θ_{init}	Initial water content or total water content before freezing, $\text{m}^3 \text{m}^{-3}$ or $\text{cm}^3 \text{cm}^{-3}$
θ_l	Liquid-water content, $\text{m}^3 \text{m}^{-3}$ or $\text{cm}^3 \text{cm}^{-3}$
θ_t	Total water content including liquid-water and ice, $\text{m}^3 \text{m}^{-3}$ or $\text{cm}^3 \text{cm}^{-3}$
ρ_b	Bulk density (dry), kg m^{-3}
ρ_g	Density of air, 1.225 kg m^{-3}
ρ_i	Density of ice, 961.7 kg m^{-3}
ρ_s	Particle density, kg m^{-3}
ρ_w	Density of water, 1000 kg m^{-3}
τ	A parameter proportional to the increase rate of ϵ_w between min. and max. ϵ_w
ϕ	Porosity, $\text{m}^3 \text{m}^{-3}$ or $\text{cm}^3 \text{cm}^{-3}$
A_n	The depolarization factors for the de Looer model ($n = 1 \dots 3, \sum A_n = 1$)
ν	Coefficient of self-consistency for the mixing model
ASW	Discrete and confocal models in a air-solid-water configuration
Avg-Dev	Average deviations
FOW	Friedman-Or-Wraith
NMR	Nuclear magnetic resonance
NS-Eff	Nash-Sutcliffe Efficiency
RMSERoot mean square error
SFC	Soil freezing characteristic
SFTC	Soil freezing and thawing curve
SIWA	Discrete and confocal models in a solid-ice -water -air configuration
SMRC	Soil moisture retention curve
SWA	Discrete and confocal models in a solid-water-air configuration
SWIA	Discrete and confocal models in a solid-water-ice-air configuration

2.2. Introduction

It has been well established that unfrozen liquid-water and ice coexist in soils at subfreezing temperatures [Cannell and Gardner, 1959; Anderson and Tice, 1972; Miller, 1980]. The importance of accurate measurement of unfrozen liquid-water content and accurate simulation of freezing and thawing processes has long been recognized for both engineering and environmental issues. For example, engineers are concerned with frost heave-induced problems in connection with the design, construction and maintenance of roads, railroads, airfields, buried cables, pipelines, and buildings. Soil scientists, hydrologists, and agronomists are interested in such problems as soil-atmosphere energy exchange, water resources management, and partitioning of winter rainfall and snowmelt into infiltration and surface runoff, predicting soil erosion and floods, and the fate of contaminants introduced into the soil.

In cold regions, snowmelt water may contribute to the recharge of soil moisture reservoirs that are closely linked to ecosystem productivity. Significant deep drainage (groundwater recharge) may also occur at times of snowmelt infiltration because of the low evapotranspirational demand during these periods. Snowmelt infiltration may also be re-frozen or aid in soil thawing depending on its heat content. Snowmelt, however, may become runoff [Cary *et al.*, 1978; Kane, 1980; Miller, 1980] if soil infiltration capacity is inhibited by ice lenses, ice-filled pores or ice on the soil surface. Accurate estimates of changes of unfrozen liquid-water content (θ_l) and ice content (θ_i) in frozen soils is required to understand and perhaps manage these complicated processes.

The water-ice phase composition of freezing/frozen soils depends on many factors such as soil-atmosphere energy exchange, soil temperature, temperature gradient-induced water redistribution, soil texture and specific surface area, shape, size and dielectric properties of the solid particles [Koopmans and Miller, 1966; Anderson and Tice, 1972; Tice *et al.*, 1981], organic matter content [Drotz *et al.*, 2009], presence of solutes [Banin and Anderson, 1974; Yong *et al.*, 1979; Tice *et al.*, 1981; Patterson and Smith, 1985; Watanabe and Mizoguchi, 2002; Drotz *et al.*, 2009], and initial water content, θ_{init} [Tice *et al.*, 1981, 1989; Roth and Boike, 2001; Kozlowski, 2003; Suzuki, 2004].

A variety of techniques and methods have been developed to determine θ_l in frozen soils, including dilatometry [Pusch, 1979; Patterson and Smith, 1985; Spaans and Baker, 1995],

adiabatic calorimetry [Kolaian and Low, 1963], isothermal calorimetry [Anderson and Tice, 1971, 1972], differential scanning calorimetry [Tice et al., 1976; Yong et al., 1979; Kozlowski, 2003, 2004], nuclear magnetic resonance (NMR) [Tice et al., 1981; Smith et al., 1988; Watanabe and Mizoguchi, 2002; Sparrman et al., 2004; Kleinberg and Griffin, 2005; Watanabe and Wake, 2009], x-ray diffraction [Anderson and Hoekstra, 1965], dielectric spectroscopy [Bittelli et al., 2004], and TDR [Patterson and Smith, 1980, 1981; Smith et al., 1988; Stahli and Stadler, 1997; Christ and Park, 2009]. Of these methods, TDR is easily multiplexed and automated [Spaans and Baker, 1995]. It has become the most widely used technique for both field and lab measurements. The TDR technique is based on the measurement of the travel time of an electromagnetic wave pulse (usually < 1.5 GHz) generated by a TDR cable tester through a wave guide (also called probe) inserted in soil, unfrozen or frozen. The travel time of the wave through the probe is a function of the bulk or effective permittivity of soil, ϵ_{eff} , which in turn is a function of permittivities of the individual constituents in the soil (air, water, solids, and ice), their volumetric fractions, and geometric arrangements. This permits estimation of unfrozen water content through a calibration relationship between the ϵ_{eff} and θ_l . Permittivity or dielectric constant is a measure of the ability of a material to store electrical energy [Sihvola, 1999].

Initial work on using TDR to measure θ_l in frozen soils [Smith et al., 1988; Spaans and Baker, 1995] resulted in empirical relationships by relating TDR-measured ϵ_{eff} to independently measured θ_l by other methods such as NMR and gas dilatometry. These empirical relationships are usually specific to certain soil saturation statuses and soil types and are not valid for general purposes. Sometimes equations for unfrozen soils such as Topp et al. [1980] were applied directly to obtain θ_l in frozen soils. However, there have been reports about the discrepancy between the predicted and measured θ_l [Seyfried and Murdock, 1996; Yoshikawa and Overduin, 2005], which may be attributed to the effects of ice and temperature [Seyfried and Murdock, 1996]. The assumption that freezing affects the dielectric permittivity the same as drying in unfrozen soils is not entirely valid because the drying process in an unfrozen soil involves the replacement of water with air, but the freezing process involves the replacement of water by ice. The dielectric permittivity of ice is about three times greater than air (i.e., 3.2 compared to 1).

Therefore, the ϵ_{eff} of a frozen soil will be greater than the ϵ_{eff} of an unfrozen soil with the same liquid-water content as long as there is ice present.

Empirical relationships from prior studies for measurement of θ_l without considering the influence of ice on ϵ_{eff} are prone to errors and the influence of θ_l and θ_i on ϵ_{eff} needs to be considered simultaneously [Spaans and Baker, 1995]. One possible way is with multi-phase composite dielectric mixing models that relate the ϵ_{eff} of soils to the permittivities of its constituents and their volumetric compositions. Two- to four-phase dielectric mixing models have been widely applied in unfrozen soils [Birchak et al., 1974; Dobson et al., 1985; Roth et al., 1990; Sareni, 1997; Friedman, 1998; Jones and Friedman, 2000; Miyamoto et al., 2005]. Examples of such models are the randomly distributed discrete and confocal ellipsoids in a homogeneous background [Sihvola and Kong, 1988; Sihvola and Lindell, 1990; Jones and Friedman, 2000]. For frozen soils, ice can be explicitly incorporated in a manner analogous to that in unfrozen soils by introducing an extra ice-phase term into the model [Seyfried and Murdock, 1996; Watanabe and Wake, 2009]. Mixing models provide a better description of the relationship among ϵ_{eff} , θ_l , θ_i , θ_{init} , temperature, and bulk density.

Seyfried and Murdock [1996] compared the empirical relationships and simple dielectric mixing models for estimating θ_l in frozen soils, but concluded that the mixing models did not include all factors affecting the measured dielectric permittivity in frozen soils. Recently, Watanabe and Wake [2009] investigated the use of a power law model (or Birchak et al., 1974 model) to simulate the TDR-measured ϵ_{eff} with NMR-measured θ_l in unsaturated frozen soils of different soil textures. The bound water effect was included and their study showed the α parameter of the Birchak model may vary with soil type. The estimation of θ_l for fine-textured soils was not as good as that of coarse-textured soils was attributed to bound water effects.

Many uncertainties of the TDR method exist in frozen soil research and no comprehensive study of factors affecting the permittivity was found by the authors. In this paper, we investigated the influence of temperature, ice, bound water, texture, particle shape (aspect) and self-consistency on permittivity using two physically based dielectric discrete and confocal ellipsoid mixing models. Predictions of the effective permittivity for frozen and unfrozen soils were generated from these models and compared to published data. In addition, new data consisting of $\epsilon_{eff}(T)$ relationships measured on western Canadian soil samples of a variety of

textures will be presented. This data will be used to show differences between soil freezing and thawing curves.

2.3. Theory

2.3.1. Physically-based dielectric mixing models

Soil may be conceptualized as a mixture of dielectric components (e.g., minerals, organic matter, water, air, and ice). Extensive literature on the effective permittivity of dielectric mixtures is available. An example of such work is that of *Sihvola* [1999] which summarizes mixing models for heterogeneous dielectric mixtures with simple geometries. The classical conception of dielectric mixtures is a background or host medium with permittivity, ϵ_0 , within which dielectric inclusions (scatterers) of simple geometry are randomly distributed. When an electrical field is applied to this mixture, there is a displacement of charged components in the medium from their equilibrium positions. This displacement temporarily polarizes the material and the magnitude of the polarization is directly proportional to the magnitude of the dipole moment. This polarization occurs on both the atomic and molecular levels. Polarization mechanisms vary depending on the material and many mechanisms may occur simultaneously. The theoretical mixing models summarized in this section assume that the polarizability of a mixture is the sum of the polarizabilities of its constituent materials, and the polarizability of each constituent is the sum of the polarizability induced by all of the polarization mechanisms (i.e., relaxation). A summary of polarization mechanism is found in Chapter 2 of *Sihvola* [1999].

For a mixture with inclusions of many different types, the polarizabilities of each type contribute to the effective permittivity of the material proportional to their numbers [*Sihvola and Lindell, 1990*]:

$$\frac{\epsilon_{eff} - \epsilon_0}{\epsilon_{eff} + 2\epsilon_0} = \sum_i \frac{n_i \alpha_i}{3\epsilon_0} \quad [2-1]$$

where ϵ_{eff} is the effective permittivity ($A \ s \ V^{-1} \ m^{-1}$, but is often divided by the permittivity of free space to become the dimensionless), ϵ_0 is the permittivity of the host phase, n_i is the number of inclusions per unit volume of the mixture of phase i , and α_i is the polarizability ($A \ s \ m^2 \ V^{-1}$) of phase i . Thus estimating the effective permittivity requires determination of the dipole moment induced in the inclusions and their resulting polarizability (α). In order to do this, the

internal field of an inclusion in the presence of a quasi-static field must be characterized which requires the solution of the Laplace equation. The solution, therefore, is also function of the geometry of the inclusions and also depends on the assumptions about the distance between the inclusions (i.e. the density of the mixture). Equation [2-1] assumes that the mixture is sparse and the permittivity “seen” outside of the inclusions under the influence of an electric field is equal to that of the host background, ϵ_0 [Sihvola and Lindell, 1992]. For very dense mixtures this may not be the case and Eq. [2-1] is further modified to include the interaction effects of the permittivity of adjacent inclusions by including a coefficient of self-consistency, ν (i.e., an indicator of how the polarization of adjacent inclusions are accounted in calculation of the dipole moment of a single scatter/inclusion or the effective permittivity of the mixture is proportion to itself):

$$\frac{\epsilon_{eff}-\epsilon_0}{\epsilon_{eff}+2\epsilon_0+\nu(\epsilon_{eff}-\epsilon_0)} = \sum_i \frac{n_i \alpha_i}{3[\epsilon_0+\nu(\epsilon_{eff}-\epsilon_0)]} \quad [2-2]$$

The multiphase expressions for the effective permittivity presented in the next section are based on Eq. [2-2].

2.3.2. Randomly distributed discrete ellipsoids in a homogenous background (isotropic)

For an isotropic mixture composed of discrete ellipsoids of $i = 1 \dots K$ materials with permittivity $\epsilon_1, \epsilon_2, \dots, \epsilon_K$ randomly distributed and randomly oriented in a homogenous background material of permittivity, ϵ_0 (Fig. 2-1: A), the effective permittivity, ϵ_{eff} , of the $K + 1$ phase mixture is expressed as [Sihvola and Kong, 1988; Jones and Friedman, 2000]:

$$\epsilon_{eff} = \epsilon_0 + \frac{\frac{\epsilon_0}{3} \sum_{i=1}^K \phi_i (\epsilon_i - \epsilon_0) \sum_{j=x,y,z} \frac{n \alpha_j}{\epsilon_0 + \nu(\epsilon_{eff} - \epsilon_0)}}{1 - \frac{1}{3} \sum_{i=1}^K \phi_i (\epsilon_i - \epsilon_0) \sum_{j=x,y,z} N_j^{(i)} \frac{n \alpha_j}{\epsilon_0 + \nu(\epsilon_{eff} - \epsilon_0)}} \quad \text{where,}$$

$$\frac{n \alpha_j}{\epsilon_0 + \nu(\epsilon_{eff} - \epsilon_0)} = \frac{1}{[\epsilon_0 + \nu(\epsilon_{eff} - \epsilon_0)] + N_j^{(i)} (\epsilon_i - \epsilon_0)} \quad [2-3]$$

where ϕ_i is the volumetric fraction of the i^{th} material and $N_j^{(i)}$ are the depolarization factors of the i^{th} material with permittivity ϵ_i in the x , y and z directions (see Eqs. [2-5] & [2-6]). Each material may have a unique set of depolarization factors. The depolarization factors are a function of the shape of the ellipsoids (e.g., Eq. [2-5]). The sum of the depolarization factors is

always equal to 1 [Sihvola and Kong, 1988]. Special cases where $N_j = (1/3, 1/3, 1/3)$, $N_j = (0, 0, 1)$ and $N_j = (0, 0.5, 0.5)$ represent spheres, discs and needles, respectively [Sihvola and Kong, 1988].

When the coefficient of self-consistency, ν , does not equal zero, Eq. [2-3] becomes implicit for ϵ_{eff} , and iterative methods have to be used to acquire the effective permittivity of the mixture. Equation [2-3] represents the *Maxwell-Garnett* [1904], *Polder and van Santen* [1946] and coherent potential [Tsang and Ishimaru, 1985] and *Gyorffy, Koringa and Mills* models for the cases where $\nu = 0$, $\nu = 1$, $\nu = 1 - N_j$ and $\nu = 3$, respectively [Sihvola and Kong, 1988; Jones and Friedman, 2000; Robinson and Friedman, 2005]. The mixing model presented by *de Loor* [1968] is equivalent to the *Polder and van Santen* [1946] mixing model for the case where *de Loor's* ϵ^* parameter is made equivalent to ϵ_{eff} . *Sihvola* [1989] also suggested that the value of ν may be established through fitting of Eq. [2-3] to measured data. The values of and the effects of coefficient of self-consistency will be discussed in further detail later in the chapter.

For the case of spherical inclusions, the mixture is inherently isotropic. If the ellipsoids are preferentially oriented along one of their semi-axes, the mixture will be anisotropic and ϵ_{eff} will depend on the direction of the applied electrical field. If the ellipsoids are randomly oriented, the mixture will be isotropic and ϵ_{eff} will be the same regardless of the direction of the applied electrical field. The effects of anisotropic mixtures on ϵ_{eff} are beyond the scope of this paper and only isotropic mixtures are considered. If a soil has anisotropic structure, however, the reader should be aware that the TDR-measured effective permittivity will depend on the orientation of the TDR probe with respect to the principle axes of the soil particles or structural units [Jones and Friedman, 2000].

2.3.3. Randomly distributed confocal ellipsoids in a homogeneous background (isotropic)

For an isotropic mixture composed of confocal (layered) ellipsoids composed of 1..K materials with permittivity $\epsilon_1, \epsilon_2, \dots, \epsilon_K$ randomly distributed in a homogenous background material of permittivity, ϵ_0 (Fig. 2-1: B), the effective permittivity, ϵ_{eff} , of the mixture is expressed as [Sihvola and Lindell, 1990; Jones and Friedman, 2000]:

$$\epsilon_{eff} = \epsilon_0 + \frac{\frac{1}{3}[\epsilon_0 + \frac{1}{3}\nu(\epsilon_{eff} - \epsilon_0)] \sum_{j=x,y,z} \frac{n\alpha_j}{\epsilon_0 + \frac{1}{3}\nu(\epsilon_{eff} - \epsilon_0)}}{1 - \frac{1}{3} \sum_{j=x,y,z} N_j^{(l)} \frac{n\alpha_j}{\epsilon_0 + \frac{1}{3}\nu(\epsilon_{eff} - \epsilon_0)}} \quad \text{where,} \quad [2-4]$$

$$\frac{n\alpha_j}{\epsilon_0 + \frac{1}{3}v(\epsilon_{eff} - \epsilon_0)} = \frac{[\phi_1 + \phi_2 + \dots + \phi_K] \cdot \left\{ (\epsilon_1 - \epsilon_0) + \left[\epsilon_1 + N_j^{(1)}(\epsilon_0 - \epsilon_1) + \frac{1}{3}v(\epsilon_{eff} - \epsilon_0) \right] \frac{(\epsilon_2 - \epsilon_1) \frac{\phi_2 + \dots + \phi_K}{\phi_1 + \dots + \phi_K} + \left[\epsilon_2 + N_j^{(2)}(\epsilon_1 - \epsilon_2) + \frac{1}{3}v(\epsilon_{eff} - \epsilon_0) \right] \frac{(\epsilon_3 - \epsilon_2) \frac{\phi_3 + \dots + \phi_K}{\phi_1 + \dots + \phi_K} + \dots}{\left[\epsilon_2 + N_j^{(2)}(\epsilon_2 - \epsilon_1) + \frac{1}{3}v(\epsilon_{eff} - \epsilon_0) \right] + N_j^{(2)}(1 - N_j^{(2)})(\epsilon_2 - \epsilon_1) \frac{(\epsilon_3 - \epsilon_2) \frac{\phi_3 + \dots + \phi_K}{\phi_2 + \dots + \phi_K} + \dots}{\left[\epsilon_2 + N_j^{(3)}(\epsilon_3 - \epsilon_2) + \frac{1}{3}v(\epsilon_{eff} - \epsilon_0) \right] + \dots} \right\}}{\left\{ \left[\epsilon_0 + N_j^{(1)}(\epsilon_1 - \epsilon_0) + \frac{1}{3}v(\epsilon_{eff} - \epsilon_0) \right] + N_j^{(1)}(1 - N_j^{(1)})(\epsilon_1 - \epsilon_0) \cdot \frac{(\epsilon_2 - \epsilon_1) \frac{\phi_2 + \dots + \phi_K}{\phi_1 + \dots + \phi_K} + \left[\epsilon_2 + N_j^{(2)}(\epsilon_1 - \epsilon_2) + \frac{1}{3}v(\epsilon_{eff} - \epsilon_0) \right] \frac{(\epsilon_3 - \epsilon_2) \frac{\phi_3 + \dots + \phi_K}{\phi_1 + \dots + \phi_K} + \dots}{\left[\epsilon_2 + N_j^{(3)}(\epsilon_3 - \epsilon_2) + \frac{1}{3}v(\epsilon_{eff} - \epsilon_0) \right] + \dots} \right\}} \left\{ \left[\epsilon_1 + N_j^{(2)}(\epsilon_2 - \epsilon_1) + \frac{1}{3}v(\epsilon_{eff} - \epsilon_0) \right] + N_j^{(2)}(1 - N_j^{(2)})(\epsilon_2 - \epsilon_1) \cdot \frac{(\epsilon_3 - \epsilon_2) \frac{\phi_3 + \dots + \phi_K}{\phi_2 + \dots + \phi_K} + \dots}{\left[\epsilon_2 + N_j^{(3)}(\epsilon_3 - \epsilon_2) + \frac{1}{3}v(\epsilon_{eff} - \epsilon_0) \right] + \dots} \right\}}$$

This specific form of the confocal ellipsoid model is not published. Using a concentric sphere model with self-consistency (Eq. [2-19] in *Sihvola* [1989]) and a confocal ellipsoid model without self-consistency (Eqs. [2-51] and [2-54] in *Sihvola and Lindell* [1990]) as guides, Eq. [2-4] was derived. Because Eq. [2-4] gives the same results as the published equations for special cases it was derived from, confidence in its correctness is warranted [*A. Sihvola*, personal communication, 2012].

As above, the sum of the depolarization factors for each material must equal 1. For confocal ellipsoids, the depolarization factors of each material are not equal except in the special case of concentric spheres [$N_j = (1/3, 1/3, 1/3)$; *Sihvola and Lindell*, 1990]. For the case of confocal ellipsoids, the dimensions of the semiaxes must obey the equality: $a_1^2 - a_k^2 = b_1^2 - b_k^2 = c_1^2 - c_k^2 \neq 0$ where a_i, b_i, c_i are the dimensions of the i^{th} material ellipsoid semiaxes in the x, y and z directions, respectively. Depolarization factors are calculated by [*Sihvola and Kong*, 1988]:

$$N_j^{(i)} = \int_0^\infty \frac{(abc)du}{2(u_i + k^2) \sqrt{(u_i + a_K^2)(u_i + b_K^2)(u_i + c_K^2)}} \begin{cases} (k = \sqrt{u_i + a_K^2}) j = x \\ (k = \sqrt{u_i + b_K^2}) j = y \\ (k = \sqrt{u_i + c_K^2}) j = z \end{cases} \quad [2-5]$$

where a_K, b_K, c_K are the dimensions of the semiaxes of the reference (inner) ellipsoid (K^{th} material) and u_i is a scalar defining the surface of the ellipsoid of the i^{th} material. The scalar, u_i , is a function of the volume of the composite sphere encompassing the $K - i \dots K$ materials.

For example, in a 3-phase soil system, the inner ellipsoid may be assigned to the solid phase (ϵ_2) which is surrounded by water (ϵ_1) in a background of air (ϵ_0) like the soil-water-air (SWA) configuration (in order from the center toward the outer layer of confocal ellipsoid: soil, water and air) of *Friedman* [1998] and *Jones and Friedman* [2000]. As water content increases, the thickness of the water shell surrounding the inner soil particle ellipsoid increases and therefore the depolarization factors for the water phases changes as a function of water content. The magnitude of the scalar, u , is calculated by equating the total volume of the composite ellipsoid $\left(\frac{4}{3}\pi\sqrt{(u_i + a_K^2)(u_i + b_K^2)(u_i + c_K^2)}\right)$ to the sum of the volumetric fractions of the constituents making up the sphere (e.g., the sum of the volumetric solid and water content in the 3-phase SWA example). This requires finding the root of a third order polynomial in u_i .

For the case of ellipsoids of revolution, (ellipsoids with two of the three semiaxes having equal dimensions), *Jones and Friedman* [2000] developed a second-order approximation to Eq. [2-5] as a function of the aspect ratio of the a and b semi-axis ($a : b$):

$$N_x^{(i)} = \frac{1}{1+1.6(a_i:b_i)+0.4(a_i:b_i)^2} \quad N_y^{(i)} = 0.5(1 - N_x^{(i)}) \quad N_z^{(i)} = N_y^{(i)} \quad [2-6]$$

2.3.4. Choice of geometry and self-consistency with physically-based dielectric mixing models

Even though the dielectric mixing models presented above incorporate various degrees of complexity, they are simple compared to most soils. The solid fraction of a medium-textured soil could potentially be visualized as a mixture with a continuum of particle shapes, from spheres to discs. The variability and distribution of these shapes and sizes would then further influence the geometry of water films (bound and free) and ice. For the discrete ellipsoids model (Eq. [2-3]) different particle shapes for each size fraction (i.e., sand, silt and clay) could potentially be incorporated, but the assignment of different shapes (depolarization factors) to different size fractions would have to be confirmed with direct observations of particle shapes (i.e., microscopy) to be justified and it is still unclear how this subdivision of the solid fraction would potentially affect the shapes of the other phases (i.e., water and ice). Without additional information, assuming simple geometries is likely adequate.

The concentric spherical and confocal ellipsoidal mixing models used by *Friedman* [1998], *Jones and Friedman* [2000] and *Miyamoto et al.* [2005] did not include the coefficient of self-

consistency, ν , but averaged two different configurations of the mixing models according to effective medium approximation theory [Sen *et al.*, 1981; Friedman, 1998]. In the Friedman [1998] and Miyamoto *et al.* [2005] models each material forms a shell of the composite sphere and the permittivity of the infinite background is equal to ϵ_{eff} which is another method for incorporating self-consistency. In the Sihvola model (Eq. [2-4]), all but one of the materials forms a shell of the composite ellipsoid. The 0th material acts as the infinite background in which the composite ellipsoids are embedded. Therefore, even in the special case of concentric spheres and $\nu = 0$, Eq. [2-4] does not give the same result as the equations presented by Friedman [1998] and Miyamoto *et al.* [2005].

2.3.5. Bound water in frozen soils

The effect of bound water on the effective permittivity of unfrozen soils has been treated by Friedman [1998], Or and Wraith [1999], Robinson *et al.* [2002], Robinson and Friedman [2005], Friedman *et al.* [2006], Regalado [2006] and Schwartz *et al.* [2009] and for frozen soils by Watanabe and Wake [2009]. Or and Wraith [1999] used the Debye [1929] equation to estimate the increasing bound water layer thickness as a function of the increased water viscosity with decreasing temperature and then assumed a constant permittivity of 12 for the bound water. Friedman [1998] used the harmonic mean of an exponential function to estimate the increasing average permittivity of the entire water phase (bound and free water) with increasing thickness of water films on soil particles. Robinson *et al.* [2002] used the arithmetic mean of a different exponential equation than that of Friedman [1998] to model the increasing permittivity of the water phase as function of water film thickness and hygroscopic (air-dry) water content. In this work, the influence of bound water on the effective permittivity of frozen soils will be treated in two ways. The first method attempts to synthesize the temperature-viscosity effects described by Or and Wraith [1999] with the function of Friedman [1998]. The second method is very similar to that of Robinson *et al.* [2002] except it uses a linear function similar to that of Watanabe and Wake [2009].

2.3.6. Temperature-dependent modified Friedman [1998] and Or and Wraith [1999] approach

Friedman [1998] presented a model for the mean (harmonic) permittivity of soil water as a function of thickness of water films on particle surfaces:

$$\epsilon_w(d_w) = \frac{d_w \epsilon_{max}}{d_w + \frac{1}{\tau} \ln \left[\frac{\epsilon_{max} - (\epsilon_{max} - \epsilon_{min}) e^{-\lambda d_w}}{\epsilon_{min}} \right]} \quad [2-7]$$

where ϵ_w is the effective permittivity of water as a function of water film thickness, d_w (m), ϵ_{max} is the upper bound of the effective water permittivity, ϵ_{min} is the lower bound and τ is a parameter proportional to the rate of increase of ϵ_w between ϵ_{min} and ϵ_{max} . Friedman chose $\epsilon_{min} = 5.5$ (similar to the effective permittivity of soil particles), $\epsilon_{max} = 80$ and $\tau = 10^{10}$ m.

Or and Wraith [1999] developed a temperature-dependent model of the thickness of bound water films based on the decreased viscosity of water with decreasing temperature. Utilization of the *Debye* [1929] relationship between relaxation time, viscosity and temperature to derive an equation that predicts the thickness of the bound water layer as a function of temperature yields:

$$\delta(T) = \frac{a}{-d' + T \ln \left[\frac{k}{8\pi^2 r^3 c f T} \right]} \quad [2-8]$$

where δ is the thickness of the bound water layer (m) as a function of temperature, T (K), k is the Boltzman constant ($1.3806488 \times 10^{-23}$ J K⁻¹), r is the radius of a water molecule (1.8×10^{-10} - 2.8×10^{-10} m), f is the cutoff frequency (Hz) and a (m), c (Pa S), and d' (K), are empirical constants describing the water viscosity as a function of temperature and distance from the particle surface. In their work, *Or and Wraith* [1999] set $r = 2.5 \times 10^{-10}$ m, $f = 1$ GHz, $a = 1621 \times 10^{-10}$ m, $c = 9.5 \times 10^{-7}$ Pa s and d' (or d in the original paper) = 2047 K.

The model in Eq. [2-8] is sensitive to the choice of the water molecule radius, r . While $r = 2.8 \cdot 10^{-10}$ m is the generally accepted value, *Or and Wraith* [1999] cite evidence for an effective rotational radius between 1.44×10^{-10} m and 2.2×10^{-10} m [*Sposito*, 1981; *Fripiat et al.*, 1982]. The value of $r = 2.0 \times 10^{-10}$ m was chosen for this temperature-dependent model because higher values of r result in singularities in Eq. [2-8] at moderately freezing temperatures. With $r = 2.0 \times 10^{-10}$ m, Eq. [2-8] is defined for temperatures as low as -20 °C.

The values of parameter c and d chosen by *Or and Wraith* [1999] were based on viscosity measurements for unfrozen water at temperatures greater than 0 °C. For super-cooled water below 0 °C, $c = 1.44 \times 10^{-8}$ Pa s and $d' = 3198$ K are more suitable [*Hallett*, 1963]. Thus, the thickness of bound liquid-water layers in soils at freezing temperatures can be estimated using Eq. [2-8] with temperature-dependent c and d' parameters.

It is well known that the effective permittivity of free water (ϵ_{fw}) increases with decreasing temperature according to [Haynes and Lide, 2011]:

$$\epsilon_{fw}(T) = 249.21 - 0.79069(T - 25) + 7.2997 \times 10^{-4}(T - 25)^2 \quad [2-9]$$

Therefore, the temperature-dependence of free water permittivity can be incorporated into Friedman's 1998 model by setting $\epsilon_{max} = \epsilon_{fw}(T)$, $\epsilon_{min} = \epsilon_{solids}$, and $d_w = \delta(T)$. The problem with this modification, however, is that it predicts an increased soil water permittivity at freezing temperatures that are higher than non-freezing temperatures. The bound water thickness increases at freezing temperatures according to Eq. [2-8] and the effective permittivity of bound water is lower than free water. As such, an increased thickness of the bound water layer should decrease the average permittivity of the soil water. I therefore, suggest that the τ parameter in the Friedman model be made a function of temperature.

Setting $r = 2.0 \times 10^{-10}$ m, and holding all other parameters the same as *Or and Wraith* [1999], Eq. [2-8] predicts $\delta(T) = 3.0 \times 10^{-10}$ m at 20 °C. At this thickness, Eq. [2-7] with $\tau = 10^{10}$ m, $\epsilon_{min} = 5$ and $\epsilon_{max} = 83$ (the permittivity of free water at 20 °C) predicts $\epsilon_w = 52$ or 63% of $\epsilon_{fw}(T)$. If τ is adjusted to 9×10^9 m in Eq. [2-7], then $\epsilon_w = 41.5$ or 50% of $\epsilon_{fw}(20)$ at $d_w = \delta(20)$. Therefore, to estimate the temperature dependence of soil water as a function of bound water thickness, τ was adjusted such that $\epsilon_w = 0.5 \cdot \epsilon_{fw}(T)$ at a water film thickness equal to $\delta(T)$. The results of this derivation are presented in Fig. 2-2. The slight modification of $\tau = 9 \times 10^9$ at 20 °C does not change the original Friedman formulation very much. As in *Friedman* [1998], the dielectric permittivity as a function of water content is estimated by substituting $\theta / (A_s \rho_b)$ for $d_w = \delta(T)$ in Eq. [2-7] where θ is the volumetric water content ($\text{m}^3 \text{m}^{-3}$), A_s is the specific surface area ($\text{m}^2 \text{kg}^{-1}$) and ρ_b is the bulk density (kg m^{-3}).

The derivation of this temperature-dependent permittivity hinges on the *Friedman* [1998] model passing through what seems to be an arbitrary permittivity-water film thickness point. The bound water film thickness estimation at each temperature is physically-based, but is still a simplification of reality. It does not take into consideration the influences of solutes in the soil solution, for example. The 50% of free water permittivity requirement is not physically-based, but is based on the fact that it is close to the original model by *Friedman* [1998]. Unfortunately there is very little data of the effective permittivity of bound water available. What data are

available are variable and only measured at room temperature (see values in *Or and Wraith* [1999], *Robinson et al.* [2002], and *Friedman et al.* [2006]). To the authors' knowledge, there are no observations of the dielectric permittivity of bound water as a function of temperature, making it difficult to not use over-simplified approaches.

The advantages of having a continuous soil water permittivity function is that it simplifies the use of multiphase dielectric permittivity models because bound water is not separated from the rest of the liquid-water phase (i.e., all liquid-water belongs to one phase of the model). This is advantageous for frozen soils because the methods used to estimate liquid-water in frozen soils do not distinguish between bound and unbound water.

2.3.7. Temperature-dependent linear function based on *Robinson et al.* [2002]

Measurements of bound water permittivity cited by *Or and Wraith* [1999], *Robinson et al.* [2002], and *Friedman et al.* [2006] show the permittivity of the water phase increases with distance from the particle surface, approaching the permittivity of free water within 3 or 4 molecular diameters. The simplest model for this phenomenon is a linear “ramp” function:

$$\epsilon_w(x, T) = \begin{cases} \frac{x}{d_0} \epsilon_{fw}(T) + \frac{x-d_0}{-d_0} \epsilon_s & 0 \leq x < d_0 \\ \epsilon_{fw}(T) & x \geq d_0 \end{cases} \quad [2-10]$$

where $\epsilon_w(x, T)$ is the soil water permittivity as a function of distance, x (m) from the soil particle surface, $\epsilon_{fw}(T)$ is the free water permittivity as a function of temperature, ϵ_s is the permittivity of the solid phase and d_0 is the thickness of the bound water layer. For this work we set d_0 approximately equivalent to 4 water molecule diameters ($d_0=12 \times 10^{-10}$ m). Like *Robinson et al.* [2002], the mean permittivity of the soil water is estimated by taking the arithmetic mean of Eq. [2-10]:

$$\epsilon_w(d, T) = \frac{1}{d} \int_0^d \epsilon_w(x, T) dx \quad [2-11]$$

where d is the thickness of the water films on the soil particles (m) and, as above, is related to volumetric water content by $d = \theta / (A_s \rho_b)$.

The two models presented here represent two bounds for incorporating the influence of bound water on the mean soil water permittivity in frozen soils. The underlying assumption of

both models is that bound water exists only due to adhesive forces between the water and soil particles and do not consider Gibbs-Thompson or any other effects. The modified Friedman-Or-Wraith approach based on the harmonic mean of an exponential function represents what is possibly a maximum decrease of mean soil water permittivity as a function of increased bound water with decreasing temperatures. The arithmetic mean of the linear model represents a minimum influence of bound water and the only temperature effects on free water permittivity are considered. Because of the limited data available on the temperature-dependent permittivity of bound water as a function of distance from soil particles, combining the soil water permittivity models with dielectric mixing models followed by comparison with actual measurements of soil effective permittivity is the only practical test available.

2.4. Materials and Methods

2.4.1. Published data sets

For the simulation of unfrozen soil with discrete and confocal mixing models, the data of *Friedman* [1998] and *Miyamoto et al.* [2005] were digitized. For frozen soils, TDR-measured ϵ_{eff} and independently measured θ_l by gas dilatometer [*Spaans and Baker*, 1995] and by pulsed NMR [*Watanabe and Wake*, 2009] were used. The frozen soil datasets were selected on the criteria that: (1) θ_l was measured on frozen soil samples independently of TDR; and (2) θ_l was measured on frozen soil samples with at least two unique initial volumetric water contents ($\theta_{l,init}$) prior to freezing. It was assumed that frost heave was insignificant, which means the sum of volumetric fraction of soil, ice, water, and air maintain unchanged at all temperatures. Ice content was included in the *Spaans and Baker* [1995] dataset, but was calculated according to mass balance for *Watanabe and Wake*'s data by the following equation:

$$\theta_{i,T} = (\theta_{l,init} - \theta_{l,T}) \rho_w / \rho_i \quad [2-12]$$

where $\theta_{i,T}$ is the estimated ice content at temperature, T , $\theta_{l,init}$ is the initial liquid-water content of the sample prior freezing, $\theta_{l,T}$ is the measured liquid-water content at temperature, T , ρ_w is the density of water (assumed to be 1 g cm⁻³) and ρ_i is the density of ice (assumed to be 0.917 g cm⁻³). The reader is referred to the original papers for a complete description of methodologies. Differences in the methodologies between the two papers relevant to this work will be

highlighted in the discussion section of this paper. The soil microcosms used by *Spaans and Baker* [1995] and *Watanabe and Wake* [2009] were closed so that the total mass of water in the soil sample, regardless of phase did not change throughout the experiment and was equal to the initial water content.

For the soils without measurements of specific surface area (A_s , $\text{m}^2 \text{g}^{-1}$), it is calculated according to the equation for montmorillonite-dominate soils presented by *Or and Wraith* [1999]

$$A_s = 5.65 * CL - 18.9 \quad [2-13]$$

where CL is the clay content in percent. An $A_s = 0.005 \text{ m}^2 \text{g}^{-1}$ was assigned to industry sand and the phosphogypsum was treated in the same manner as real soil.

2.4.2. Calculation and optimization in frozen soils

For both mixing models described in the Theory section, the θ_l and θ_i measurements from *Spaans and Baker* [1995] and *Watanabe and Wake* [2009] datasets were used to model the TDR-measured ϵ_{eff} . A MathCad (version 15, Parametric Technology Corporation) program was developed to find optimized coefficient of self-consistency (ν) and aspect (Eq. [2-6]) under various assumptions about the influence of temperature and bound water on the soil water permittivity (i.e., Eqs. [2-7], [2-9] and [2-11]). The similarity between modeled and measured ϵ_{eff} and θ_l was assessed by plotting the estimated and measured ϵ_{eff} versus temperature, estimated θ_l versus the measured θ_l with 1:1 lines, and calculation of three goodness-of-fit parameters: (1) root means square error (RMSE); (2) Nash-Sutcliffe Efficiency (NS-Eff); and (3) average deviations (Avg-Dev).

The *RMSE* is calculated as [*Campbell*, 2002]

$$RMSE = \sqrt{\frac{\sum_{i=0}^n (\epsilon_{meas}^i - \epsilon_{model}^i)^2}{n}} \quad [2-14]$$

where $i = 1 \dots n$ is the index for each of the n ϵ_{eff} and θ_l measurements, $x_{1,i}$ is measured values and $x_{2,i}$ is the estimated values with mixing models.

NS-Eff is commonly used to assess the predictive power of hydrological models or quantitatively assess the predictive accuracy of model outputs. It is calculated as

$$NS-Eff = 1 - \frac{\sum_{i=1}^n (\epsilon_{meas}^i - \epsilon_{model}^i)^2}{\sum_{i=1}^n (\epsilon_{meas}^i - \overline{\epsilon_{meas}})^2} \quad [2-15]$$

where ϵ_{meas} is measured permittivity, ϵ_{model} is modeled permittivity, $\overline{\epsilon_{meas}}$ is the mean of measured permittivities. A *NS-Eff* equal to 1 indicates a perfect match of modeled permittivity to the measured permittivity. A *NS-Eff* equal to 0 corresponds to that the model predictions are as accurate as the mean of the measured permittivity, whereas a *NS-Eff* < 0 occurs when the mean of the measured permittivities is a better predictor than the modeled permittivity or when the residual variance (numerator) is larger than the data variance (denominator).

The Avg-Dev is calculated as

$$Avg-Dev = \frac{1}{n} \sum_{i=1}^n (\epsilon_{model}^i - \epsilon_{meas}^i) \quad [2-16]$$

The Avg-Dev could be zero, negative or positive that indicates the modeled results equal to, underestimate or overestimate the measured values in general, respectively.

2.4.3. Additional measurement on local soil samples

Six soils from Alberta and Saskatchewan, Canada, were used in this study and are named according to mapping series where appropriate: Asquith B horizon (sandy loam), Brightbank C horizon (loamy sand), Malmo A horizon (silty clay loam), Mundare A horizon (loamy sand), and phosphogypsum tailings from a phosphate fertilizer production industrial site. An industrial sand was also tested. See Table 2-1 for selected physical properties of the six soils.

Air-dry soil samples of all six soils were wetted with known quantities of deionized water to obtain various saturation levels, from air-dry to near saturation at increments of around 0.05 kg kg⁻¹ and then equilibrated for at least 24 hours in sealed freezer bags at room temperature. The mixed soil samples at each of the prescribed moisture contents were then uniformly packed to a depth of 15 cm in a copper cylinder of 5.08 cm i.d. and of 21 cm in length and sealed with a copper cap to prevent evaporation. The cylinder was wrapped with a cooling coil constructed from 5 mm i.d. copper tubing and bonded to the copper soil cylinder with heat-conducting epoxy. The cooling coil was connected to a temperature-controlled water bath (Isotemp Refrigerated Circulators 3013S, Fisher Scientific, USA) with a 50/50 Ethylene glycol-water mixture by volume is used as a coolant. Temperature was controlled to cool the soil samples from 20°C

down to -30°C and then back up to 20°C in 1.5°C steps between 0.5 and -5°C , 2°C steps for temperatures between -5 and -10°C , and 5°C steps for temperatures less than -10°C and greater than 5°C . For each soil, the freezing and thawing cycles took approximately 1.5 days.

A TDR probe consisting of three parallel stainless steel rods of 1.6 mm in diameter, 10 cm in length with 1 cm inter-rod spacing was inserted in the center of the cylinder, and connected to a TDR cable tester (Tektronix 1502C, Beaverton, Or, USA). The Tacqbeta software [Evelt, 2000] was programmed to continuously record the TDR traces every 10 seconds during the freezing and thawing processes. Three small 0.5 mm diameter thermistors were installed at 5 cm below the soil surface adjacent to the TDR probe rods and connected to a data logger (CR1000, Campbell Scientific Canada, Edmonton, Canada) for soil temperature measurement of the soil volume sampled by the TDR probe. After the experiment was done, Tacqbeta was used to manually analyze the TDR waveform to estimate ϵ_{eff} . Again, we assume that frost heave is insignificant that the total volume remained constant.

2.4.4. Additional freeze-thaw cycles

The medium-textured Malmo silt loam and coarse textured Mundare loamy sand (see Table 2-1) were selected for additional freeze-thaw experiment. Two samples of each soil were tested, $\theta_{init} = 0.2$ and $0.36 \text{ m}^3 \text{ m}^{-3}$ for Malmo silt loam and $\theta_{init} = 0.125$ and $0.36 \text{ m}^3 \text{ m}^{-3}$ for Mundare loamy sand. The sample preparation and measurement procedures follow the similar manner as previous experiment described above except two cycles of freezing and thawing were conducted. The first freezing cycle decreased the soil to a temperature of -15°C and the second cycle to -30°C . Temperature changes were similar to the aforementioned freezing and thawing experiments. The permittivity measurements were made when the soil temperature did not change for approximately 0.5 h. Approximately 3 days were required to complete the two freeze-thaw cycles.

2.5. Results

2.5.1. Sensitivity of discrete and confocal ellipsoid mixing models for unfrozen, 3-phase soils

To better understand the behavior of the discrete and confocal ellipsoid mixing models (Eqs. [2-3] and [2-4]), effective permittivity-water content relationships ($\epsilon_{eff}(\theta)$) were simulated for unfrozen soils using a 3-phase ($K = 2$) version of the models. For the simulation, the total porosity of the soil was assumed to be $0.5 \text{ m}^3 \text{ m}^{-3}$, $\epsilon_w = 81$ (soil water permittivity), $\epsilon_s = 5$ (soil solids permittivity), and $\epsilon_g = 1$ (air permittivity). Both discrete and confocal models were set to a solid-water-air (SWA) configuration such that $\epsilon_2 = \epsilon_s$, $\epsilon_1 = \epsilon_w$ and $\epsilon_0 = \epsilon_g$. For the discrete model, it was assumed the aspect of all phases were the same (i.e., the depolarization factors for each phase are equal).

Figure 2-3 summarizes the influence of particle shape (aspect) on $\epsilon_{eff}(\theta)$. For the discrete model (Fig. 2-3: A), the self-consistency coefficient, ν , was set to 1 and $\nu = 0$ for the confocal model (Fig. 2-3: B). The aspect in Fig. 2-3 represents the ratio of the dimensions of the semiaxes of the x and y directions ($a : b$; Fig. 2-1). When aspect < 1 , the ellipsoids are prolate, and oblate when the aspect > 1 . Because of the random orientation of the ellipsoids in both the discrete and confocal models, the $\epsilon_{eff}(\theta)$ relationships for extreme oblate or prolate shapes are quite similar which would not be observed if the ellipsoids had a preferred orientation [Jones and Friedman, 2000]. Because the soil water permittivity is much higher than the other solid and air phases, it is the aspect of the water ellipsoids to which the $\epsilon_{eff}(\theta)$ relationship is most sensitive. The cases of disc-like (aspect = 0.01) and spherical (aspect = 1) represent bounds for $\epsilon_{eff}(\theta)$ with disc-like particles showing an almost linear relationship and spheres showing the most nonlinear relationship.

The influence of the coefficient of self-consistency, ν , for the case of spherical ellipsoids for both discrete and confocal models is presented in Fig. 2-4. For discrete spheres, increasing ν increases the effective permittivity at higher water contents and results in a $\epsilon_{eff}(\theta)$ relationship that might be observed for a real soil, and confirms the assertion that discrete model with $\nu = 0$ is more appropriate mixtures that are less dense than soils [Sihvola and Lindell, 1992]. In the case of concentric spheres, increasing ν significantly reduces the curvature of the $\epsilon_{eff}(\theta)$ relationship.

When ν is set to higher values (i.e., 2), the discrete and confocal models are very similar. Therefore, it is possible to represent the same dataset with two very different models which introduces a problem of non-uniqueness if parameters to be optimized for fitting a data set.

The concentric sphere models used by *Friedman* [1998] and *Miyamoto et al.* [2005] showed strong differences with respect to configuration. The discrete and confocal models presented in Figs. 2-3 and 2-4 were for solid-water-air (SWA, $\epsilon_2 = \epsilon_s$, $\epsilon_1 = \epsilon_w$, and $\epsilon_0 = \epsilon_g$) configurations. The SWA configuration for the cases discrete and concentric spheres is compared to an air-solid-water (ASW, $\epsilon_2 = \epsilon_a$, $\epsilon_1 = \epsilon_s$, and $\epsilon_0 = \epsilon_w$) configuration in Fig. 2-5. For both discrete and concentric spheres, configuration changes $\epsilon_{eff}(\theta)$ significantly when ν is equal for both SWA and ASW configurations. However, as shown in Fig. 2-5, setting $\nu = 2$ in the SWA configuration results in a very similar $\epsilon_{eff}(\theta)$ relationship to the ASW configuration with $\nu = 0$. Therefore the ability to manipulate ellipsoid shape and the self-consistency parameter makes these models very flexible, but optimization of model parameters is likely difficult because two very different models may describe the same data set equally well with slight parameter adjustments.

2.5.2. Simulation of effective permittivity in frozen soils with 4-phase discrete and concentric spheres

Analysis of 3-phase discrete and concentric sphere mixing models showed very similar $\epsilon_{eff}(\theta)$ relationships at high values of the ν parameter. But how does the $\epsilon_{eff}(\theta)$ relationship change when an additional ice phase is added to simulate freezing conditions? Figures 2-6 and 2-7 show $\epsilon_{eff}(\theta)$ curves for 4-phase ($K = 3$) discrete and concentric spheres for unfrozen and frozen conditions for $\nu = 0, 1$ and 2. Frozen conditions were simulated by holding the total water content (ice + liquid-water) constant, but replacing water with ice according to Eq. [2-12] instead of replacing water with air as in a drainage process under unfrozen conditions. For Figs. 2-6 and 2-7, the total porosity of the soil was assumed to be $0.5 \text{ m}^3 \text{ m}^{-3}$, $\epsilon_w = 81$, $\epsilon_s = 5$, $\epsilon_a = 1$, as in the 3-phase model and $\epsilon_{ice} = 3.2$. Both discrete and confocal models were set to a solid-water-ice-air (SWIA) configuration such that $\epsilon_3 = \epsilon_s$, $\epsilon_2 = \epsilon_w$, $\epsilon_1 = \epsilon_{ice}$ and $\epsilon_0 = \epsilon_a$ (Fig. 2-6; Fig. 2-7: A~C). In addition, another solid-ice-water-air (SIWA; $\epsilon_3 = \epsilon_s$, $\epsilon_2 = \epsilon_{ice}$, $\epsilon_1 = \epsilon_w$ and $\epsilon_0 = \epsilon_a$) configuration was simulated for the confocal model (Fig. 2-7: D~F).

Whereas the discrete and confocal models are very similar under unfrozen conditions for $\nu = 2$, they show different behavior for frozen conditions (Figs. 2-6: C and 2-7: C) and the confocal model is very sensitive to the position that ice occupies in the composite ellipsoid (Fig. 2-7). It should be noted that the 4-phase version of Eq. [2-4] gives identical results to the 3-phase version when the volumetric ice content is set to zero which can be used as a check that the model is consistent.

Because of this difference in behavior between the discrete and concentric sphere models for frozen conditions, the problems with identification of the model and model parameters that best describes the data that were apparent in the 3-phase simulations of unfrozen soils, are likely not as severe for the 4-phase simulation of frozen soils.

2.5.3. Performance of three phase discrete and confocal ellipsoid models for describing measured $\epsilon_{eff}(\theta)$ relationships in the literature

2.5.3.1. Unfrozen soils

For testing the discrete and confocal mixing models on real soils, data for both unfrozen and frozen scenarios were used. For unfrozen soils, published data from *Friedman* [1998] and *Miyamoto et al.* [2005] and six local soils described in Table 2-1 were used. For frozen soils, published data from *Spaans and Baker* [1995] and *Watanabe and Wake* [2009] were used.

For the *Friedman* [1998] and *Miyamoto et al.* [2005] unfrozen soils, 3-phase ($K = 2$) discrete and confocal ellipsoid models were tested for constant soil water permittivity and including bound water effects by assuming the mean soil water permittivity varied with water content according to the *Friedman* [1998] model (Eq. [2-7]). The models fit the data well for both constant and variable soil water permittivity (Table 2-2), but the model parameters differed for the two soil water permittivity scenarios. Fitting with variable water permittivity is shown in Fig. 2-8. It is also noteworthy that a good fit was accomplished with the SWA configuration of the models whereas *Friedman* [1998] and *Miyamoto et al.* [2005] averaged two configurations (SWA and ASW) to model the same data. Comparison of measured and modeled $\epsilon_{eff}(\theta)$ for the local soils is presented in Table 2-3 and Fig. 2-9. Both discrete and confocal (concentric sphere) model fit the data well.

2.5.3.2. Frozen soils

For the frozen soil datasets originally published by *Spaans and Baker* [1995] and *Watanabe and Wake* [2009], 4-phase ($K = 3$) discrete and confocal ellipsoid models with SWIA configurations were fit to the data for 4 different soil water permittivity models: (1) temperature-dependent, Friedman-Or-Wraith synthesis (Fig. 2-2, Eqs. [2-7] & [2-8]); (2) temperature-dependent linear model (Eqs. [2-10] & [2-11]); (3) soil water permittivity equal to temperature-dependent free water permittivity (Eq. [2-9]); and (4) constant soil water permittivity equal to the permittivity of free water at 0 °C ($\epsilon_w = 88$). For the confocal model, the SIWA configuration was explored as well, but it did not perform any better than the SWIA configuration. Therefore, only the results for the more realistic SWIA configuration will be presented.

Comparison of modeled and measured $\epsilon_{eff}(T)$ and best-fit model parameters are presented in Table 2-4. With respect to the RMSE, the performance of both the discrete and confocal models was very similar, and good agreement was generally achieved. For the confocal model, the best-fit aspect parameter ranged between 1 and 2. For the discrete model, the aspect of one or more of the phases was adjusted which increased the number of fitting parameters to 4 (aspects for solid, ice and water phases and self-consistency), compared to 2 for the confocal model (one aspect and the coefficient of self-consistency). Despite the increased number of fitting parameters for the discrete model, it did not outperform the confocal model, only showing a marginally better fit for the Tottori and Waukegan soils. Also, the various assumptions about the effects of bound water on the average soil water permittivity did not dramatically change the goodness of fit for either discrete or confocal models compared to the assumption of a constant ϵ_w except in the case of the Waukegan silt loam [*Spaans and Baker*, 1995] where assuming the linear soil water permittivity resulted in a significantly better fit for the confocal model. The measured and modeled $\epsilon_{eff}(T)$ relationships for the frozen soil data sets are presented in Figs. 2-10 and 2-11 for the discrete and confocal models respectively for the $\epsilon_w = 88$ scenario. From the *Watanabe and Wake* [2009] dataset, the models best described the coarse soils compared to the structured, medium textured soils.

Using the best-fit models for each soil for the $\epsilon_w = 88$ scenario, the model-predicted liquid-water content at each temperature was calculated and compared to measured liquid-water content (Fig. 2-12). In most cases, the modeled liquid-water content is in fairly good agreement with the

liquid-water content but some bias is apparent in the medium-textured soils. For example, in the Mie Andisol the modeled liquid-water content is greater than the measured liquid-water content in frozen conditions at high initial water contents (Fig. 2-12: C). In the Fujimori soil, the modeled liquid soil water content is generally underestimated in frozen conditions (Fig. 2-12: D).

2.5.4. Measurement of $\epsilon_{eff}(T)$ during soil freezing and thawing

Freezing and thawing curves measured on the Mundare loamy sand and Malmo silty loam soils (Table 2-1) for two separate initial water contents are presented in Figs. 2-13 and 2-14, respectively. The figures show both ϵ_{eff} and θ_l as a function of temperature. The liquid-water content was estimated using the parameters from the 3-phase discrete model for the Malmo soil and the confocal model for the Mundare soil fitted to unfrozen $\epsilon_{eff} - \theta_l$ measurements which were then used in a 4-phase model to estimate θ_l under frozen conditions. The validity of using an unfrozen model to estimate water contents in a frozen soil will be discussed later. The purpose of calculating the liquid-water content for these freezing and thawing curves was to show that thawing curves start at different water contents (permittivities) depending on the degree of freezing (i.e., final freezing temperature) prior to thawing.

During the freezing cycles, there are some sharp changes in effective permittivity (Fig. 2-13: C and Fig. 2-14: A&C). This is likely a result of super cooling of water followed by latent heat release when seed ice forms during the phase change. The heat release causes a disruption in ice formation and appears to also melt some ice as indicated by the sharp increase in effective permittivity during the transient stage. This phenomenon has also been observed by *Suzuki* [2004]. There also appears to be hysteresis between freezing and thawing cycles which is more apparent in the medium-textured Malmo soil than in the coarse-textured Mundare soil. For both soils the freezing curves track on top of each other except for occurrences latent heat release. In the coarse-texture Mundare soil, the thawing curves generally track on top of each other, but in the medium textured Malmo soil, the thawing curves do not always track on top of each other especially at $T < -5$ °C. There were also some difference noticed for $T > 0$ °C, but these are likely due to experimental error or lack of thermal equilibrium because it is difficult to conceive of ice existing at temperatures above 0 °C.

2.6. Discussion

2.6.1. Physical significance of mixing model parameters

The discrete and confocal ellipsoid mixing models appear to do a reasonable job of describing TDR-measured effective permittivity on unfrozen and frozen soils when the aspect and self-consistency parameters are optimized. However, as indicated by *Sihvola and Lindell* [1990], and observed in this work, more than one model can adequately describe the same measurements. Therefore, even though the dielectric mixing models are physically-based, the physical significance of their parameters is not entirely clear. For the confocal model, the assumption of concentric spheres or slightly oblate ellipsoids is adequate for the soils presented in this paper. The best fit self-consistency parameter ν varied between ~ 0.05 - ~ 1.4 depending on soil type. The discrete ellipsoid model describes the measurements just as well as concentric spheres model in most circumstances, but only when the aspect of one or more of the phases is adjusted. This would indicate that even though the simple geometry of concentric spheres is not exactly representative of real soils, the relative positions of soil constituents is perhaps the most important attribute of the model for a physically realistic representation of the soil (e.g., *Friedman* [1998], *Miyamoto et al.* [2005] and *Blonquist et al.* [2006]). The ability to place the various soil constituents next to or away from one another is not part of the discrete ellipsoid model and, therefore, the aspect of the ellipsoids (and coefficient of self-consistency) has to be adjusted to get similar results to the concentric sphere model. Because the confocal model is more parsimonious (only two fitting parameters) and allows a physically realistic configuration of the phases, it is likely the preferred model. Best fit parameters were different for each soil suggesting soil-specific calibrations are required when using these models.

An interaction between the distinct geometries of the discrete and confocal ellipsoid models and the coefficient of self-consistency is also apparent. For the unfrozen and frozen soils presented in this paper, $0.05 < \nu < 1.4$ for the confocal ellipsoid model when the permittivity of soil water was assumed to be constant. In the case of the frozen soils $0.2 < \nu < 0.5$, the smaller values of the coefficient of self-consistency for the frozen soils gives a family of $\epsilon_{eff}(\theta)$ similar to those shown in Fig. 2-7: A&B. The magnitude of self-consistency parameter was consistently smaller for the discrete model, compared to the confocal model. This interaction between self-consistency and model geometry, especially in frozen conditions may be clarified by considering

how the water and ice phases are treated in the two different models. First consider the 3-phase concentric sphere model representing unfrozen conditions. Drying conditions result in a smaller water shell within the composite sphere, but the increasing volume of air is not explicitly accounted for in the model because air acts as an infinite background. The drying process in an unfrozen soil is simulated similarly in the discrete spheres model - water is disappearing from the mixture. Under freezing conditions, however, the shrinking water shell on the concentric spheres is being replaced by a growing ice shell and the response of the effective permittivity is very sensitive to whether water or ice is adjacent to the solid phase (Fig. 2-7). In the discrete ellipsoids model, the ellipsoids are randomly distributed and there is no mechanism to preferentially place one phase next to another and so the effective permittivity is only sensitive to the total volume of each phase.

2.6.2. Consistency of 3-phase and 4-phase mixing model parameters

When independent measurements of liquid-water, ice and effective permittivity are available, it is possible to find one set of model parameters that reasonably describe both frozen and unfrozen conditions as shown in this work (Table 2-4; Figs. 2-10, 2-11, and 2-12). This suggests that it may be possible to fit a 3-phase mixing model to a set of $\epsilon_{eff} - \theta_l$ measurements obtained in unfrozen conditions and use those parameters in a 4-phase mixing model for frozen conditions, but the only way to confirm this possibility is to have independent measurements of liquid-water and ice contents under frozen and unfrozen conditions. The difficulty in obtaining independent measurements of liquid-water and ice under frozen conditions, however, makes it very difficult and time consuming to obtain mixing model parameters under frozen conditions. It is relatively easy, however, to obtain measurements of ϵ_{eff} under frozen conditions and the results shown here suggest that it is reasonable to use parameters obtained under unfrozen conditions for frozen soils with caution. For the datasets in this paper, there were too few unfrozen water contents (2 for *Spaans and Baker* [1995], and only 3 or 4 for all but one of the *Watanabe and Wake* [2009] soils) to fit the models using unfrozen data only, and then compare to frozen data.

2.6.3. Bound water

The results presented in this work suggest that accounting for bound water effects on the permittivity of the soil water phase is not necessary for calibrating TDR for frozen soils.

Assuming various models for the effects of bound water on the soil water permittivity caused the best fit parameters to change, but did not result in an overall better description of the measurements. In unfrozen soils, using a combination of discrete and concentric sphere mixing models, *Blonquist et al.* [2006] concluded that soil microstructure and the configuration of soil constituents explained the $\epsilon_{eff}(\theta)$ relationship without having to invoke bound water effects. *Jones and Friedman* [2000] showed that the particle shape effects play an equal role in modeling ϵ_{eff} for particles of high respect ratio and can reduce the surface area effects. The viscosity-based Debye model developed by *Or and Wraith* [1999] does not include the effects of solutes in the soil solution which may be important when considering frozen soils. During freezing, the formation of ice excludes ions resulting in a more concentrated solution in the liquid-water phase. When solutes are considered, the thickness of the diffuse double layer in colloidal dispersions is actually inversely proportional to the square root of solute concentration and linearly proportional to the square root of temperature [*Russel et al.*, 1992]:

$$\kappa^{-1} = \sqrt{\frac{\epsilon_r \epsilon_a k T}{2 N_A e^2 I}} \quad [2-17]$$

where κ^{-1} (m) is the Debye length, ϵ_r is the relative permittivity of the solution, ϵ_a is the permittivity of free space (air, A s V⁻¹ m⁻¹), k is the Boltzman constant (1.3806488×10⁻²³ J K⁻¹), T is temperature (K), N_A is Avagadro's number (mole⁻¹), e is the elementary charge (C), and I is ionic strength of the solution (mole m⁻³). If it is assumed that the thickness of the bound water layer is proportional to the Debye length, then Eq. [2-17] suggests the permittivity of the solution within the Debye radius increases with increasing ionic strength, and also increases with decreasing temperature.

This, however, does not exclude the possibility of viscosity effects because of the exponential increase in viscosity with decreasing temperature. However, the model developed by *Or and Wraith* [1999] did not account for the influence of solutes on the viscosity of water. Some solutes such as ammonium chloride, potassium chloride and potassium nitrate decrease the viscosity of water [*Haynes and Lide*, 2011]. Further the strong exponential relationship between viscosity and temperature for pure water does not seem to apply to salt solutions [*Melinder*, 2007]. The physical and chemical dynamics of the soil solution at freezing temperatures are complex. With only room temperature measurements of bound water permittivity available, it is

difficult to incorporate bound water effects into dielectric mixing models. The observations in this paper, however, suggest that bound water effects on mean soil water permittivity are difficult to quantify and are likely soil-specific.

2.6.4. Hysteresis in soil freezing and thawing curves

The hysteresis between the measured soil freezing and thawing curves is most likely attributable to super-cooling and osmotic freezing point depression. Both processes result in water freezing at a much lower temperature than ice melts. Super-cooling is apparent in some of the freezing curves presented in Figs. 2-13 and 2-14. Super-cooling is the process by which water reaches a temperature well below freezing before significant ice crystal nucleation occurs. Once significant ice crystals form, latent heat is released which may melt microscopic ice crystals in the surrounding solution which likely explains the sharp increase in effective permittivity in some of the freezing curves; this feature was not evident on all freezing curves, however, once formed, the ice melts at higher temperature than water freezes. The osmotic effect results in a freezing point depression and because solutes are generally excluded from ice crystals there is no corresponding melting point depression for the ice.

The measured freezing curves generally track on top of one another, except in the case where latent heat release from ice nucleation causes momentary melting. However, thawing curves which start after two different freezing cycles down to two different temperatures do not track on top of each other, especially in the medium-textured Malmo soil. The explanations for hysteresis between the freezing and thawing curves may also help to explain why two different thawing curves do not correspond to one another. At a given initial water content, the amount of ice formed during freezing will depend on the final temperature to which the soil is frozen. The lower the final freezing temperature prior to the commencement of thawing, the greater the amount of ice formed. Therefore, the thawing curve starting at $-15\text{ }^{\circ}\text{C}$ shows an effective permittivity greater than or equal to the thawing curve starting at $-30\text{ }^{\circ}\text{C}$ because there is less ice at the beginning of thawing and this trend continues throughout the thawing process if thermal equilibrium is not reached at temperature because more heat will be required to melt a greater amount of ice. Even under thermal equilibrium conditions, hysteresis could still possibility occur because of solute exclusion during freezing. This process potentially creates “pure” ice which would melt at a higher temperature than the soil solution freezes. A short period of 0.5 h was

used in the hysteresis test of the two local soils to get thermally equilibrated to reduce the time required to measure so many points on the freezing-thawing curves. There might be equilibrium bias at duration of phase change but it is assumed to be fairly small at low negative temperatures because only small volumes of water are involved in phase changes at these temperatures. *Watanabe and Wake* [2009] indicated that the soil samples prepared for NMR determination of θ_l were first frozen by dipping them in liquid nitrogen and then equilibrated at $-20\text{ }^\circ\text{C}$ in a freezer, but the soil samples prepared for K_c measurement by TDR were not submerged in liquid nitrogen prior to equilibration in a $-15\text{ }^\circ\text{C}$ cooling bath. Using these two different methods of sample preparation indicates that the NMR samples and TDR samples were on two separate thawing curves, starting at $-15\text{ }^\circ\text{C}$ for the TDR samples and at a much lower temperature for the NMR samples, but their samples were given much more time to reach thermal equilibrium. If freezing/thawing hysteresis is a result of osmotic effects rather than thermal equilibrium effects, this may explain some of the disagreement between the mixing models and measurements especially in the Fujimori silt loam and Mie Andisol (loam).

2.7. Conclusions

Several effects that influence effective permittivity in unfrozen and frozen conditions have been identified using two dielectric mixing models, the discrete and confocal ellipsoid model, through the analysis of published and new unfrozen and frozen data. The principles and significance of self-consistency and particle shape (aspects) of dielectric mixing models were illustrated in detail and comparison was made with other models appeared in literature. The study demonstrates that the bound-water effect and temperature-dependent water permittivity (ϵ_w) do not need to be considered for calibrating TDR to frozen soils, but the influence of bound water on the permittivity of bulk water in frozen soils still merits further study. The discrete and confocal ellipsoid models show potential for estimating θ_l through parameter optimization. The mechanisms for the observed hysteresis between freezing and thawing curves will continue to be investigated.

Table 2-1. Description of six local soils used to measure freezing and thawing curves

Soil type	location	Classification	Particle size distribution ^a (%)			Particle density ^b	Organic carbon	Air-dry water content ^c
			Sand	Silt	Clay	Mg m ⁻³	%wt	Mg Mg ⁻¹
Industry sand	n/a	n/a	100	0	0	2.67	0	0.0002
Brightbank loamy sand, C horizon	Legal, Alberta	Orthic Black Chernozem	80.87	14.13	5.00	2.64	n/a	0.0096
Asquith sandy loam, B horizon	Near Saskatoon, Saskatchewan	Orthic D. Br. Chernozem	68.80	20.20	11.00	2.65	n/a	0.0015
Malmo silty loam, A horizon	Ellerslie research farm, Alberta	Eluviated Bl. Chernozem	28.13	54.87	17.00	2.53	5.26 ^d	0.0168
Mundare loamy sand, A horizon	Near Ft. Saskatchewan, AB	Eluviated Bl. Chernozem	84.00	10.97	5.03	2.53	2.33 ^e	0.0107
Phosphogypsum tailings	Agrium, Inc, Ft. Saskatchewan, AB	n/a	32.50	60.44	7.16	2.31	n/a	0.0003

^a ISSS classification, hydrometry method; gypsum particles expressed in the manner of soil particle.

^b pycnometry method.

^c gravimetry method, oven dry at 105°C for 24 h; gypsum was oven dried at 50 °C for 48 h.

^d *Feng* [2009].

^e *Hallin* [2009].

Table 2-2. Best fit parameters and goodness of fit for each published unfrozen soil data to predict permittivity (ϵ_{eff}) using discrete and confocal models of a SWA configuration with water permittivity calculated using *Friedman 1998* model (Eq. [2-7]) and $\epsilon_w = 80$

Soil type	Parameters	$\epsilon_w = \text{Friedman 1998}$		$\epsilon_w = 80$	
		Discrete	Confocal	Discrete	Confocal
Kumamoto Andisol ^a	Self-consistency	0.75	0.737	0.425	0.501
	Aspect ^b	1	2.546	3.083	2.851
	RMSE	0.894	0.662	0.757	0.443
	NS-Eff	0.986	0.992	0.99	0.997
	Avg-Dev	-0.187	-0.106	-0.183	-0.029
Miyazaki Andisol ^a	Self-consistency	1.098	1.395	0.899	1.089
	Aspect ^b	1	1	1.393	1
	RMSE	0.651	0.696	0.619	0.544
	NS-Eff	0.99	0.989	0.991	0.993
	Avg-Dev	-0.089	-0.023	-0.185	-8E-05
Wet aggregates (1.0 - 2.0 mm) ^a	Self-consistency	0.78	1.023	0.695	0.869
	Aspect ^b	1	1	1	1
	RMSE	1.788	1.857	1.622	1.688
	NS-Eff	0.943	0.939	0.953	0.95
	Avg-Dev	-0.035	0.078	-0.066	0.112
Wet aggregates (0.1 - 0.25 mm) ^a	Self-consistency	0.925	1.253	0.8	1.003
	Aspect ^b	1.074	1	1	1
	RMSE	0.938	1.024	0.806	0.845
	NS-Eff	0.981	0.978	0.986	0.985
	Avg-Dev	-0.167	7.52E-03	-0.171	0.031
Sandy Clay (vertisol) ^c	Self-consistency	0.653	0.461	0.368	0.189
	Aspect ^b	0.302	0.149	4.725	0.116
	RMSE	0.605	0.382	0.43	1.363
	NS-Eff	0.997	0.999	0.999	0.985
	Avg-Dev	-0.199	3.83E-03	-0.129	0.406
Bet Dagan SL ^c	Self-consistency	1.184	0.277	1.016	0.16
	Aspect ^b	1.221	0.191	1.52	0.173
	RMSE	0.234	0.562	0.252	1.076
	NS-Eff	0.999	0.997	0.999	0.989
	Avg-Dev	-0.048	0.228	-0.046	0.496
Glass beads ^c	Self-consistency	1.45	0.098	1.45	0.098
	Aspect	1.274	0.261	1.275	0.261
	RMSE	0.284	1.217	0.284	1.218

NS-Eff	0.999	0.976	0.999	0.976
Avg-Dev	0.049	0.787	0.049	0.787

^a Soils of *Miyamoto et al.* [2005].

^b The aspects for both solid and water phases were assumed to be the same for discrete model.

^c Soils of *Friedman* [1998].

Table 2-3. Best fit parameters and goodness of fit for each local unfrozen soil data to predict permittivity (ϵ_{eff}) using discrete and confocal models with constant water permittivity ($\epsilon_w = 88$). ϵ_{eff} of each initial water content θ_{init} was averaged from data ≥ 5 °C

Soil type	Industrial sand		Asquith sandy loam		Brightbank loamy sand		Malmo silty loam		Mundare loamy sand		Phosphogypsum tailings	
	Discrete	Confocal	Discrete	Confocal	Discrete	Confocal	Discrete	Confocal	Discrete	Confocal	Discrete	Confocal
Self-consistency	0.86	0.15	1.363	0.144	1.167	0.05	1.021	0.629	1.203	0.2	1.19	0.371
Aspect ^a	1	1	1	0.348	1	0.35	1	0.994	1	0.313	1.652	0.239
RMSE	1.67	0.752	0.373	0.399	0.506	0.701	0.67	0.517	0.563	0.487	0.81	1.613
NS-Eff	0.937	0.987	0.997	0.997	0.994	0.988	0.991	0.995	0.994	0.996	0.991	0.966
Avg-Dev	0.338	0.215	0.256	0.127	0.139	0.249	-0.061	0.02	0.049	0.12	0.027	0.747

^aThe aspect of the solid and water phases were assumed to be equal to each other.

Table 2-4. Best fit parameters and goodness of fit for published frozen soil data to predict permittivity (ϵ_{eff}) using discrete and confocal models for different water permittivity (ϵ_w) scenarios. ϵ_w = modified using ϵ_w calculated with Friedman-Or-Wraith (FOW) approach (Fig. 2-2, Eqs. [2-7] & [2-8]), $\epsilon_w(T)$ using Eq. [2-9], and ϵ_w = linear using Eqs. [2-10] & [2-11]

Soil	parameters	discrete model				confocal model			
		ϵ_w =modified	ϵ_w =linear	$\epsilon_w(T)$	ϵ_w =88	ϵ_w =modified	ϵ_w =linear	$\epsilon_w(T)$	ϵ_w =88
Waukegan silt loam ^a	self-consistency	1.265	1.614	0.916	1.063	0.774	1.045	0.424	0.458
	aspect ^b	1, 2, 1	1, 2, 1	1, 2.57, 1	1, 1.947, 1	1	2.008	1	1
	RMSE	0.395	0.405	0.357	0.36	0.388	0.217	0.932	0.875
	NS-Eff	0.99	0.989	0.992	0.992	0.99	0.997	0.945	0.951
	Avg-Dev	-0.166	-0.059	0.035	0.014	0.151	3.89E-03	0.416	0.391
Toyoura sand ^c	self-consistency	0.763	0.714	0.712	0.752	0.227	0.203	0.21	0.222
	aspect ^b	1, 2.252, 1	1, 2.602, 1	1, 2.588, 1	1, 2.381, 1	1.004	1.646	1.476	1.418
	RMSE	1.324	1.324	1.324	1.324	1.135	1.138	1.153	1.139
	NS-Eff	0.951	0.951	0.951	0.951	0.964	0.964	0.963	0.964
	Avg-Dev	0.225	0.233	0.234	0.232	0.297	0.326	0.343	0.33
Mie Andisol ^c	self-consistency	1.041	0.609	0.621	0.671	0.882	0.455	0.421	0.442
	aspect ^b	1, 1, 1	1, 2, 1	1, 2.008, 2.061	1, 1.685, 2.058	1	1.464	1.346	1.321
	RMSE	2.459	2.425	2.363	2.348	2.379	2.156	2.125	2.093
	NS-Eff	0.921	0.924	0.927	0.928	0.927	0.94	0.941	0.943
	Avg-Dev	-0.785	-1.069	-0.736	-0.748	-0.735	-0.242	-0.078	-0.11
Fujinomori silt ^c	self-consistency	1.029	0.76	0.74	0.73	0.811	0.398	0.356	0.365
	aspect ^b	1.036, 1.779, 1	1, 1, 1	1, 1, -0.076	1, 1, 1	1	1	1	1
	RMSE	1.889	1.554	1.516	1.542	1.662	1.194	1.211	1.2
	NS-Eff	0.925	0.949	0.952	0.95	0.942	0.97	0.969	0.97
	Avg-Dev	-0.0072	-0.0077	-0.019	-0.025	-0.129	0.382	0.483	0.438
Tottori dune sand ^c	self-consistency	1.196	1.196	1.194	1.204	0.39	0.391	0.388	0.399
	aspect ^b	1, 1, 1	1, 1, 1	1, 1, 1	1, 1, 1	1	1	1	1
	RMSE	0.599	0.599	0.599	0.599	0.773	0.772	0.777	0.762
	NS-Eff	0.973	0.974	0.973	0.973	0.956	0.956	0.955	0.957
	Avg-Dev	0.17	0.17	0.171	0.171	0.141	0.146	0.16	0.152

^a Soils of *Spaans and Baker* [1995].

^b Aspect was allowed to vary for each phase and is presented in order of solid, water and ice.

^c Soils of *Watanabe and Wake* [2009].

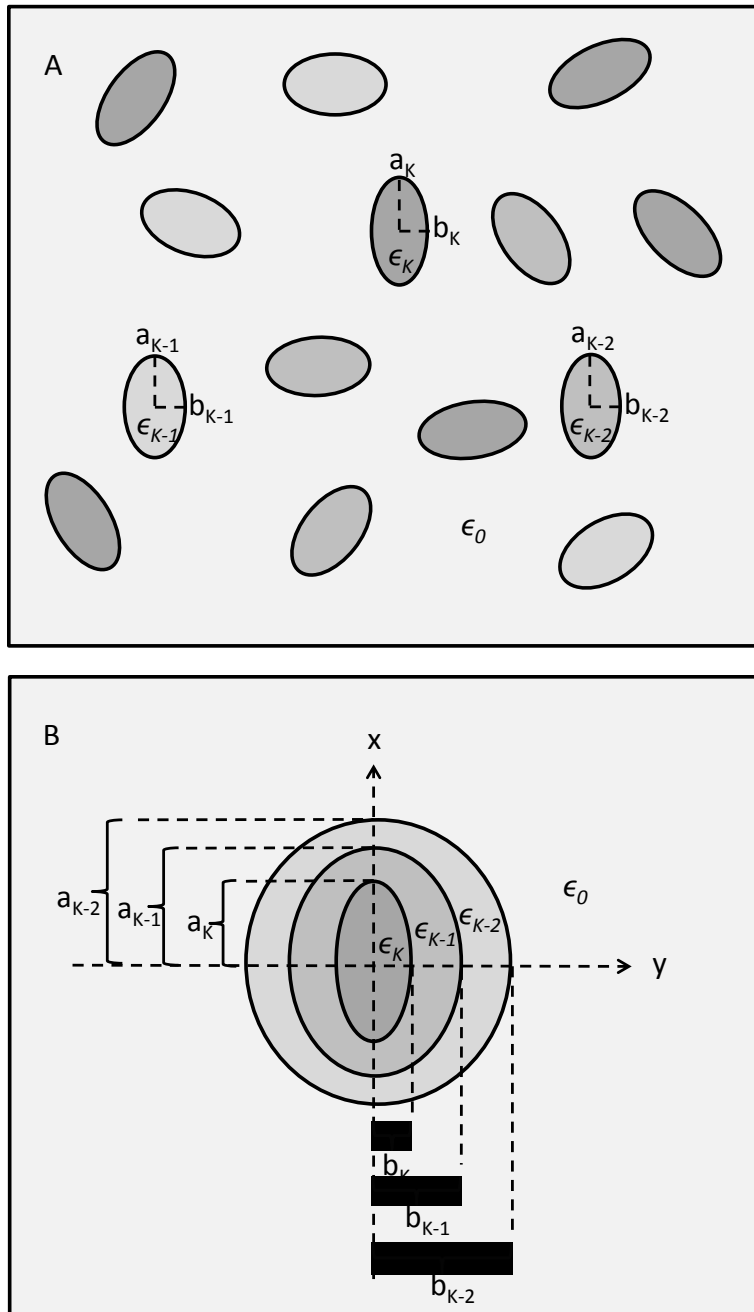


Fig. 2-1. Simplified discrete ellipsoid (A, dimension: a , b , c) and confocal ellipsoid (B, dimension: a , $b = c$, c is not shown) conceptual diagrams for a multiphase mixture. One of the constituents acts as the host matrix (ϵ_0 , usually air), and the other components (ϵ_K , ϵ_{K-1} , and ϵ_{K-2}) are embedded as discrete or confocal inclusions in it.

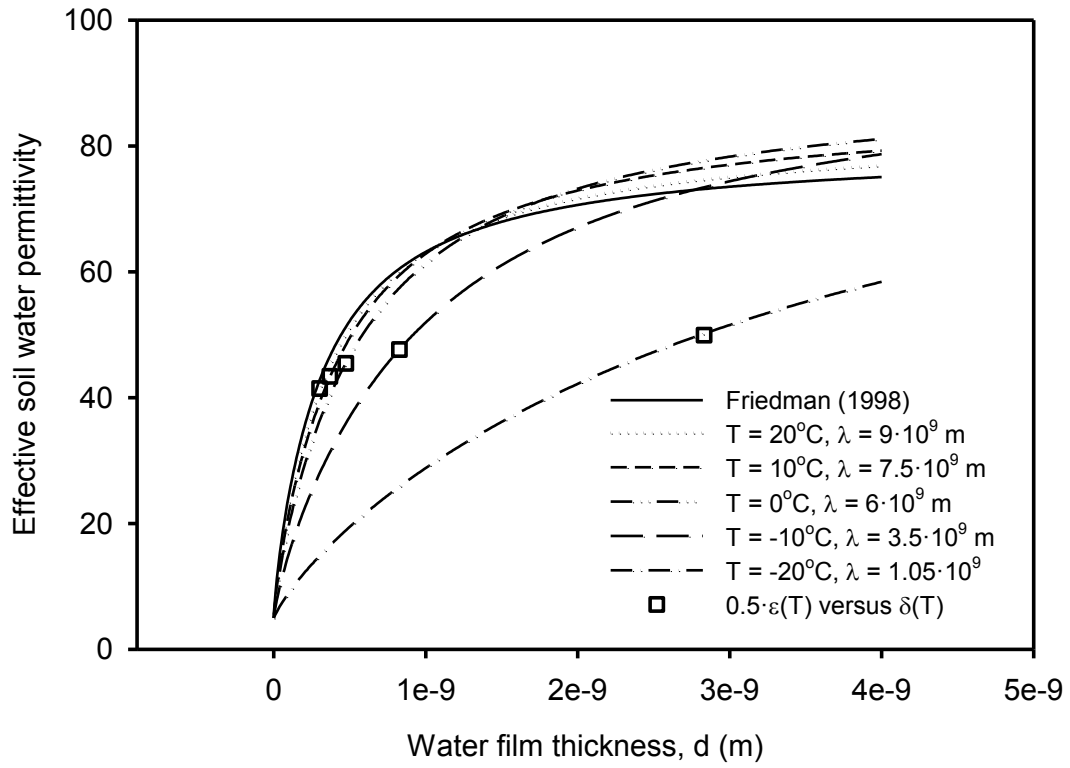


Fig. 2-2. The temperature-dependent effective water permittivity (ϵ_w) as a function of water film thickness based on modified *Friedman* [1998] and *Or and Wraith* [1999] models (Eqs. [2-7] & [2-8]).

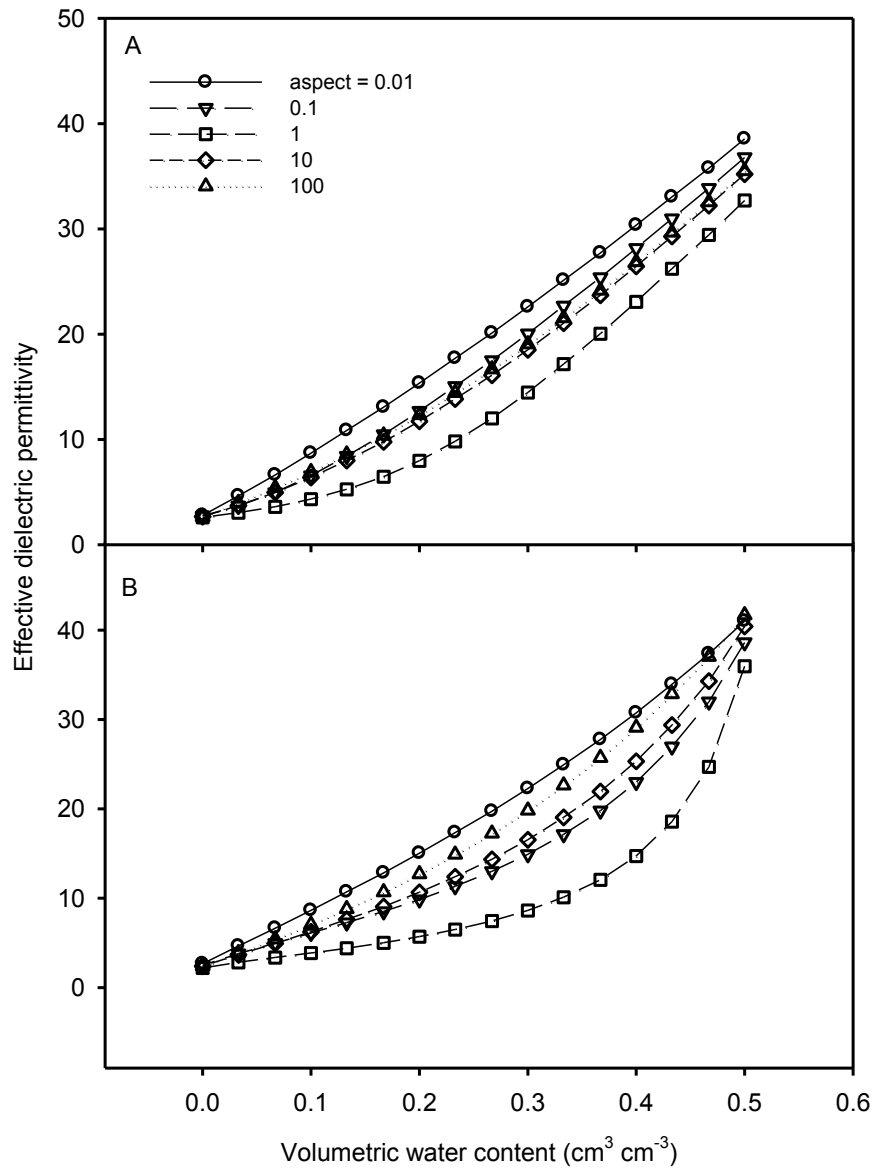


Fig. 2-3. Influence of particle shape (aspect) on $\epsilon_{eff}(\theta)$ for the discrete ellipsoid model with self-consistency coefficient $\nu = 1$ (A) and confocal ellipsoid model with $\nu = 0$ (B) with solid-water-air (SWA) configuration.

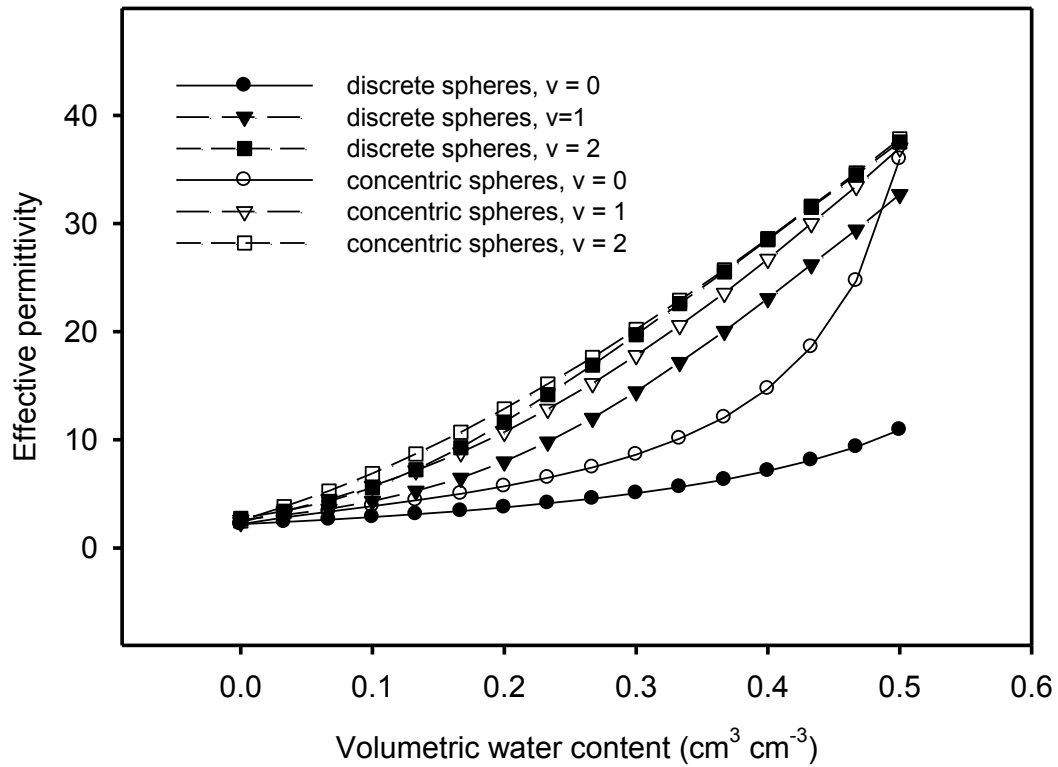


Fig. 2-4. Influence of self-consistency (v) on discrete and confocal models with spherical inclusions (aspect = 1 or $a = b = c$) in a solid-water-air (SWA) configuration.

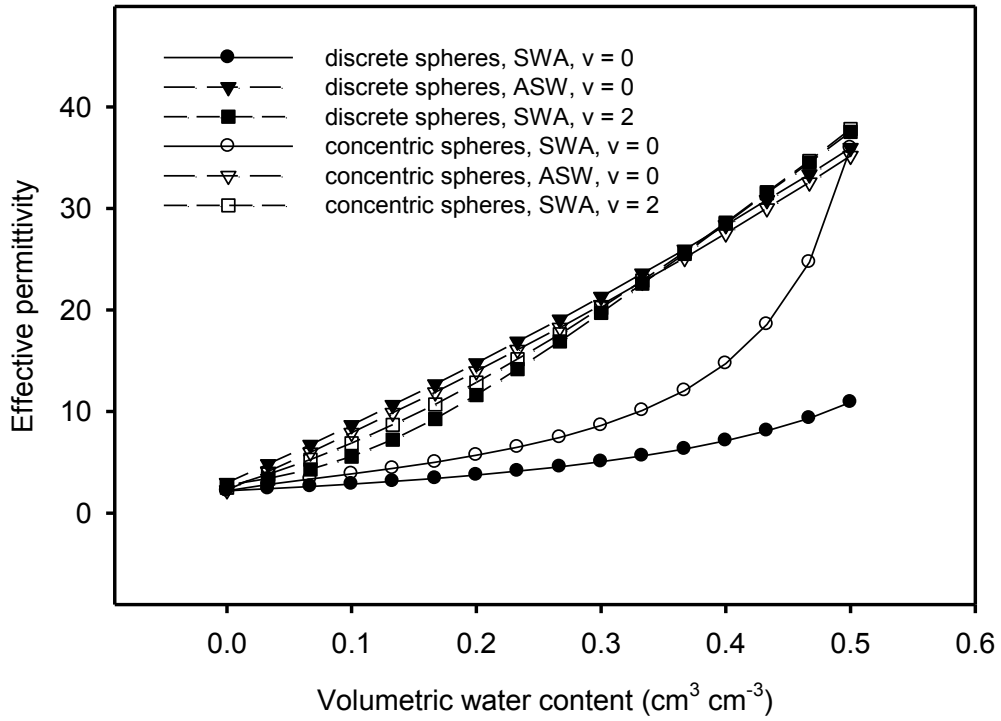


Fig. 2-5. Influence of configuration of mixture inclusions (SWA versus ASW) for the discrete and confocal models with spherical inclusions and two levels of self-consistency.

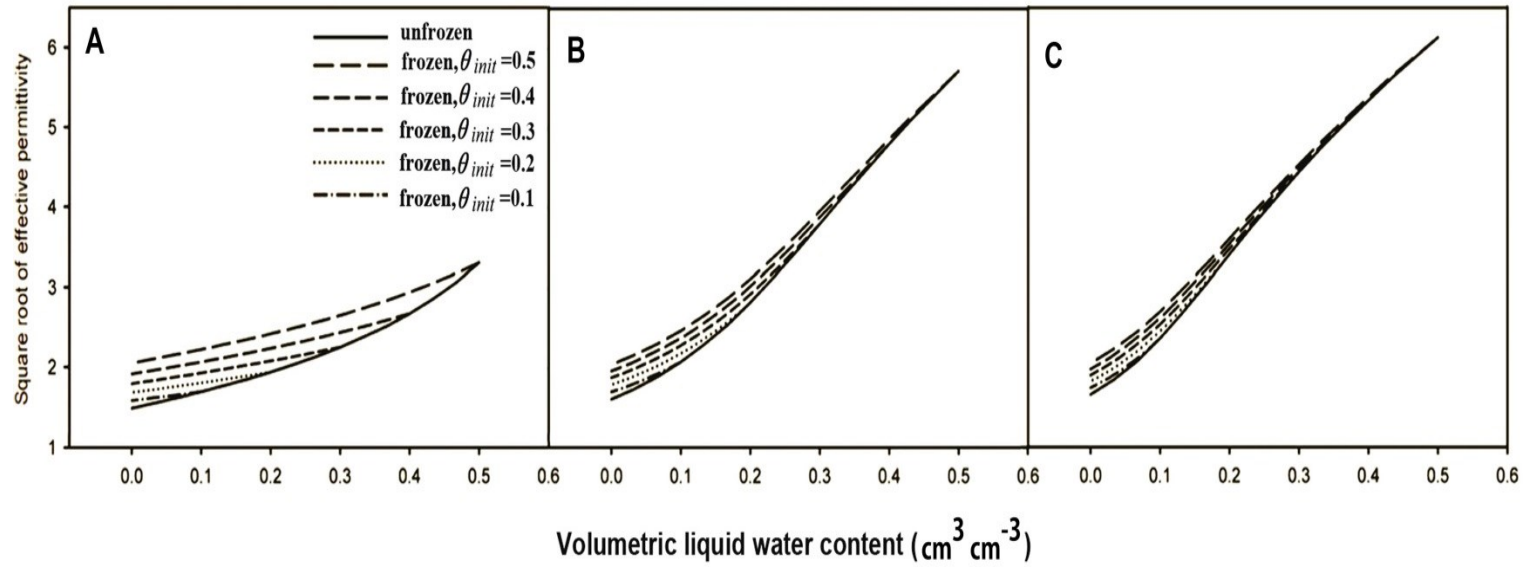


Fig. 2-6. Simulation of freezing for discrete spherical inclusions (aspect = 1) of a solid-water-ice-air (SWIA) configuration with (A) $\nu = 0$, (B) $\nu = 1$ and (C) $\nu = 2$. Total porosity of the soil was assumed to be $0.5 \text{ m}^3 \text{ m}^{-3}$, $\epsilon_w = 81$, $\epsilon_s = 5$, $\epsilon_g = 1$, and $\epsilon_{ice} = 3.2$ for 4-phase model.

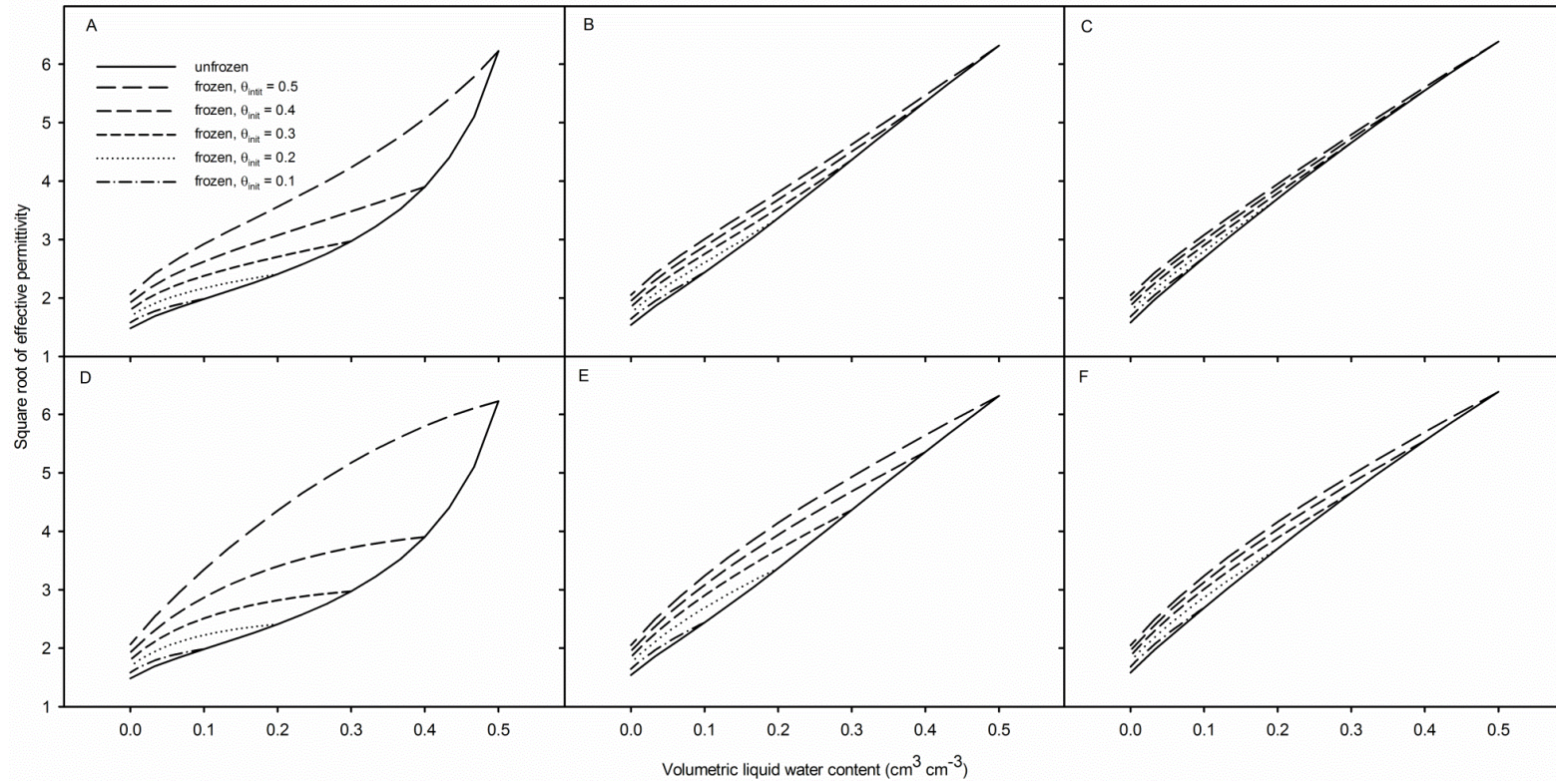


Fig. 2-7. Simulation of freezing for concentric sphere inclusions (confocal model with aspect = 1) of a solid-water-ice-air (SWIA) configuration with (A) $\nu = 0$, (B) $\nu = 1$ and (C) $\nu = 2$, and solid-ice-water-air (SIWA) configuration with (D) $\nu = 0$, (E) $\nu = 1$ and (F) $\nu = 2$. Total porosity of the soil was assumed to be $0.5 \text{ m}^3 \text{ m}^{-3}$, $\epsilon_w = 81$, $\epsilon_s = 5$, $\epsilon_g = 1$, and $\epsilon_{ice} = 3.2$ for 4-phase model.

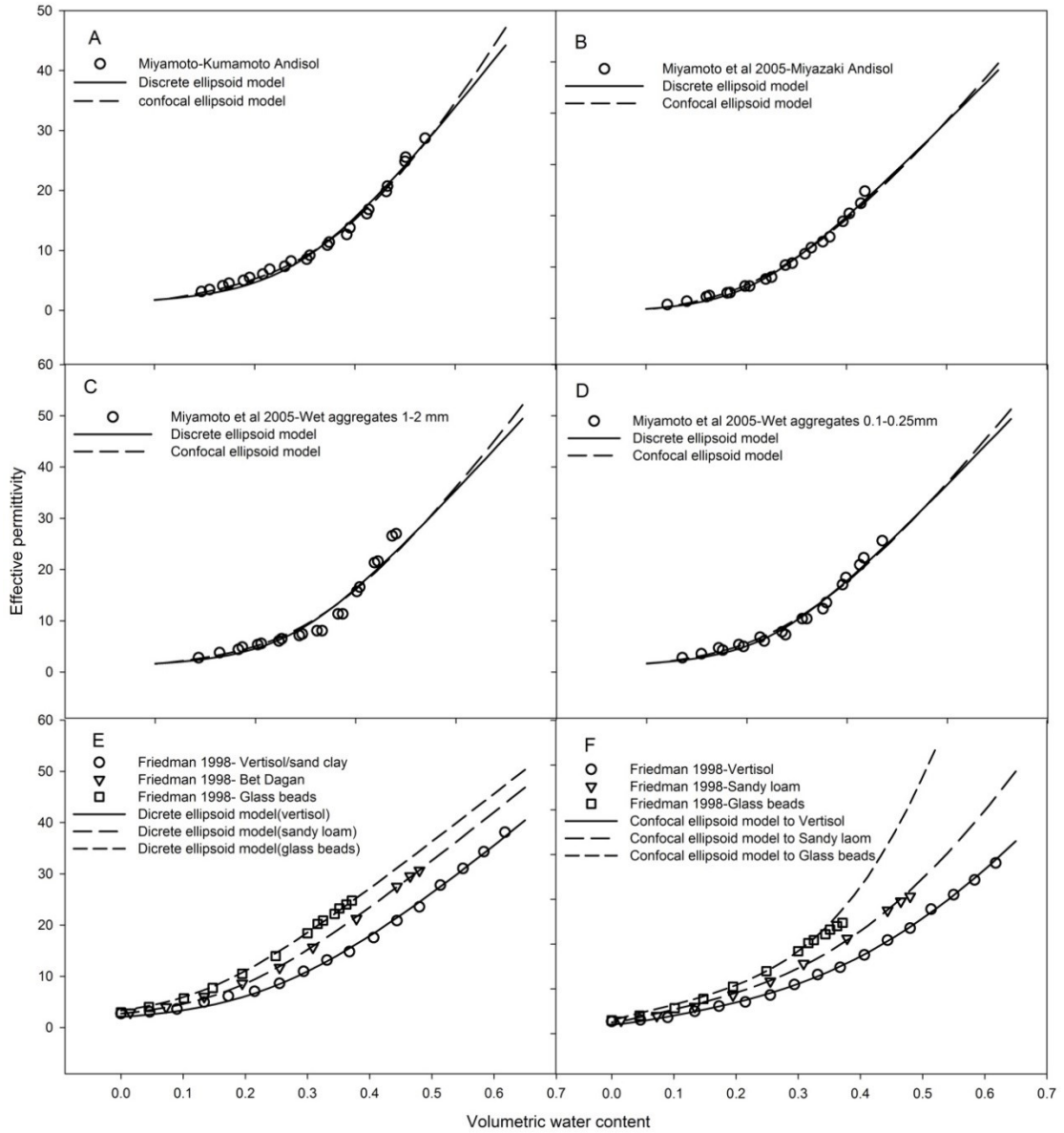


Fig. 2-8. Miyamoto and Friedman soils with *Friedman* [1998] water permittivity model $\lambda = 10^{10}$ (see Table 2-2 for the parameters and goodness of fit).

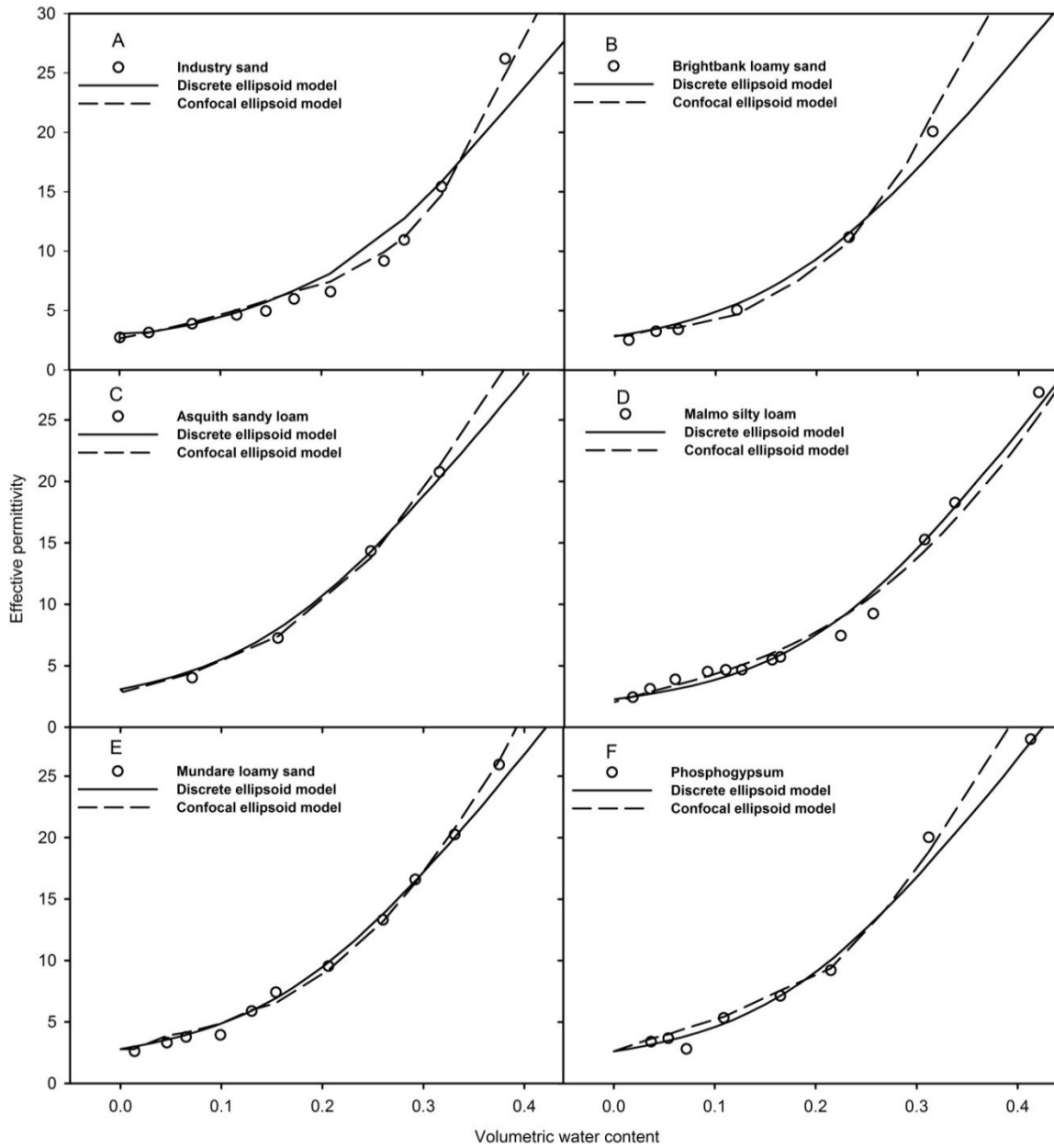


Fig. 2-9. Unfrozen data from six western Canadian soils with discrete and confocal models for constant water permittivity (see Table 2-3 for the parameters and goodness of fit).

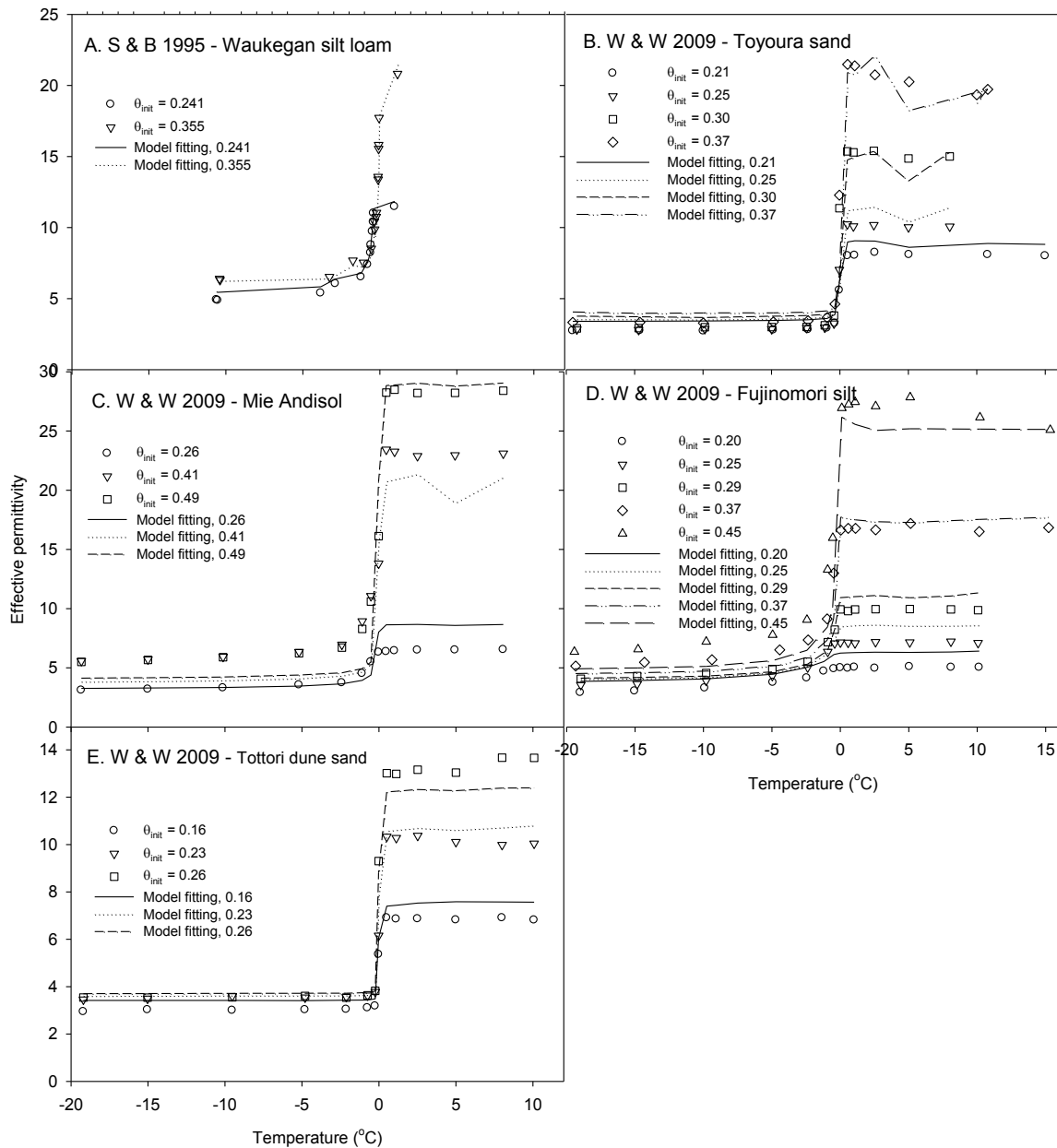


Fig. 2-10. Comparison of modeled and measured effective permittivity at different temperatures with the discrete model for $\epsilon_w = 88$ (see Table 2-4 for the parameters and goodness of fit).

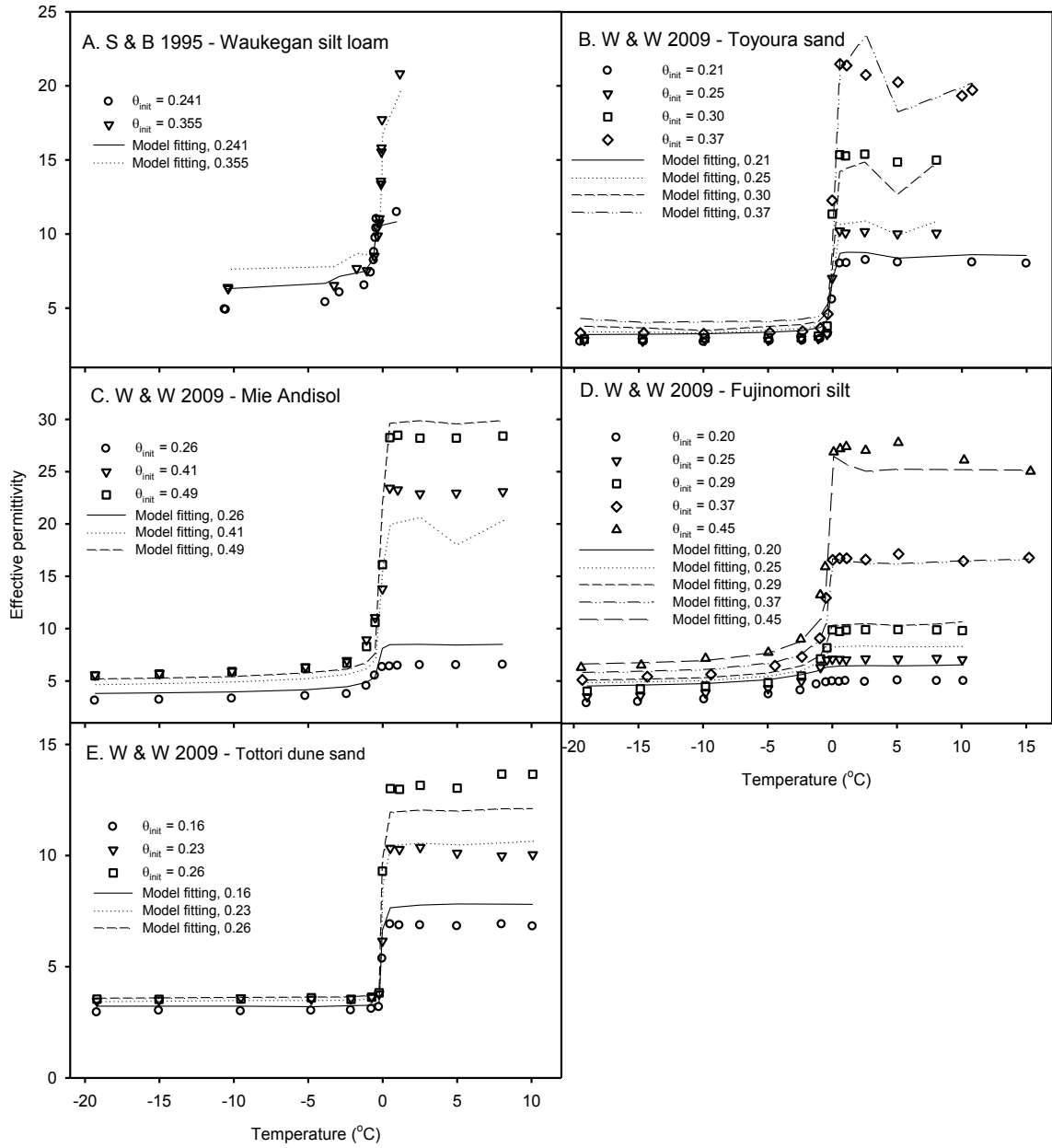


Fig. 2-11. Comparison of modeled and measured effective permittivity at different temperatures with the confocal model for $\epsilon_w = 88$ (see Table 2-4 for the parameters and goodness of fit).

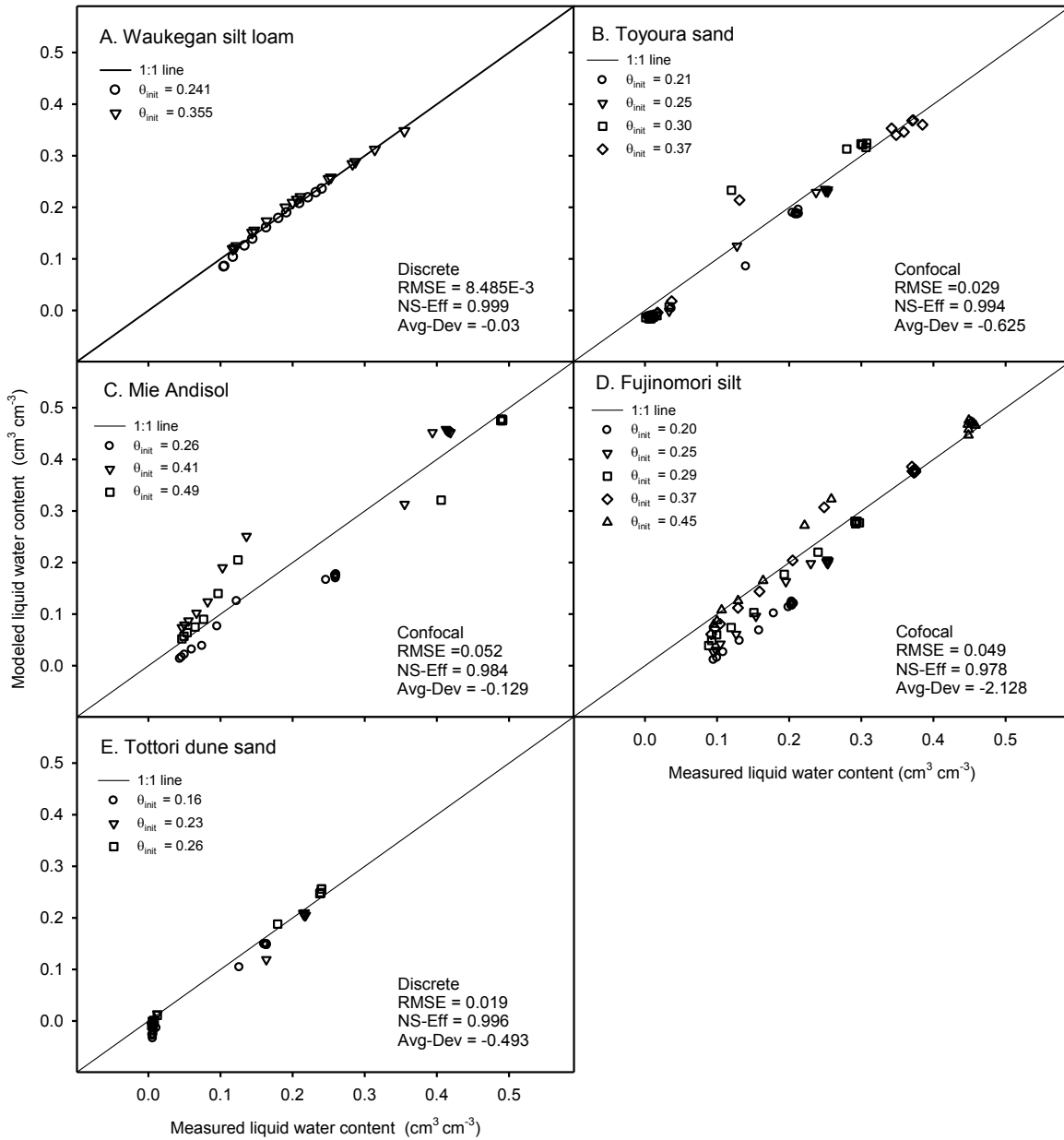


Fig. 2-12. Comparison of the measured and modeled liquid-water content for $\epsilon_w = 88$ with best fitted discrete or confocal model from prediction of permittivity (see Table 2-4 for the parameters and goodness of fit).

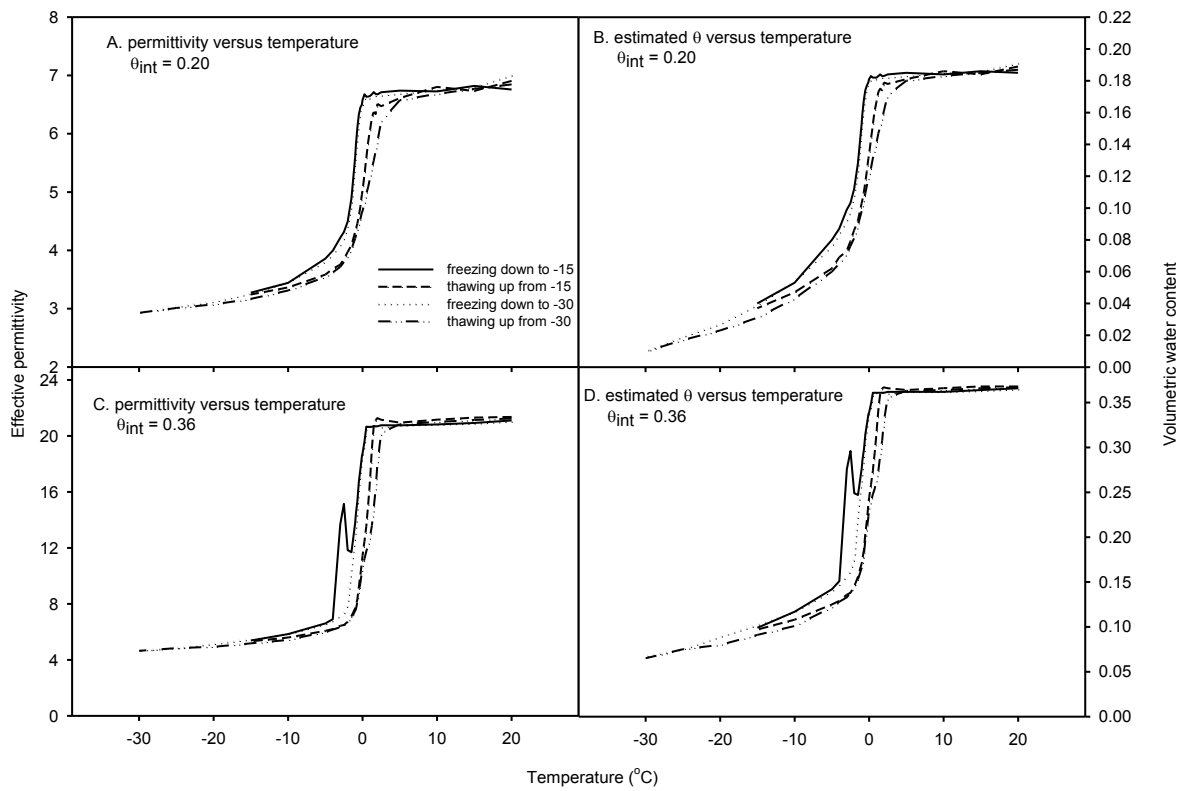


Fig. 2-13. Soil freezing and thawing curves showing hysteresis measured on Malmo silty loam (described in Table 2-1) with two different initial water contents. A and C are measured permittivity and B and D are the estimated liquid-water content. Liquid-water content is estimated by the discrete model (parameters in Table 2-3).

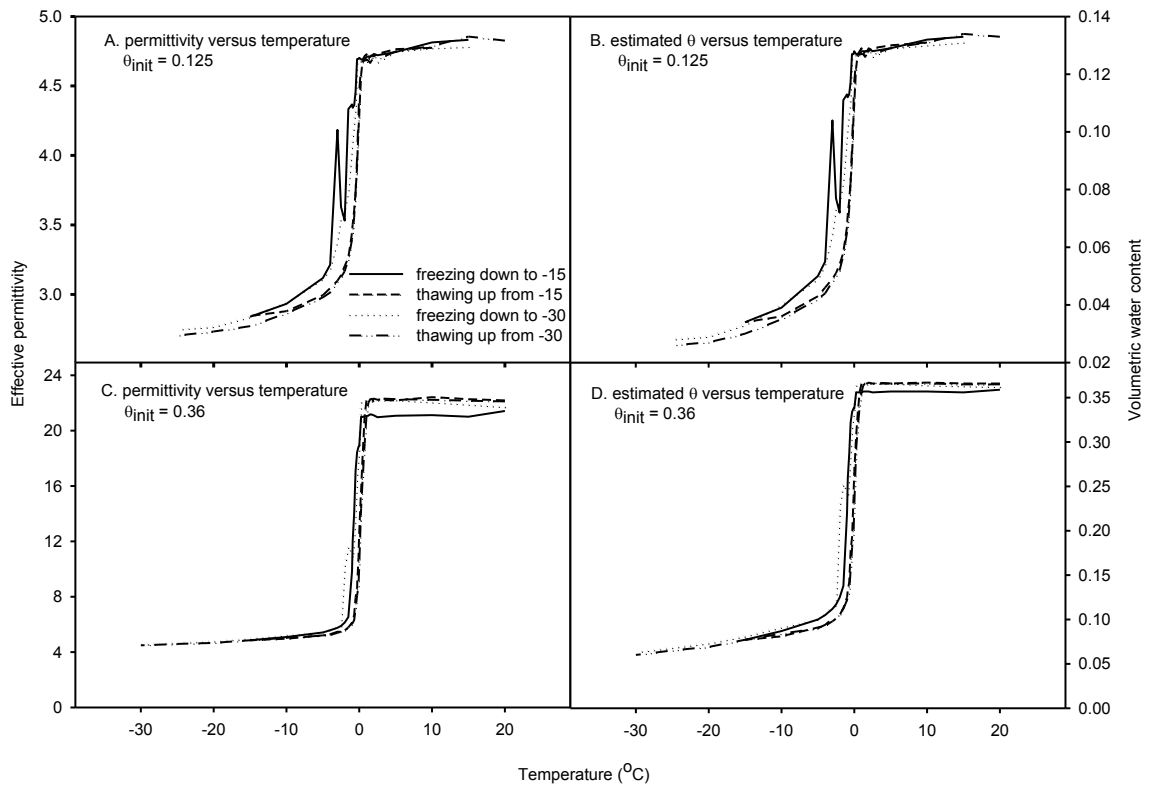


Fig. 2-14. Soil freezing and thawing curves showing hysteresis measured on Mundare loamy sand (described in Table 2-1) with two different initial water contents. A&C are measured permittivity and B&D are the estimated liquid-water content using the confocal model (parameters in Table 2-3).

Chapter 3 Soil Freezing-Thawing Characteristics and Snowmelt Infiltration under Natural Boundary Conditions at Breton Plots, Alberta, Canada

3.1. Abstract

Soil freeze-thaw processes and snowmelt infiltration significantly influence the hydrological cycle and ecosystem productivity in cold, semi-arid areas. In this chapter, 5-years (2008 - 2013) of soil moisture, temperature (0 - 100 cm depth) and meteorological data monitored at the Breton Plots, University of Alberta (Canada) were used to: (1) test the feasibility of multiphase dielectric mixing models developed in Chapter 2 to estimate the unfrozen water and ice content from TDR-measured soil dielectric permittivity in field conditions; and (2) understand the soil freezing and thawing phenomena and snowmelt infiltration under natural boundary conditions. The results showed the dielectric mixing model can be applied to field measurements, but careful interpretation is required during freeze-thaw cycles when the total soil water content of frozen soil is most likely to change. The field data demonstrated that the timing of snowpack accumulation and soil wetness prior to freezing were the main factors determining the winter soil thermal regime. Deep frost penetration (≥ 50 cm) was found in years of late snow accumulation and dry fall soil conditions while shallow frost occurred in years of early snow accumulation and wet fall soil conditions. In addition, soil freezing and thawing curves (SFTCs) under natural boundary conditions were used to understand the freeze-thaw processes, and comparisons were made with soil freezing characteristic (SFC) measured in the laboratory where constant total soil water content and near-thermal equilibrium could be achieved. Field-measured SFTCs differ from SFCs because of changing total soil water content under field conditions from snowmelt infiltration or frost induced water redistribution and transient temperature conditions. Furthermore, the results also suggested that air-filled porosity of the top 10 cm and storage of top 30 cm measured in the fall appear to be the main factors governing soil water storage change following spring snowmelt.

List of symbols and acronyms:

ϵ_{eff}	Composite dielectric permittivity
θ_i	Ice content, $m^3 m^{-3}$ or $cm^3 cm^{-3}$
θ_{init}	Initial water content or total water content before freezing, $m^3 m^{-3}$ or $cm^3 cm^{-3}$
θ_l	Liquid-water content, $m^3 m^{-3}$ or $cm^3 cm^{-3}$
S	Soil storage, m or mm
Avg-Dev	Average deviations
NS-Eff	Nash-Sutcliffe Efficiency
RMSERoot mean square error
SFC	Soil freezing characteristic
SFTC	Soil freezing and thawing curve
SMRC	Soil moisture retention curve
SWE	Snow water equivalent
TRFCs	Thawing and refreezing cycles

3.2. Introduction

In cold, semi-arid areas, snowmelt may recharge soil water and groundwater reservoirs that are closely linked to agricultural and ecosystem productivity. Snowmelt on the other hand may become runoff if soil infiltration capacity is inhibited by ice lenses, ice-filled pores or basal ice layers on the soil surface [*Cary et al.*, 1978; *Kane*, 1980; *Miller*, 1980; *Stahli*, 2005]. Snowmelt runoff significantly increases erosion of fertile surface soils [*Zuzel et al.*, 1982], migration of pesticides and other agricultural chemicals and pollution of soil and surface waters [*Rascher et al.*, 1987; *Williams and Melack*, 1991; *Groffman et al.*, 2001; *Cade-Menun et al.*, 2013; *Likens*, 2013], and may trigger spring flooding [*Shanley and Chalmers*, 1999; *Janowicz et al.*, 2002; *Hall et al.*, 2012]. Therefore, the partitioning of snowmelt infiltration and runoff has important implications for water resource management and the development of mitigation strategies to reduce environmental risks. This is especially important for the Canadian Prairie region where climate change which is predicted to reduce depth of soil frost and frost duration [*Cutforth et al.*,

2004], increase the number of freezing and thawing cycles during winter, and significantly change the amount, timing and phase (snow or rainfall) of winter precipitation [IPCC, 2007].

Snowmelt infiltration into frozen soils is more complicated than water infiltration into unfrozen soils because it involves coupled water and heat transport with phase changes. The factors affecting snowmelt infiltration consist of soil and air temperature regimes [Iwata *et al.*, 2008, 2011], soil hydraulic, thermal and physical properties [Kane, 1980], soil water content at the onset of freezing [Kane and Stein, 1983b; Stadler *et al.*, 2000; Watanabe *et al.*, 2013], soil depth [Christensen *et al.*, 2013], freeze-thaw cycles [Fouli *et al.*, 2013], characteristics of the overlying snowpack and its melt rate [Shanley and Chalmers, 1999; Decker *et al.*, 2003; Iwata *et al.*, 2010], the thermal regime of the infiltrating water and soil, meteorological conditions (e.g. wind speed, precipitation, and albedo) and their interactions [Granger *et al.*, 1984; Stahli, 2005]. Although many studies have been conducted to find out the factors that influence snowmelt infiltration, few field studies [Granger *et al.*, 1984; Iwata *et al.*, 2008; Sutinen *et al.*, 2008] without manipulated boundary conditions were found to quantitatively examine the relationship between snowmelt infiltration and controlling factors. This may be attributed to the logistical and technical difficulties of performing long-term and comprehensive field work in cold environments [Kane, 1980; Iwata *et al.*, 2010]. In the absence of field observations, numerical models [Flerchinger and Saxton, 1989; Zhao *et al.*, 1997; Jansson, 1998] may be employed and sensitivity analysis was used to examine the influence of different factors. These methods are useful for the purpose of understanding the processes, but the results are largely dependent on the detailed input data (that may only be available at well evaluated site) and choice of parameters and algorithms. An alternative to process models are empirical relationships such as those describing snowmelt infiltration developed by Granger *et al.* [1984] and Zhao and Gray [1997a]. These models may have practical site-specific applications to water management problems and only require a few variables. But applicability of these models may be subject to geographic and meteorological settings and it is difficult to apply across landscapes of large area (or scale up) [Henry, 2007; Iwata *et al.*, 2008].

The difficulties of conducting long term and comprehensive field studies can be overcome, to some extent, through the establishment of soil monitoring stations or expanding synoptic weather stations by installing soil moisture and temperature sensors. Rather than manipulating the boundary layer conditions (e.g. snow cover or initial moisture contents) that influence the soil

freezing processes and snowmelt infiltration, long term observations include various boundary scenarios at the same site in different years that can be used for comparison and analysis. In Alberta, Canada, 48 such stations were established beginning in 2005 to form a Drought Monitoring Network for long term monitoring of soil conditions [Walker, 2006]. In this study, the University of Alberta Breton Plots station, near Breton, AB was chosen as an example. Because of its relatively long monitoring history and comprehensive datasets, it provides a unique opportunity to investigate snowmelt infiltration into frozen soils with different scenarios of initial soil moisture contents, snow cover, and thawing-refreezing cycles.

Because of the strong relationship between snowmelt infiltration and soil thermal properties on soil liquid-water and ice content, interpretation of data from soil monitoring stations during freezing, thawing and frozen soil periods is difficult because soil moisture sensors are usually only calibrated for unfrozen soil conditions. Recently, *He and Dyck* [2013] applied a unique multiphase dielectric mixing model to estimate unfrozen water content and ice content in frozen soils using TDR-measured soil dielectric permittivity. The major limiting assumption of He and Dyck's approach was that it required that total soil water content (i.e., mass of ice and liquid-water) remains constant within the sampling volume of the TDR probe. Under field conditions, frozen soil processes such as water redistribution under temperature gradients and snowmelt infiltration may cause total soil water content to change, but these periods may be brief. Therefore, the objectives of this paper are to interpret the TDR-measured soil dielectric permittivity in concert with soil and air temperature, snow pack and precipitation data to: (1) determine the extent to which the assumption of constant total water-content is violated under field conditions; and (2) investigate the processes of soil freezing and thawing and snowmelt infiltration into partially frozen soils.

3.3. Material and Methods

3.3.1. Site description

The Breton Plots (lat. 53° 05'N, long. 114° 26'W, 850 m above the sea level) were established southwest of Breton, Alberta, in 1930 by the University of Alberta to conduct agricultural and soil fertility research in the gray soil zone of Alberta. The area is described as cold and semi-arid to sub-humid having a mean annual temperature of 3.70 °C and a mean annual precipitation of

564 mm (with 413 mm in the form of rainfall mainly occurring between May and August and 151 mm as snow; calculated from 1974 - 2007 data downloaded from Environment Canada http://climate.weather.gc.ca/index_e.html#access, hereafter Environment Canada). The average temperature from December through February is -8.24 °C, and -4.4 °C from November through April and 15.25 °C from June through August (Environment Canada). The growing season typically starts middle to late April as marked by a mean daily temperature > 1 °C for a period of 5 consecutive days, and the growing season usually lasts through to early September when the maximum duration of sunshine, calculated from latitude and Julian day, decreases below 13.5 h.

Soil at the site is classified as a loam-textured, Gleyed Dark Gray Luvisol, developed on medium-textured glacial till parent material under boreal forest vegetation (Table 3-1). This type of soil is low in organic matter with dense subsoil, is moderately acidic (pH ~6.0) and deficient in several plant nutrients. It should also be noted that the meteorological station at the Breton site is located on a grassed, upper southwest slope with 4.5% gradient, free from ponded water and does not receive major surface runoff originating on adjacent areas. The site is defined as imperfectly drained, only a few earthworms were found during the installation of sensors, and 2 cm of weakly decomposed plant litter above the mineral soil was found [*Walker*, 2006].

3.3.2. Instrumentation

The soil and meteorological instrumentation is contained in a grass-covered area with approximate dimensions of 15m×28m that is not disturbed by the agricultural activities at the site. ThetaProbes (type ML2x sensors, Delta-T Devices Ltd, Cambridge, England) and 107BAM thermistors (Campbell Scientific, Edmonton, Canada) were used for measurement of soil moisture and temperature, respectively. The ThetaProbe consists of 4 parallel rods 60 mm long. One center rod is surrounded by three peripheral rods, evenly distributed on a circle of 26.5 mm diameter. Changes in apparent dielectric constant are calibrated to the DC voltage output of the probe which is proportional to dielectric permittivity and can be calibrated to water content. Below-ground ThetaProbes and temperature sensors were installed following the installation procedure described by *Walker* [2003]. Basically, ThetaProbes were installed at 5, 20, 50, and 100 cm from the mineral surface in a hand-excavated pit (~80 cm length×25 cm width×25 cm depth). Probes at 5 and 20 cm were horizontally installed into laterally offset bore-holes drilled into the side of the pit, while probes at 50 and 100 cm were installed in the bore-holes started

near the bottom edge of the soil pit at a 45° angle. Temperature sensors were installed close to the ThetaProbe. ThetaProbe and temperature data were automatically logged on an hourly basis.

Meteorological variables such as air temperature, precipitation (weighing gauge), wind speed and direction, humidity, and snow depth were simultaneously recorded by dataloggers. Snow depth was recorded once a day at 10AM MST. The hourly and daily data of precipitation, snowfall, average air temperature and daily data of snow depth from October 2008 to October 2013 were used in this study.

3.3.3. ThetaProbe calibration

Soil-specific calibration of the moisture sensors was conducted in the laboratory using soil cores collected during the installation of the ThetaProbes and temperature sensors [Walker and Tadjek, 2003]. For all four depths, soil cores of each depth were equilibrated on pressure plates to get different water contents before ThetaProbes measurements were taken. The soil cores were then oven dried and plotted against the ThetaProbe-measured permittivity (ϵ_{eff}) to get the calibration parameters. In this study, we converted the soil moisture back to ϵ_{eff} using the equations and parameters provided in the calibration report [Walker and Tadjek, 2003], which is

$$\epsilon_{eff} = a_0 + a_1\theta \quad [3-1]$$

where, θ is water content ($\text{cm}^3 \text{cm}^{-3}$), a_0 and a_1 are parameters shown in Table 3-2.

3.3.4. Estimation of unfrozen water and ice content with ThetaProbe-measured permittivity

Freezing of soils affects the dielectric permittivity (ϵ_{eff}) similarly to the drying of unfrozen soils but the drying process in unfrozen soils involves the displacement of water with air and the freezing process involves the replacement of water by ice. The ϵ of ice is about three times greater than air (i.e., 3.2 compared to 1). Therefore, ϵ_{eff} of a frozen soil will be greater than ϵ_{eff} of an unfrozen soil with the same liquid-water content as long as there is ice present. The amount of ice present at a given temperature is proportional to the water content prior to freezing.

Chapter 2 showed that dielectric models could be used to calibrate ThetaProbeThetaProbe for the measurement of unfrozen water and ice content in frozen soils. In addition, they presented strong evidence to illustrate that the mixing models could be parameterized using unfrozen soil at

a variety of water contents and then extended to frozen soils given that the total water content (i.e., mass of ice and unfrozen water content) remains constant while the soil is frozen. Therefore, the main limitation of this calibration method is that it only remains valid if the total water content within the measurement volume of the ThetaProbe probe remains unchanged while the soil is frozen/freezing. This condition is easy to satisfy in laboratory conditions, but may not always be satisfied in the field because frost-induced water redistribution and water infiltration may change the total soil water content required for the estimation of liquid-water content (θ_l) and ice content (θ_i) as alluded to earlier. How this assumption affects the estimation of θ_l and θ_i for the field measurements presented in this paper and their interpretation will be discussed.

To estimate the θ_l and θ_i , the discrete dielectric mixing model presented in Chapter 2 was used. The model was modified and calibrated from the discrete ellipsoid model that was initially developed by *Sihvola and Lindell* [1990]. In this study, parameters of the discrete mixing model were optimized using Mathcad software (Parametric Technology Corporation 2010) such that the mean squared difference between ThetaProbe-measured ϵ_{eff} and the modeled ϵ were minimized, based on the calibrated $\theta_l - \epsilon_{eff}$ data in unfrozen soils by *Walker* [2003]. Once the model is parameterized, it can be used to estimate θ_l and θ_i with the ThetaProbe-measured ϵ_{eff} , but requires an estimate of the total water content. At the onset of soil freezing, we assumed that the water content measured just prior to soil freezing, (θ_{init} in Table 3-5) was equal to the total water content of the soil. The onset of soil freezing was considered to be the simultaneous decrease in ThetaProbe-measured ϵ_{eff} and soil temperature below 0 °C. During frozen soil conditions, the assumed θ_{init} at each depth was double-checked and updated if there was thawing and refreezing cycle and the magnitude of ϵ_{eff} changed when soil temperature went above 0 °C for 5 consecutive hours (soil is assumed to completely thawed) over the winter. This approach likely reduced the errors of estimating θ_l and θ_i due to change of $\theta_{init}/\epsilon_{eff}$ resulting from the possible infiltration into or percolation out of the soil volume. The ThetaProbe calibration curves we used to calculate θ_l and θ_i are presented in Fig. 3-1.

3.3.5. Estimation of soil water storage

The soil profile, ranging from 0 - 100 cm depth from the mineral surface downward, is divided into four layers. Probes at depths of 5, 20, 50 and 100 cm represent the layers of 0 - 10, 10 - 30,

30 - 70 and 70 - 100 cm, respectively. Therefore, total soil water storage to 100 cm at any given time of measurement was estimated as:

$$S = \theta_{t,5} \cdot 10 + \theta_{t,20} \cdot 20 + \theta_{t,50} \cdot 40 + \theta_{t,100} \cdot 30 \quad [3-2]$$

where S is the total soil water storage (cm), $\theta_{t,5}$, $\theta_{t,20}$, $\theta_{t,50}$ and $\theta_{t,100}$ are the estimated total water contents at 5, 20, 50 and 100 cm respectively and 10, 20, 40 and 30 are the layer thicknesses (cm) represented by the ThetaProbes.

In the field, soil water storage can be affected by a number of processes including infiltration (rain and snowmelt), deep percolation, groundwater discharge and evapotranspiration. These processes may occur simultaneously and therefore, attributing changes in soil water storage to specific processes required careful interpretation.

3.3.6. Groundwater

Four piezometers and 5 water table wells were installed at the Breton Plots in the summer of 2012. A water table well was installed near the meteorological station and the daily water level was monitored by an automated level logger between Jul. 25th, 2012 and Oct. 23rd, 2013. This record was used to assess the influence of groundwater on measured soil moisture. The limited records available show that water table was 180 - 200 cm below the ground surface in March, 2013 just prior to snowmelt, then rose to approximately 25 cm below the surface in April, 2013 and June, 2013 and subsequently decreased at a steady rate to 175 cm below the ground surface for the remainder of the record (October, 2013). Based on the presence of gleyed horizons in the soil profile and limited groundwater measurements, it appears that groundwater levels near the meteorological station vary seasonally and likely influence root zone moisture contents during the growing season. It is also likely that temporal variations in the regional water balance cause annual variability in the minimum and maximum groundwater elevations at the site which is apparent in changes in soil moisture storage presented later in this chapter. In general, it appears that water table levels increase rapidly in the spring during snowmelt and generally decrease throughout the growing season, fall and winter months. Therefore, we assume that water dynamics in the root zone are most influenced by groundwater during the growing season and less influenced by groundwater in the winter months.

3.3.7. Additional lab experiments on collected soils from Breton Plots site for the measurement of soil freezing-thawing curves (SFTCs)

Soil samples collected at the Breton Plots site were screened through 2 ~ 4 mm sieves and the plant residues were removed. Then they were equilibrated with pressure plates or hanging water columns to reach different water contents and then uniformly packed to a depth of 15 cm in a copper cylinder of 5.08 cm i.d. and of 21 cm in length and sealed with a copper cap to prevent evaporation. Each column was instrumented with a conventional three-prong customized ThetaProbe probe of 1.6 mm rod dia., 14 cm in length with 1 cm inter-rod spacing, a thermistor (TMC6HD, Onset Computer Corp., MA, USA) was inserted 4 cm below the soil surface adjacent to the ThetaProbe probe.

These soil columns were directly put in the temperature controlled water-ethylene glycol bath and were frozen to -20°C from 20°C and then thawed back to 20°C in 5°C steps between 20 and 5°C , 2°C steps between 5 and 0°C , 0.5°C steps between 0 and -5.5°C , and 5°C steps between -5 and -20°C . The ThetaProbe probes were multiplexed with a SDMX 50 that was connected to a ThetaProbe 100 (Campbell Scientific, Edmonton, Canada) controlled by a Campbell CR 1000 data logger. The ThetaProbe was programmed to take measurements on one soil column for one time and then proceeded to the next, the process was repeated three times at an interval of 5 min. The TMC temperature sensors were logged every 1 min. The duration of this experiment was 3 weeks. Frost heave was assumed to be insignificant, which means the sum of volumetric fraction of soil particles, ice, water, and air is equal to 1.

3.4. Results and Discussion

3.4.1. Overview of 5-year record

Figure 3-2 shows the weather and soil conditions over the 5-year period of 2008 - 2013. The annual cycle of daily average air temperature is somewhat sinusoidal, but winter air temperatures appear to deviate from the sinusoidal pattern more than summer and fall temperatures because of freeze-thaw cycles (Fig. 3-2: A). Average air and soil temperatures for the hydrological year (Nov. 1st - Oct. 31st), average snow-covered (Nov. 15th - Apr. 15th) and snow-free (Apr. 16th - Nov. 14th) periods are presented in Table 3-3. Temperatures of winter months (Dec. 1st - Feb. 28th) and soil freezing-thawing dates are also given. Winter 2010/2011 was the coldest with an average

air temperature of $-9.27\text{ }^{\circ}\text{C}$, winter 2011/2012 the warmest ($-3.54\text{ }^{\circ}\text{C}$), and other three winters ranged from -5 to $-7\text{ }^{\circ}\text{C}$, the average winter air temperature was $-6.3\text{ }^{\circ}\text{C}$. Temperatures of winter months contribute the most variation that influences the soil temperatures of snow-covered periods and the hydrological year.

The temporal pattern in soil temperature at 5 cm below the soil mineral surface (7 cm below the ground surface, Fig. 3-2: C) fluctuated similar to the air temperature during summer but little change was observed during winter. At the 20, 50 and 100 cm depths (Fig. 3-2: D~F), increased lag and decreased amplitude are observed in the annual temperature cycles. The depths at which sub-zero soil temperatures were observed varied over the 5 years reported. Soil temperature fell below $0\text{ }^{\circ}\text{C}$ at 50 cm in the winters of 2008/2009 (average winter air temperature as shown in Table 3-3, below average snowpack as shown in Table 3-4) and 2011/2012 (above-average air temperature, below-average snowpack), 20 cm in winter 2009/2010 (average air temperature, average snowpack), and 5 cm in winter 2010/2011 (below average air temperature, above average snowpack) and 2012/2013 (below average air temperature, above average snowpack), while soil temperature at 100 cm never fell below $0\text{ }^{\circ}\text{C}$ over the 5 years (Fig. 3-2: F and Table 3-5). Lower winter air temperatures did not necessarily result in lower soil temperature. For example, during the winter 2010/2011, soil temperature fell below zero at 5 cm depth, but during winter 2008/2009 with similar air temperature conditions, the soil temperature at 50 cm fell below $0\text{ }^{\circ}\text{C}$ (Fig. 3-2: E and Table 3-3). This varied response of soil temperature to atmospheric forcing is likely influenced by snowpack thickness and fall soil moisture condition and will be discussed in depth in section 3.4.2.

Estimated soil liquid-water content is generally a reflection of the precipitation and groundwater during the frost- and snow-free periods. Fluctuations in the soil water content at 5 cm (Fig. 3-2: C) between May and October were due to periodic rainfall events followed by periods of evapotranspiration and redistribution within the profile. Changes in soil water content at 20 cm (Fig. 3-2: D) were attenuated compared to 5 cm and only small changes at depths of 50 cm and 100 cm (Fig. 3-2: E&F) were observed. The small changes in moisture content (near saturation) at 50 and 100 cm are likely explained by high water tables during the growing season.

Soil data were not available from mid-October to mid-November 2009, but ~ 35 mm of rain fell during this gap in the soil moisture record and this rainfall is likely the cause of the increased

moisture content at 5 and 20 cm following the data gap. The slight increase in volumetric moisture content at 100 cm over this period may also be a result of rising groundwater. The change in soil moisture storage over this period is estimated at 24 mm, 11 mm less than the 35 mm of rainfall during this time. It is possible that not all 35 mm of precipitation infiltrated because of surface runoff and/or evaporation of intercepted rainfall. Nevertheless, this discrepancy between rainfall and change in soil moisture storage is within measurement error of the soil moisture sensors (i.e., a 1% change in average water content between 0 and 100 cm is equivalent to a 10 mm change in storage).

During winter periods, estimated soil liquid-water content is calculated with the ThetaProbe-measured permittivity constrained by the total water content estimate. During late fall and early winter, ThetaProbe-measured permittivity was observed to decrease as soil temperature fell below zero. Air temperatures were generally below zero during these periods and any precipitation remained on the soil surface as part of the snowpack. Therefore, a combination of decreasing permittivity with soil temperature falling below 0 °C was interpreted as soil freezing (i.e., the formation of soil ice). Assuming no change in total soil water content, a decrease in soil permittivity is a result of a decrease in θ_l in an increase in θ_i (not shown). During spring snowmelt, increases in θ_l are likely a result of soil thawing (phase change), snowmelt infiltration, and rising groundwater elevations or their combination. The assumption of a constant total water content during spring melt is likely not valid, but as we discuss below, this is a relatively short time period and once the soil is completely thawed, soil liquid-water content estimates are not constrained by assumptions of total water content.

Precipitation (i.e., rainfall and snow) varied within and between years (Fig. 3-2: B and Table 3-4). The 2008/2009 hydrological year (Nov. 1st to Oct. 31st) was relatively dry, with a total precipitation of 332 mm and snowfall accounting for about 75 mm water equivalent. The 34-year (1974 - 2007) average annual precipitation is about 413 mm rainfall and 151 mm water equivalent of snowfall (Environment Canada). The following 4 years were much wetter (Fig. 3-2: B) with annual precipitation ranging from 433 mm (2012/2013) to 618 mm (2009/2010). Accumulated precipitation and snowfall at this site in 2009/2010 and 2011/2012 exceeded the 34-year average. Snowfall in the other 4 years ranged from 64 to 128 mm water equivalent. The snowpack generally lasted from middle/late November to middle/late April, except for an early snowmelt in 2010 (Fig. 3-2: B, Mar. 25th, 2010), sharp decrease in snow depth during winter

2011/2012 (Fig. 3-2: B, Jan. 4th, 2012) and early snow accumulation in winter 2012/2013 (Nov. 7th, 2012; Fig. 3-2: B). Maximum snow depths were similar in 2008/2009, 2009/2010 and 2011/2012 (~32 cm), while 2010/2011 had the thickest maximum snowpack depth of 71 cm (Fig. 3-2: B and Table 3-4). Maximum snow depths generally occurred in March except 2009/2010 when it occurred in Dec. More details related to precipitation, snowpack, and SWE are referred to Table 3-4 and Fig. 3-2: B.

There is an increasing trend in soil moisture storage (Eq. [3-2]) over the five year period corresponding to the trends in annual precipitation (Fig. 3-3). Fig. 3-3: A&B are the meteorological conditions at the surface that are repeated from Fig. 3-2 to show the correlation between surface boundary conditions and the soil water storage of the 100 cm below. The shaded areas in Fig. 3-3: C represent soil freezing periods (decrease in soil permittivity and soil temperature falling below 0 °C) at 5 cm depth, the width of the shadowed area indicates the length of soil freezing period.

Soil storage in the spring was 36, 33, 28, 56 and 24 mm greater than that in the fall for hydrological year 2008/2009, 2009/2010, 2010/2011, 2011/2012 and 2012/2013, respectively. The positive storage change indicates that snowmelt water infiltrated into partially frozen soils. Again, a spike in water storage was observed during winter 2011/2012 (marked with an arrow on Fig. 3-3: C), during a freeze-thaw cycle at 5 cm as noted above. This mid-winter snowmelt infiltration event increased the soil storage by estimate 34 mm. Soil water storage increased a further 35 mm during the following spring. More details can be found in Table 3-5.

3.4.2. Soil freezing and thawing phenomena

The major soil freezing and thawing dynamics and physical processes will be discussed as three temporal stages: (1) initial soil freezing and snowpack accumulation; (2) mid-winter freeze-thaw cycles and snowpack depth dynamics; and (3) soil thawing and snowmelt infiltration.

3.4.2.1. Initial soil freezing, snowpack accumulation and maximum depth of soil frost

This section focuses on soil freezing and thawing dynamics and their interaction with fall moisture levels and early winter snowpack dynamics. Information presented in Fig. 3-4 through Fig. 3-8, Table 3-3 through Table 3-5 will be the focus of discussion. Figure 3-4 through Fig. 3-8 present detailed time series of air temperature, precipitation, depth of snowpack and soil

temperature, dielectric permittivity and liquid moisture content of selected soil depths for the winters of 2008/2009, 2010/2011, 2011/2012 and 2012/2013, respectively. A portion (~1 month) of the soil dielectric permittivity record during soil freezing is missing from the winter 2009/2010, making interpretation difficult and won't be discussed. Soil freezing-thawing curves (SFTCs) measured during the winters of 2008/2009 and 2011/2012 and presented in Fig. 3-9 and Fig. 3-10, respectively, will be used to facilitate the interpretation of soil freezing from the beginning of the freezing processes.

Over the 5 years from 2008 to 2013, snow usually started and accumulated in early to mid-November. Any snow falling prior to November did not usually accumulate. A 5 cm threshold is used for the start of snowpack accumulation in Table 3-4 because it was observed early season snowpack with depths of 5 cm or less often disappeared with modest changes in temperature or because of wind redistribution. The start of snowpack accumulation was earliest in winter 2012/2013 (Fig. 3-8: B, Nov. 8th, 2012), latest in winter 2008/2009 (Fig. 3-4: B, Dec. 9th, 2008) and similar for winters 2010/2011 (Fig. 3-6: B, Nov. 18th, 2010), 2011/2012 (Fig. 3-7, Nov. 17th, 2011) and winter 2009/2010 was Nov. 30th, 2009 (Fig. 3-5).

Dates for start and end of soil freezing also varied among years (Table 3-3). We define the start of soil freezing in the fall by soil temperature dropping below 0 °C accompanied by a decrease in permittivity, which is a little different from the meteorological definition that soil freezes when daily average temperature < 0 °C [Zhang, 2005]. Soil at 5 cm started freezing as early as Nov. 4th (Fig. 3-7: C, Table 3-3) in winter 2011/2012; soil freezing started around a week later for winter 2009/2010 (Fig. 3-5: C, Nov. 13th). Freezing dates are similar for the other three winters: Nov. 20th for winter 2008/2009 (Fig. 3-4: C, Table 3-3), Nov. 24th for winter 2010/2011 (Fig. 3-6: C, Table 3-3), and Nov. 25th for winter 2012/2013 (Fig. 3-8: C, Table 3-3).

Air temperature, timing of snow accumulation and fall soil moisture conditions all appear to interact with the timing of soil freezing and the depth of soil frost penetration. For instance, snow accumulated after the soil began to freeze in winters 2008/2009 (Fig. 3-4: B~E) and 2011/2012 (Fig. 3-7: B~E) and the maximum frost depth of these two winters exceeded 50 cm. Surface soil water contents (e.g. ~0.15 cm³ cm⁻³ at 5 cm) prior to soil freezing were relatively low in these two years as well (Fig. 3-4: B, Fig. 3-7: B, and Table 3-5). During the winters of 2010/2011 (Fig. 3-6: B&C) and 2012/2013 (Fig. 3-8: B&C), on the other hand, snow accumulated prior to soil

freezing under relatively wet surface soil water contents (e.g., $\sim 0.3 \text{ cm}^3 \text{ cm}^{-3}$ at 5 cm) and the freezing front did not reach 20 cm. For winter 2009/2010, soil froze before snow accumulated but since the soil water content was relatively high ($\sim 0.26 \text{ cm}^3 \text{ cm}^{-3}$), the frost penetration was intermediate, between 20 and 50 cm (Fig. 3-5: B~D and Table 3-5).

Thus there are two pairs of winters with similar conditions: (1) the winters of 2008/2009 and 2011/2012 are characterized by relatively dry fall soil moisture conditions, onset of soil freezing prior to snowpack accumulation and relatively deep (> 50 cm) soil frost penetration; and (2) the winters of 2010/2011 and 2012/2013 are characterized by relatively wet fall soil moisture conditions, onset of soil freezing before snowpack accumulation, and relatively shallow (< 20 cm) frost penetration. The differences in frost penetration exhibited by these two types of winters are a result of a combination of differences in soil thermal properties (e.g., thermal conductivity and soil thermal storage/heat capacity), heat conduction and latent heat. Since the soil physical properties (e.g., bulk density, soil texture, and structure) of the Breton Plots weather station are assumed to be the same over the years investigated, differences in soil heat capacity and thermal conductivity between years are mainly due to the magnitude of soil water/ice contents. Studies of unfrozen soils [Lu *et al.*, 2007] indicated that thermal conductivity increases sharply with water content at low water contents because of the bridging effect of soil water connecting soil particles, facilitating heat conduction, but the magnitude of increase in thermal conductivity decreases as water content increases further past a threshold. In frozen soils, thermal conductivity will follow the similar increasing pattern as in unfrozen soils before phase change takes place, but thermal conductivity also increases with ice content [Hansson *et al.*, 2004]. Soil water contents were low in winters of 2008/2009 and 2011/2012 and the soil heat capacity would be lower in these winters relative to 2010/2011 and 2012/2013 with wetter soil conditions. Latent heat released from phase change (i.e., transformation of water to ice) could be easily offset by heat conduction. In addition, thermal conductivity likely increased due to the bridging effects of water/ice and heat loss at deep depths could take place, as reflected by simultaneous decreases in temperature and water content/permittivity. The late snow accumulation provided a longer time period for upward heat conduction to the atmosphere and phase change at deeper depths. Therefore, soils in winters of 2008/2009 and 2011/2012 froze to a depth over 50 cm. The opposite is true for winters of 2010/2011 and 2012/2013, high soil water content prior to freezing meant more heat conduction is required for offsetting latent heat produced by phase change. The early timing of snowpack

accumulation, however, prevented further significant heat loss because of insulation by the snowpack even though larger amounts of ice may increase heat conduction. Therefore, high water content and early snow accumulation together slowed down the freezing processes and only soils at shallow depth were frozen.

The interactions between timing of snowpack accumulation, soil freezing and fall moisture conditions are also apparent in the soil freezing-thawing curves (SFTCs). SFTCs measured in 2008/2009 and 2011/2012 are presented in Fig. 3-9, and 2010/2011 and 2012/2013 in Fig. 3-10. The SFTCs presented in Figs. 3-9 and 3-10 are plots of soil dielectric permittivity or estimated soil liquid-water content versus temperature for the entire winter period, but are split into 2-week to 1-month periods that are represented by different colors, arrows of the same colors at each period are used to illustrate the direction of freezing or thawing. The black, red and green parts of the SFTCs will be used along with the time series in Fig. 3-4 through Fig. 3-8 to highlight and interpret soil freezing and snowpack interactions during soil freezing and the onset of snowpack accumulation in the early part of the winter. Daily values of permittivity (A&B) and liquid-water content (C&D) were used for these figures to reduce the number of points and allow easier interpretation; data have neither been smoothed nor filtered but parts of the graphs at the above freezing temperature (e.g. > 1 for Fig. 3-9 or $0.2\text{ }^{\circ}\text{C}$ for Fig. 3-10) were truncated.

The SFTCs for the winters of 2008/2009 and 2011/2012 (dry fall, early soil freezing, deep frost) are presented in Fig. 3-9, and the winters of 2010/2011 and 2012/2013 (wet fall, late soil freezing, shallow frost) are in Fig. 3-10. Soil freezing commenced at different subfreezing temperatures for the two types of winters. For example, permittivity kept relatively constant when temperature dropped below $-1\text{ }^{\circ}\text{C}$ in winter 2011/2012 (Nov. 1st - Jan. 4th, Fig. 3-9: B) and $-1.5\text{ }^{\circ}\text{C}$ in winter 2008/2009 (Nov. 1st - Nov. 28th, Fig. 3-9: A), but no/little phase change occurred during this period of time (small amount of water infiltration might occur at the end of this period as marked by the steeply increased permittivity). For winter 2010/2011 (Nov. 30th - Dec. 20th, Fig. 3-10: A) and winter 2012/2013 (Nov. 22nd - 30th, Fig. 3-10: B), a slight decrease of permittivity was observed before the sharp decrease took place at around $-0.3 \sim -0.4\text{ }^{\circ}\text{C}$. This period of slight decline in permittivity can be interpreted as the onset of ice formation or water migration out of the moisture probe (ThetaProbe) sampling volume. The large decrease in permittivity with relatively constant temperature which followed is most likely a result of significant ice formation.

It should be noted that the SFTCs presented in Fig. 3-9 and Fig. 3-10 are different from soil freezing characteristic (SFC), the concept of which is derived from the soil moisture retention characteristic (SMRC) by *Miller* [1965]. The SFC is used to describe the quantity and energy status of unfrozen water at equilibrated states in frozen/freezing soils of which the total soil water content is constant [*Miller*, 1965; *Koopmans and Miller*, 1966]. In the field, however, soils likely seldom reach thermodynamic equilibrium because of the transient boundary conditions (e.g., air temperature, variable snowpack depth, and precipitation) and water redistribution changes the total water content. Therefore, unlike freeze-thaw experiments in lab under controlled boundary conditions (Fig. 3-11; Figs. 2-13&2-14 or Figs. 13&14 in *He and Dyck* [2013]), and Figs. 5&7 in *Tian et al.* [2014]), complete, monotonic freeze-thaw cycles (i.e., uninterrupted temperature decreases from above zero to well below zero and then back to above zero) rarely occur under field conditions and freezing/thawing cycles are usually interrupted by temporary increases or decreases in temperature [*Parkin et al.*, 2013]. Previous studies [*Kelleners and Norto*, 2012; *Parkin et al.*, 2013] showed a field-measured SFTC similar to a SFC might be retrieved when weather conditions allow for monotonic freeze-thaw cycles, but these conditions are rare and usually only for a short temperature range. We found the same phenomenon in this study as well.

3.4.2.2. Mid-winter freeze-thaw cycles and snowpack depth dynamics

This section focusses on soil freezing and thawing dynamics and their interaction following soil freezing (December through March), but prior to soil thawing and snowmelt. Information presented in Fig. 3-4 through Fig. 3-10, Table 3-3 through Table 3-5 will be the focus of discussion. Figures 3-12 and 3-13 are selected SFC shaped SFTCs from field observations, which are used for comparison to the lab simulated SFTCs taken on soil samples from Breton Plots (Fig. 3-11).

Winter air temperature, soil temperature, soil dielectric permittivity and snowpack depth were quite variable over the five years. A number of thawing and refreezing cycles (TRFCs) at various soil depths were observed in all five winters (Table 3-5). A TRFC is defined as a period of time when daily average air or soil temperature increases above 0 °C and then back to below 0 °C. These soil TRFCs were usually interpreted to be the result of sensible heat exchange between the soil and the snowpack and, in a couple of extreme cases, mid-winter snowmelt infiltration events.

Depth of snowpack varied with small fluctuations in air temperature during the winter, but generally continued to increase until spring snow ablation. In all 5 winters investigated, shorter warming periods were observed where air temperatures occasionally rose above zero and these periods corresponded to reductions in snowpack depth proportional to the length and intensity of the warm periods that mostly occurred between mid-January and mid-February (Fig. 3-4: A&B, Fig. 3-5: A&B, Fig. 3-6: A&B, Fig. 3-7: A&B, and Fig. 3-8: A&B). The observed increase in air temperature and reductions in snowpack also corresponded to increased soil temperature and dielectric permittivity at shallow depths (e.g., 5 cm depth) as well (Fig. 3-6: C, Fig. 3-7: C, and Fig. 3-8: C). These observed increases in dielectric permittivity are interpreted to be a result of the melting of soil ice to liquid-water and perhaps snowmelt infiltration.

In winter 2011/2012 when there was a significant warming period starting Jan. 2nd, 2012 (Fig. 3-7: A&B, marked with an arrow in Fig. 3-7: B) with air temperature as high as ~ 10 °C. This warm period lasted for about 1 week and corresponded to a $> 60\%$ decrease in snowpack depth and a sharp rise in soil dielectric permittivity at 5 and 20 cm (Fig. 3-7: C&D). At the start of this warming period, soil temperature was still slightly below 0 °C but soon went above 0 °C with permittivity exceeding the magnitude prior to freezing. This rise in dielectric permittivity and soil temperature is attributed to snowmelt infiltration and resulted in a change in total water content that is taken into consideration when calculating θ_l and θ_i for the rest of the record. Since the soil water content prior to freezing was low (i.e., $0.14 \text{ cm}^3 \text{ cm}^{-3}$), melt water could infiltrate into the frozen soil through the air-filled pores. The following drop in air temperature from Jan. 6th to 9th, 2012 resulted in refreezing of snow cover and soil as indicated by the decreased permittivity. After this, another increase in air temperature lead to more snowmelt and infiltration that increased the permittivity (and total water content) again although no significant decrease in snow depth was observed. The mechanism for snowmelt in the absence of a change in snow depth is that, because of the previous TRFC, the snowpack became dense and icy with a relatively stable structure and the following thawing period did not result in a significant change in depth of the snowpack, and no significant precipitation was recorded during this period of time confirmed this. The warming-freezing-warming-freezing during the period of Jan. 4th to 10th, 2012 formed a fork-shaped peak in the permittivity/liquid-water content time series (Fig. 3-7: C&D, marked with a double arrow). This winter infiltration can be found in the SFTCs as a “y” shaped segment (red on Fig. 3-10: B&D, Jan. 4th - 10th). Similar winter infiltration was found in

the winter of 2012/2013 (Jan. 13th - 22nd, 2013, Fig. 3-8: A~C, marked with a double arrow) when the increase of permittivity/liquid-water content was associated with increase in air temperature and decrease in snowpack depth, but this increase of permittivity could be a result of the melting of soil ice and perhaps a small amount of snowmelt infiltration because the permittivity did not exceed the value just prior to soil freezing and the soil temperature was relatively unchanged.

The mid-winter changes in soil temperature, dielectric permittivity and liquid-water content are visible as hysteresis loops in the SFTCs. This is especially apparent at the 5 cm depth (yellow, blue, purple and cyan segments of the curves in Fig. 3-9 and Fig. 3-10). Mechanisms contributing to hysteresis in SFCs are not well understood yet but some of the factors influencing hysteresis in soil moisture characteristics (drying and wetting) are used for explanations because both drying and freezing processes involve the replacement of liquid-water with another phase. The possible mechanisms accounting for hysteresis in SFCs include but not limited to: (1) metastable nucleation and supercooling/undercooling; (2) freezing-point depression due to solute in soil water; (3) final freezing temperature before thawing [*He and Dyck*, 2013]; and (4) “ink bottle” effects [*Tian et al.*, 2014]. STFCs measured in field are not really SFCs as alluded to earlier and the reasons why they are hysteric will be discussed shortly. STFCs measured on Breton soil in the laboratory are presented in Fig. 3-11. These STFCs represent more closely true SFCs because they were measured under conditions where total water content in the soil could be maintained at a constant level and soil temperature could be controlled and wasn't changed until the measured permittivity didn't change (i.e., near thermal equilibrium). Significant supercooling takes place without water loss as indicated by the flat permittivity vs temperature around zero degrees on the freezing curve and followed by a sharp decrease in permittivity that represents significant phase change from water to ice. Soil does not begin to thaw significantly until temperature is above zero. The total water content in the small cores remained constant as indicated by the consistent permittivity before freezing and after thawing.

The hysteresis loops in the field-measured SFTCs are likely influenced by the hysteretic nature of the SFC, but are most likely influenced by transient boundary conditions which do not allow thermal equilibrium and constant total water content. During winter time under natural conditions, the main driver of soil temperature change is the air temperature. Fluctuations in air temperature, attenuated by the snowpack are reflected as changes of permittivity/liquid-water

content and soil temperature. However, neither the freezing nor thawing trends were long enough to form a complete loop (i.e., completely thawed soil to frozen soil at the minimum recorded winter temperature) or reach thermal equilibrium. The end of one freezing cycle (decrease in temperature and permittivity) is usually the start of one thawing cycle (increase in temperature and permittivity), which in turn may become the start of a subsequent freezing cycle. Despite these very transient conditions, two SFC-shaped complete SFTCs were chosen for: winter 2010/2011 at 5 cm (Fig. 3-12) and winter 2011/2012 at 20 cm (Fig. 3-13), which represent mild and severe freezing conditions, respectively.

It is also noted that the SFTCs are hysteric because of changes in the total water content within the sampling volume of the soil moisture probe - true SFCs would represent soil with constant total water content. For example, an apparent decline in permittivity was observed before soil temperature went below zero from the freezing curves, which might be attributed to water migration out of the sampling volume of the moisture probe to the freezing front propagating from the soil surface. The decline in permittivity at the onset of freezing (Fig. 3-12 and Fig. 3-13) is not as steep as the lab measured SFTCs (Fig. 3-11) that show phase change without water loss. On the thawing part of the curves, a steep increase in permittivity was observed before soil temperature went above zero that is likely attributed to infiltration of snowmelt. This is significantly different from the lab measured SFTCs (Fig. 3-11) that show soil only began to thaw significantly at temperatures above zero. In addition, under natural boundary conditions, hysteresis between the freezing and thawing curves was observed occasionally to be reversed: the thawing curve showed greater permittivity than the freezing curve at the same temperature (Fig. 3-14). This is a result of soil freezing under dry soil conditions followed by a mid-winter infiltration event, followed by soil thawing (i.e., a change in total water content).

3.4.2.3. Soil thawing and snowmelt infiltration

This section will focus on the period of snowmelt and soil thawing. The focus will be soil water storage change (mainly due to snowmelt infiltration), and soil water storage prior to soil freezing presented in Fig. 3-15 and Fig. 3-16. Relevant aspects of Fig. 3-4 through Fig. 3-10 and Table 3-3 through Table 3-5 will also be discussed.

The duration from the start of significant snowmelt to < 5 cm of snow depth was usually around 1 week, but it took approximately 1 month from the start of significant snowmelt until

complete loss of snowpack due to repeated thawing and freezing events and occasional snowfall. The soil generally thawed in a few days after beginning of significant snowmelt. More details can be found in Table 3-4. The completion of soil thawing is defined as an increase in permittivity/liquid-water content accompanied by soil temperature rising and remaining above 0 °C for the rest of growing season. The simultaneous rise in soil dielectric permittivity and the increase in soil temperature are interpreted as the melting of soil ice and the infiltration of snowmelt.

Soil at 5 cm completely thawed on Apr. 8th for winter 2011/2012 (Fig. 3-7: C, Table 3-3); but thawed one week earlier compared to 2011/2012. Thawing dates are similar for the other three winters: Apr. 8th for winter 2008/2009 (Fig. 3-4: C, Table 3-3) and winter 2010/2011 (Fig. 3-6: C, Table 3-3), and Apr. 6th for winter 2012/2013 (Fig. 3-8: C, Table 3-3). Soil generally freezes from top down but thaws from above and below under temperature gradients (warmer surface and deep ground soil than the middle frozen soils). This trend is apparent in the winter of 2009/2010. Soil at 5 cm started freezing on Nov. 13th, 2009 which was one month earlier than that at 20 cm, while soil at 20 cm depth thawed on Mar. 13th, 2010 which was 16 days earlier than soil thawing at 5 cm depth (Fig. 3-5: C&D, Table 3-3). Winter 2011/2012 was similar, but not as obvious as winter 2009/2010, soil froze on Nov. 4th, 2011, Jan. 14th, 2012, and Jan. 27th, 2012, respectively for 5, 20, and 50 cm while the corresponding depths thawed on Apr. 8th, Apr. 10th and Apr. 7th, 2012, respectively (Fig. 3-7: C~E, Table 3-3). During spring melt in 2012, the permittivity at 50 cm began to increase about 2 weeks prior to that at 20 cm, but soil temperature indicates complete thawing only differed by 3 days between the two depths, suggesting rising groundwater elevation was responsible for the increased permittivity. The characteristic of thawing from both top and down and leaving a middle frozen layer may impede the infiltration given that ice filled pores are high (i.e., high ice content).

Snow surveys were conducted 4 ~ 5 times between November and March each year since winter 2009/2010 by the Alberta Agriculture and Rural Development (Ralph Wright, Alberta Agriculture and Rural Development, personal communication). The snow survey in March each year was selected for calculation of snow water equivalents (SWE). This value together with the precipitation thereafter till the end of significant snowmelt was used to calculate the water availability for infiltration during spring melt. The calculated water available for infiltration in the spring was 60, 61, 143, 95, and 122 mm for 2009 to 2013, respectively.

As mentioned above, snowmelt infiltration likely affects the thawing portion of the SFTC, reflected as a steep increase in permittivity within a short temperature range which usually occurred during spring snowmelt (e.g., Apr. 4th - 30th, Fig. 3-9: A, Mar. 30th - Apr. 30th, Fig. 3-10: B, Mar. 29th - Apr. 30th, Fig. 3-10: A, and Mar. 30th - Apr. 30th, Fig. 3-10: B). The same phenomenon was observed during mid-winter infiltration events (Jan. 4th - 10th, Fig. 3-9: B). During the period from mid-November to early April, evapotranspiration is assumed to be negligible due to the limited plant photosynthetic activity and low air temperature, but sublimation and runoff processes (not measured) would reduce the amount of water in the snowpack and precipitation available for infiltration into the soil. Since surface runoff, deep drainage below 100 cm, and/or groundwater migration above 100 cm may occur during snowmelt, the storage change of the top 100 cm, although likely influenced by snowmelt infiltration, is not necessarily equal to snowmelt infiltration. The change in storage between fall and spring for each winter can be found in Table 3-5 and Fig. 3-15. Because of the relatively stable groundwater-influenced water contents at 50 and 100 cm, water content measurements by the 5 cm and 20 cm moisture probes (together representing the top 30 cm) are likely the most influenced by spring snowmelt. Change in soil water storage calculated in the top 30 cm of soil is presented in Fig. 3-16.

Snowmelt infiltration into seasonally frozen soils is a complicated process and it usually can be divided into three categories based on the infiltration potential: (1) unlimited (heavily cracked or preferential flow dominated soil); (2) limited (un-cracked soils without any impervious layer); and (3) restricted (existence of ice layer on soil surface or high ice content layer within infiltration zone) [Granger *et al.*, 1984]. Snowmelt infiltration studies mainly focus on the type of limited infiltration and factors that affect this process have been extensively described in a qualitative manner [Kane, 1980; Kane and Stein, 1983a; Granger *et al.*, 1984; Eigenbrod, 1996; Iwata *et al.*, 2008, 2010, 2011; Christensen *et al.*, 2013]. Characteristics of the overlying snowpack and its melt rate [Granger *et al.*, 1984; Shanley and Chalmers, 1999; Decker *et al.*, 2003; Iwata *et al.*, 2010] and surface soil moisture content at the onset of freezing or snowmelt [Kane and Stein, 1983b; Granger *et al.*, 1984; Stadler *et al.*, 2000; Watanabe *et al.*, 2013] are of great importance and are used for modelling snowmelt infiltration [Zhao and Gray, 1999; Gray *et al.*, 2001].

It is widely accepted that infiltration has an inverse relationship with soil moisture content [Kane, 1980; Zhao and Gray, 1999; Gray et al., 2001], but there is discrepancy in the depth of soil moisture that determines infiltration. Kane and Stein [1984] concluded that soil moisture of top 10 - 20 cm dominated snowmelt infiltration, while Granger et al. [1984] found soil moisture content of top 30 cm was the dominant factor, and the research of Gray's group [Zhao and Gray, 1997a, 1997b; Zhao et al., 1997; Gray et al., 2001] suggested the use of soil moisture content of top 40 cm to predict snowmelt infiltration. Assuming that the change in storage between fall and spring in the top 30 cm of the Breton soil was a result of snowmelt infiltration, our results concur with other results in the literature (Figs. 3-15 and 3-16). The amount snowmelt infiltration is influenced by the storage capacity available for infiltration as indicated by fall storage or fall air-filled porosity. This agrees with the snowmelt infiltration study on a reclaimed site that greater capping soil depths are associated with greater potential for infiltration and percolation [Christensen et al., 2013]

In Figs. 3-15 and 3-16, a significant linear relationship is observed between fall surface air-filled porosity of top 10 cm or fall storage of top 30 cm and the change in soil moisture storage between soil freezing and spring thaw. This suggests that available storage capacity in the top 30 cm of the soil in the fall is at least partially filled by snowmelt infiltration. The point for 2009 in Fig. 3-15 deviates from the straight line is due to the large air filled porosity of top 10 cm or the dry soil due to the small precipitation in the fall (data not shown). Although water availability in this year was almost the same as the air filled porosity of top 30 cm, part of the available water for infiltration may have become runoff or percolated below 100 cm since the ground water table was low in 2009. This phenomenon is also reflected in Fig. 3-16 in which the sum of storage change between fall and spring and initial fall storage is less than the total saturated water storage (calculated using total porosity in Table 3-1) although the available water (i.e., snowmelt + precipitation) for infiltration may exceed the air-filled porosity. The difference might be attributed to surface runoff, not all pores may be available for water flow and storage, and/or deep percolation (the amount exceeds the field capacity of soil) that reduce the recorded amount of soil water storage change of top 100 cm. Surface runoff may occur when the rate of snowmelt exceeds the rate of infiltration or impeded by ice lenses, ice-filled pores or basal ice layers on the soil surface [Cary et al., 1978; Kane, 1980; Miller, 1980; Stahli, 2005].

3.5. Conclusion

Soil data (e.g., temperature and moisture) and meteorological data (e.g., precipitation, air temperature, and snow) collected at the University of Alberta Breton Plots over a course of five years (2008 - 2013) were used to investigate the feasibility of multiphase dielectric mixing model to estimate unfrozen water and ice content for field application and to understand soil freezing-thawing processes and snowmelt infiltration into partially frozen soils under natural boundary conditions. The dielectric mixing model is based on the assumption of constant total soil water content measured prior to soil freezing by ThetaProbe. The total soil water content, however, can be affected by a number of processes including infiltration (rain and snowmelt), deep percolation, groundwater discharge and evapotranspiration. These processes may occur simultaneously and therefore there are uncertainties in estimates of liquid-water and ice content. Change in soil temperature and snow depth that may indicate the change of total soil water content were carefully investigated at each time when soil temperature went above zero and there were change in snow depth. Therefore, estimation of unfrozen water and ice content by the dielectric mixing model are not expected to cause a misinterpretation of the processes occurring in the field when interpreted with supporting meteorological measurements. Furthermore, the storage change estimates are based on soil water measurements in unfrozen soils (pre and post freezing) where the constant water content assumption is no longer required.

The results also suggest that soil frost depth is controlled by soil moisture content prior to soil freezing and the timing of snowpack establishment. Soil generally froze to a deeper depth (≥ 50 cm) if snow cover accumulated on the ground later than soil started freezing and soil was dry in the preceding fall due to the increase of soil thermal conductivity (water/ice connect soil particles) and small heat capacity. Greater amounts of soil water can reduce the frost penetration because of higher soil heat capacity that requires longer times to remove heat through sensible heat flux. Early accumulation of a deep snowpack prevents further significant exchange of latent heat and sensible heat, which prevents deep penetration of frost front although the soil thermal conductivity increases with water content. More thawing and refreezing events were found at shallow soil depths with early snowpack accumulation which indicates heat exchange can occur across thick snowpack especial during snowmelt infiltration events. Frequent thawing and refreezing may enhance frost induced water redistribution. Soil freezing and thawing curves

(permittivity/liquid-water content as a function of temperature) are used to facilitate the interpretation of soil freezing phenomena including supercooling of soil water, water migration, and infiltration. Soil freezing and thawing curve is different from the soil freezing characteristic that is retrieved under controlled boundary conditions where soil water content is constant and soil water and temperature are in equilibrium.

The air-filled porosity of top 10 cm and storage of the top 30 cm in the fall appear to be the dominant factor governing snowmelt infiltration at Breton Plots site, similar to the depths of 10 to 40 cm reported in previous studies. And we found a good relationship between snowmelt infiltration and soil water storage prior to soil freezing, which confirms that pore ice blocks water entry in initially wet soils and water can flow and store in the air-filled pores of initially dry soils. In addition, winter infiltration during thawing period may increase the overall infiltration amount without significantly reduce spring snowmelt infiltration. This study contributes to understanding of the soil freezing and thawing characteristics and snowmelt infiltration under natural boundary conditions with the influence of the climate change and aid in water resources management and development of environmental risk strategies.

Table 3-1. Selected soil characteristics

Horizons depths (cm)	Layer	Chemical properties					Physical properties		
		pH	EC	S	Si	C	Bulk density (cm ³ cm ⁻³)	Porosity	Texture
2 - 0	L	-	-	-	-	-	-	-	Plant litter
0 - 19 ^a	Ap	7.2	1.05	27	46	27	1.27	0.52	Loam to clay loam
19 - 25 ^b	Aegj	7.4	0.74	30	45	25	1.58	0.40	Loam to clay loam
25 - 80 ^c	Btgj	7.3	0.93	31	44	25	1.58	0.40	Clay loam to clay
80 - 110 ^d	Ckgj	7.1	0.80	38	33	29	1.81	0.32	Clay loam to clay

^a Properties except texture at this depth were measured on cores taken from 5 cm.

^b Properties except texture at this depth were measured on cores taken from 20 cm.

^c Properties except texture at this depth were measured on cores taken from 50 cm.

^d Properties except texture at this depth were measured on cores taken from 100 cm.

Table 3-2. ThetaProbe calibration, model parameters, and goodness of fit of Breton Plots site

Depth (cm)	Calibration		Model Fit				
	a ₀	a ₁	Self-consistency	Aspect	RMSE	NS-Eff	Avg-Dev
5	1.63	8.59	0.601	11.266	0.093	1	-0.027
20	1.82	8.48	0.617	14.254	0.121	1	-0.045
50	1.82	8.48	0.617	14.254	0.121	1	-0.045
100	1.89	9.2	1.191	8.922	0.069	1	-0.022

Table 3-3. Comparison of air and soil temperatures (value in parenthesis is standard error) and dates of soil freezing and thawing

Year	Depth	Average temperature (°C)					Soil freezing/thawing dates		
		Nov. 31 st	1 st -Oct. 15 th	Nov. 15 th	15 th -Apr. 28 th	Dec. 28 th	1 st -Feb.	Apr. 16 th -Oct. 31 st	Freezing
2008 -2009	air	2.88 (0.61)	-7.04 (0.17)	-10.03 (0.22)	10.55 (0.46)			Oct/08/2008	Apr/29/2009
	5	6.23 (0.43)	-1.22 (0.03)	-1.96 (0.02)	12.75 (0.35)			Nov/20/2008	Apr/08/2009
	20	6.34 (0.38)	-0.56 (0.02)	-1.03 (0.01)	12.22 (0.32)			Nov/28/2008	Apr/08/2009
	50	6.20 (0.32)	0.46 (0.02)	0.20 (0.02)	11.02 (0.29)			Jan/02/2009	Apr/11/2009
	100	6.25 (0.26)	1.91 (0.03)	1.89 (0.02)	9.80 (0.27)			-	-
2009 -2010	air	3.61 (0.53)	-5.09 (0.15)	-9.59 (0.18)	10.58 (0.37)			Oct/08/2009	Apr/12/2010
	5	7.62 (0.40)	-0.26 (0.02)	-0.76 (0.01)	12.50 (0.33)			Nov/13/2009	Mar/29/2010
	20	7.51 (0.38)	0.16 (0.01)	-0.23 (0.01)	12.10 (0.30)			Dec/16/2009	Mar/13/2010
	50	7.36 (0.32)	1.28 (0.01)	1.10 (0.01)	11.21 (0.26)			-	-
	100	7.17 (0.26)	2.43 (0.02)	2.43 (0.01)	10.25 (0.24)			-	-
2010 -2011	air	2.25 (0.63)	-9.27 (0.16)	-11.13 (0.20)	11.01 (0.35)			Oct/25/2010	Apr/20/2011
	5	6.91 (0.38)	-0.05 (0.01)	-0.12 (0.00)	12.54 (0.35)			Nov/24/2010	Apr/08/2011
	20	6.90 (0.35)	0.43 (0.01)	0.38 (0.00)	12.08 (0.32)			-	-
	50	6.89 (0.29)	1.45 (0.01)	1.45 (0.01)	11.15 (0.29)			-	-
	100	6.93 (0.24)	2.66 (0.02)	2.72 (0.01)	10.19 (0.26)			-	-
2011 -2012	air	4.46 (0.51)	-3.54 (0.13)	-4.89 (0.17)	10.98 (0.46)			Oct/26/2011	Apr/16/2012
	5	6.69 (0.42)	-0.81 (0.02)	-1.32 (0.03)	12.86 (0.40)			Nov/04/2011	Apr/08/2012
	20	6.66 (0.38)	-0.33 (0.02)	-0.59 (0.03)	12.35 (0.36)			Jan/14/2012	Apr/10/2012
	50	6.74 (0.32)	0.86 (0.02)	0.95 (0.03)	11.42 (0.31)			Jan/27/2012	Apr/07/2012
	100	6.86 (0.26)	2.22 (0.03)	2.47 (0.03)	10.44 (0.27)			-	-
2012 -2013	air	3.33 (0.57)	-6.56 (0.13)	-7.77 (0.17)	11.54 (0.38)			Oct/11/2012	May/01/2013
	5	6.63 (0.37)	-0.08 (0.00)	-0.18 (0.00)	12.15 (0.36)			Nov/25/2012	Apr/06/2013
	20	6.62 (0.35)	0.33 (0.01)	0.25 (0.00)	11.76 (0.33)			-	-
	50	6.68 (0.29)	1.41 (0.01)	1.40 (0.01)	10.89 (0.30)			-	-
	100	6.75 (0.24)	2.63 (0.02)	2.69 (0.01)	9.94 (0.27)			-	-

Table 3-4. Precipitation and snowpack depth and SWE (value in parenthesis is standard error)

Year	Precipitation and snowpack	Nov.1 st -Oct.31 st	Nov.15 th -Apr.15 th	Dec.1 st -Feb.29 th
2008-2009	Precipitation (mm)	332	100	55
	Snow depth avg. (mm)	-	159 (7)	160(7)
	SWE (mm) ^a	-	31	31
	Snow depth max. (mm)	-	335	289
	SWE measured max. (mm) ^a	-	69	59
	Start of snowpack	Dec/09/2008	-	-
	Snowmelt period	Mar/22-Apr/29/2009	-	-
2009-2010	Precipitation(mm)	618	65	50
	Snow depth avg. (mm)	-	216 (9)	262 (5)
	SWE (mm) ^a	-	43	53
	Snow depth max. (mm)	-	322	322
	SWE measured max. (mm) ^b	-	62	62
	Start of snowpack	Nov/29/2009	-	-
	Snowmelt period	Mar/1-Mar/25/2010	-	-
2010-2011	Precipitation(mm)	524	154	105
	Snow depth avg. (mm)	-	386 (15)	357 (16)
	SWE (mm) ^a	-	80	74
	Snow depth max. (mm)	-	715	575
	SWE measured max. (mm) ^b	-	123	83
	Start of snowpack	Nov/18/2010	-	-
	Snowmelt period	Mar/24-Apr/25/2011	-	-
2011-2012	Precipitation(mm)	536	133	40
	Snow depth avg. (mm)	-	107 (4)	102 (4)
	SWE (mm) ^a	-	19	18
	Snow depth max. (mm)	-	313	182
	SWE measured max. (mm) ^b	-	60	37
	Start of snowpack	Nov/17/2011	-	-
	Snowmelt period	Mar/7-Apr/17/2012	-	-
2012-2013	Precipitation(mm)	433	114	57
	Snow depth avg. (mm)	-	238 (6)	251 (5)
	SWE (mm) ^a	-	48	51

Snow depth max. (mm)	-	403	331
SWE measured max. (mm) ^b	-	108	72
Start of snowpack	Nov/8/2012	-	-
Snowmelt period	Mar/21-Apr/19/2013	-	-

^a SWE is calculated based on $SWE(mm) = 2.1714 * \text{snow depth}(cm) - 3.8676$, the equation is regression model with snow survey data at the Breton Plots over the years from 2010 to 2013.

^b SWE maximum is selected from the snow survey.

Table 3-5. Selected characteristics

Year	Snowpack accumulation (>5 cm prior to freezing)	Fall moisture content (cm ³ cm ⁻³)				Soil water storage (mm)			Max. frost depth (cm)	Winter freeze-thaw cycles based on daily temperature					Water under gradient Evidence	redistribution temperature Magnitude (mm)	Winter infiltration
		5 cm	20 cm	50 cm	100 cm	Prior to freezing	After snowmelt	Storage change		air	5 cm	20 cm	50 cm	100 cm			
2008-2009	No	0.15	0.26	0.31	0.29	281.3	317.1	35.8	>50	21	1	2	1	0	Yes	6.61	No
2009-2010	N/A	0.26	0.26	0.30	0.32	295.66	328.2	32.6	>20	15	0	2	0	0	Yes	1.48	No
2010-2011	Yes	0.29	0.31	0.36	0.32	329.5	357.6	28.17	>5	10	3	0	0	0	Yes	6.87	No
2011-2012	No	0.14	0.32	0.32	0.32	292.9	349.3	56.4	>50	20	7	0	0	0	Yes	12.90	Yes
2012-2013	Yes	0.32	0.32	0.35	0.32	331.1	355.2	24.1	>5	15	4	0	0	0	Yes	6.16	No

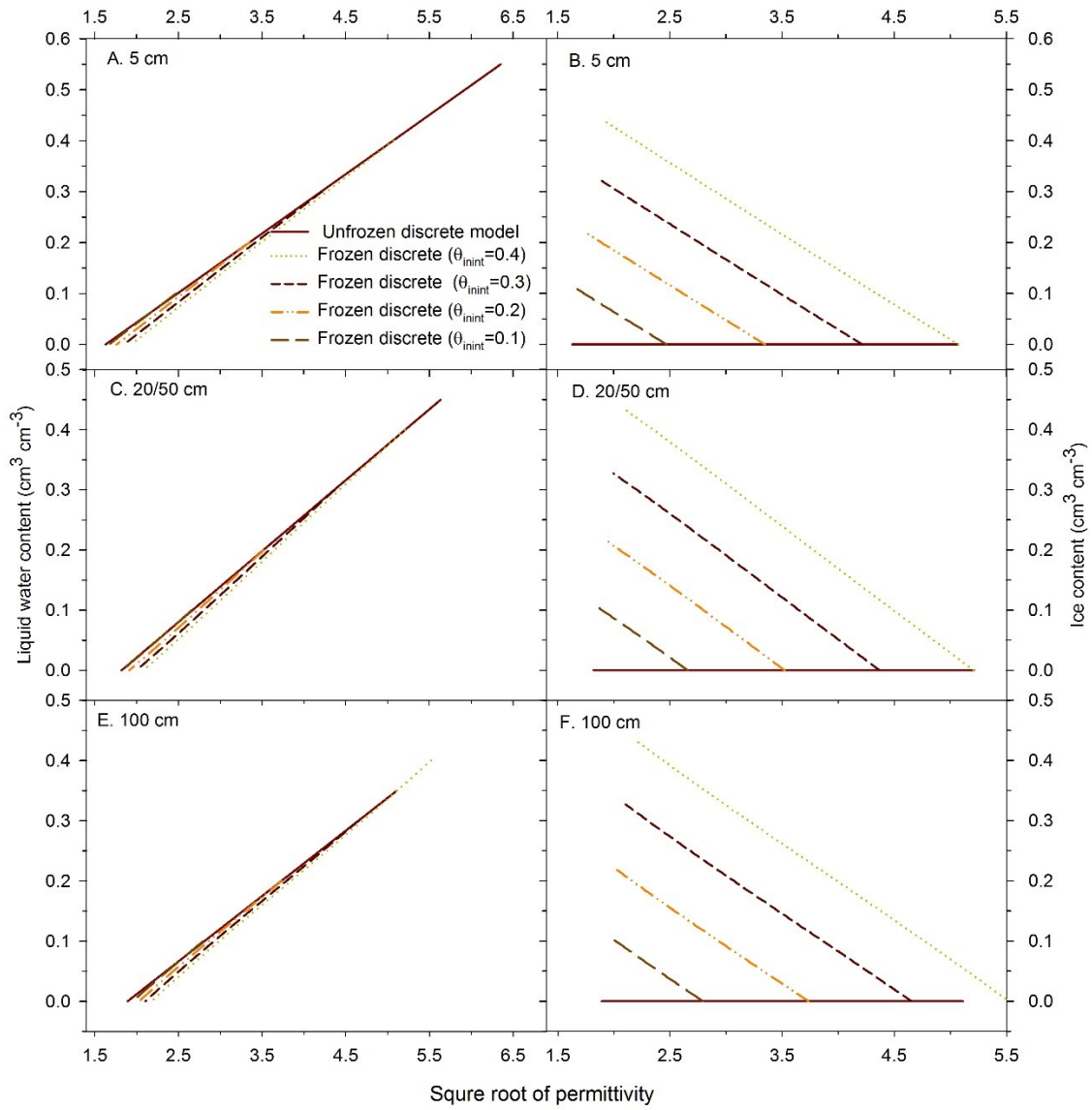


Fig. 3-1. ThetaProbe calibration curves (parameters are shown in Table 3-2) for the estimation of liquid-water content and ice content from the ThetaProbe measured permittivity ($\sqrt{\epsilon_{eff}}$) for soil at 5 cm (A&B), 20 and 50 cm (share the same calibration, C&D), and 100 cm (E&F).

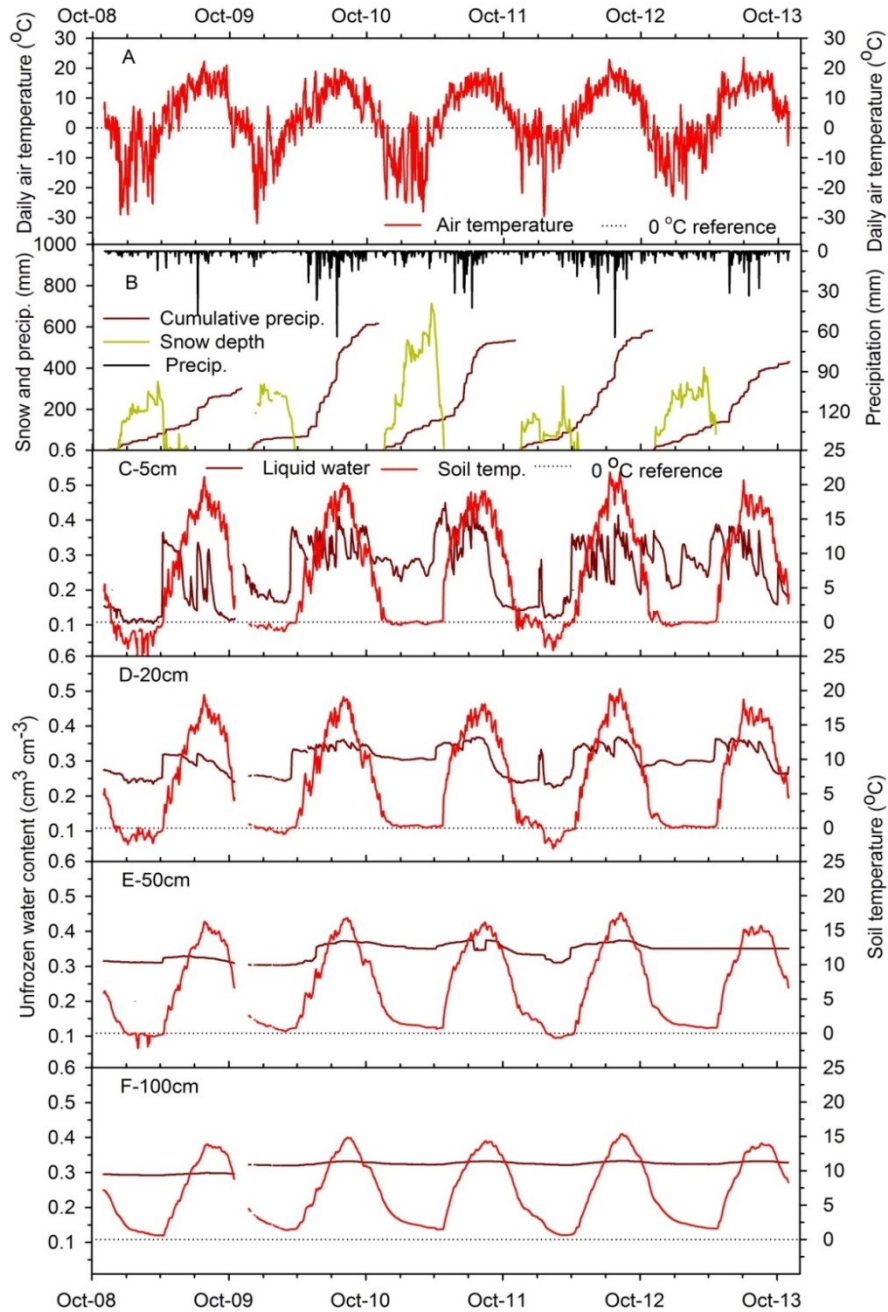


Fig. 3-2. Time series of 5-year (Nov. 2008 - Oct. 2013) daily air temperature (A), precipitation, cumulative precipitation (calculated from Nov. 1st - Oct. 31st each year), depth of snowpack (B) and volumetric moisture content and soil temperature for 5 cm (C), 20 cm (D), 50 cm (E), and 100 cm (F) depths.

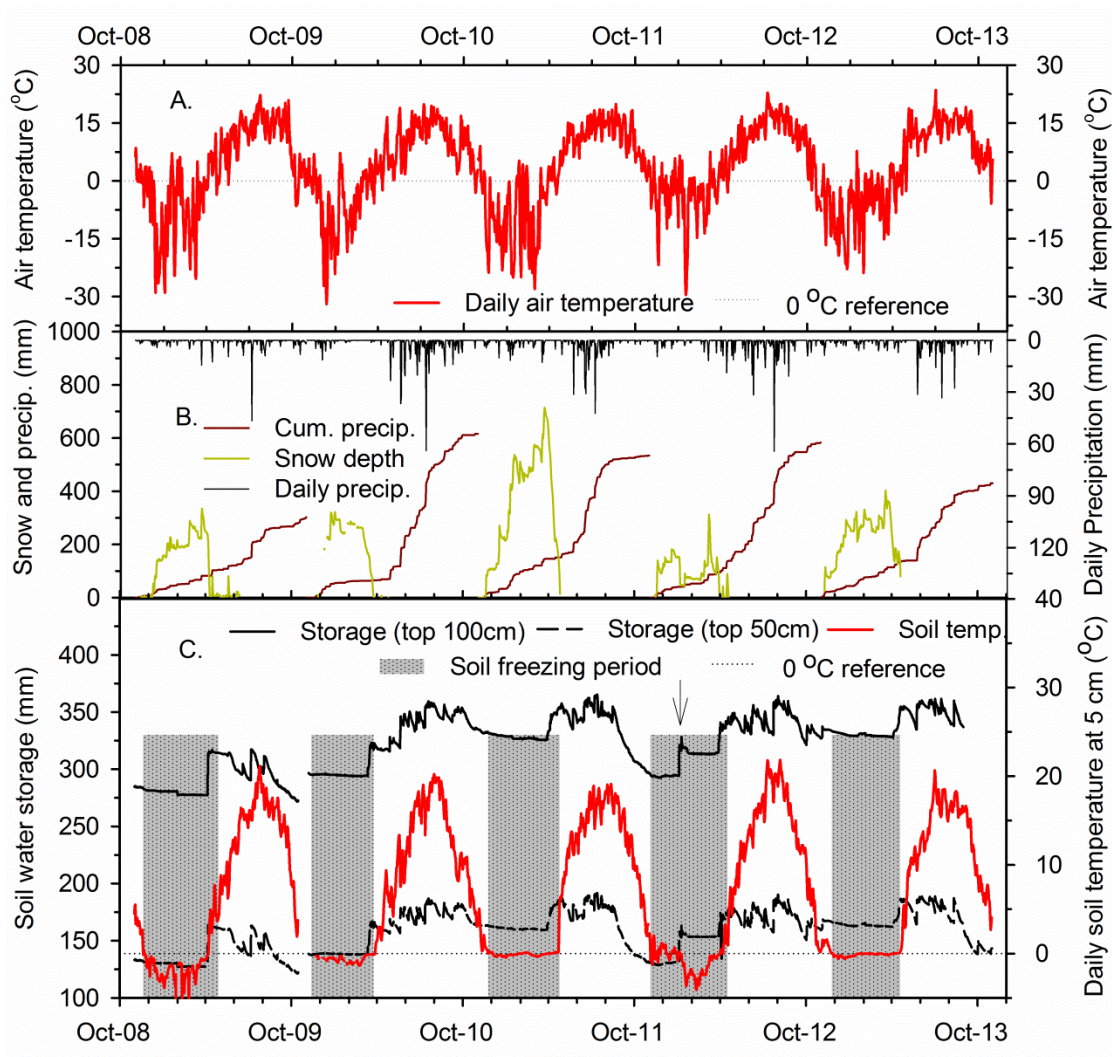


Fig. 3-3. Time series of 5-year (2008 - 2013) daily air temperature (A), precipitation, cumulative precipitation (calculated from Nov. 1st - Oct. 31st), depth of snowpack (B) and soil temperature at 5 cm and total soil water storage for top 50 and 100 cm (C). Arrow in C indicates the possible winter infiltration induced storage change.

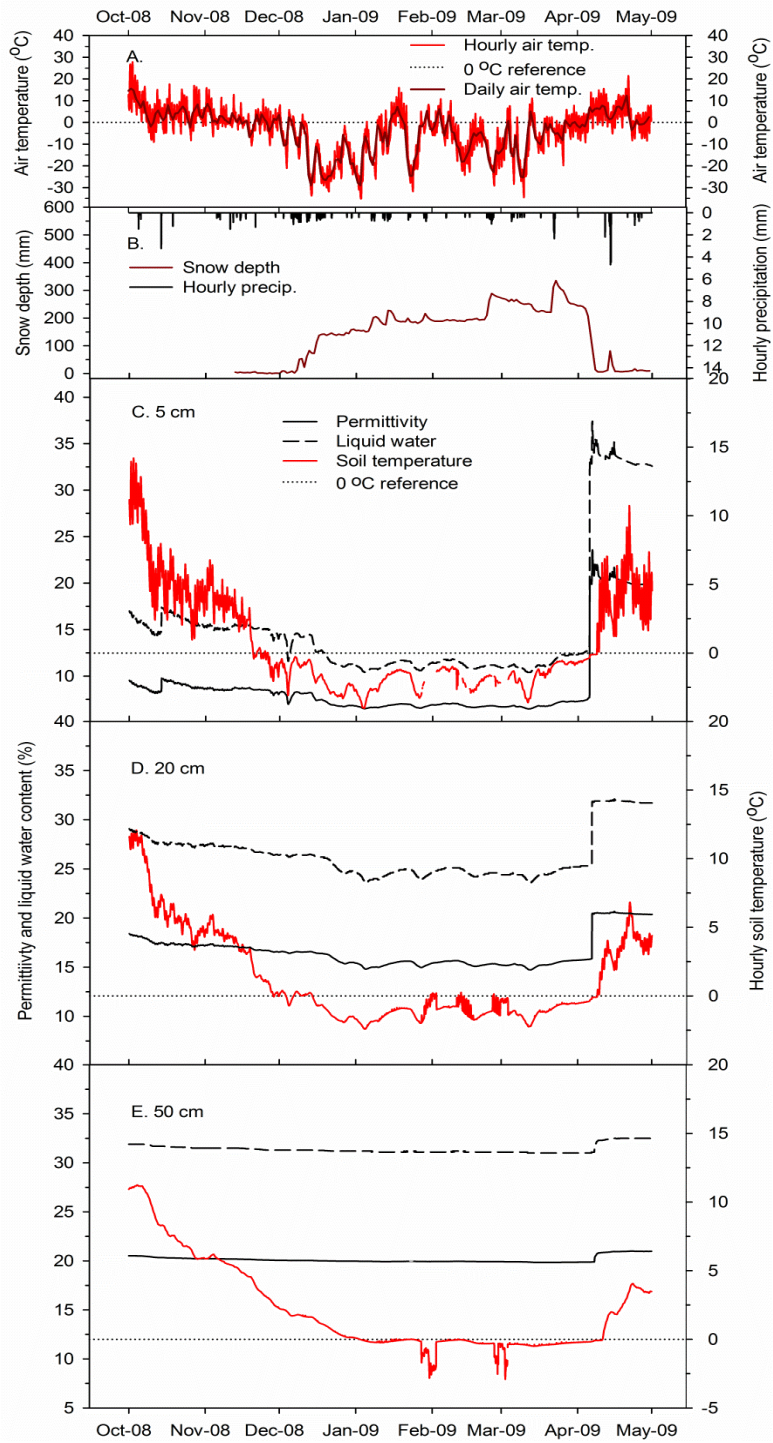


Fig. 3-4. Time series of hourly air temperature (A), precipitation, daily snow depth (B) and hourly permittivity, liquid-water content (expressed in %), and soil temperature for 5 cm (C), 20 cm (D), and 50 cm (E) between Oct. 1st, 2008 and Apr. 30th, 2009.

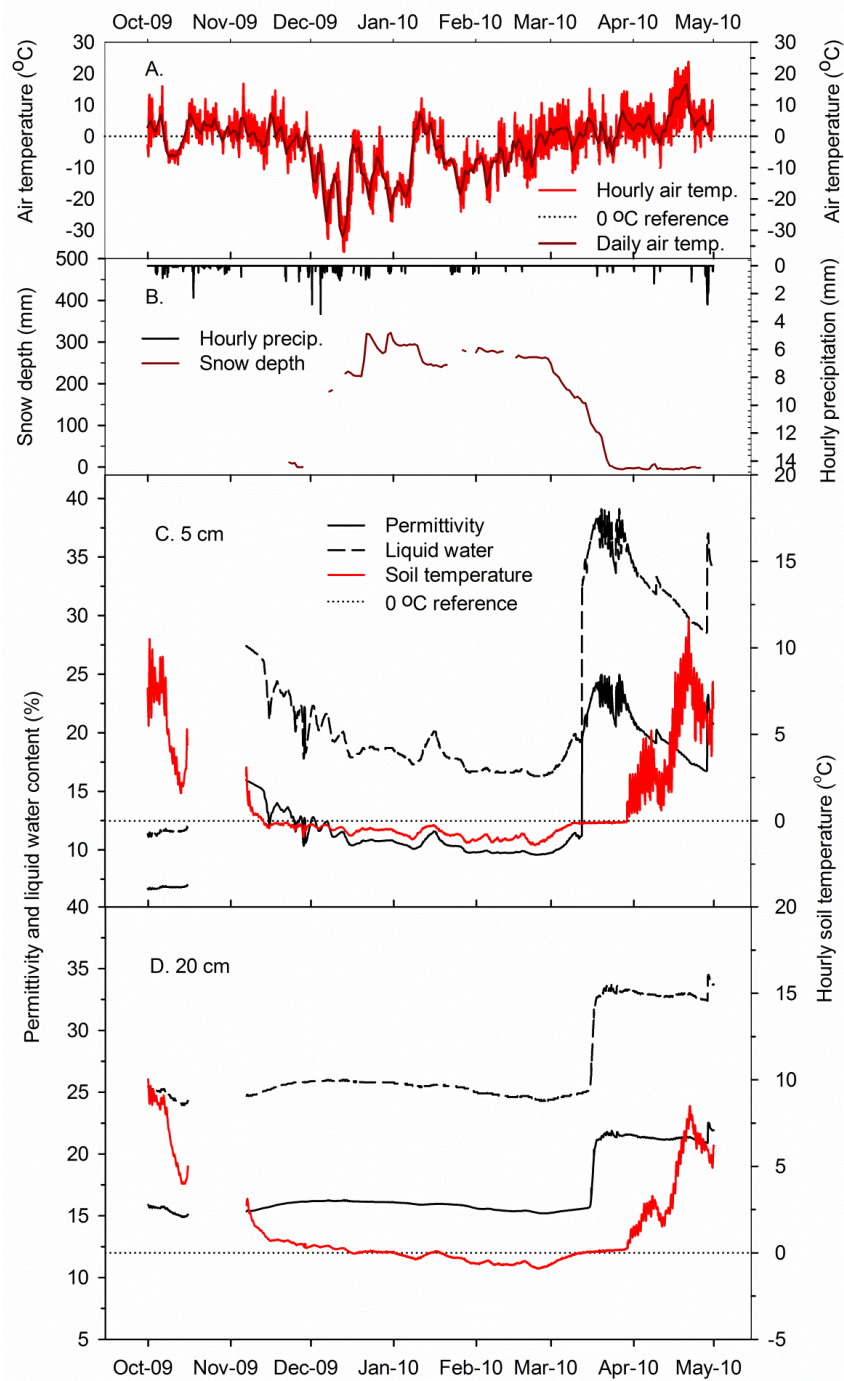


Fig. 3-5. Time series of hourly air temperature (A), precipitation, daily snow depth (B) and hourly permittivity, liquid-water content (expressed in %), and soil temperature for 5 cm (C) and 20 cm (D) between Oct. 1st, 2009 and Apr. 30th, 2010. Soil data between mid-October to early November were missing.

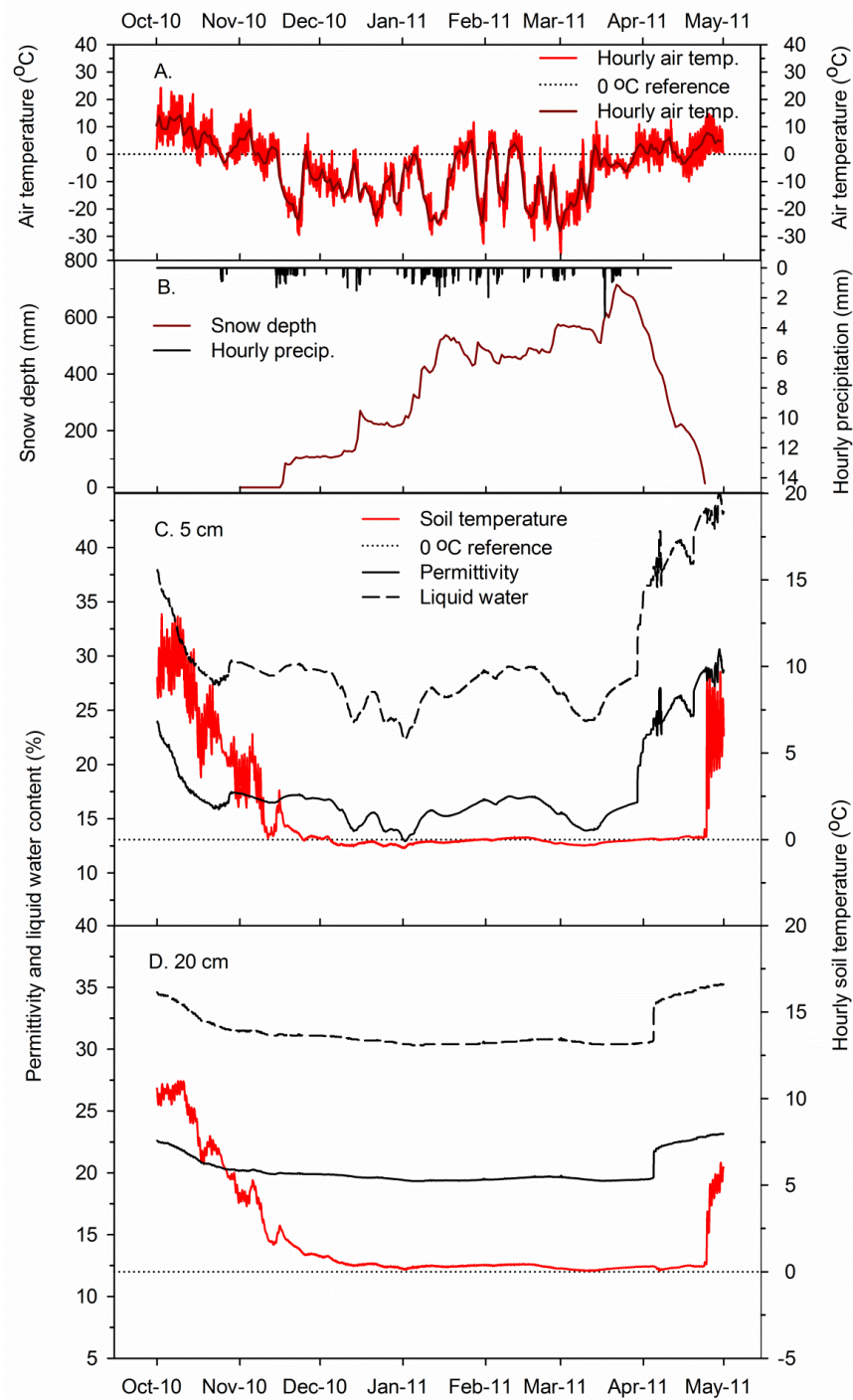


Fig. 3-6. Time series of hourly air temperature (A), precipitation, daily snow depth (B) and hourly permittivity, liquid-water content (expressed in %), and soil temperature for 5 cm (C) and 20 cm (D) between Oct. 1st, 2010 and Apr. 30th, 2011.

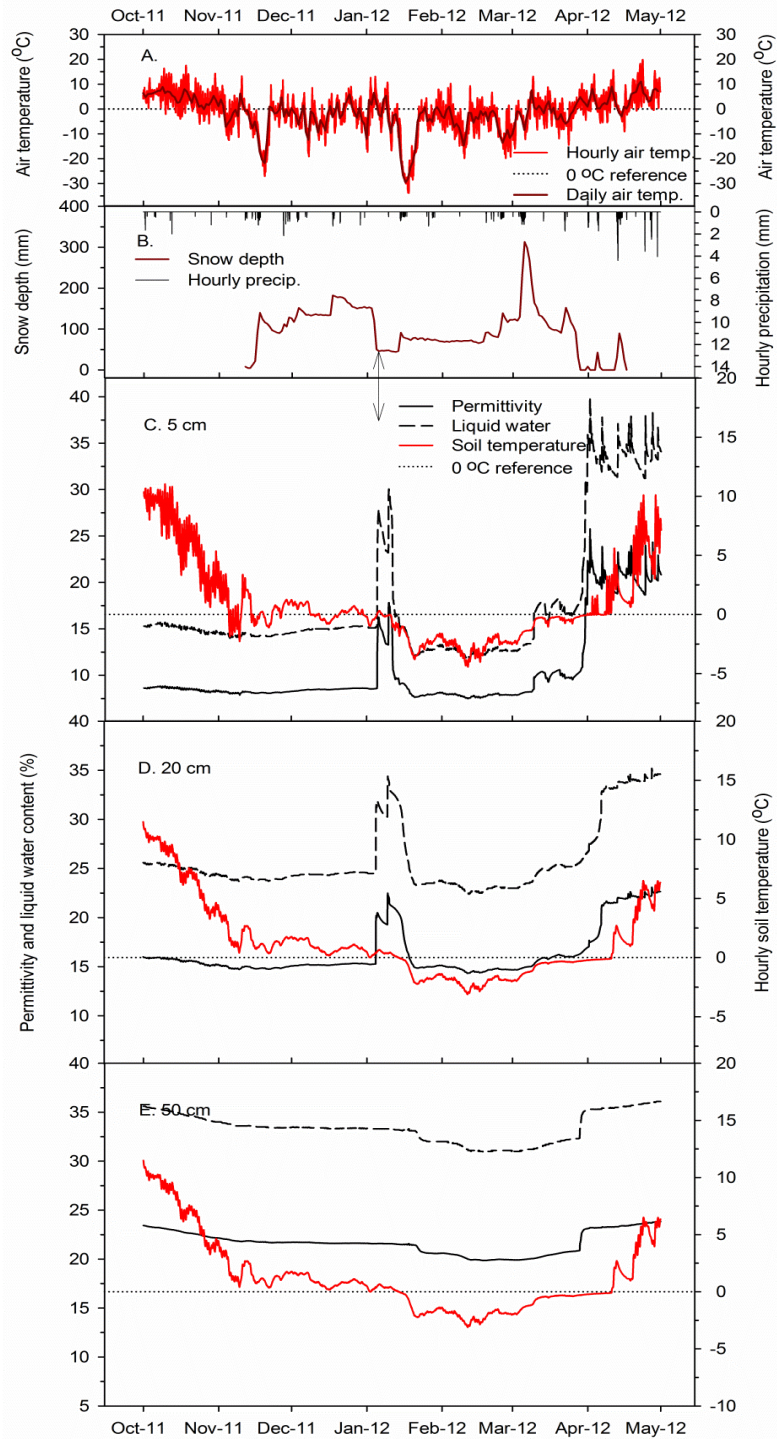


Fig. 3-7. Time series of hourly air temperature (A), precipitation, daily snow depth (B) and hourly permittivity, liquid-water content (expressed in %), and soil temperature for 5 cm (C), 20 cm (D), and 50 cm (E) between Oct. 1st, 2011 and Apr. 30th, 2012. Arrow in B and C indicates the possible winter snowmelt.

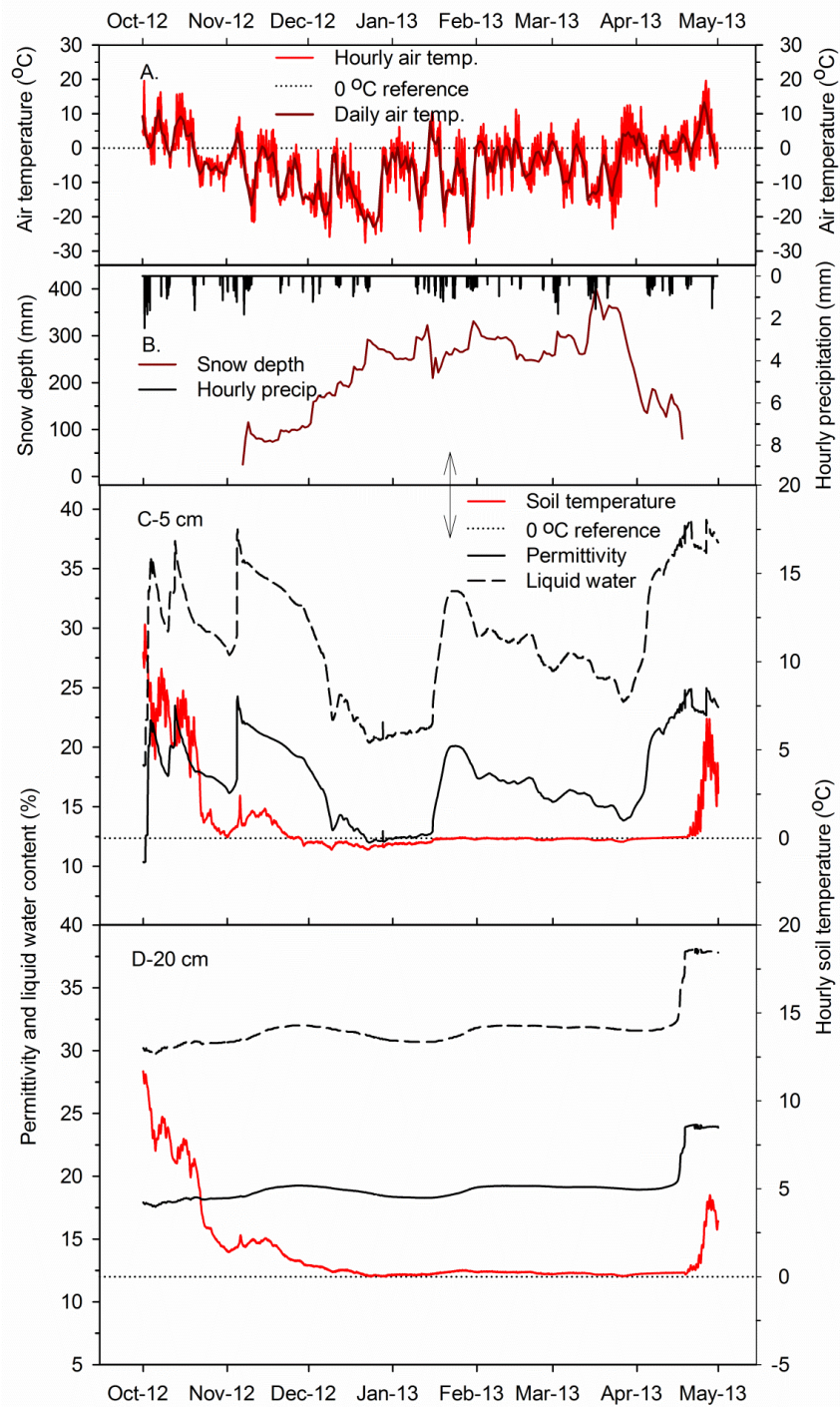


Fig. 3-8. Time series of hourly air temperature (A), precipitation, daily snow depth (B) and hourly permittivity, liquid-water content (expressed in %), and soil temperature for 5 cm (C) and 20 cm (D) between Oct. 1st, 2012 and Apr. 30th, 2013. Arrow in B and C indicates the possible winter snowmelt.

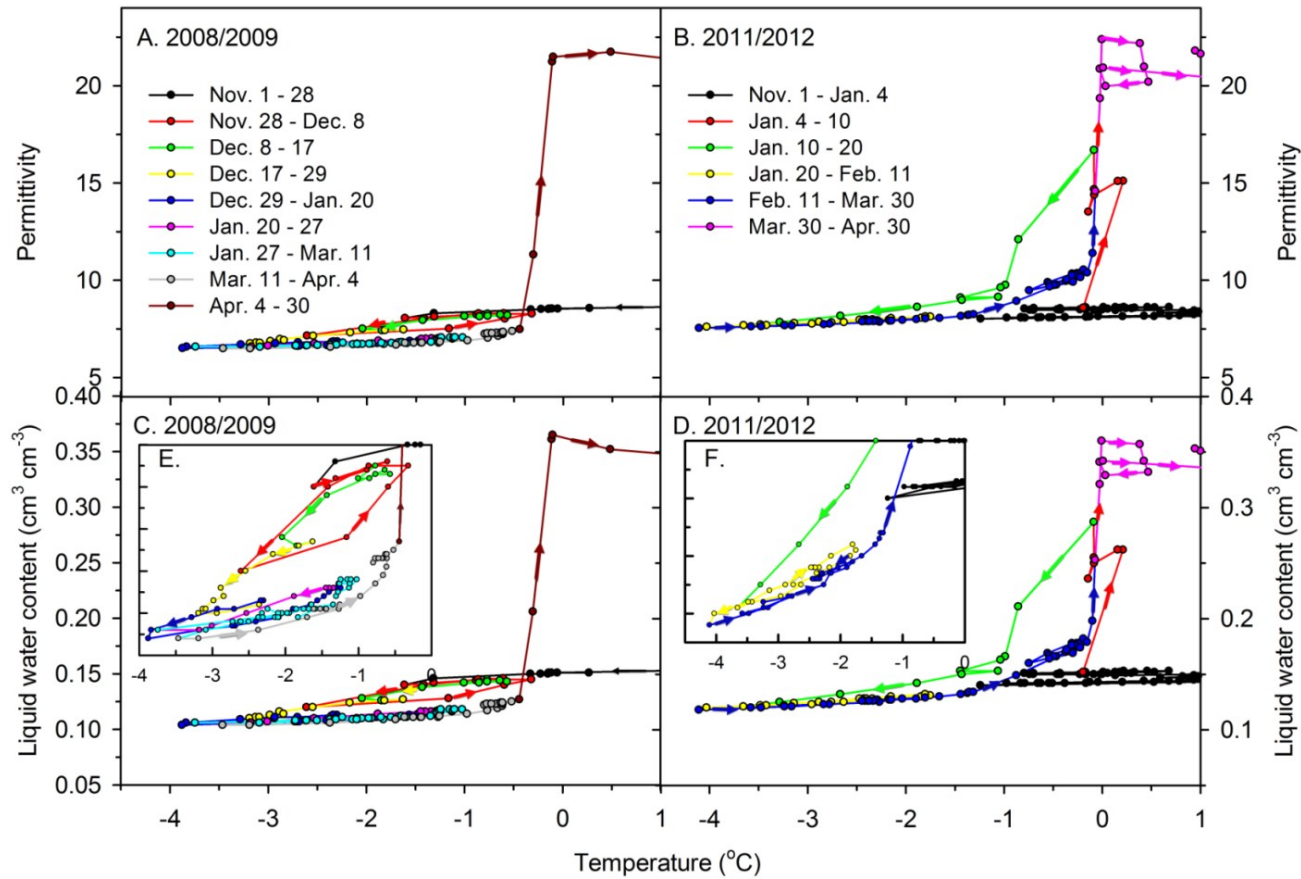


Fig. 3-9. Daily permittivity (A&B) and the interpreted liquid-water content (C&D) at 5 cm depth as a function of temperature during the period over Nov. 1st - Apr. 30th for years 2008/2009 and 2011/2012. Zoom in graphs for temperature between -4 and 0 °C each year are showed in E and F, respectively. Arrows are used to show the direction of each freezing/thawing segments. A&C share the legend in A, and B&D share the legend in B.

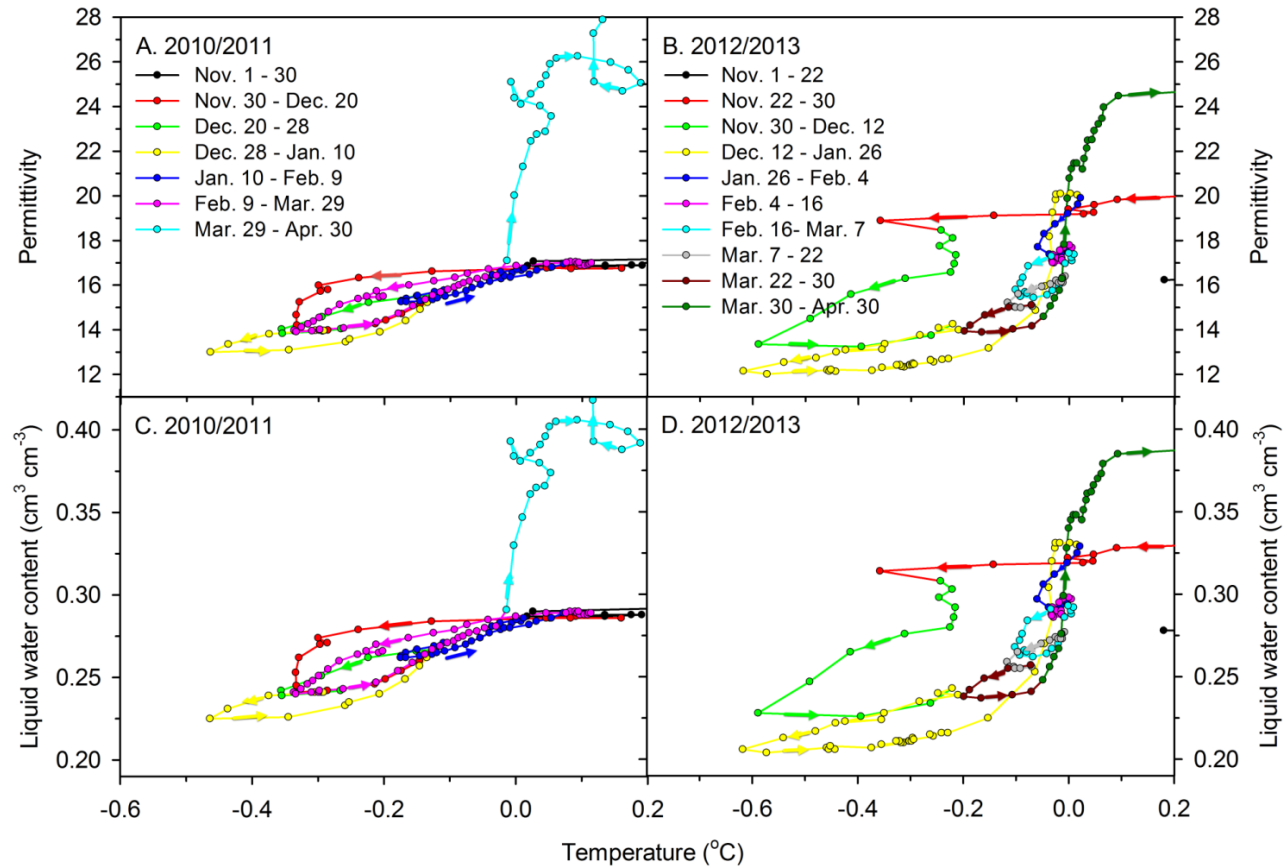


Fig. 3-10. Daily permittivity (A&B) and the interpreted liquid-water content (C&D) at 5 cm depth as a function of temperature during the period over Nov. 1st - Apr. 30th for years 2010/2011 and 2012/2013. Arrows are used to show the direction of each freezing/thawing segments. A&C share the legend in A, and B&D share the legend in B.

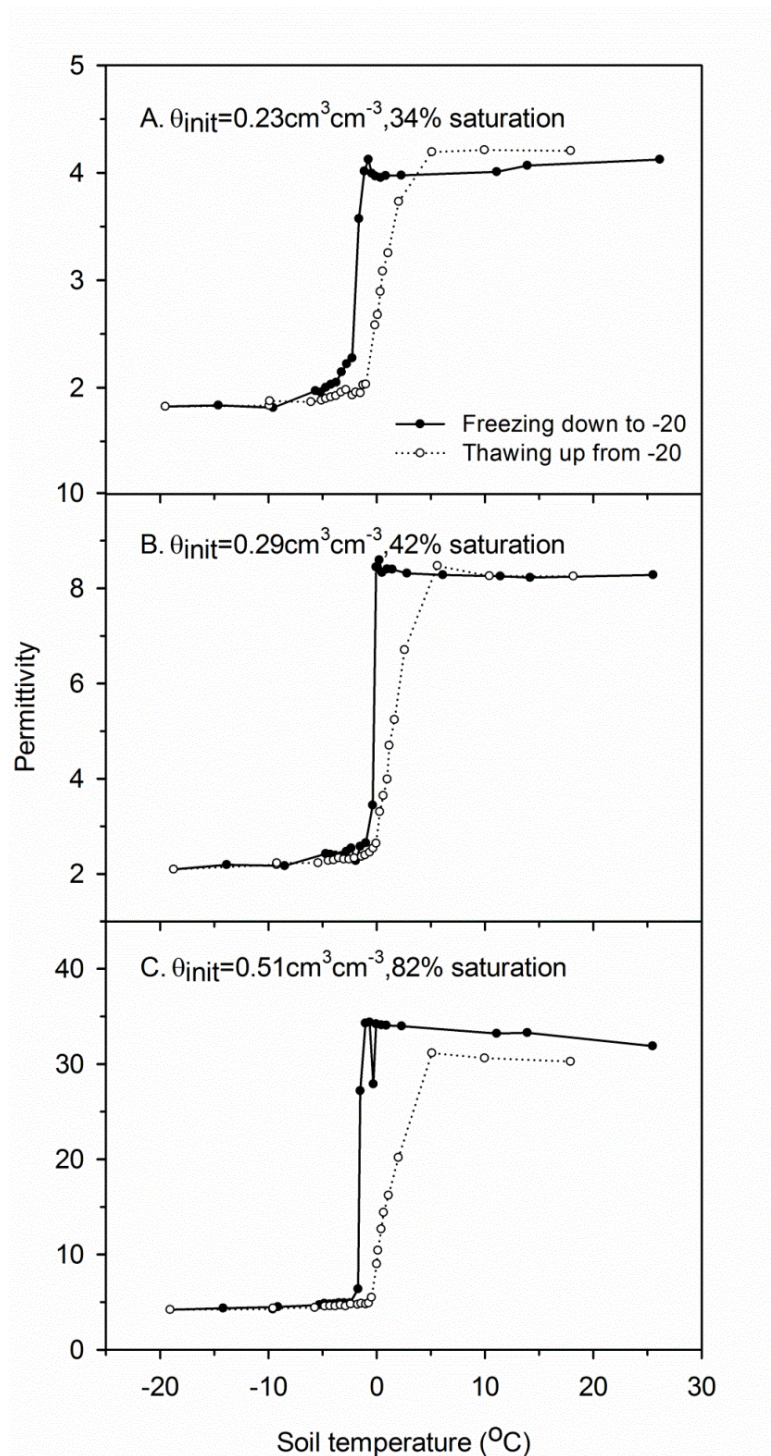


Fig. 3-11. Soil freezing and thawing curves (SFTCs) measured under lab conditions on soils collected from Breton Plots.

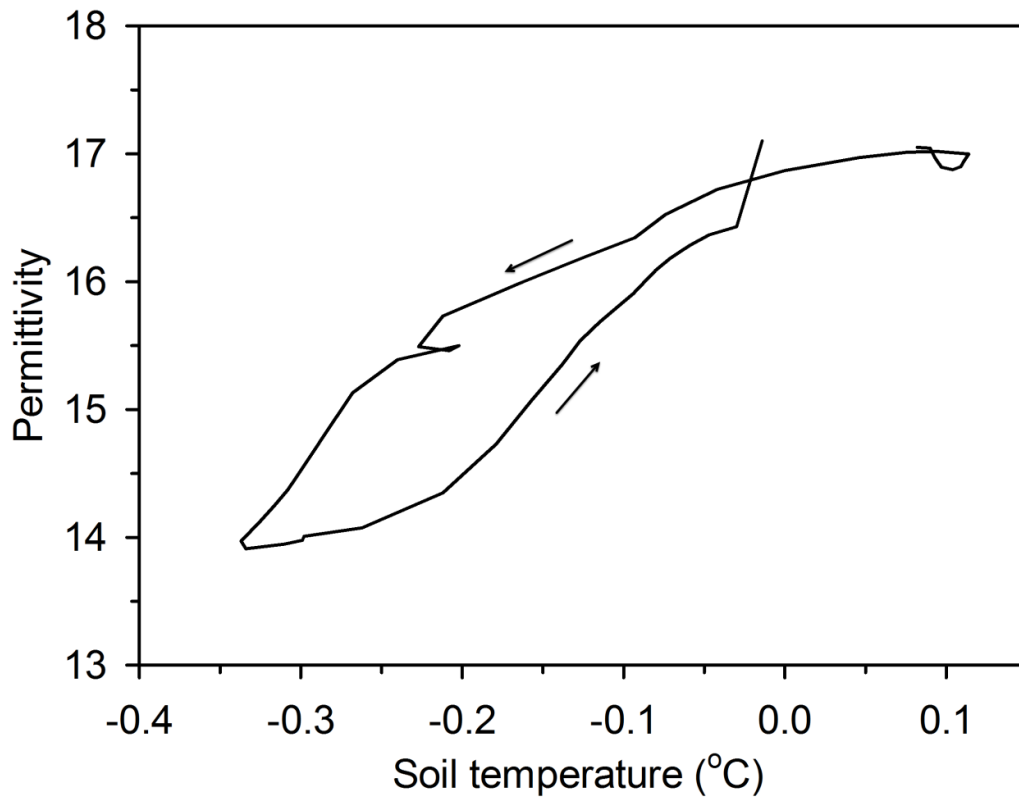


Fig. 3-12. Soil freezing characteristic (SFC) shaped soil freezing and thawing curves (SFTCs, Feb. 9th - Mar. 29th, 2011, daily permittivity vs temperature) at 5 cm depth during the winter 2010/2011 (mild winter).

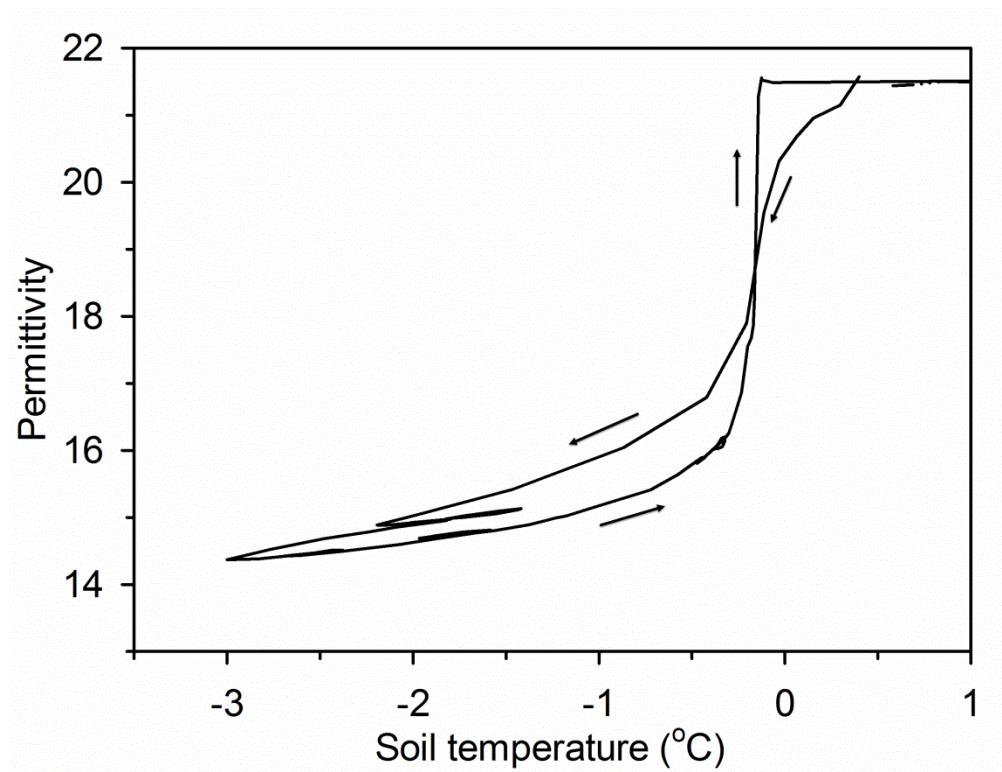


Fig. 3-13. Soil freezing characteristic (SFC) shaped soil freezing and thawing curves (SFTCs, Nov. 1st - Apr. 30th, 2012, daily permittivity vs temperature) at 20 cm depth during the winter 2011/2012 (severe winter).

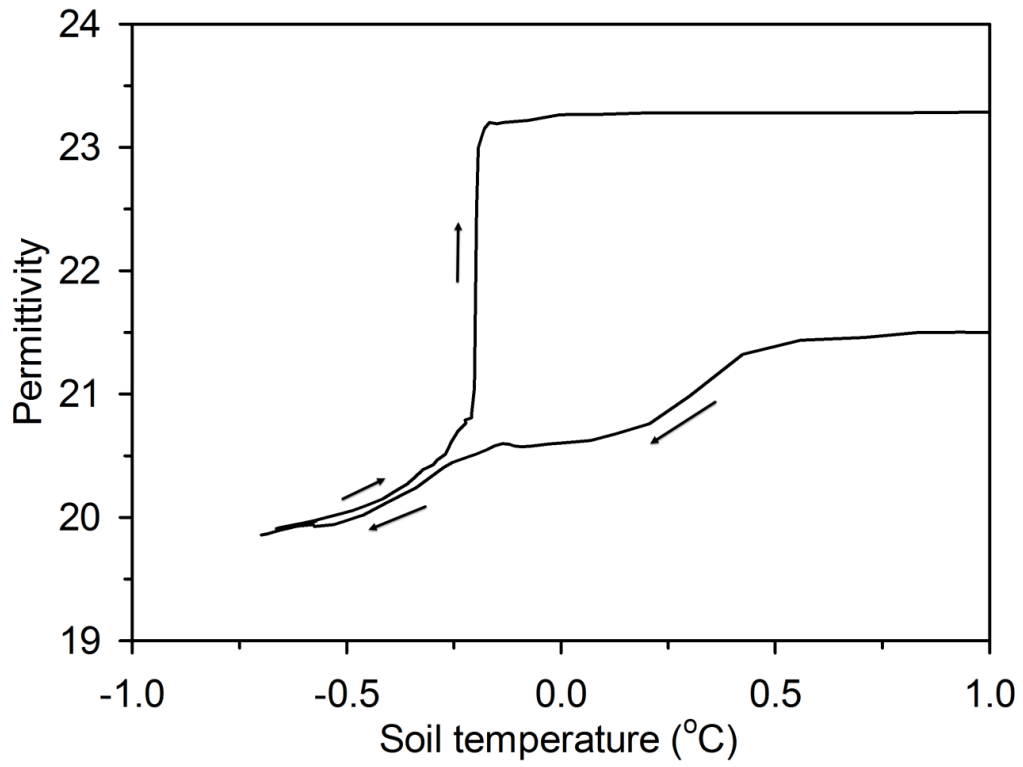


Fig. 3-14. Soil freezing and thawing curves (SFTC, Jan. 20th - Apr. 30th, 2012, daily permittivity vs temperature) at 50 cm depth during the winter 2011/2012.

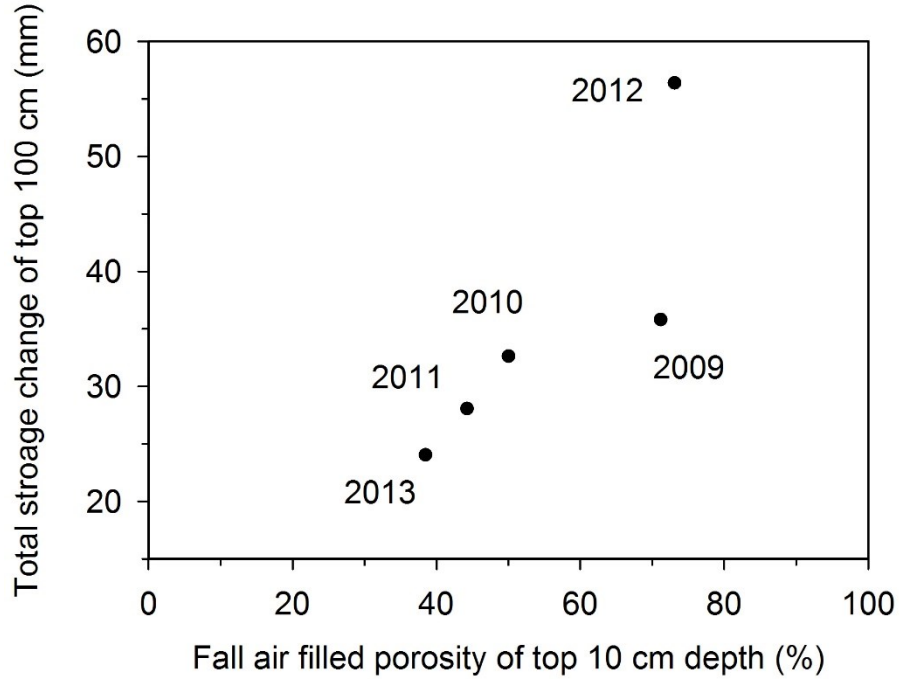


Fig. 3-15. Maximum storage change (period from at the onset of freezing in the fall to spring snowmelt) of top 100 cm plotted against air filled porosity of top 10 cm (use air-filled porosity at 5 cm depth) at the onset of freezing.

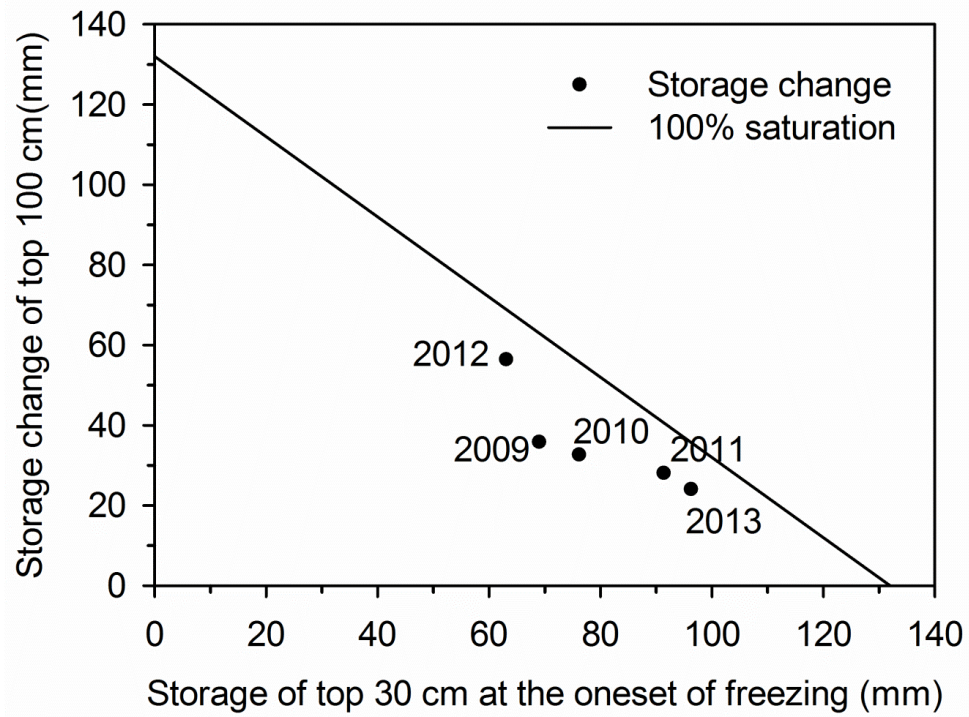


Fig. 3-16. Maximum storage change (period from at the onset of freezing in the fall to spring snowmelt) of top 100 cm v storage of top 30 cm prior to soil freezing.

Chapter 4 Evaluation of TDR Method for Quantifying Ice Melting Caused by the Heat Pulse Method in Frozen Soils

4.1. Abstract

Soil thermal properties are critical parameters for modelling energy and mass transport in frozen/freezing porous media. Currently, the heat pulse (HP) method is the standard for in-situ measurement of soil thermal properties, but its application in frozen soils is confounded by melting and refreezing of ice that changes thermal properties being measured. The objective of this chapter was to evaluate the use of TDR methods in combination with HP methods to extend the possibility of using HP methods to estimate thermal properties in frozen soils. We explore two possibilities: (1) TDR estimated liquid-water content (θ_l) before and after the HP can be used to quantify ice melting; and (2) quantitative comparison of heat capacity (C_v) calculated from TDR-estimated θ_l and ice content (θ_i) and HP-estimated apparent heat capacity (C_a). Two experiments were conducted on two different soils of the same water content ($0.25 \text{ cm}^3 \text{ cm}^{-3}$). Different heat pulse durations (e.g., 8, 15, 30, and 60 s) and strengths (e.g., $\approx 35 \sim 60 \text{ W m}^{-1}$ or $280 \sim 2100 \text{ J m}^{-1}$) across a wide range of temperatures (thawing from -35 to 25 °C and then freeze back to -35 °C) were investigated. The results showed that TDR waveforms can be used to qualitatively show the evidence of ice melting, but uncertainty in the TDR-measured dielectric permittivity made it hard for estimation of θ_l and θ_i . In addition, low resolution and frequency of TDR records may miss the peak ice melting point. Comparison of C_v calculated from TDR-estimated θ_l and θ_i and HP-estimated C_a at each temperature showed: (1) Ice melting is limited when temperature is < -5 °C and thermal properties estimated at this range may approach the real thermal properties; (2) application of the HP method between -5 and 0 °C is largely affected by ice melting, the amount of melting ice peaked at -1.5 to -0.5 °C during soil thawing, but ice melting during soil freezing is small; (3) the maximum estimated change in θ_i from melting is small (ranging from 0.005 to $0.02 \text{ cm}^3 \text{ cm}^{-3}$), but still results in significant problems in estimating specific heat capacity; (4) like the soil freezing characteristic, C_v and C_a are hysteretic, because of different ice contents at the same temperature during freezing and thawing; and (5) a good

relationship between TDR-estimated C_v and HP-estimated C_a and energy input by the HP probes was found and it can be used to guide the optimum heat application for frozen soil and potentially to create correction function that could be applied to HP-estimated specific heat capacity in frozen soils.

List of symbols and acronyms

ϵ_{eff}	Composite dielectric permittivity
ϵ	Parameter for calculation in the heat pulse method
θ_i	Ice content, $\text{m}^3 \text{m}^{-3}$ or $\text{cm}^3 \text{cm}^{-3}$
θ_{init}	Initial water content or total water content before freezing, $\text{m}^3 \text{m}^{-3}$ or $\text{cm}^3 \text{cm}^{-3}$
θ_l	Liquid-water content, $\text{m}^3 \text{m}^{-3}$ or $\text{cm}^3 \text{cm}^{-3}$
θ_t	Total water content including liquid-water and ice, $\text{m}^3 \text{m}^{-3}$ or $\text{cm}^3 \text{cm}^{-3}$
κ	Thermal diffusivity, $\text{m}^2 \text{s}^{-1}$
λ	Thermal conductivity, $\text{W m}^{-1} \text{°C}^{-1}$
π	Constant, 3.141
ρ_b	Bulk density (dry), kg m^{-3}
ρ_g	Density of air, 1.225 kg m^{-3}
ρ_i	Density of ice, 961.7 kg m^{-3}
ρ_s	Particle density, kg m^{-3}
ρ_w	Density of water, 1000 kg m^{-3}
ϕ	Porosity, $\text{m}^3 \text{m}^{-3}$ or $\text{cm}^3 \text{cm}^{-3}$
C_a	Apparent heat capacity calculated by HP method, $\text{J m}^{-3} \text{°C}^{-1}$
c_g	Specific heat capacity of soil air, $\text{J kg}^{-1} \text{°C}^{-1}$
c_i	Specific heat capacity of ice, $\text{J kg}^{-1} \text{°C}^{-1}$
c_l	Specific heat capacity of unfrozen liquid-water, $\text{J kg}^{-1} \text{°C}^{-1}$
c_s	Specific heat capacity of soil solid, $\text{J kg}^{-1} \text{°C}^{-1}$

C_v	Volumetric heat capacity, $J m^{-3} °C^{-1}$
$E_1(x)$	Exponential integral
$exp(x)$	Exponential function
Q	Strength of heat source (heater of thermo-TDR), $m^2 °C$
q	Heat input per unit length of the line source, $J m^{-1}$
R_{htr}	Resistance of heater, Ω
R_{ref}	Resistance of reference resistor, Ω
r	Probe spacing of thermo-TDR or distance from heater, m or mm
t	Time, s
t_0	The duration of heat pulse release, s
t_m	The time at which the maximum change of temperature (ΔT_m) is reached, s
$T(r, t)$	Temperature change at time t , r away from the heater, $°C$
$T(t)$	Temperature-time data
ΔT_m	The maximum change of temperature, $°C$
V_{drop}	Voltage drop across the heater circuit, volt
Avg-Dev	Average deviations
DSC	Differential scanning calorimetry
HP	Heat pulse
NS-Eff	Nash-Sutcliffe Efficiency
RMSERoot mean square error
SFC	Soil freezing characteristic
SFTC	Soil freezing and thawing curve
SMRC	Soil moisture retention curve
TDR	Time domain reflectometry
Thermo-TDR	Combination of HP and TDR probes and methods

4.2. Introduction

Freezing and thawing processes at the soil surface are important for quantifying the surface soil energy balance [Tanaka *et al.*, 2003] and its interaction with hydrological processes [Luo *et al.*, 2000]. Nonetheless, understanding and predicting freezing and thawing processes in soil is hampered by the lack of methods for measuring soil thermal properties under freezing/frozen conditions [Ochsner and Baker, 2008]. Conventional methods such as heat flux plates are mainly dependent on measurements of soil temperature and soil heat flux without considering the latent heat from phase changes and cannot measure soil thermal properties. Measurement of soil thermal properties in unfrozen soils has been improved by the application of heat pulse methods, specifically the dual probe heat pulse (DPHP) method [Campbell *et al.*, 1991; Bristow *et al.*, 1994a]. The DPHP has been reported to accurately measure soil thermal properties in unfrozen soils [Kluitenberg *et al.*, 1995; Bristow *et al.*, 2001; Liu and Si, 2011b], and has been adapted for measurement of soil water flux [Ren *et al.*, 2000; Wang *et al.*, 2002; Mori *et al.*, 2005; Kluitenberg *et al.*, 2007; Kawai *et al.*, 2008] and soil bulk density [Ochsner *et al.*, 2001; Ren *et al.*, 2003b; Liu *et al.*, 2008] etc.

Implementation of the DPHP method in frozen/freezing soils, however, has been primarily confounded by the fact that melting and re-freezing of soil ice due to the application of heat [Putkonen, 2003; Ochsner and Baker, 2008; Zhang *et al.*, 2011; Kojima *et al.*, 2013], which results in a significant amount of the heat pulse energy being directed to phase change rather than conduction and temperature change [Putkonen, 2003]. Ice melting increases the DPHP-predicted volumetric heat capacity (C_v) and decreases the soil thermal diffusivity (κ) because the general assumptions of the DPHP method, derived under unfrozen conditions (i.e., no phase change and temperature-invariant thermal properties), does not apply to frozen/freezing soils. In addition, C_v and κ show a distinct dependence on the ambient soil temperature in frozen soils compared to that in unfrozen soils [Ochsner and Baker, 2008]. For example, the DPHP melts less ice when the soil ambient temperature is very low and the DPHP-measured thermal properties approach the real thermal properties [Putkonen, 2003; Liu and Si, 2011a; Zhang *et al.*, 2011] and vice versa.

The DPHP-induced ice melting and changes of thermal properties may be reduced by (1) controlling the ice melting through optimized heat application or (2) accounting for the influence

of the ice melting on measured thermal properties. The first approach was investigated by *Liu and Si* [2011a] and *Zhang et al.* [2011], but their research showed that HP-induced ice melting could only be controlled at very low temperatures and ice melting is large at high subzero temperatures, especially around 0 °C. *Ochsner and Baker* [2008] incorporated the ice melting effects into apparent thermal properties which can be used to estimate lumped conduction and latent heat fluxes.

Chapters 2 and 3 showed the use of composite dielectric mixing models could estimate the unfrozen liquid-water and ice content fairly well. This together with the method of *Ochsner and Baker* [2008] may achieve the goal of estimating the amount of ice melted by the heat pulse in the conventional DPHP method for estimating the volumetric specific heat capacity in frozen soil. Two possible solutions therefore are proposed to quantify the ice melting: (1) use of the TDR measured ice content before and after the heat pulse to quantify the change of ice content given that the amount of ice melting is greater than the error range of TDR method; and (2) comparison of the calculated specific heat capacity (C_v) using TDR-measured liquid-water and ice contents before the heat pulse and the HP-measured apparent specific heat capacity (C_a) which is affected by ice melting. Once the ice melting is quantified, HP methods could be modified to more accurately measure soil thermal properties. Thus, the purpose of this chapter was to evaluate the TDR methods for quantifying the ice melting arising from the use of heat pulse method in frozen/freezing soils.

4.3. Theory

Dual probe heat pulse (DPHP) probes usually consist of a heater (line heat source) and one or more temperature sensors mounted some distance (usually 6 mm) away from the heater. The temperature sensors detect the temperature change as a function of time during the measurement when a short duration of the heat pulse is applied to the heater. The propagation of heat from the heater to the temperature sensors is described by the heat conduction equation with phase change in frozen soils, in the radial coordinate system [*Overduin et al.*, 2006; *Ochsner and Baker*, 2008]:

$$C_v \frac{\partial T}{\partial t} = \lambda \left(\frac{\partial^2 T}{\partial t^2} + \frac{1}{r} \frac{\partial T}{\partial r} \right) - L_f \rho_l \frac{\partial \theta_l}{\partial t} \quad [4-1]$$

where C_v is volumetric heat capacity ($\text{J m}^{-3} \text{ }^\circ\text{C}^{-1}$), T is temperature ($^\circ\text{C}$), t is time after heat pulse being applied (s), λ is thermal conductivity ($\text{W m}^{-1} \text{ }^\circ\text{C}^{-1}$), r is the radial distance from the center of the heater (m), L_f is latent heat of fusion for water (334 kJ kg^{-1}), ρ_l is water density (kg m^{-3}), and θ_l is volumetric water content ($\text{m}^3 \text{ m}^{-3}$). C_v is related to the heat capacity and volume fraction of soil components and can be expressed as [de Vries, 1963]:

$$C_v = \sum_j \theta_j \rho_j c_j = \theta_l \rho_l c_l + \theta_i \rho_i c_i + \left(1 - \frac{\rho_b}{\rho_s} - \theta_l - \theta_i\right) \rho_g c_g + \rho_b c_s \quad [4-2]$$

where θ is the volumetric fraction of soil constituents ($\text{m}^3 \text{ m}^{-3}$), c is specific heat capacity ($\text{J kg}^{-1} \text{ }^\circ\text{C}^{-1}$), subscripts l , i , g and s are related to unfrozen liquid-water, ice, air and soil solids, respectively, ρ is density (kg m^{-3}), ρ_b and ρ_s are bulk density and particle density (kg m^{-3}), respectively. ρ_l and ρ_i are assumed to be 1000 and 916.7 kg m^{-3} , respectively. Specific heat capacity of air is three orders of magnitude smaller than the other components and is usually neglected. Without any bulk density change in the soil solids, Eq. [4-2] may be used to calculate heat capacity with TDR-estimated liquid-water and ice content as described in the previous chapters.

Equation [4-1] can also be expressed in the form of [Ochsner and Baker, 2008]

$$C_a \frac{\partial T}{\partial t} = \lambda_a \left(\frac{\partial^2 T}{\partial r^2} + \frac{1}{r} \frac{\partial T}{\partial r} \right) \quad [4-3]$$

Rearranging the equation in this way effectively lumps convective heat flux in flowing water under temperature gradients in the apparent thermal diffusivity (λ_a) parameter and latent heat fluxes associated with phase change in the apparent volumetric heat capacity parameter (C_a), called the apparent volumetric heat capacity ($\text{J cm}^{-3} \text{ }^\circ\text{C}^{-1}$)

$$C_a = C_v + L_f \rho_l \frac{\partial \theta_l}{\partial T} \quad [4-4]$$

The apparent heat capacity can be explained as the amount of energy required to raise the temperature of a unit volume of bulk frozen soils by one degree while phase change between liquid-water and ice occurred due to the heat pulse method [Anderson et al, 1973; Pusch et al., 1978; Ochsner and Baker, 2008; Kozlowski, 2012]. L_f is latent heat of fusion, $3.34 \times 10^5 \text{ J kg}^{-1}$. Equation [4-4] can be rearranged to separate the variables and then integrated:

$$\int \partial \theta_l = \frac{C_a - C_v}{L_f \rho_l} \int \partial T \quad [4-5]$$

Equation [4-5] assumes that C_a and C_v are not functions of temperature. This assumption is likely only reasonable over very small ranges in temperature. Further, based on the assumption of small changes in temperature, and that the change in liquid-water content is equal to the change in ice content as long as differences in density are accounted for, the amount of HP-induced ice melting may be estimated as

$$\Delta \theta_{i,m} = \frac{(C_a - C_v) \rho_i}{L_f \rho_l^2} \Delta T_m \quad [4-6]$$

where $\Delta \theta_{i,m}$ is the maximum ice melting ($\text{m}^3 \text{ m}^{-3}$) at the maximum temperature change/rise ΔT_m . C_v is calculated with TDR estimated liquid-water and ice content as described in Eq. [4-2] and the C_a can be calculated with the HP method as below.

Since there is no exact analytical solution to Eq. [4-1], the analytical solution of infinite line source in soil without phase change is used instead to solve Eq. [4-3] in frozen soils with phase change [Ochsner and Baker, 2008]. Thus the apparent thermal properties can be calculated by fitting the measured data with analytical solution to Eq. [4-3] [de Vries, 1952; Carslaw and Jaeger, 1959] (similar to Eq. [1-7] but modified for frozen soils):

$$\Delta T(r, t) = \begin{cases} -\frac{q}{4\pi t_0 \kappa_a C_a} E_i\left(\frac{-r^2}{4\kappa_a t}\right) & 0 < t \leq t_0 \\ \frac{q}{4\pi t_0 \kappa_a C_a} \left[E_i\left(\frac{-r^2}{4\kappa_a(t-t_0)}\right) - E_i\left(\frac{-r^2}{4\kappa_a t}\right) \right] & t > t_0 \end{cases} \quad [4-7]$$

where r is distance between heating needle and temperature sensor needle (m), t is time (s) after the beginning of the heat pulse, t_0 is the duration of heat pulse (s), q is energy input/heat strength per unit time (J m^{-1}), λ_a is apparent thermal conductivity ($\text{W m}^{-1} \text{ }^\circ\text{C}^{-1}$), C_a is apparent heat capacity ($\text{J m}^{-3} \text{ }^\circ\text{C}^{-1}$), κ_a is apparent thermal diffusivity ($\text{m}^2 \text{ s}^{-1}$), $\kappa_a = \lambda_a / C_a$, and $-Ei(-x)$ is the exponential integral. The method of fitting Eq. [4-7] to extract thermal properties (e.g., C_a , λ_a and κ_a) is called the non-linear model fit (NMF) method [Bristow et al., 1995]. Bristow et al. [1994b] presented the equation using the peak points, the maximum temperature change ΔT_m ($^\circ\text{C}$) and time (t_m) to get ΔT_m ($^\circ\text{C}$) on the recorded temperature-time, $T(t)$ data to estimate C_a , which is the single point method (SPM)

$$C_a = \frac{q}{4\pi t_0 \kappa_a \Delta T_m} \left[E_i \left(\frac{-r^2}{4\kappa_a (t_m - t_0)} \right) - E_i \left(\frac{r^2}{4\kappa_a t_m} \right) \right] \quad [4-8]$$

The simplified calculation for C_a is [Knight and Kluitenberg, 2004]

$$C_a = \frac{q}{e\pi r^2 \Delta T_m} \left(1 - \frac{\varepsilon^2}{8} \left(\frac{1}{3} + \varepsilon \left(\frac{1}{3} + \frac{\varepsilon}{8} \left(\frac{5}{2} + \frac{7\varepsilon}{3} \right) \right) \right) \right) \quad [4-9]$$

where $\varepsilon = t_0/t_m$.

It should be noted that HP-estimated soil thermal properties in frozen soils change with unfrozen water and ice content which change over time during the heat pulse application. Both SPM and NMF methods assume homogeneous soil thermal properties between the heater and temperature sensors that remain constant during the heat pulse period. C_a calculated from NMF method is influenced by the all points on the $T(t)$ data, while SPM predicts C_a at the peak point of the $T(t)$ data based on t_m and ΔT_m . The approach of SPM fit better to the hypothesis of this study that takes advantage of the peak point measurement on the $T(t)$ data and therefore SPM is used in this chapter. SPM method was also used in field study of frozen soil by *Ochsner and Baker* [2008] and *Tokumoto et al.* [2010].

4.4. Material and Methods

4.4.1. Probe design and construction of thermo-TDR and conventional TDR

Thermo-TDR probes used in this study consisted of five, parallel stainless steel tubes 4 cm long. The center and surrounding needles are spaced 6 mm apart. The center needle of the thermo-TDR probe houses a resistance heater and also serves as the centre TDR electrode. The surrounding four needles each house a thermistor at its midpoint and also act as TDR ground electrodes (Fig. 4-1). Probes used in the first experiment described below were constructed by East 30 Sensors, Pullman, Washington, USA, and probes used in the second experiment were constructed in the lab by the author. All the probes have similar designs but differ in heater resistance (see Table 4-1).

The conventional TDR was constructed by the author. The probe consists of three parallel stainless steel rods of 1.6 mm in diameter, 14 cm in length with 1 cm inter-rod spacing.

4.4.2. Experimental procedure

This lab study was designed to examine the influence of ice melting on DPHP-measured thermal properties caused by the heat pulse method in frozen/freezing soils. A range of heat pulse strengths and durations across different subfreezing temperatures were tested with two experiments.

The first experiment was designed to test if TDR can detect ice melting induced by the heater of the HP probe. Air-dry, loam-textured soil samples collected from the Ellersile farm at the University of Alberta, Canada (see Table 2-1 for soil properties) were wetted with known quantity of deionised water to obtain a water content of 0.25 g g^{-1} and equilibrated for at least 24 hours at room temperature. The mixed soil sample was then uniformly packed to a depth of 8 cm in 2 cm increments into a copper cylinder of 5.08 cm i.d. and of 15 cm in length and sealed with a copper cap to prevent evaporation. The cylinder was wrapped with a cooling coil of 5 mm i.d. copper tubing and bonded to the copper soil cylinder with heat-conducting epoxy. The bulk density of the soil was 0.98 g cm^{-3} so the volumetric water content was $0.245 \text{ cm}^3 \text{ cm}^{-3}$. The cooling coil was connected to a temperature-controlled water bath (Isotemp Refrigerated Circulators 3013S, Fisher Scientific, USA), filled with a 50/50 (v/v) Ethylene glycol-water mixture. A thermo-TDR probe was inserted in the center of the cylinder, and connected to a TDR cable tester (Tektronix 1502C, Beaverton, Or, USA) and a data logger (CR1000, Campbell Scientific, Edmonton, Canada) for measurement of bulk/effective dielectric constant/permittivity (ϵ_{eff}) and temperature T , respectively. Temperature was controlled to cool the soil samples from $10 \text{ }^\circ\text{C}$ down to $-30 \text{ }^\circ\text{C}$ and then back to $10 \text{ }^\circ\text{C}$ in $5 \text{ }^\circ\text{C}$ increments for temperatures between 10 and $0 \text{ }^\circ\text{C}$, $0.5 \text{ }^\circ\text{C}$ steps for temperatures between 0 and $-5 \text{ }^\circ\text{C}$, in $1 \text{ }^\circ\text{C}$ steps for temperatures between -5 and $-10 \text{ }^\circ\text{C}$, in $2 \text{ }^\circ\text{C}$ steps for temperatures between -10 and $-20 \text{ }^\circ\text{C}$ and in $5 \text{ }^\circ\text{C}$ steps for temperatures between -20 and $-30 \text{ }^\circ\text{C}$. The TACQ software [Evet, 2000] was programmed to continuously record the TDR traces once every $\sim 10 \text{ s}$ during the freezing and thawing processes. The heat pulse was controlled by programming the data logger to release after the temperature differences among all four needles were less than $0.05 \text{ }^\circ\text{C}$ after at least 20 minutes had passed since the previous heat pulse. A heat pulse duration of 8 s ($q = 492 \text{ J m}^{-1}$) was used and measurements were repeated four times at each temperature step. One week was spent on this experiment. The detail of the experiment design is shown in Table 4-1.

In the second experiment, different heat pulse durations (8 - 60 s) and strengths (280 - 2100 J m⁻¹) were used to induce different ice melting responses in a Brightbank loamy sand. The soil samples were prepared and packed in the similar way as the one above, but with a water content of 0.15 g g⁻¹ and with a constant bulk density of 1.69 g cm⁻³, the resulting volumetric water content was 0.25 cm³ cm⁻³. Seven soil columns in total were used, 6 of which were instrumented with 6 thermo-TDR probes in the middle and covered with copper cap to prevent evaporation. Another column with 15 cm of packed soil was instrumented with a conventional three-prong TDR probe described above and a thermistor (TMC6HD, Onset Computer Corp., MA, USA, 0.01°C) was inserted 4 cm below the soil surface adjacent to the TDR probe. More details can be found in the Table 4-1. Instead of using a cooling coil, these seven columns were directly put in the temperature controlled water bath for the sake of time saving and uniform measurement conditions. Soil columns were frozen to -30°C without any heat pulse measurement and then the temperature was controlled to warm back up to 20 °C in 5 °C steps between -30 and -20 °C, 2 °C steps between -20 and -10 °C, 1 °C steps between -10 and -5 °C, 0.5 °C steps between -5 and 0 °C, and 5 °C steps between 0 and 20 °C with heat pulse measurement. Freezing was induced with the same temperature steps but at an opposite order. The TDR probes of the thermo-TDRs and conventional TDR were multiplexed with a SDMX 50 that was connected to a TDR 100 (Campbell Scientific Canada, Edmonton, Canada) controlled by a Campbell CR 1000 digital logger. The TDR was programmed to take measurements on one soil column for one time and then preceded to the next, and the process was repeated three times at an interval of 10 min. Similarly, the heat pulse probes were controlled by another programmed CR 1000 data logger and took measurements at the same time of TDR measurements. Heat pulses were applied after the soil temperature equilibrated with the temperature of the coolant for 30 min minimum. The duration of this experiment was 1 month. Frost heave in both experiment one and two were assumed to be insignificant, which means the sum of volumetric fraction of soil particles, ice, water, and air is equal to 1.

4.4.3. Specific heat capacity of soil solids

A differential scanning calorimeter (DSC, TA Q2000, TA Instruments, DE, USA) was used to verify the specific heat capacity of soil solids. The DSC is a thermo-analytical technique that measures the difference in the amount of heat required to increase the temperature of the sample and the reference as a function of temperature. The specific heat of soil solids c_s ($\text{J g}^{-1} \text{ }^\circ\text{C}^{-1}$) can be expressed as:

$$c_s = \frac{dH/dt \times 60}{dT/dt \times M} \times E \quad [4-10]$$

where dH/dt is heat flow signal (mW or mJ s^{-1}), dT/dt is the heating rate ($^\circ\text{C}/\text{min}$), 60 is conversion constant (min \rightarrow sec), M is sample mass (mg), and E is calibration constant (dimensionless). The samples (~ 30 mg) were equilibrated at -30 $^\circ\text{C}$ and then increased to 110 $^\circ\text{C}$ at a ramp of 5 $^\circ\text{C min}^{-1}$. Four samples of each soil were tested and averaged to get the specific heat capacity.

4.4.4. Specific heat capacity of water and ice

Specific heat capacity of liquid-water is expressed as [Dorsey, 1940; Kozlowski, 2012]

$$c_l = 4.2048 - 0.001768T + 0.00002645T^2 \quad [4-11]$$

and for ice as [Dickinson and Osborne, 1915; Kozlowski, 2012]

$$c_i = 2.114 + 0.007789T \quad [4-12]$$

where T is temperature ($^\circ\text{C}$). Specific heats in Eqs. [4-11] and [4-12] are expressed on mass basis ($\text{J g}^{-1} \text{ }^\circ\text{C}^{-1}$). c_l increases with decrease of temperatures, however, on the other hand c_i shows a different trend decreasing with decrease of temperature.

4.4.5. Calibration of Thermo-TDR and conventional TDR

Because the thermal property estimates of the HP method are sensitive to the needle spacing, the exact needle spacing was calibrated before and after the test in agar-stabilized water 6 g/L in the similar manner described by Campbell *et al.* [1991].

TDR is a standard tool for measurement of water content in unfrozen soils and is widely applied in frozen soil studies [*Kane, 1978; Patterson and Smith, 1980; Kane and Stein, 1983; Watanabe and Wake, 2009; Watanabe et al., 2013*]. This method is essentially based on interpreting the sampled TDR waveforms to estimate the dielectric permittivity (ϵ_{eff}) and then convert it to water content via empirical relationships or dielectric mixing models, which is the process of TDR calibration. The logged waveforms alone can be used to qualitatively reflect the change of water contents in both unfrozen and frozen soils. Readers are referred to *Noborio et al. [2001]* and *Robinson et al. [2003]* for more details about TDR and TDR method.

For calibration of TDR for the measurement of unfrozen water and ice content in frozen soils, the study of *He and Dyck [2013]* (Chapter 2) showed that composite dielectric mixing models could be used. They presented evidence to show that the mixing models could be parameterized using unfrozen soil at a variety of water contents and then extended to frozen soils. It has been shown to be useful for frozen soil studies [*Christensen et al., 2013*]. The assumption of constant total water content (sum of unfrozen water and ice content) within the measurement volume of the TDR probe stay constant during the freezing/thawing processes is fully satisfied in this study since the soil column is a closed system.

The composite dielectric mixing model was derived from the model developed by *Sihvola and Lindell [1990]*, and calibrated by *He and Dyck [2013]* (Chapter 2) using unfrozen soil samples of a variety of textures and water contents. With experimental data of soil water content, permittivity, and other physical property values, the parameters for the mixing model were optimized using MathCAD software based on the goodness of fit parameters such as root mean squared difference (RMSE), Nash-Sutcliffe Efficiency (NS-Eff) and average deviations (Avg-Dev) between TDR-measured permittivity and the modelled permittivity as described in chapter 2. In this study, the same procedure was performed for TDR calibration of thermo-TDR.

For the calibration of dielectric permittivity to liquid moisture content for the thermo-TDR in unfrozen soils, eight soil water contents (3%, 5%, 8%, 10%, 12%, and 15% by weight) were tested. Soil samples were prepared and packed in the same way as the abovementioned experiments but in soil columns of different dimension (8 cm i.d. and 5 cm in length), the same TDR measurement system was used as in the experiment two for repeated measurements of 5 times for each water content at room temperature. For the conventional 3-prong TDR, the same

parameters as in Chapter 2 were used since the same probe type and soil were used. The best fit parameters and goodness of fit for calibration of thermo-TDR and conventional TDR are tabulated in Table 4-2.

4.5. Results and Discussion

4.5.1. Specific heat capacity of soil solids

Estimates of specific heat capacity of soil constituents across a wide range of ambient temperatures is necessary for accurate estimation of C_v using Eq. [4-2]. However, accurate experimental data are scarce and incomplete and very often limited to specific soils since the lack of suitable measurement devices or potential measurement errors [Smits *et al.*, 2013]. DSC has showed great advantages of quick and accurate measurements, it has been proved to accurately measure specific heat capacity and has been widely used in related studies in soil science [Liu and Si, 2011b; Kozłowski, 2012]. Like the specific heat capacity of water (c_l) and ice (c_i), the specific heat capacity of soil solids (c_s) is temperature dependent and the DSC-measured data is fitted to ($R^2 = 0.9951$)

$$c_s = 494.5 + 2.1T + 9 \times 10^{-3}T^2 - 10^{-4}T^3 \quad [4-13]$$

The c_s decreased with temperature, ranging from 5.393 J g⁻¹ at 20 °C to 4.945 J g⁻¹ at 0 °C to 4.569 J g⁻¹ at -20 °C. These measured values of c_s are significantly less than literature values (e.g., 6.5 ~ 8 J g⁻¹). It is also noteworthy that the assumption of constant c_s for all temperatures in the study of soil thermal properties may not always be justified even if the effect of c_l may, to some extent, offset the effects of c_s and c_i while temperature changes. Therefore, choice of c_s for specific soils of interest needs to be carefully considered.

4.5.2. Evidence of ice melting using TDR waveforms

In this study, TDR waveforms and heat pulse data were always logged at each temperature to ensure the two values can be easily compared, but it was difficult to perfectly synchronize collection of TDR waveforms with heat pulse applications. For example, the TDR waveforms in Figs. 4-2 and 4-3 at 0 s were recorded on or just before the heat pulse started, the TDR waveform

at 7 s was measured at 7 s after the heat pulse activated, and similarly, TDR waveform at 14 s was measured at 14 s after the heat pulse activated, and so on.

TDR waveforms presented in Fig. 4-2 were selected from experiment one, the heat pulse duration was 8 s. Note that the t_1 and t_2 in Fig. 4-2 are the start and end point of the apparent distance an electromagnetic waveform travels in the soil, the difference between t_1 and t_2 is used to calculate permittivity which is related to water content. For above zero temperatures, we found that TDR waveforms with or without heat pulse treatment overlapped each other (Fig. 4-2: A&B, and t_1 and t_2 are the same for both A and B), which may indicate that a heat input of 61.5 w m^{-1} for 8s does not result in any change of measurable water content in the sampling volume of the probe, thus water movement under the temperature gradient and evaporation is negligible. This is in good agreement with previous studies that transient/non-stationary methods can reduce or prevent temperature gradient induced soil water movement compared to steady-state methods [*de Vries*, 1952; *Farouki*, 1981; *Shiozawa and Campbell*, 1990]. It also echoes the recent studies of soil evaporation that heat pulse method with relatively large heat input (J m^{-1}) required for phase change at positive temperatures [*Trautz et al.*, 2014]. At subzero temperatures, the distance between t_1 and t_2 (Fig. 4-2: C&D) is smaller than that at above zero temperature (Fig. 4-2: A&B), which means part of the soil water was frozen. Logged TDR waveforms overlapped each other when no heat pulse was applied (Fig. 4-2: C), but differences were noticed when there was heat pulse (Fig. 4-2: D). The difference between the logged waveforms (Fig. 4-2: C&D) can therefore be attributed to the occurrence of ice melting.

Figure 4-3 is an example to qualitatively show the TDR waveform changes of probes #2 ~ #5 (Experiment 2, with similar heat strength, see Table 4-1) logged at -30, -10, -3.5, and -1 °C for duration of 8, 15, 30, and 60 s during soil thawing, respectively. As is shown in Fig. 4-3, little or no changes of TDR waveform were found at -30 and -10 °C for different durations of heat pulse (Fig. 4-3: A-1&2, B-1&2, C-1&2, and D-1&2) which suggests no/little ice melting occurred or the amount of melting was too small to be detected by the TDR. As the soil temperature increased to -3.5 °C, we noticed increased travel time of the TDR wave with increased duration of heat pulse applied (Fig. 4-3: A-3, B-3, C-3, and D-3). A similar trend was observed at -1 °C but with even greater travel time, which means more heat pulse energy was consumed for melting ice at higher subfreezing temperatures. The greater travel time can be explained by a

greater amount of liquid-water content (i.e., greater amount of ice melting) in the measured domain following application of the heat pulse. The heat input per second is similar for probes #2 ~ #5, therefore, longer heat pulse durations increased the amount of heat energy injected into the soil resulting in a greater amount of ice melting and the increased permittivity persisted for a longer period especially at soil temperatures of -3.5 and -1 °C. This is consistent with previous studies that ice melting largely depends on ambient temperature and the magnitude is low at low subfreezing temperatures and high at high subfreezing temperatures [Putkonen, 2003; Liu and Si, 2011a; Zhang *et al.*, 2011]. Thus the heat pulse method could potentially be used at low subzero temperatures without correcting for latent heat fluxes, but temperatures this low (e.g., ≤ -10 °C) are not often observed in natural conditions. Closer to the freezing point, the errors become much more significant [Putkonen, 2003; Liu and Si, 2011a; Zhang *et al.*, 2011].

The differences in observed ice melting at different ambient subfreezing temperatures may be better explained by the soil freezing and thawing curve (SFTC) or soil freezing characteristic (SFC). SFTC and SFC are used to describe the change of unfrozen water (or dielectric permittivity) as a function of temperature as alluded to previous chapters (Chapters 2 and 3). The shape is similar to the soil moisture retention characteristic (SMRC) that it is flat at low temperatures (analogous to the dry end of the SMRC) and it shows a large slope at high subfreezing temperatures (e.g., between 0 and -2 °C, analogous to the wet end of the SMRC). The SMRC is usually expressed as liquid-water content as a function of energy while SFTC/SFC expressed as liquid-water content as a function of temperature, temperature and energy can be converted with the Clapeyron equation under thermodynamic equilibrium [Spaans and Baker, 1996]. At the flat part of the SFTC/SFC, large changes in temperature do not result in large changes in liquid-water content, while small changes in temperature result in large changes in liquid-water content at the steep slope part of the SFTC/SFC. The SFTC differs from SFC in that it does not usually reach thermodynamically equilibrated status. For soil in thermodynamic equilibrium, the change of same amount of energy corresponds to less change of water content at low temperatures than at high temperatures. The energy input of HP method provides the heat source for phase change at each temperature. For a certain amount of heat input from HP, the resulting phase change from ice to water is smaller at low subfreezing temperatures (i.e., ≤ -5 °C) than it is when temperature approaches freezing/thawing point. Therefore, the SFTC or SFC of a certain soil may be used to facilitate the determination of temperature range in which less ice

melting could take place and is best for the heat pulse method. In addition, temperature largely determines the amount of liquid-water content and ice content, and the phase of soil moisture affects the thermal conductivity of frozen soils. Low subfreezing soil temperature usually indicates small amount of liquid-water or large quantity of ice and also means increase of thermal conductivity. Thermal conductivity increases with decrease of soil temperature may due to: (1) “bridge effects” of ice, formation of ice better connect the soil particles that facilitates heat conduction; and (2) difference of thermal properties of ice and water as a function of temperature. The thermal capacity of water decrease with and the thermal conductivity increase with the decrease of temperature as shown in Fig. 4-4.

Although the recorded TDR traces could be used to show the ice and unfrozen water content changes caused by heat input, it is difficult to quantify the amount of ice melting due to the relatively low frequency of TDR measurements compared to the heat pulse duration. It takes around three/four seconds for TDR 100 with data logger to record one trace of 251 points that is averaged from four waveforms, much more time is needed for logging waveforms from Tektronix TDR cable testers (i.e., 7 s) with software such as TACQ [Evet, 2000] or WinTDR [Scott, 2004]. The relatively large log interval (e.g. ≥ 3 s) may miss out the peak of ice melting and TDR with higher resolution and more frequent measurements are required to improve the analysis. In addition, the difference between the waveforms before and after heat pulse is small and difficult to measure. Prior to the use of TDR equipment of higher resolution, the alternative approach to solve this problem may be by comparing C_v calculated from TDR-measured unfrozen water content and ice content using Eq. [4-2] before the heat pulse and the HP-measured C_a during the heat pulse, it would be a better approach hitherto to quantify ice melting.

4.5.3. Quantification of ice melting by comparing TDR-estimated C_v before HP and HP-estimated C_a during HP period

4.5.3.1. Comparison of TDR part of thermo-TDR to conventional TDR

TDR waveforms measured by the Thermo-TDR probes before heat pulse release were selected and averaged at each temperature step. TDR waveforms measured with conventional probes were selected at the same temperatures corresponding to that of thermo-TDR for the purpose of

comparison. Permittivity (ϵ_{eff}) interpreted from the thermo-TDR probes (#2 ~ #7) and conventional TDR probe (#8) as a function of temperature is presented in Fig. 4-5.

Figure 4-5 shows that thermo-TDR measured ϵ_{eff} falls in a narrower range than that measured by conventional TDR, with smaller permittivities measured at above zero temperatures and greater permittivities at subfreezing temperatures and large variation between probes (Fig. 4-5). Fig. 4-6 shows the calibration curves for thermo-TDR and conventional TDR probes for estimation of liquid-water and ice content, and a large difference was found between these two relationships. This is not consistent with previous research of *Ren et al.* [2003a] which showed thermo-TDR is able to give reasonable estimates of water content in unfrozen soil conditions. No report about accuracy of TDR measurements of thermo-TDR in frozen soils was found by the authors and further study of this part would be helpful. The discrepancy between conventional TDR probes and thermo-TDR probes may be attributed to: (1) differences in probe construction, permittivity is very sensitive to probe length and offset. Previous TDR evaluation studies suggested a minimum probe length of 10 cm to provide accurate measurements [*Heimovaara*, 1993; *Robinson et al.*, 2003]. *Olmanson and Ochsner* [2008] also found thermo-TDR probe with 0.04 m waveguides may detract from the accuracy and precision of water content measurements; (2) introduction of multiple-needles narrowly-spaced (e.g., 6 mm) thermo-TDRs into soils may change local soil structure (e.g., bulk density and hence soil moisture), *Knight et al.* [1992] recommended that the ratio of rod distance and rod diameter for TDR should not be greater than ≈ 10 , and the value of rod diameter should be as large as possible compared with the value of rod distance as long as there is no significant compaction and local disturbance; (3) the repeated application of heat pulse may result in change of the soil water conditions; and/or (4) other unknown reasons.

Because of the uncertainty in using the small thermo-TDR probes for moisture content estimation, we will use permittivity and moisture estimates from the conventional TDR probes for the remainder of the analysis in this chapter. The unfrozen water content and ice content was estimated using the calibration curve (conventional TDR in Fig. 4-6) that derived from dielectric confocal model as presented in Chapter 2 and the parameters of loamy sand are tabulated in Table 4-2.

4.5.3.2. Interpretation of HP and conventional TDR data

It is noted that the shape of $T(t)$ data changes with ambient temperatures. At low subfreezing temperatures, the shape of $T(t)$ data is similar to that in unfrozen soils as a positive skewed bell (i.e., long tail is on the right hand side) (Fig. 4-7), while at high negative temperatures, they are usually characterized with long, flat tails and small, drawn out peaks (i.e., maximum temperature rise) when temperatures approach the thawing point (Fig. 4-7). The same phenomenon was also observed by *Ochsner and Baker* [2008] and *Zhang et al.* [2011]. *Ochsner and Baker* [2008] attributed the differences in $T(t)$ curves to ambient temperatures. Close to the freezing point, large amounts of heat released by HP methods are used to melt ice rather than increasing the temperature of local frozen soil or conducting it to surrounding soils, while refreezing of the melted ice releases heat and will maintain the peak temperature for a greater period of time. Thus, the closer the temperature is to the freezing/thawing point, the more ice melting and refreezing took place, which results in smaller magnitude and extended duration temperature changes in response to the heat pulse.

HP-estimated C_a was retrieved by SPM method based on Eq. [4-9] with a program written in Matlab by the author. The HP-estimated C_a of four temperature sensors surrounded the heater were averaged at each temperature step to minimize effects of local soil variability. TDR-estimated θ_l and θ_i was used to estimate C_v with Eq. [4-2] (hereafter TDR-estimated C_v), TDR-estimated C_v is only related to θ_l and θ_i and is not affected by latent heat. The results of HP-estimated C_a and TDR-estimated C_v are presented in Fig. 4-8.

4.5.3.3. Comparison of TDR-estimated C_v and HP-estimated C_a

Figure 4-8 shows TDR-estimated C_v and HP-estimated C_a as a function of temperature during soil thawing (-35 to 25 °C) for the Brightbank soil with 4 different heat-pulse durations and 3 different heat strengths. The relative difference of the two volumetric heat capacity estimates, $(C_v - C_a)/C_v$ (hereafter ratio), as a function of temperature during soil thawing and freezing is presented in Fig. 4-9 (Interpolation was used to estimate C_a and C_v during soil freezing and thawing processes at temperatures of 25, 20, 15, 10, 5, 0, -0.5, -1, -1.5, -2, -2.5, -3, -3.5, -4, -4.5, -5, -6, -7, -8, -9, -10, -12, -14, -16, -18, -20, -25, -30, and -35 °C). During soil freezing, C_a and C_v only differed by 10% or less for the standard, 8 s heat pulse. As expected, the HP-estimated

C_a and the ratio peaked just below the thawing point for all soil columns on the thawing curve. This peak is a result of energy consumption for phase change from ice to water (or latent heat of fusion) which influences C_a [Ochsner and Baker, 2008]. With the same heat pulse strength (q), the longer the heat pulse duration t_0 the higher the peak C_a (Fig. 4-8: A~D) and ratio (Fig. 4-9 brown circle < green circle < brown triangle down < orange triangle up). For treatments with the same heat pulse duration, greater heat pulse strength (q) resulted in C_a and ratio peaks over a wider temperature range (Fig. 4-8: A, E&F and Fig. 4-9 brown circle < brown square < green square). The higher peaks in C_a and ratio may indicate more heat release from the heat pulse is used for phase change from ice to water, while the wider spike may indicate that significant ice melting starts at lower temperatures. Figure 4-8 also shows that HP-estimated C_a between ~ -0.5 and 0 °C dropped to values similar to those in unfrozen soil, which may mean ambient temperature was not low enough and not much ice existed, therefore heat released by heater is enough to raise the soil temperature to above zero (e.g., $T(t)$ of temperature at -0.59 °C in Fig. 4-7) besides melting ice. This is different from field research of Ochsner and Baker [2008] which the resulted $T(t)$ curve at -0.19 °C still show long and flat peak. This may be attributed to (1) different soils have different SFTCs/SFCs, the same temperature change may result in changes of different amount of liquid-water and (2) a smaller heat strength was used and the total soil water content was greater compared to this study (e.g., 85 vs > 220 W m^{-1} and 0.3 vs 0.25 $\text{cm}^3 \text{cm}^{-3}$).

It is noted that TDR-estimated C_v (Eq. [4-2]) and HP-estimated C_a agreed well at temperatures smaller than -10 °C (i.e., ratio $\rightarrow 0$, Fig. 4-9) during soil freezing for treatments of similar heat strength but different HP durations (Fig. 4-8: A~D). Above this temperature, C_v declined slightly with temperature and was generally greater than the HP-estimated C_a that declined with temperature to a greater extent. It might be that large amount of ice at low temperatures and low ambient temperature facilitated heat conduction and because the soil freezing curve is flat at low temperatures (small changes in ice content even with significant changes in temperature). This is reflected apparently in Fig. 4-10: A&B that the maximum temperature rise ΔT_m increased with decreasing temperatures while the time to get ΔT_m for each treatment was constant for temperatures below ~ -4 °C (Fig. 4-10: C&D). The other reason for the discrepancy between TDR-estimated C_v and HP-estimated C_a below -10 °C is that errors in the TDR-estimated permittivity-water content calibration may result in liquid-water content being over-estimated. For columns with high heat strength treatments (Fig. 4-8: E&F), greater

HP-estimated C_a compared to C_v at each temperature is likely attributed to the greater amount of ice melting than the treatments with smaller heat pulse strength (Fig. 4-8: A~D). This is in good agreement with previous studies [Ochsner and Baker, 2008; Liu and Si, 2011a] that the HP method with small heat strength can be used to approximate the real thermal properties of frozen soils at low subfreezing temperatures. Large heat pulse strengths (Fig. 4-8: E~F), on the other hand, result in significant ice melting even at low temperatures and affect the estimation of real thermal properties. Therefore, quantification of the ice melting caused by heat pulse method may facilitate the application of HP in frozen soils.

HP-estimated C_a with different heat strengths and heat pulse durations are compared with TDR-estimated C_v during soil freezing in Fig. 4-11. The ratio as a function of temperature during soil freezing is presented in Fig. 4-9B which shows the similar pattern as Fig. 4-11. The freezing curve of column #7 was not measured and will not be discussed. Like the thawing curve (Fig. 4-8), an apparent trend in difference between HP-estimated C_a and TDR-estimated C_v is observed on the freezing curve. But the magnitude is much smaller as observed in Fig. 4-11 and Fig. 4-10B&D. The trend of increasing difference is interrupted by the possible phase change indicated by the spike in Fig. 4-11: C (between 0 and -5 °C), which is likely a result of latent heat release following sudden ice formation. The same phenomenon was observed in our previous study [Figs. 2-13 and 2-14 in Chapter 2] on the same soil type with continuous TDR measurements (e.g., every 7 s). This may be attributed to that latent heat cannot propagate quickly to surrounding soils and result in the temperature rise of local soil that also accompanied by remelting of part of the newly formed ice. Since the discrete TDR and HP measurements in this study and the short-lived period of phase change during soil freezing, this phenomenon was not consistently observed in other soil columns. Discrepancies between HP-estimated C_a and C_v (Eq. [4-2]) at above zero temperatures (Fig. 4-11: A~E) are in a reasonable range. HP-estimated C_a and C_v are in good agreement between 0 and -10 °C for column #2 (Fig. 4-11: A), while the others only overlapped during phase change period (Fig. 4-11: B, C&E). Differences between HP-estimated C_a and TDR-estimated C_v increase with heat pulse durations (Fig. 4-11: A~D) and heat strengths (Fig. 4-11: A&E). The greatest difference between C_a and C_v was observed in the probe with the greatest energy input and heat pulse duration (Fig. 4-11: D) which was similar to the thawing curves.

TDR-estimated C_v with Eq. [4-1] and HP-estimated C_a were hysteretic. The C_v calculated with Eq. [4-2] is more like hysteresis of the soil freezing characteristic (SFC) and soil freezing-thawing curves (SFTC) as described in Chapter 2 since C_v changes with the liquid-water content and ice content. Interestingly, the freezing portion of the SFC, SFTC and C_v (T) curves are generally greater during freezing than during thawing (i.e., C_v on the thawing curve is greater than that on the freezing curve at each temperature), however, the opposite is true for the freezing and thawing curve of HP-estimated C_a . At subfreezing temperatures, the ice content on the thawing curve would be greater than that on the freezing curve according to the SFC and SFTC. Therefore, more energy input by heat pulse would be used for phase change over conduction and the ΔT_m would be smaller and the t_m would be greater on the thawing curve, especially at phase change period (Fig. 4-10: A&C vs B&D). Therefore, the thawing curve of HP-estimated C_a is above the freezing curve.

4.5.3.4. Ice melting

Generally, a good agreement between TDR-estimated C_v (Eq. [4-2]) and HP-estimated C_a (Eq. [4-9]) at above zero temperatures where no phase change occurs (vaporization is not considered in this study) indicates that difference between the two values may be used to quantify the magnitude of ice melting. Ice melting therefore is calculated with Eq. [4-6]. The results are shown in Fig. 4-12: A&B. Fig. 4-12: A shows the amount of ice melting as a function of temperature during the thawing processes for the 6 treatments (different heat pulse durations and strengths, Table 4-1) and Fig. 4-12: B is for freezing processes.

It is apparent in Fig. 4-12: A that the amount of ice melting was small when temperature was $< \sim -5$ °C, while the magnitude of ice melting rose exponentially above this temperature until 0 °C for all 6 columns/treatments. This is probably due to almost all water existing in the state of ice that efficiently dissipated heat away from the heater when temperature < -5 °C. Unfrozen water content is very sensitive to the heat input above this temperature which usually called phase change period; a small heat release may result in large amount of ice to thaw. It is noted that the longer heat pulse duration results in more ice melting which is in line with the previous discussion that longer heat pulse duration is associated with greater C_a . The amount of ice melted ranged from 0.5 to 2% for heat pulse durations of 8 to 60 s (Fig. 4-12: A). The greatest ice melting occurred mostly at temperature around -0.5 °C except col #7 (8 s) that at ~ -1.5 °C. This

is in agreement with *Zhang et al.* [2011] who found ice melting is large between 0 and -2 °C and application of heat pulse method in this range is difficult.

Compared to ice melting on the thawing curve, ice melting during soil freezing is small (Fig. 4-12: B), which is in the similar manner as the TDR-estimated C_v and HP-estimated C_a in Fig. 4-8. The difference can be attributed to that soil water might be super cooled at ~ -0.5 °C and the peak of ice melting would not appear until significant phase change took place, which would be ~ -5 °C as shown in Fig. 4-12: B. It is noteworthy the magnitude of ice melting at -5 °C on both the freezing and thawing curves are similar, which also indicates that super-cooling is accounted for the difference of ice melting at ~ -0.5 °C and no spike was observed in at this temperature. The only exception in Fig. 4-12: B is the col #4 (30 s) of which ice melting spiked just below 0 °C which might be due to the early significant phase change occurred in this treatments as alluded to earlier, and HP and TDR measurements might catch part of the early phase change that affects the TDR-calculated C_v and HP-estimated C_a and hence ice melting.

The amount of ice melted during the heat pulse period is small ($0.02 \text{ cm}^3 \text{ cm}^{-3}$ max. between 8s and 60 s in Fig. 4-12: A), but the heat capacity differs one order of magnitude ($\sim 1.2 \times 10^7 \text{ J m}^{-3} \text{ }^\circ\text{C}^{-1}$ for 8 s in Fig. 4-8: A; and $\sim 1.5 \times 10^8 \text{ J m}^{-3} \text{ }^\circ\text{C}^{-1}$ for 60 s in Fig. 4-8: D). This means small changes in liquid-water content/ice contents can cause large differences in thermal properties. Thus the heat pulse method would be less likely to be an appropriate approach for estimating frozen soil thermal properties without further corrections. Numerical models might be helpful to interpret the real thermal properties measured by heat pulse methods. A linear relationship is observed between the changed thermal properties and the energy input by heat pulse method as shown in Fig. 4-14.

The other issue raised with this is that the resulted estimate of ice melting is the average change in ice between the heater and the temperature sensors. The resulted C_a from Eq. [4-9] is very sensitive to ΔT_m and is less sensitive to ε , the ratio between t_0 and t_m . However, the ΔT_m in Eqs. [4-6] and [4-9] are measured 6 mm away from the heater. It is likely that most of the ice melting occurs near the heating needle and much less melting further away as indicated by the difference in temperatures between the heater and the temperature sensors. This can be seen clearly from the simulated temperature distribution around the heater in unfrozen soils (Fig. 4-13, derived by fitting Eq. [A4] of *Campbell et al.* [1991]), how the temperature is distributed around

the heater in frozen soil is not well known but assumed to be in the similar way. The ice melting consumes heat for phase change at near the heater (lowering ΔT_m) and creates spatially and temporally heterogeneous C_a and thermal conductivity (λ_a) or thermal diffusivity (κ_a , ratio of λ_a and C_a) that affects ε . The estimated κ_a would be less than the actual diffusivity, thermal conductivity likely affects the estimate of C_a but it is mostly the latent heat flux that affects $(C_a - C_v)/C_v$. The ice melting process violates the assumption of constant thermal properties between the heater and temperature sensors during the heat pulse period for Eqs. [4-6] and [4-9]. Despite temporal and spatial heterogeneity in the thermal properties induced by the HP method in frozen soils, a decent linear relationship between heat input and $(C_a - C_v)/C_v$ is observed and so it is likely still possible to correct frozen soil thermal properties at least for C_v .

According to the relationship presented in Fig. 4-14, an energy input of 98.8 J m^{-1} or heat strength of 12.3 W m^{-1} for 8 s can reduce ice melting and result in a C_a 10% greater than the original C_v (i.e., $(C_a - C_v)/C_v = 10\%$) when the total soil moisture content is $0.25 \text{ cm}^3 \text{ cm}^{-3}$. For frozen soil with higher moisture content, the ice melting effects would be further reduced and heat pulse method can be used to approximately estimate thermal properties with in a wider range of temperatures (e.g., $< -2 \text{ }^\circ\text{C}$). This relationship may be used as reference or guidance for application of heat pulse in frozen soils to determine the optimized design of heat pulse sensors and the temperature ranges that the estimated soil thermal properties are not significantly affected by ice melting. It could be used to correct HP-measured C_a in the field or undisturbed cores could be taken from soil profiles and the correction curve made for each horizon or layer as a function of volumetric water content. Further, a similar approach may be used for the thermal conductivity and thermal diffusivity. However, since this work resulted from a single soil and water content, the nature of how the relationship presented in Fig. 4-14 varies with soil type (i.e., SFC) and total water content needs to be further explored.

4.6. Conclusion

I have presented the data measured from two experiments to apply the TDR method presented in Chapter 2 to develop a correction factor for HP method-measured specific heat capacity in frozen soils. The first experiment showed qualitative evidence of ice melting resulting from heat pulse with TDR traces. The second experiment quantified the latent heat flux associated with ice

melting by comparing the HP-measured C_a to C_v calculated with Eq. [4-2] and TDR-estimated liquid-water and ice content as a function of heater strength ($\sim 35 - 60 \text{ W m}^{-1}$) and duration (8 - 60 s). The maximum ice melting was estimated to between 0.5 and 2% in this sandy soil at a total water content of 25%. This small amount of ice melting results in a significant change in HP-estimated soil thermal properties. The heat pulse method without further corrections is less likely appropriate for frozen soil applications when temperatures are below $-5 \text{ }^\circ\text{C}$. The TDR and HP estimated heat capacity are hysteretic as the soil freezing characteristics and soil freezing and thawing curve. A significant interaction between the SFC and HP-estimated C_a as a function of temperature was observed. Namely, HP-estimated C_a was most influenced by latent heat fluxes during soil thawing rather than soil freezing. This result is unique and has not been previously reported in the literature. Practically, this result can be used to aid interpretation of HP-measure thermal properties in frozen soils. This result also gives further insight into soil freezing and thawing processes. Ice formation during soil freezing occurs very quickly over a short temperature range, whereas the reverse process appears to occur more slowly over a wider range of temperatures. A good relationship was found between the TDR and HP estimated heat capacity and energy input by heat pulse method. The relationship can be used as guidance for optimum design of HP probes for frozen soil application, together with the SFTC or SFC can be used as reference for determination of the temperature ranges in which the estimated thermal properties are not affected significantly by heat pulse induced ice melting. In addition, the relationship could be used to correct HP-measured apparent heat capacity, potentially apparent diffusivity and apparent diffusivity. TDR method with dielectric mixing model that is based on the assumption of constant total soil water content can be easily satisfied in lab conditions. A series of lab tests on different soil water content can be used to interpret the application of HP in the field conditions where frost induced water redistribution and water infiltration may lead to change in soil water content.

Table 4-1. Experiment design

Exp. Batch	Soil column	Probe number	Probe type	Bulk density	Particle density	Total water content	Heater resistance	Heat pulse duration	Heat strength	Energy input
				ρ_b (g cm ⁻³)	ρ_s (g cm ⁻³)	θ_t (cm ³ cm ⁻³)	R _{htr} (Ω)	t ₀ (s)	q (W m ⁻¹)	Q (J m ⁻¹)
experiment 1	1	#1	Thermo-TDR ^a	0.98	2.64	0.245	54.36	8	61.5125	492.1
	2	#2	Thermo-TDR ^a	1.69	2.64	0.25	53.31	8	35.5675	284.54
	3	#3	Thermo-TDR ^a	1.69	2.64	0.25	53.31	15	36.43467	546.52
	4	#4	Thermo-TDR ^a	1.69	2.64	0.25	53.31	30	34.71033	1041.31
experiment 2	5	#5	Thermo-TDR ^a	1.69	2.64	0.25	53.31	60	35.56717	2134.03
	6	#6	Thermo-TDR ^a	1.69	2.64	0.25	35.54	8	48.50875	388.07
	7	#7	Thermo-TDR ^a	1.69	2.64	0.25	35.54	8	57.525	460.2
	8	#8	TDR ^b	1.69	2.64	0.25	-	-	-	-

^a probe length is ~ 4 cm for all 5 needles

^b probe length is 14 cm for all three needles

Table 4-2. The best fit parameters and goodness of fit for the estimation of liquid unfrozen water content and ice content with dielectric confocal model for TDR calibration of thermo-TDR and conventional TDR

TDR	Self-consistency	Aspect	RMSE	NS-Eff	Avg-Dev
Conventional TDR	0.05	0.35	0.701	0.988	0.249
Thermo-TDR	0.855	0.621	3.616	0.792	-0.746

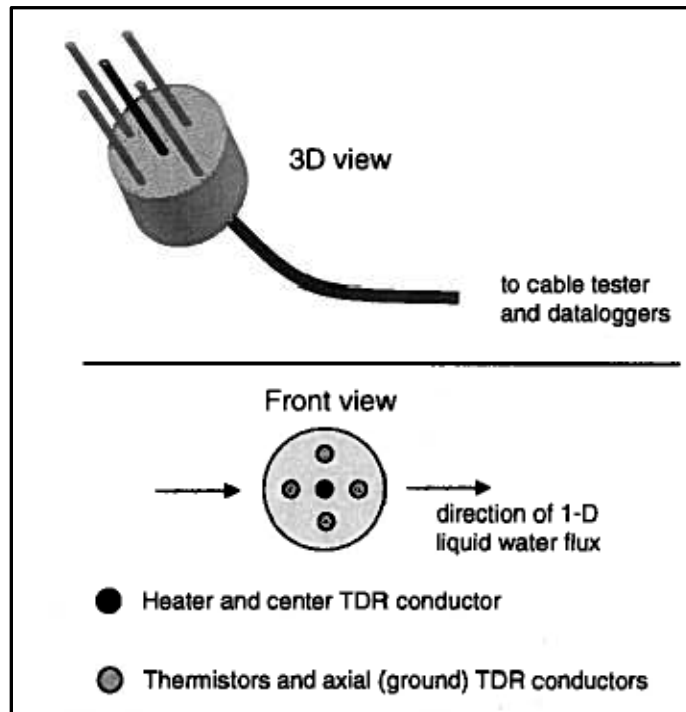


Fig. 4-1. Schematic of thermo-TDR probe.

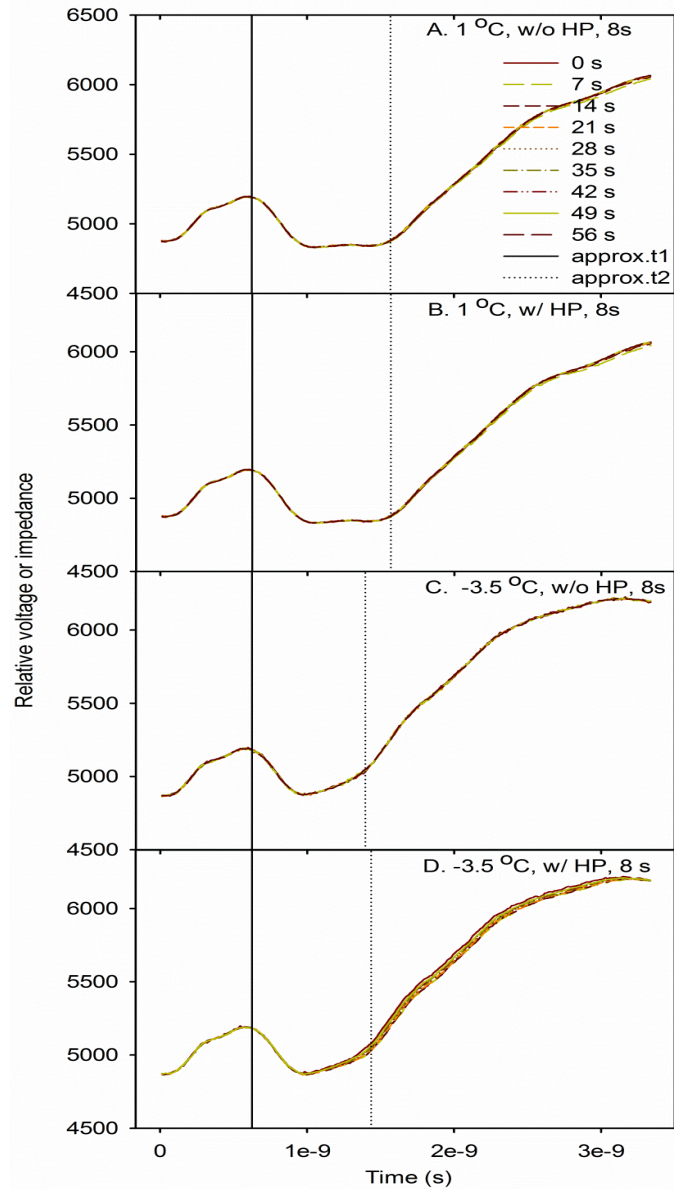


Fig. 4-2. TDR waveform at above zero temperature (A&B, 1 °C) and at subzero temperatures (C&D, -3.5 °C, evidence of ice melting) recorded from experiment one. t_1 and t_2 are usually used to calculate the travel time of electromagnetic waveform in soil along probe and can be converted to permittivity and then soil water content. The heat pulse duration is 8 s, and TDR waveform is measured with Tektronix 1502C and logged with TACQ.

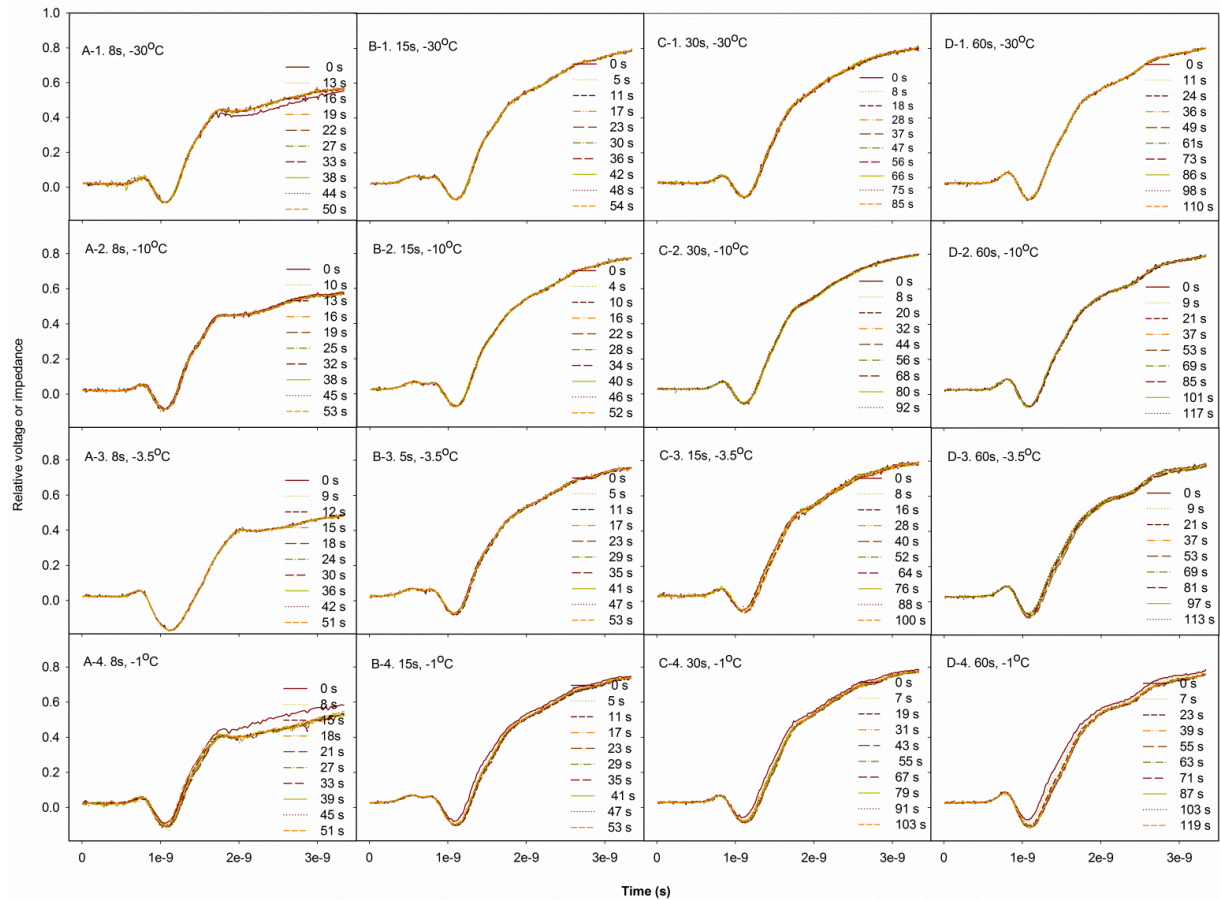


Fig. 4-3. Changes of TDR traces logged at different subfreezing temperatures on the thawing curve ($-30\text{ }^{\circ}\text{C}$ for A-1 ~ D-1, $-10\text{ }^{\circ}\text{C}$ for A-2 ~ D-2, $-3.5\text{ }^{\circ}\text{C}$ for A-3 ~ D-3, and $-1\text{ }^{\circ}\text{C}$ for A-4 ~ D-4) for measurements with heat pulse duration of 8s (probe #2, A-1 ~ A-4), 15 s (probe #3, B-1 ~ B-4), 30 s (probe #4, C-1 ~ C-4), and 60 s (probe #5, D-1 ~ D-4) in experiment two., TDR 100 was used for the measurement and a CR1000 was programmed for logging waveform.

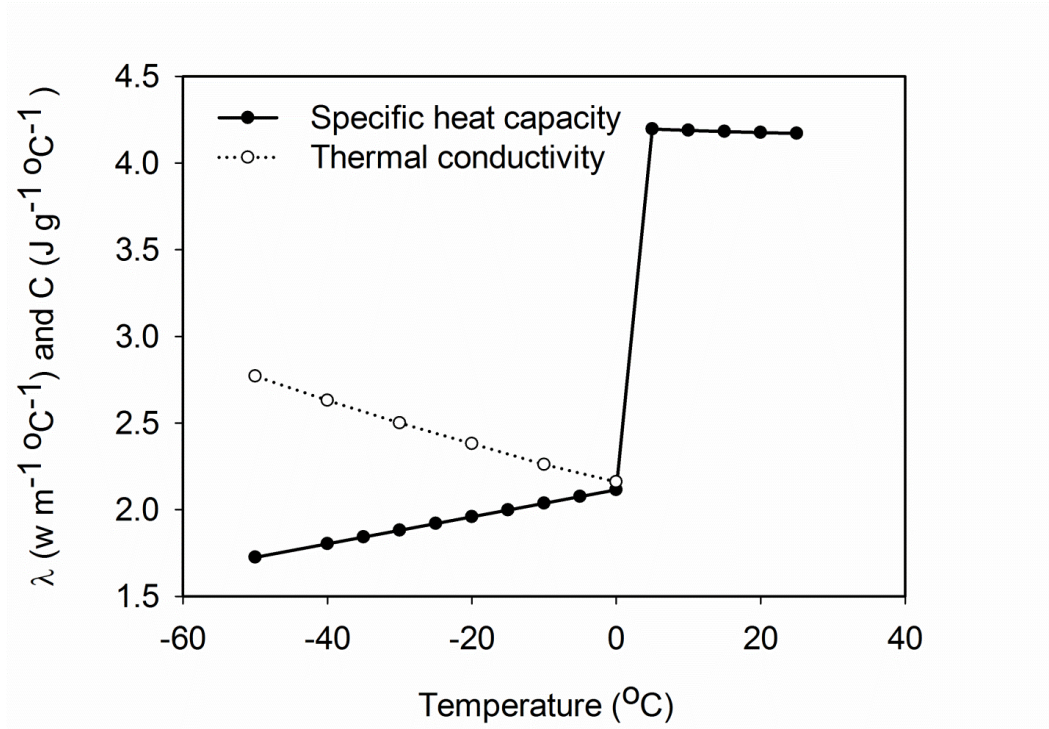


Fig. 4-4. Thermal properties of water as a function of temperature (water is considered as ice when temperature ≤ 0 °C, specific heat capacity is calculated from [4-11] and [4-12], thermal conductivity is from handbook of chemistry and physics [p.6-12, *Haynes and Lide*, 2011]).

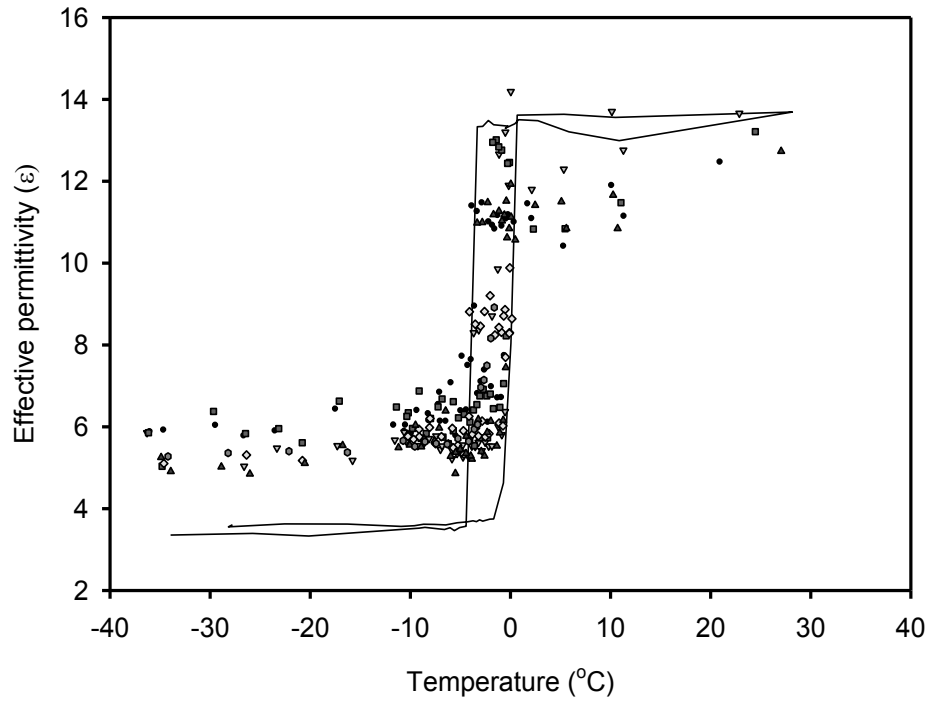


Fig. 4-5. Comparison of measurements made by conventional TDR (line) and thermo-TDR (different symbols represent different probes).

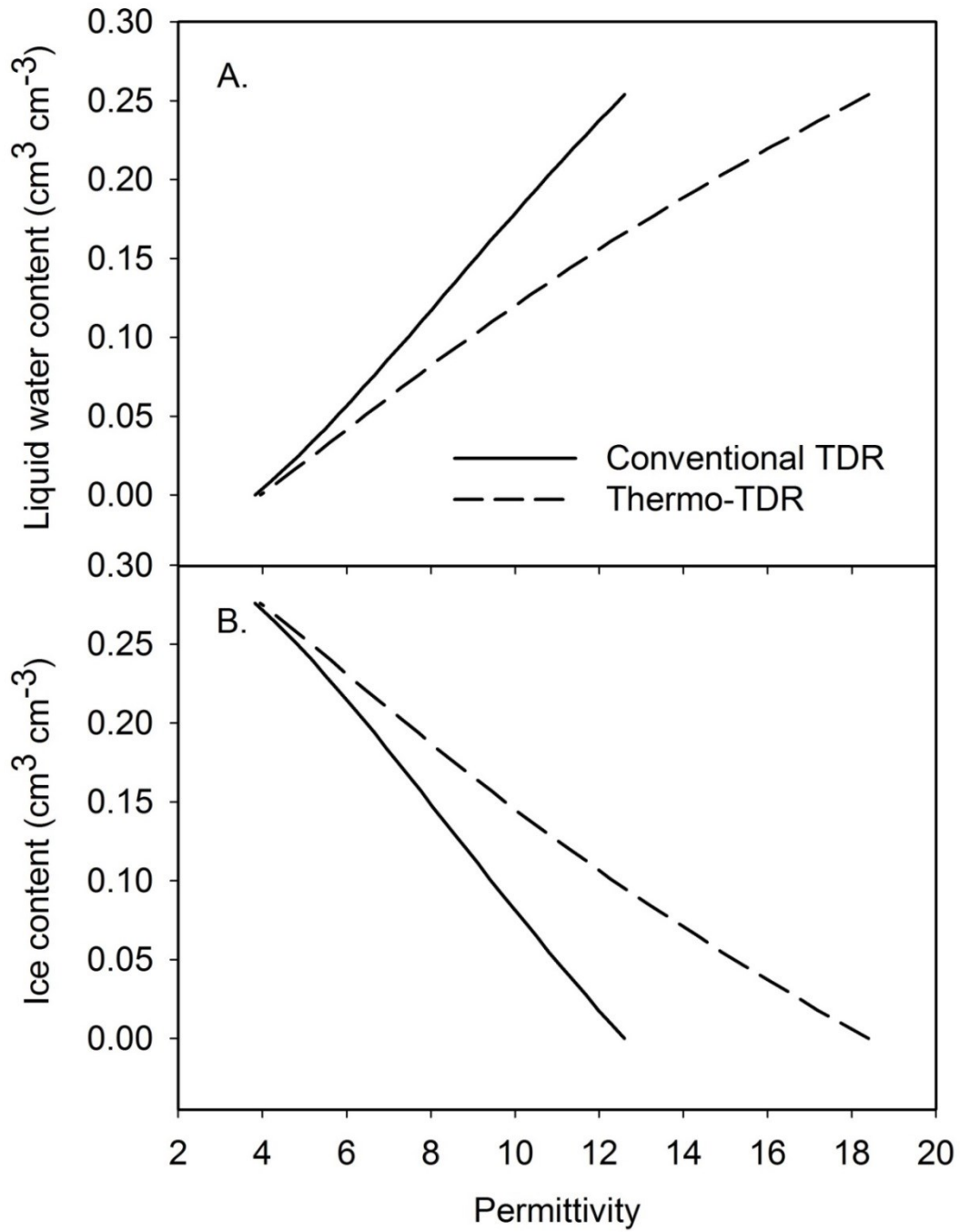


Fig. 4-6. Calibration curves for estimation of liquid-water and ice content for conventional TDR and thermo-TDR (initial water content = 0.25 cm³ cm⁻³).

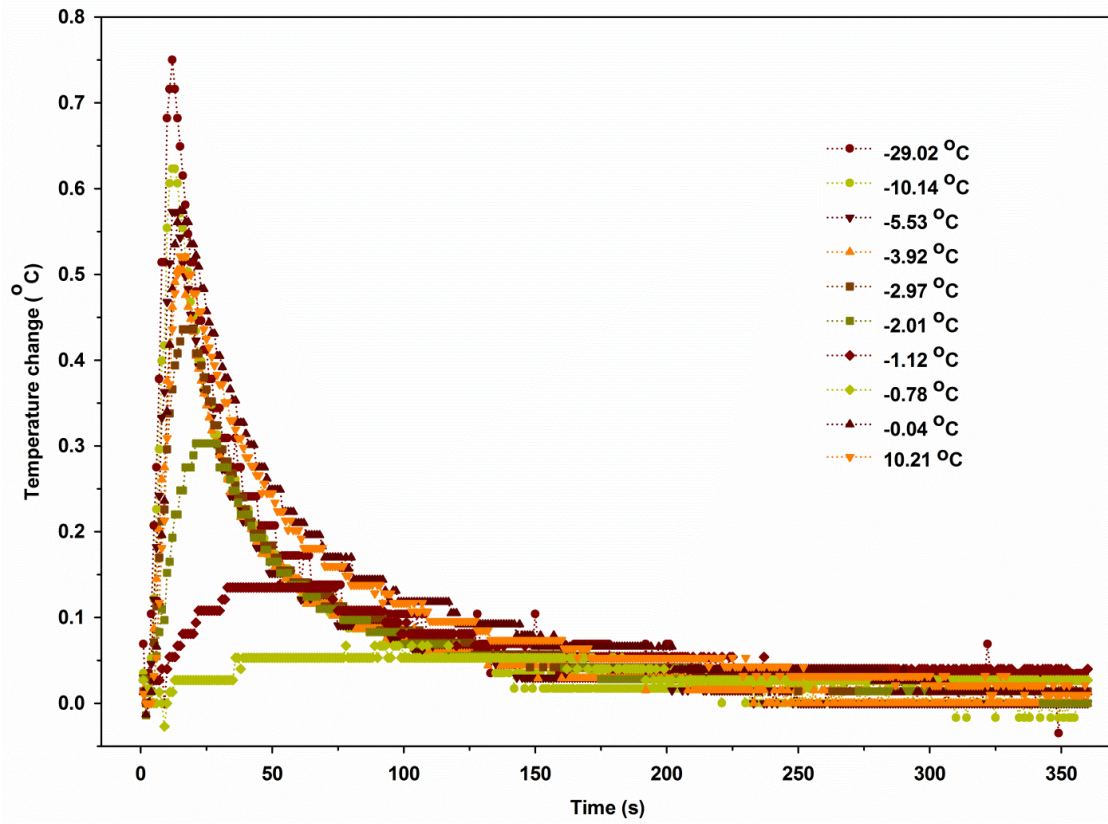


Fig. 4-7. Temperature change as a function of time, $T(t)$ for soil at different temperatures (probe #6, heat strength 48.51 W m^{-1} , heat duration 8 s), see Table 4-1 for more details.

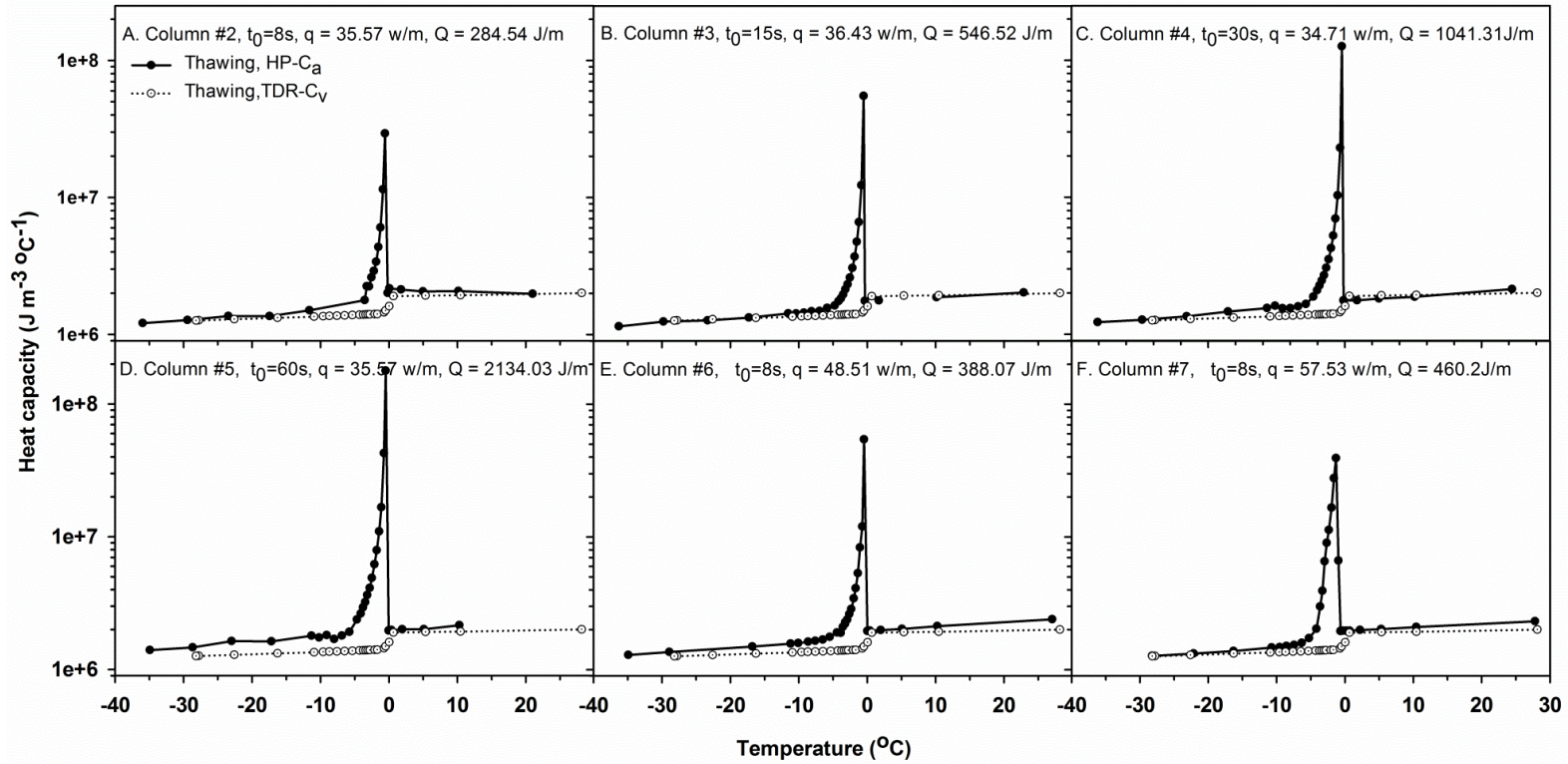


Fig. 4-8. TDR-calculated C_v (conventional 3-needle TDR) and HP-estimated C_a using SPM method during soil thawing (-35 to 25 °C) with 4 heat pulse duration (A-8 s, B-15 s, C-30 s, and D-60 s, strength is $\sim 36 \text{ W m}^{-1}$) and three heat strength treatments (A- 35.57 W m^{-1} , E- 48.51 W m^{-1} , and F- 57.53 W m^{-1} , heat pulse duration is 8 s), see Table 4-1 for more details.

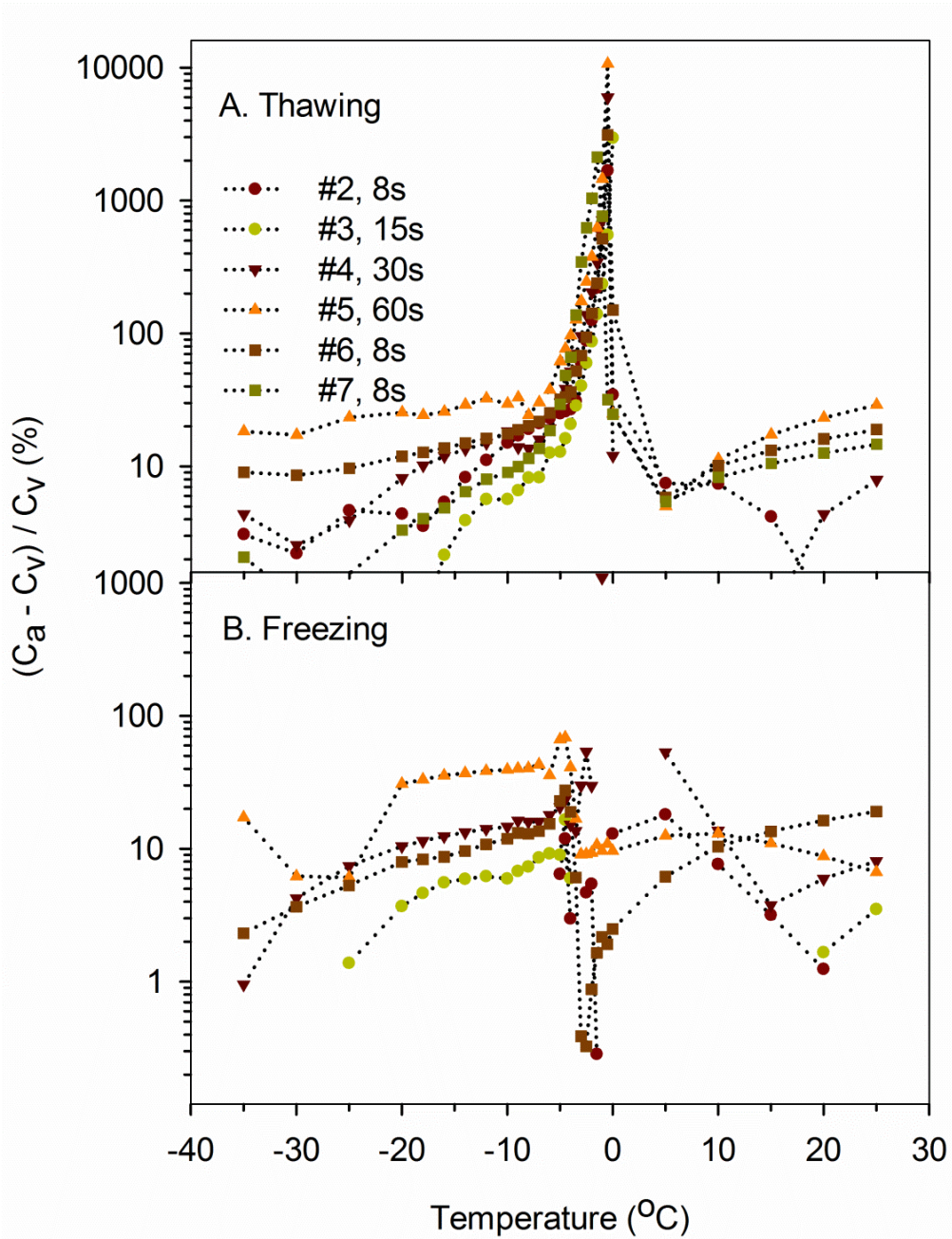


Fig. 4-9. $(C_a - C_v)/C_v$ as a function of temperature during soil thawing (-35 to 25 °C) and freezing (25 to -35 °C) with 4 heat pulse duration (8 s, 15 s, 30 s, and 60 s, strength is $\sim 36 \text{ W m}^{-1}$) and three heat strength treatments (35.57 W m^{-1} , 48.51 W m^{-1} , and 57.53 W m^{-1} , heat pulse duration is 8 s), C_a was estimated by SPM methods. See Table 4-1 for more details.

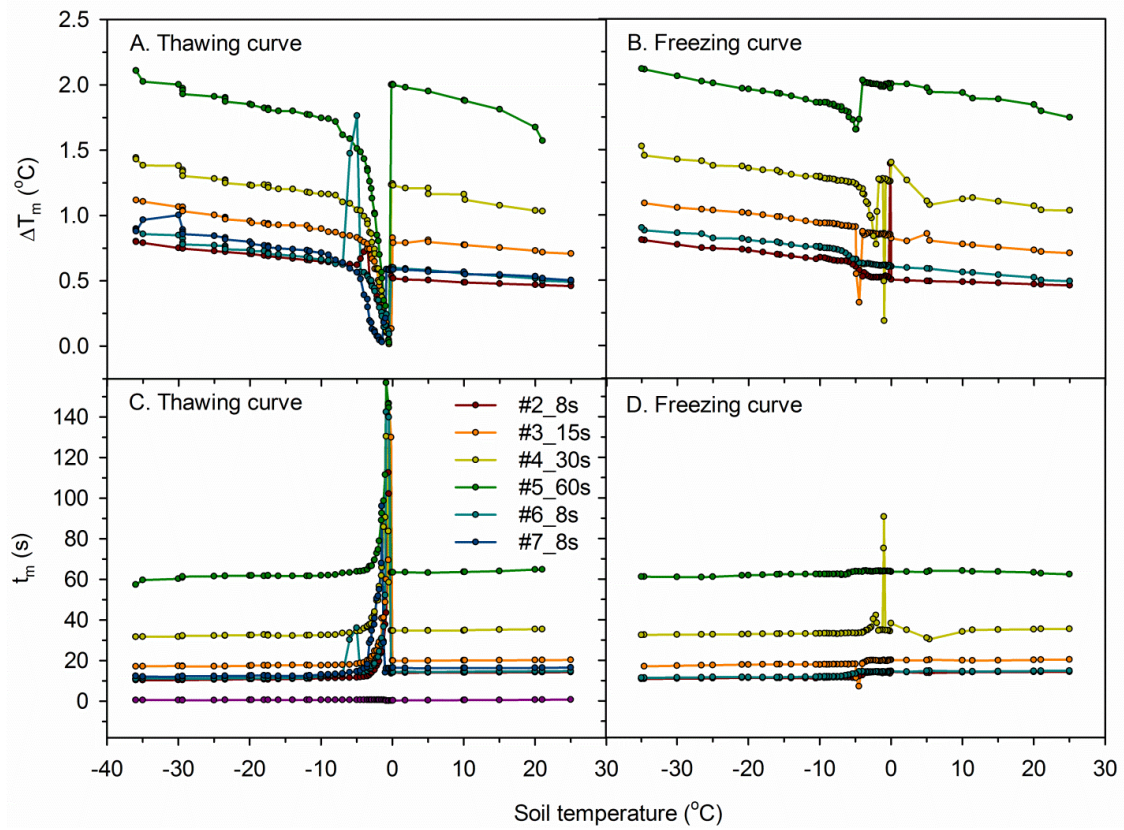


Fig. 4-10. Maximum temperature rise ΔT_m and time t_m needed to get ΔT_m across all temperatures for columns #2 ~ #7 with 8 - 60 s of heat pulse.

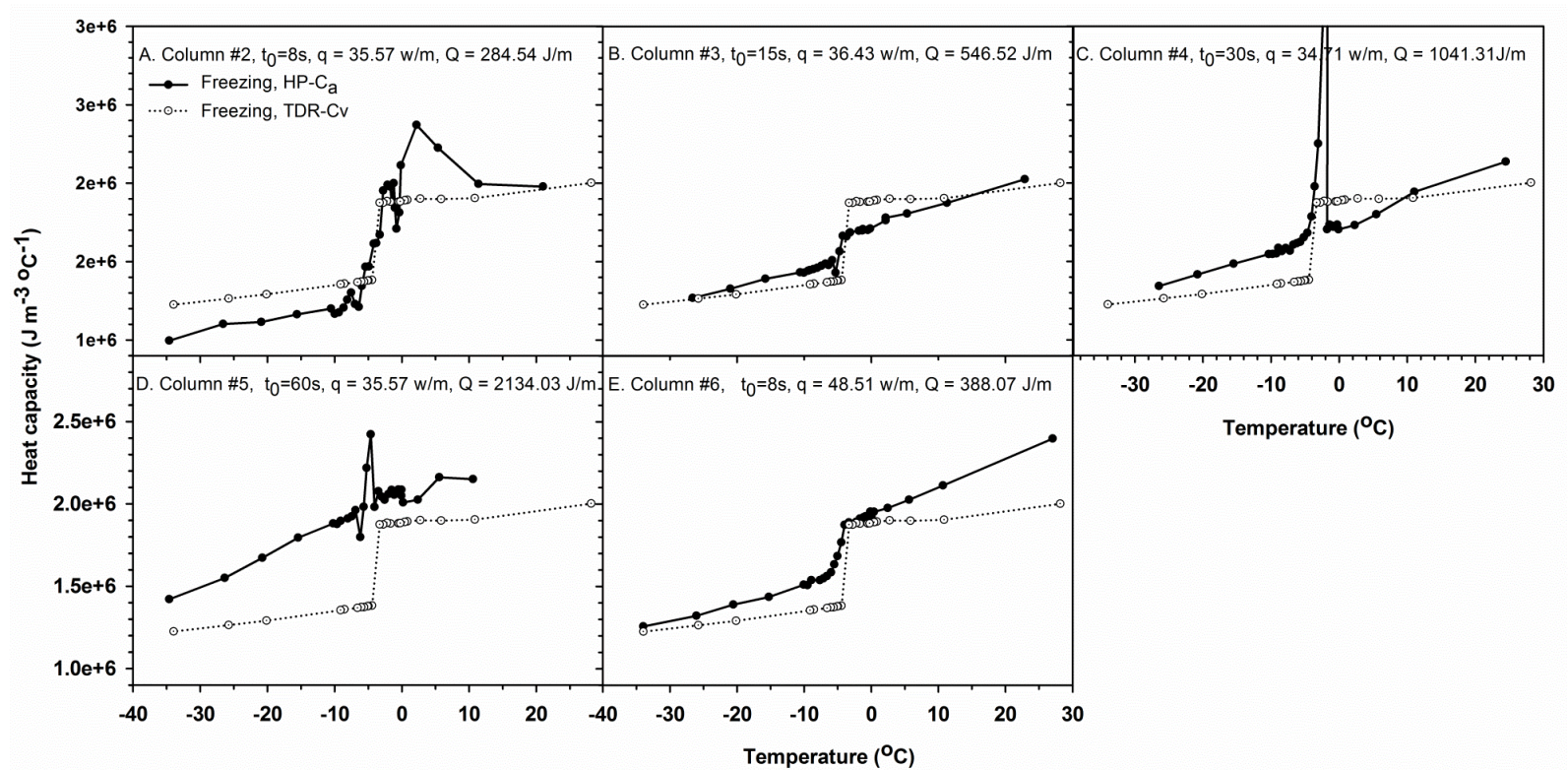


Fig. 4-11. TDR-calculated C_v (conventional 3-needle TDR) and HP-estimated C_a (with SPM method) during soil freezing (25 to -35°C) with 4 heat pulse duration (A-8 s, B-15 s, C-30 s, and D-60 s, strength is $\sim 36 \text{ W m}^{-1}$) and three heat strength treatments (A- 35.57 W m^{-1} , E- 48.51 W m^{-1} , and F- 57.53 W m^{-1} , heat pulse duration is 8 s). The spike in C is $30 \text{ MJ m}^{-3} \text{ } ^\circ\text{C}^{-1}$ and is not shown completely. Freezing curve in F is missing.

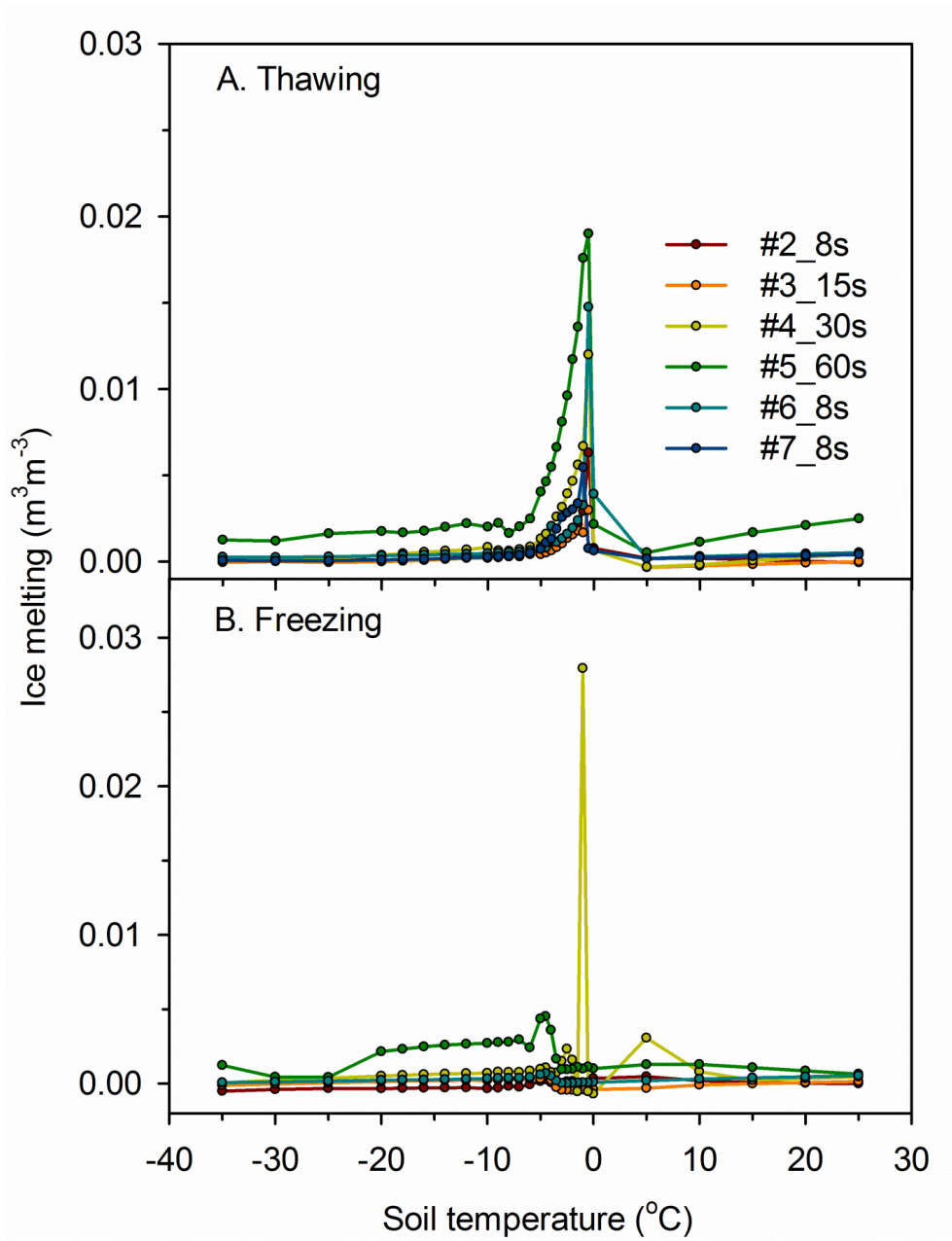


Fig. 4-12. Ice melting for probe of different heat strength and duration at subfreezing temperatures (SPM).

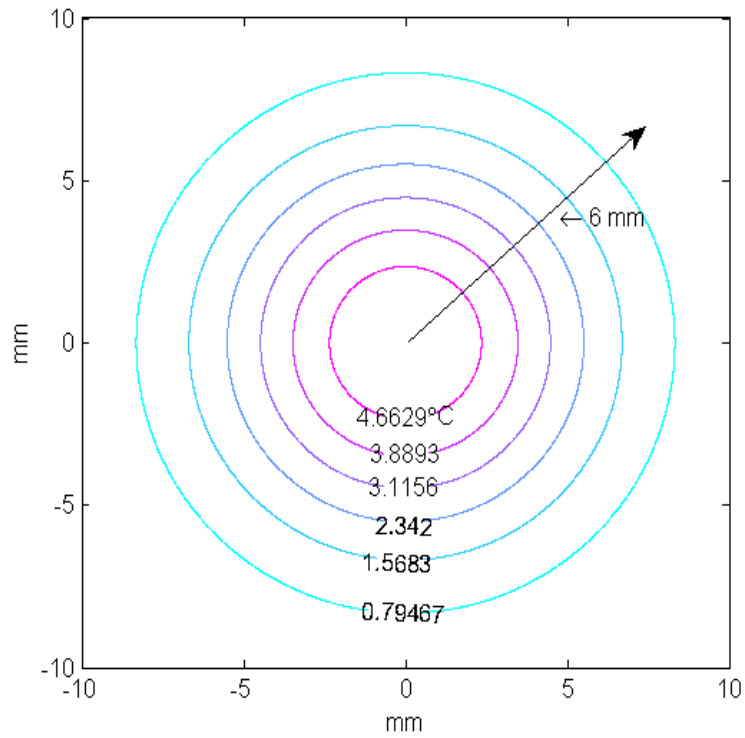


Fig. 4-13. Simulated temperature distribution cross-section of the heater in a homogeneous and isotropic soil. $q = 500 \text{ J m}^{-1}$, $t_0 = 8 \text{ s}$, $t_m = 18 \text{ s}$, $K = 5 \times 10^{-7} \text{ m}^2 \text{ s}^{-1}$, and $C_v = 10^6 \text{ J m}^{-3} \text{ }^\circ\text{C}^{-1}$ (derived by fitting Eq. [A4] of *Campbell et al.* [1991]).

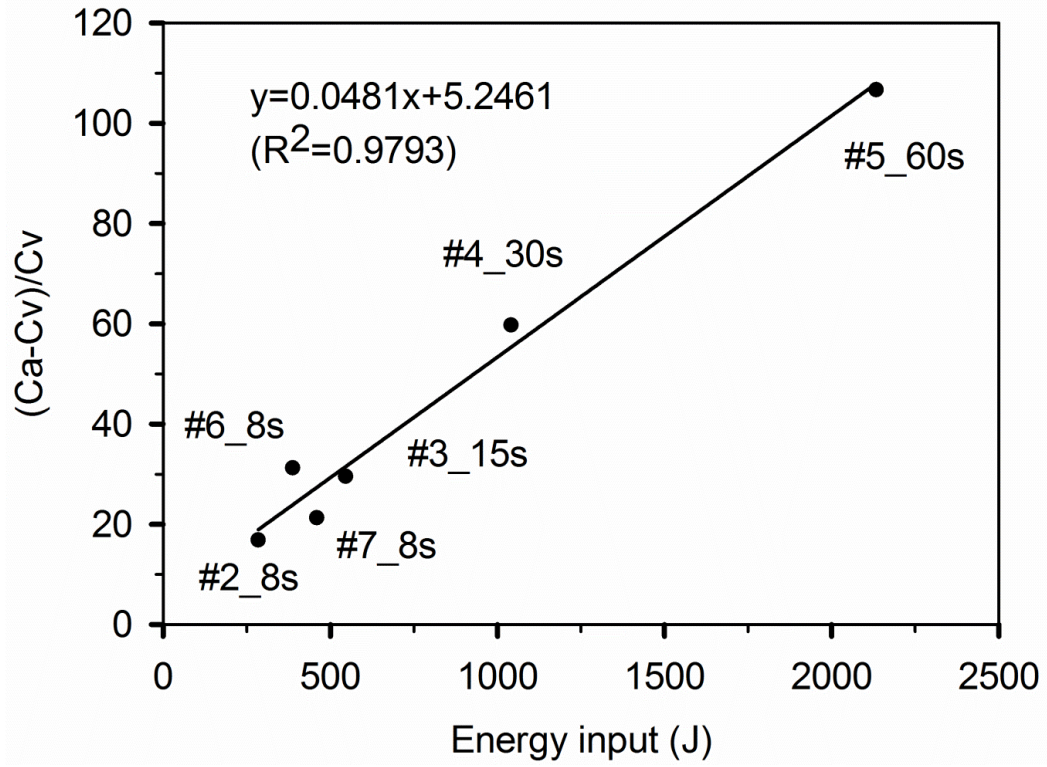


Fig. 4-14. Relationship between TDR- C_v , HP- C_a and energy input.

Chapter 5 General Discussion and Conclusion

5.1. Summary and contribution of this PhD work

The main objective of this dissertation was to develop and evaluate time domain reflectometry (TDR) and heat pulse (HP) methodologies to better understand the physics of water flow and heat transport in seasonally frozen soils. In order to achieve this objective, extensive experiments were conducted in the lab, datasets from published work and the soil moisture monitoring stations were also used in this study. The major contributions and conclusions of this thesis are:

- (1) The TDR methodology described in Chapter 2 modifies and develops two 4-phase composite dielectric mixing models based on works of *Sihvola* [1999]. This method improved the precision of simultaneous estimation of liquid-water content and ice content in frozen soils with TDR. These models can be parameterized with unfrozen soils and used in frozen soils, which makes it relatively easy to implement. The good agreement between HP-measure C_a and C_v calculated using TDR-estimate θ_l and θ_i is a validation of the method. Further analysis of field observations revealed that TDR method could be used in field conditions with careful interpretation despite that this method assumes a constant total soil water content which may be violated in field conditions where freezing induced water redistribution and water infiltration change the soil water content within the TDR sampling volume (Chapter 3).
- (2) Differences between soil freezing-thawing curves (SFTCs) and soil freezing characteristic (SFC) were described. SFTC were used to facilitating the understanding of soil freeze-thaw processes (or snowmelt infiltration) in lab (Chapter 2) and in situ (under natural boundary conditions, Chapter 3) and to explain the cause why the magnitude of ice melting caused by heat pulse method in frozen soils change with ambient temperatures and to determine the temperature range that is appropriate for HP application (Chapter 4). The hysteresis between the thawing and freezing curves of SFTC could be mainly attributed to supercooling of soil water, snowmelt infiltration (Chapter 2 and Chapter 3), and latent heat flux (Chapter 4).

- (3) Soil moisture monitoring station data showed frost depth was sensitive to soil water content prior to freezing and timing of snowpack establishment. The results also suggested that air-filled porosity of the surface 10 cm and the surface 30 cm measured in the fall appear to be the main factors governing soil water storage change following spring snowmelt (Chapter 3).
- (4) The TDR method was examined to quantify ice melting caused by heat pulse method in frozen soils based on the theory presented by *Ochsner and Baker* [2008]. It showed ice melting caused by the heat pulse was small but has significant influence on the estimated soil thermal properties. A decent relationship between HP-estimated apparent heat capacity, TDR-estimated heat capacity and HP heat input indicate it is possible to correct HP measured heat capacity and potentially thermal diffusivity and conductivity. This would advance heat pulse method into frozen soils (Chapter 4).

5.2. Future research

This dissertation provides a foundation for a variety of future research trajectories. The time domain reflectometry (TDR) method developed in chapter 2 can be used by many dielectric permittivity based electromagnetic soil moisture methods (e.g., impedance and capacitance probes, TDR, and ground penetrating radar) for accurately estimate unfrozen water and ice contents at different scales. The similar approach for the test of this method with organic/peat soil would be of great interest and importance as increasing concern of the climate change on soil carbon and nitrogen cycles at regions of high latitude. Combination of TDR and lysimetry could be used to quantify the snowmelt percolation and runoff to develop or modify current snowmelt infiltration model. The datasets in Chapter 4 could be used to model the spatial and temporal change of frozen soil thermal properties between the heater and the temperature sensors during the heat pulse period. Similar approach presented in Chapter 4 can be used to establish relationship between energy input and heat pulse measured thermal diffusivity and conductivity that would advance heat pulse into frozen soil application and used to better understand the soil freezing-thawing processes and facilitate the land surface modelling. This study could also serve the research pertaining to global circulation model and carbon and nitrogen cycling in cold regions in respect of understanding the influences of freeze-thaw cycles, permafrost thaw, soil moisture and temperature, and snowmelt runoff etc.

References

- Ågren, A., I. Buffam, M. Berggren, K. Bishop, M. Jansson and H. Laudon (2008), Dissolved organic carbon characteristics in boreal streams in a forest-wetland gradient during the transition between winter and summer, *J. Geophys. Res. Biogeo.* (2005–2012) *113*, G03031.
- Amon, R. M. W., A. J. Rinehart, S. Duan, P. Louchouart, A. Prokushkin, G. Guggenberger, D. Bauch, C. Stedmon, P. A. Raymond, R. M. Holmes, J. W. McClelland, B. J. Peterson, S. A. Walker and A. V. Zhulidov (2012), Dissolved organic matter sources in large Arctic rivers, *Geochim. Cosmochim. Ac.*, **94**, 217-237.
- Anderson, D. M. and P. Hoekstra (1965), Migration of interlamellar water during freezing and thawing of Wyoming Bentonite, *Soil Sci. Soc. Am. J.*, *29*(5), 498-504.
- Anderson, D. M. and A. R. Tice (1971), Low-temperature phases of interfacial water in clay-water systems, *Soil Sci. Soc. of Am. Proc.*, *35*(1), 47-54.
- Anderson, D. M. and A. R. Tice (1972), Predicting unfrozen water content in frozen soils from surface measurement, *Highw. Res. Rec.*, *393*, 12.
- Anderson, D. M., A. R. Tice, and H. L. McKim (1973), The unfrozen water and apparent specific heat capacity of frozen soils, *Proceedings of the 2nd international conference on permafrost, Yakutsk, USSR*, 289-295.
- Baker, J. M. (2011), Frozen soil: Water movement into, in *Encyclopedia of Water Science*, 2nd Ed. 398-400, Taylor and Francis, New York.
- Banin, A. and D. M. Anderson (1974), Effects of salt concentration changes during freezing on the unfrozen water content of porous materials, *Water Resour. Res.*, *10*, 124-128.
- Birchak, J. R., C. G. Gardner, J. E. Hipp, and J. M. Victor (1974), High dielectric constant microwave probes for sensing soil moisture, *Proceedings of the IEEE*, *62*, 93-98.
- Bittelli, M., M. Flury, and K. Roth (2004), Use of dielectric spectroscopy to estimate ice content in frozen porous media, *Water Resour. Res.*, *40*, W04212.
- Black, P. B. (1994), Initial observation of salt seiving in frozen soil, *CRREL Report 94-9*.
- Blonquist, J. M., J., S. B. Jones, I. Lebron, and D. A. Robinson (2006), Microstructural and phase configurational effects determining water content: Dielectric relationships of aggregated porous media, *Water Resour. Res.*, *42*, W05424.
- Bouyoucos, G. J. (1917), Classification and measurement of the different forms of water in the soil by means of the dilatometer method, *Michigan Agricultural Experimental Station Technical Bulletin no. 36*.
- Bristow, K. L., G. S. Campbell, and K. Calissendorff (1993), Test of a heat-pulse probe for measuring changes in soil water content, *Soil Sci. Soc. Am. J.*, *57*, 930-934.
- Bristow, K. L., R. D. White, and G. J. Kluitenberg (1994a), Comparison of single and dual probes for measuring soil thermal properties with transient heating, *Soil Res.*, *32*, 447-464.
- Bristow, K. L., G. J. Kluitenberg, and R. Horton (1994b), Measurement of Soil Thermal Properties with a Dual-Probe Heat-Pulse Technique, *Soil Sci. Soc. Am. J.*, *58*, 1288-1294.

- Bristow, K. L., R. Horton, G. J. Kluitenberg, and J. R. Bilskie (1995), Comparison of techniques for extracting soil thermal properties from dual-probe heat-pulse data, *Soil Sci.*, 160, 1-7.
- Bristow, K. L., G. J. Kluitenberg, C. J. Goding, and T. S. Fitzgerald (2001), A small multi-needle probe for measuring soil thermal properties, water content and electrical conductivity, *Comput. Electron. Agric.*, 31, 265-280.
- Cade-Menun, B., G. Bell, S. Baker-Ismail, Y. Fouli, K. Hodder, D. W. McMartin, C. Perez-Valdivia, and K. Wu (2013), Nutrient loss from Saskatchewan cropland and pasture in spring snowmelt runoff, *Can. J. Soil Sci.*, 1-14.
- Campbell, G. S. (2002), *Methods of Soil Analysis. Part 4, Physical Methods*, Madison, Wis.: Soil Science Society of America (SSSA).
- Campbell, G. S., C. Calissendorff, and J. H. Williams (1991), Probe for measuring soil specific heat using a heat-pulse method, *Soil Sci. Soc. Am. J.*, 55, 291-293.
- Cannell, G. H. and W. H. Gardner (1959), Freezing-point depressions in stabilized soil aggregates, synthetic soil, and quartz sand, *Soil Sci. Soc. Am. J.*, 23, 418-422.
- Carlsaw, H. S. and J. C. Jaeger (1959), Chapter X. the use of sources and sinks in cases of variable temperature., in *Conduction of Heat in Solids*, 2nd ed., 255-281, Oxford Univ. Press, London.
- Cary, J. W., G. S. Campbell, and R. I. Papendick (1978), Is the soil frozen or not? An algorithm using weather records, *Water Resour. Res.*, 14(6)1117-1122.
- Cary, J. W. and H. F. Mayland (1972), Salt and water movement in unsaturated frozen soil, *Soil Sci. Soc. Am. J.*, 36, 549-555.
- Christ, M. and J. Park (2009), Ultrasonic technique as tool for determining physical and mechanical properties of frozen soils, *Cold Reg. Sci. Technol.*, 58, 136-142.
- Christensen, A. F., H. He, M. F. Dyck, E. Lenore Turner, D. S. Chanasyk, M. A. Naeth, and C. Nichol (2013), In situ measurement of snowmelt infiltration under various topsoil cap thicknesses on a reclaimed site, *Can. J. Soil Sci.*, 93, 497-510.
- Cutforth, H., E. G. O'Brien, J. Tuchelt, and R. Rickwood (2004), Long-term changes in the frost-free season on the Canadian Prairies, *Can. J. Plant Sci.*, 84, 1085-1091.
- Debye, P. J. W. (1929), *Polar molecules*, 172, Dover Publications 1960, New York.
- Decker, K. L. M., D. Wang, C. Waite, and T. Scherbatskoy (2003), Snow removal and ambient air temperature effects of forest soil temperatures in Northern Vermont, *Soil Sci. Soc. Am. J.*, 67(5), 1234-1243.
- de Loor, G. P. (1968), Dielectric properties of heterogenous mixtures containing water, *J. Microwave Power EE*, 3, 67-73.
- de Vries, D. A. (1952), A nonstationary method for determining thermal conductivity of soil in situ, *Soil Sci.*, 73, 83-90.
- de Vries, D. A. (1963), Thermal properties of soils, in *Physics of Plant Environment*, 382. North-Holland Publ. Co.
- de Vries, D. A. and A. J. Peck (1958), On the cylindrical probe method of measuring thermal conductivity with special reference to soils. I: Extension of theory and discussion of probe characteristics, *Aust. J. Phys.*, 11, 255-271.

- Dickinson, H. C. and N. S. Osborne (1915), *Specific Heat and Heat of Fusion of Ice* (No. 248), U.S. Govt. Print. Off.
- Dirksen, C. and S. Dasberg (1993), Improved calibration of time domain reflectometry soil water content measurements, *Soil Sci. Soc. Am. J.* 5, 661-667.
- Dobson, M. C., F. T. Ulaby, M. T. Hallikainen, and M. A. El-Rayes (1985), Microwave dielectric behavior of wet soil-part ii: dielectric mixing models, *Trans. Geosci. Remote Sensing, GE-23*, 35-46.
- Dorsey, N. E. (1940), *Properties of Ordinary Water-Substance in all its Phases: Water Vapor, Water, and all the Ices*; Compiled by N. Ernest Dorsey, New York, Reinhold Publishing Corporation.
- Drotz, H. S., E. L. Tilston, T. Sparrman, J. Schleucher, M. Nilsson, and M. G. Öquist (2009), Contributions of matric and osmotic potentials to the unfrozen water content of frozen soils, *Geoderma*, 148, 392-398.
- Eigenbrod, K. D. (1996), Effects of cyclic freezing and thawing on volume changes and permeabilities of soft fine-grained soils, *Can. Geotechnical J.*, 33, 529-537.
- Evetts, S. R. (2000), The TACQ computer program for automatic time domain reflectometry measurements: I. Design and operating characteristics, *ASAE*, 43, 1939-1946.
- Feng, X. (2009), The molecular composition of soil organic matter (SOM) and potential responses to global warming and elevated carbon dioxide (publication number AAT NR73181). Ph.D. diss., University of Toronto (Canada).
- Farouki, O. T. (1981), Thermal properties of soils, *CRREL monograph 81-1*, 136. Cold regions research and engineering lab, Hanover NH.
- Flerchinger, G. N. and K. E. Saxton (1989), Simultaneous heat and water model of a freezing snow-residue-soil system I. Theory and development. *Trans. ASAE*, 32, 565-571.
- Fouli, Y., B. Cade-Menun, and H. W. Cutforth (2013), Freeze-thaw cycles and soil water content effects on infiltration rate of three Saskatchewan soils, *Can. J. Soil Sci.*, 1-12.
- Friedman, S. P. (1998), A saturation degree-dependent composite spheres model for describing the effective dielectric constant of unsaturated porous media, *Water Resour. Res.*, 34, 2949-2961.
- Friedman, S. P., S. Jones, and D. Robinson (2006), Plenary lecture: Review of geometrical and interfacial factors determining effective permittivity–volumetric water content relationships of soils and rocks. Pap. 48, *Proc. TDR*.
- Fripiat, J., J. Cases, M. Francois, and M. Letellier (1982), Thermodynamic and microdynamic behavior of water in clay suspensions and gels, *J. Colloid Interface Sci.*, 89, 378-400.
- Fuchs, M., G. S. Campbell, and R. I. Papendick (1978), An analysis of sensible and latent heat flow in a partially frozen unsaturated soil, *Soil Sci. Soc. Am. J.*, 42, 379-385.
- Goodrich, L. (1982), The influence of snow cover on the ground thermal regime, *Can. Geotechnical J.*, 19, 421-432.
- Granger, R. J., D. M. Gray, and G. E. Dyck (1984), Snowmelt infiltration to frozen prairie soils, *Can. J. Earth Sci.*, 669-677.

- Gray, D. M., B. Toth, L. T. Zhao, J. W. Pomeroy, and R. J. Granger (2001), Estimating areal snowmelt infiltration into frozen soils, *Hydrol. Process.*, *15*, 3095-3111.
- Groffman, P. M., R. D. Fitzhugh, G. L. Tierney, J. P. Hardy, C. T. Driscoll, and T. J. Fahey (2001), Effects of mild winter freezing on soil nitrogen and carbon dynamics in a northern hardwood forest, *Biogeochemistry*, *56*, 191-213.
- Hall, D. K., J. L. Foster, N. E. DiGirolamo, and G. A. Riggs (2012), Snow cover, snowmelt timing and stream power in the Wind River Range, Wyoming, *Geomorphology*, *137*, 87-93.
- Hallett, J. (1963), The temperature dependence of the viscosity of supercooled water, *Proc. of the Phys. Soc.*, *82*, 1046.
- Hallin, I. L. (2009), Evaluation of a substrate and vegetation cover system for reclaimed phosphogypsum stacks at Fort Saskatchewan, Alberta, M.Sc. thesis, Department of Renewable Resources, University of Alberta (Canada).
- Hansson, K., J. Simunek, M. Mizoguchi, L. Lundin, and M. T. van Genuchten (2004), Water flow and heat transport in frozen soil: Numerical solution and freeze-thaw applications, *Vadose Zone J.*, *3*, 693-704.
- Haynes, W. M. and D. R. Lide (2011), *CRC handbook of chemistry and physics: A ready-reference book of chemical and physical data*, 92nd ed., CRC Press, Boca Raton, Fla.
- He, H. and M. Dyck (2013), Application of multiphase dielectric mixing models for understanding the effective dielectric permittivity of frozen soils, *Vadose Zone J.*, *12*.
- Heimovaara, T. (1993), Design of triple-wire time domain reflectometry probes in practice and theory, *Soil Sci. Soc. Am. J.*, *57*, 1410-1417.
- Heitman, J. L., J. M. Frank, P. L. Barnes, J. M. Ham, J. M. Basinger, and G. J. Kluitenberg (2003), Field evaluation of the dual-probe heat-pulse method for measuring soil water content, *Vadose zone J.*, *2*(4).
- Henry, H. A. L. (2007), Soil freeze-thaw cycle experiments: Trends, methodological weaknesses and suggested improvements, *Soil Biol. Biochem.*, *39*, 977-986.
- Hinkel, K. M., F. Paetzold, F. E. Nelson, and J. G. Bockheim (2001), Patterns of soil temperature and moisture in the active layer and upper permafrost at Barrow, Alaska: 1993-1999, *Global Planet. Change*, *29*, 293-309.
- Hirota, T., Y. Iwata, M. Hayashi, S. Suzuki, T. Hamasaki, R. Sameshima, and I. Takayabu (2006), Decreasing soil-frost depth and its relation to climate change in Tokachi, Hokkaido, Japan., *J. Meteorol. Soc. Jpn.*, *84*, 821-833.
- Hooper, F. C. and F. R. Lepper (1950), Transient heat flow apparatus for the determination of thermal conductivity, *J. Am. Soc. Heat. Vent. Eng.*, 129-140.
- IPCC (2007), Climate Change 2007: Synthesis Report. Contribution of Working Groups I, II and III to the Fourth Assessment Report of the Intergovernmental Panel on Climate Change [Core Writing Team, Pachauri, R.K and Reisinger, A. (eds.)]. IPCC, Geneva, Switzerland, 104 pp.
- Ishizaki, T., M. Maruyama, Y. Furukawa, and J. G. Dash (1996), Premelting of ice in porous silica glass, *J. Cryst. Growth*, *163*, 455-460.

- Iwata, Y., M. Hayashi, and T. Hirota (2008), Comparison of snowmelt infiltration under different soil-freezing conditions influenced by snow cover, *Vadose Zone J.*, 7, 8-8.
- Iwata, Y., M. Hayashi, S. Suzuki, T. Hirota, and S. Hasegawa (2010), Effects of snow cover on soil freezing, water movement, and snowmelt infiltration: A paired plot experiment, *Water Resour. Res.*, 46, W09504.
- Iwata, Y., M. Nemoto, S. Hasegawa, Y. Yanai, K. Kuwao, and T. Hirota (2011), Influence of rain, air temperature, and snow cover on subsequent spring-snowmelt infiltration into thin frozen soil layer in northern Japan, *J. Hydrol.*, 401, 165-176.
- Janowicz, J. R., D. M. Gray, and J. W. Pomeroy (2002), Characterisation of snowmelt infiltration scaling parameters within a mountainous subarctic watershed, *Annual meeting-eastern snow conference*, 67-82.
- Jansson, P. E. (1998), Simulating model for soil water and heat conditions: Description of the SOIL model (software manual), 81 pp. Department of Soil Sciences, Swedish University of Agricultural Sciences, Uppsala.
- Jones, S. B. and S. P. Friedman (2000), Particle shape effects on the effective permittivity of anisotropic or isotropic media consisting of aligned or randomly oriented ellipsoidal particles, *Water Resour. Res.*, 36, 2821-2833.
- Kamai, T., A. Tuli, G. J. Kluitenberg, and J. W. Hopmans (2008), Soil water flux density measurements near 1 cm d⁻¹ using an improved heat pulse probe design, *Water Resour. Res.*, 44, W00D14.
- Kane, D. L. and J. Stein (1984), Plot measurements of snowmelt runoff for varying soil conditions, *Geophysica*, 20, 123-135.
- Kane, D. L. (1980), Snowmelt infiltration into seasonally frozen soils, *Cold Reg. Sci. Technol.*, 3, 153-161.
- Kane, D. L. and J. Stein (1983a), Physics of snowmelt infiltration into seasonally frozen soils, in *Advances in Infiltration : Proceedings of the National Conference on Advances in Infiltration*, December 12-13, 1983, Hyatt Regency Illinois Center, Chicago, Illinois, pp. 178-187, St. Joseph, Mich.: American Society of Agricultural Engineers, c1983.
- Kane, D. L. and J. Stein (1983b), Water movement into seasonally frozen soils, *Water Resour. Res.*, 19, 1547-1557.
- Kelleners, T. and J. Nortto (2012), Determining water retention in seasonally frozen soils using Hydra impedance sensors, *Soil Sci. Soc. Am. J.*, 76, 36-50.
- Kleinberg, R. L. and D. D. Griffin (2005), NMR measurements of permafrost: unfrozen water assay, pore-scale distribution of ice, and hydraulic permeability of sediments, *Cold Reg. Sci. Technol.*, 42, 63-77.
- Kluitenberg, G. J., J. M. Ham, and K. L. Bristow (1993), Error analysis of the heat pulse method for measuring soil volumetric heat capacity, *Soil Sci. Soc. Am. J.*, 57(6) 1444-1451.
- Kluitenberg, G. J., K. L. Bristow, and B. S. Das (1995), Error analysis of heat pulse method for measuring soil heat capacity, diffusivity, and conductivity, *Soil Sci. Soc. Am. J.*, 59, 719-726.
- Kluitenberg, G. J., T. E. Ochsner, and R. Horton (2007), Improved analysis of heat pulse signals for soil water flux determination, *Soil Sci. Soc. Am. J.*, 71(1), 53-55.

- Knight, J. H. (1992), Sensitivity of time domain reflectometry measurements to lateral variations in soil water content, *Water Resour. Res.*, 28, 2345-2352.
- Knight, J. H. and G. J. Kluitenberg (2004), Simplified computational approach for dual-probe heat-pulse method, *Soil Sci. Soc. Am. J.*, 68, 447-449.
- Kojima, Y., J. L. Heitman, G. N. Flerchinger, and R. Horton (2013), Numerical evaluation of a sensible heat balance method to determine rates of soil freezing and thawing, *Vadose Zone J.*, 12.
- Kolaian, J. H. and P. F. Low (1963), Calorimetric determination of unfrozen water in montmorillonite pastes, *Soil Sci.*, 95(6), 376-384.
- Koopmans, R. W. R. and R. D. Miller (1966), Soil freezing and soil water characteristic curves, *Soil Sci. Soc. Am. J.*, 30(6), 680-685.
- Kozlowski, T. (2003), A comprehensive method of determining the soil unfrozen water curves: 2. Stages of the phase change process in frozen soil–water system, *Cold Reg. Sci. Technol.*, 36, 81-92.
- Kozlowski, T. (2004), Soil freezing point as obtained on melting, *Cold Reg. Sci. Technol.*, 38, 93-101.
- Kozlowski, T. (2012), Modulated Differential Scanning Calorimetry (MDSC) studies on low-temperature freezing of water adsorbed on clays, apparent specific heat of soil water and specific heat of dry soil, *Cold Reg. Sci. Technol.*, 78, 89-96.
- Lewis, G. N. and M. Randall (Eds.) (1961), *Thermodynamics*, 2nd ed., McGraw-Hill, New York.
- Likens, G. E. (2013), *Biogeochemistry of a forested ecosystem*, 3rd ed, 208. Springer Science & Business.
- Ling, F. and T. Zhang (2003), Impact of the timing and duration of seasonal snow cover on the active layer and permafrost in the Alaskan Arctic, *Permafrost Periglac.*, 14, 141-150.
- Liu, G. and B. C. Si (2008), Dual-probe heat pulse method for snow density and thermal properties measurement, *Geophys. Res. Lett.*, 35, L16404.
- Liu, G. and B. C. Si (2011a), Soil ice content measurement using a heat pulse probe method, *Can. J. Soil Sci.*, 91, 235-246.
- Liu, G. and B. C. Si (2011b), Single- and dual-probe heat pulse probe for determining thermal properties of dry soils, *Soil Sci. Soc. Am. J.*, 75, 787-794.
- Liu, X., T. Ren, and R. Horton (2008), Determination of soil bulk density with thermo-time domain reflectometry sensors, *Soil Sci. Soc. Am. J.*, 72, 1000-1005.
- Lu, S., T. Ren, Y. Gon, and R. Horton (2007), An improved model for predicting soil thermal conductivity from water content at room temperature, *Soil Sci. Soc. Am. J.*, 71, 8-14.
- Lu, Y., Y. Wang, and T. Ren (2013), Using late time data improves the heat-pulse method for estimating soil thermal properties with the pulsed infinite line source theory, *Vadose Zone J.*, 12.
- Luo, W., R. W. Skaggs, and G. M. Chescheir (2000), Drainmod Modifications for Cold Conditions, *Transac. ASAE*, 43, 1569-1582.
- Marion, G. M. (1995), Freeze-thaw processes and soil chemistry, *CRREL special report U. S. Army 95-12*.

- Maxwell Garnett, J. C. (1904), Colours in metal glasses and in metallic films, *Philos. T. Roy. Soc. A.*, *203*, 385-420.
- Melinder, Å. (2007), *Thermophysical properties of aqueous solutions used as secondary working fluids*, KTH, Stockholm.
- Merrill, R. B., (1968) Thermal conduction through an evacuated idealized powder over the temperature range of 100 to 500 K, Ph.D. dissertation, Brigham Young Univ., Provo, Utah.
- Miller, R. D. (1965), Phase equilibria and soil freezing, Permafrost International Conference: Proceedings (1963), Lafayette, Indiana, Nov.11-15, 1963.
- Miller, R. D. (1980), Freezing phenomena in soils, in *Applications of Soil Physics*, edited by D. Hillel, 254-299, Academic Press, New York, NY.
- Miyamoto, T., T. Annaka, and J. Chikushi (2005), Extended dual composite sphere model for determining dielectric permittivity of Andisols, *Soil Sci. Soc. Am. J.*, *69*, 23-29.
- Mori, Y., J. W. Hopmans, A. P. Mortensen, and G. J. Kluitenberg (2003), Multi-functional heat pulse probe for the simultaneous measurement of soil water content, solute concentration, and heat transport parameters, *Vadose Zone J.*, *2*, 561-571.
- Mori, Y., J. W. Hopmans, A. P. Mortensen, and G. J. Kluitenberg (2005), Estimation of vadose zone water flux from multi-functional heat pulse probe measurements, *Soil Sci. Soc. Am. J.*, *69*, 599-606.
- Noborio, K. (2001), Measurement of soil water content and electrical conductivity by time domain reflectometry: a review, *Comput. Electron. Agric.*, *31*, 213-237.
- Ochsner, T. E. and J. M. Baker (2008), In situ monitoring of soil thermal properties and heat flux during freezing and thawing, *Soil Sci. Soc. Am. J.*, *72*, 1025-1032.
- Ochsner, T. E., R. Horton, and T. Ren (2001), Simultaneous water content, air-filled porosity, and bulk density measurements with thermo-time domain reflectometry, *Soil Sci. Soc. Am. J.*, *65*, 1618-1622.
- Olefeldt, D. and N. T. Roulet (2014), Permafrost conditions in peatlands regulate magnitude, timing, and chemical composition of catchment dissolved organic carbon export, *Glob. Change Biol.*, *20*(10), 3122-3136.
- Olmanson, O. K. and T. E. Ochsner (2008), A partial cylindrical thermo-time domain reflectometry sensor, *Soil Sci. Soc. Am. J.*, *72*, 571-577.
- Or, D. and J. M. Wraith (1999), Temperature effects on soil bulk dielectric permittivity measured by time domain reflectometry: A physical model, *Water Resour. Res.*, *35*, 371-383.
- Overduin, P. P., D. L. Kane, and W. K. P. van Loon (2006), Measuring thermal conductivity in freezing and thawing soil using the soil temperature response to heating, *Cold Reg. Sci. Technol.*, *45*, 8-22.
- Parkin, G., A. P. von Bertoldi, and A. J. McCoy (2013), Effect of tillage on soil water content and temperature under freeze-thaw conditions, *Vadose Zone J.*, *12*(1).
- Patterson, D. E. and M. W. Smith (1985), Unfrozen water content in saline soils: results using time-domain reflectometry, *Can Geotechnical J.*, *22*, 95-101.
- Patterson, D. E. and M. W. Smith (1980), The use of time domain reflectometry for the measurement of unfrozen water content in frozen soils, *Cold Reg. Sci. Technol.*, *3*, 205-210.

- Patterson, D. E. and M. W. Smith (1981), The measurement of unfrozen water content by time domain reflectometry: results from laboratory tests, *Can. Geotechnical J.*, 18, 131.
- Pederson, G. T., S. T. Gray, C. A. Woodhouse, J. L. Betancourt, D. B. Fagre, J. S. Littell, E. Watson, B. H. Luckman, and L. J. Graumlich (2011), The unusual nature of recent snowpack declines in the North American cordillera, *Science*, 333, 332-335.
- Pham, O. T., and C. G. Smith (1986), Thermal imbalance errors and effective area in guarded hot plates, *Rev. Sci. Instrum.*, 57(1), 99-105.
- Polder, D. and J. H. van Santeen (1946), The effective permeability of mixtures of solids, *Physica*, 12, 257-271.
- Powell, R. W., and R. P. Tye (1960), Thermal and electrical conductivities of nickel-chromium (Nimonic) alloys, *Engineer*, 209(5440), 729-732.
- Pusch, P. (1979), Unfrozen water as a function of clay microstructure, *Eng. Geol.*, 13, 157-162.
- Putkonen, J. (2003), Determination of frozen soil thermal properties by heated needle probe, *Permafrost Periglac.*, 14, 343-347.
- Rascher, C. M., C. T. Driscoll, and N. E. Peters (1987), Concentration and flux of solutes from snow and forest floor during snowmelt in the West-Central Adirondack region of New York, *Biogeochemistry*, 3, 209-224.
- Regalado, C. M. (2006), A geometrical model of bound water permittivity based on weighted averages: the allophane analogue, *J. Hydrol.*, 316, 98-107.
- Ren, T., R. Horton, and K. Noborio (1999), Measuring soil water content, electrical conductivity, and thermal properties with a thermo-time domain reflectometry probe, *Soil Sci. Soc. Am. J.*, 63, 450-457.
- Ren, T., G. J. Kluitenberg, and R. Horton (2000), Determining soil water flux and pore water velocity by a heat pulse technique, *Soil Sci. Soc. Am. J.*, 64, 552-560.
- Ren, T., R. Horton, and T. E. Ochsner (2003a), Development of thermo-time domain reflectometry for vadose zone measurements, *Vadose Zone J.*, 2(4).
- Ren, T., T. E. Ochsner, R. Horton, and Z. Ju (2003b), Heat-pulse method for soil water content measurement: influence of the specific heat of the soil solids, *Soil Sci. Soc. Am. J.*, 67, 1631-1634.
- Ren, T., Z. Ju, Y. Gong, and R. Horton (2005), Comparing heat-pulse and time domain reflectometry soil water contents from thermo-time domain reflectometry probes, *Vadose Zone J.*, 4(4): 1080-1086.
- Robinson, D. A. and S. P. Friedman (2003), A method for measuring the solid particle permittivity or electrical conductivity of rocks, sediments, and granular materials, *J Geophys Res-Sol Ea*, 108.
- Robinson, D. A. and S. P. Friedman (2005), Electrical conductivity and dielectric permittivity of sphere packings: Measurements and modelling of cubic lattices, randomly packed monosize spheres and multi-size mixtures, *Physica A: Statistical Mechanics and its Applications*, 358, 447-465.
- Robinson, D. A., J. D. Cooper, and C. M. K. Gardner (2002), Modelling the relative permittivity of soils using soil hygroscopic water content, *J. Hydrol.*, 255, 39-49.

- Robinson, D. A., S. B. Jones, J. M. Wraith, D. Or, and S. P. Friedman (2003), A review of advances in dielectric and electrical conductivity measurement in soils using time domain reflectometry, *2*, 444-475.
- Roth, K. and J. Boike (2001), Quantifying the thermal dynamics of a permafrost site near Ny-Ålesund, Svalbard, *Water Resour. Res.*, *37*, 2901-2914.
- Roth, K., R. Schulin, H. Flühler, and W. Attinger (1990), Calibration of time domain reflectometry for water content measurement using a composite dielectric approach, *Water Resour. Res.*, *26*, 2267-2273.
- Russel, W. B., D. A. Saville, and W. R. Schowalter (1992), *Colloidal Dispersions*, Cambridge University Press.
- Sareni, B. (1997), Effective dielectric constant of random composite materials, *J. Appl. Phys.*, *81*(5), 2375-2383.
- Schwartz, R., S. Evett, M. Pelletier, and J. Bell (2009), Complex permittivity model for time domain reflectometry soil water content sensing: I. Theory, *Soil Sci. Soc. Am. J.*, *73*, 886-897.
- Scott, B. J. (2004), WinTDR users guide (Utah State University soil physics group).
- Sen, P. N., C. Scala, and M. H. Cohen (1981), A self-similar model for sedimentary rocks with application to the dielectric constant of fused glass beads, *Geophysics*, *46*, 769-783.
- Seyfried, M. S. and M. D. Murdock (1996), Calibration of time domain reflectometry for measurement of liquid water in frozen soils, *Soil Sci.*, *161*, 87-98.
- Shanley, J. B. and A. Chalmers (1999), The effect of frozen soil on snowmelt runoff at Sleepers River, Vermont, *Hydrol. Process.*, *13*, 1843-1857.
- Shiozawa, S. and G. S. Campbell (1990), Soil thermal conductivity, *Remote Sens. Rev.*, *5*, 301-310.
- Sihvola, A. H. (1989), Self-consistency aspects of dielectric mixing theories, *IEEE Trans. Geosci. Remote Sensing*, *27*, 403-415.
- Sihvola, A. H. (1999), *Electromagnetic mixing formulas and applications*, Institution of Electrical Engineers, London, England.
- Sihvola, A. H. and J. A. Kong (1988), Effective permittivity of dielectric mixtures, *IEEE Trans. Geosci. Remote Sensing*, *26*, 420-429.
- Sihvola, A. and I. V. Lindell (1990), Polarizability and Effective Permittivity of Layered and Continuously Inhomogeneous Dielectric Ellipsoids, *J. Electromagnet Wave*, *4*, 1-26.
- Sihvola, A. and I. Lindell (1992), Polarizability modeling of heterogeneous media, *Progress in Electromagnetics Research (PIER 6)*, *Dielectric Properties of Heterogeneous Materials*, Priou, A.(ed.), Elsevier, Amsterdam.
- Smith, M. W., A. R. Tice, and K. Senneset (1988), Measurement of the unfrozen water content of soils: a comparison of NMR and TDR methods, *CRREL Report 88-18*, 16.
- Smits, K. M., T. Sakaki, S. E. Howington, J. F. Peters, and T. H. Illangasekare (2013), Temperature dependence of thermal properties of sands across a wide range of temperatures (30-70°C), *Vadose Zone J.*, *12*(1).

- Spaans, E. J. A. and J. M. Baker (1995), Examining the use of time domain reflectometry for measuring liquid water content in frozen soil, *Water Resour. Res.*, *31*, 2917-2925.
- Spaans, E. J. A. and J. M. Baker (1996), The soil freezing characteristic: its measurement and similarity to the soil moisture characteristic, *Soil Sci.Soc.Am. J.*, *60*, 13-19.
- Sparman, T., O. Mats, L. Klemedtsson, J. Schleucher, and M. Nilsson (2004), Quantifying unfrozen water in frozen soil by high-field ^2H NMR, *Environ. Sci. Technol.*, *38*, 5420-5425.
- Sposito, G. (1981), Single-particle motions in liquid water. II. The hydrodynamic model, *J. Chem. Phys.*, *74*, 6943-6949.
- Stadler, D., M. Stahli, P. Aeby, and H. Fluhler (2000), Dye tracing and image analysis for quantifying water infiltration into frozen soils, *Soil Sci. Soc. Am. J.*, *64*, 505-516.
- Stahli, M. (2005), Freezing and thawing phenomena in soils, in *Encyclopedia of Hydrological Sciences*, vol. 2, edited by M. G. Anderson, pp. 1069-1076, John Wiley & Sons, Ltd, New York.
- Stahli, M. and D. Stadler (1997), Measurement of water and solute dynamics in freezing soil columns with time domain reflectometry, *J. Hydrol.*, *195*, 352-369.
- Stalhane, B., and S. Pyk (1931), New method for determining the coefficients of thermal conductivity, *Tek. Tidskr.*, *6*(28), 389-393.
- Sutinen, R., P. Hänninen, and A. Venäläinen (2008), Effect of mild winter events on soil water content beneath snowpack, *Cold Reg. Sci. Technol.*, *51*, 56-67.
- Suzuki, S. (2004), Dependence of unfrozen water content in unsaturated frozen clay soil on initial soil moisture content, *Soil Sci. Plant Nutr.*, *50*, 603-606.
- Suzuki, S., J. Kashiwagi, S. Nakagawa, and K. Soma (2002), Mechanism of hysteresis in thermal conductivity of frozen soils between freezing and thawing processes, *Trans. JSIDRE*.
- Tanaka, K., I. Tamagawa, H. Ishikawa, Y. M. Ma, and Z. Y. Hu (2003), Surface energy budget and closure of the eastern Tibetan Plateau during the GAME-Tibet IOP 1998, *J. Hydrol.*, *283*, 169-183.
- Tian, H., C. Wei, H. Wei, and J. Zhou (2014), Freezing and thawing characteristics of frozen soils: Bound water content and hysteresis phenomenon, *Cold Reg. Sci. Technol.*, *103*, 74-81.
- Tice, A. R., D. M. Anderson, and A. Banin (1976), The prediction of unfrozen water contents in frozen soil from liquid limit determinations, *U.S. Army. CRREL Report* 76-8.
- Tice, A. R., D. M. Anderson, and K. F. Sterrett (1981), Unfrozen water contents of submarine permafrost determined by nuclear magnetic resonance, *Eng. Geol.*, *18*, 135-146.
- Tice, A. R., P. B. Black, and R. L. Berg (1989), Unfrozen water contents of undisturbed and remolded Alaskan silt, *Cold Reg. Sci. Technol.*, *17*, 103-111.
- Tokumoto, I., K. Noborio, and K. Koga (2010), Coupled water and heat flow in a grass field with aggregated Andisol during soil-freezing periods, *Cold Reg. Sci. Technol.*, *62*, 98-106.
- Topp, G. C., J. L. Davis, and A. P. Annan (1980), Electromagnetic determination of soil water content: measurements in coaxial transmission lines, *Water Resour. Res.*, *16*, 574.
- Trautz, A. C., K. M. Smits, P. Schulte, and T. H. Illangasekare (2014), Sensible heat balance and heat-pulse method applicability to in situ soil-water evaporation, *Vadose Zone J.*, *13*.

- Tsang, L. and A. Ishimaru (1985), Radiative wave and cyclical transfer equations for dense nontenuous media, *J. Opt. Soc. Am. A.*, 2, 2187.
- Van der Held, E. F. M. and F. G. Van Drunen (1949), A method of measuring the thermal conductivity of liquids, *Physica*, 15, 865-881.
- Walker, B. D. (2003), Drought Monitoring Network: Soil moisture and temperature sensor installation procedures. Conservation and Development Branch, Alberta Agriculture, Food and Rural Development. Edmonton, AB. 17 pp.
- Walker, B. D. (2006), Drought Monitoring Network: Site and soil descriptions: 2002-2005. Conservation and Development Branch, Alberta Agriculture, Food and Rural Development. Edmonton, AB. 125pp.
- Walker, B. D. and J. Tajek (2003), Drought Monitoring Network: Soil moisture sensor calibration. Conservation and Development Branch, Alberta Agriculture, Food and Rural Development. Edmonton, AB. 33 pp.
- Wang, Q., T. E. Ochsner, and R. Horton (2002), Mathematical analysis of heat pulse signals for soil water flux determination, *Water Resour. Res.*, 38, 1091-1097.
- Watanabe, K., T. Kito, S. Dun, J. Q. Wu, R. C. Greer, and M. Flury (2013), Water infiltration into a frozen soil with simultaneous melting of the frozen layer, *Vadose Zone J.*, 12.
- Watanabe, K. and M. Mizoguchi (2002), Amount of unfrozen water in frozen porous media saturated with solution, *Cold Reg. Sci. Technol.*, 34, 103-110.
- Watanabe, K. and T. Wake (2009), Measurement of unfrozen water content and relative permittivity of frozen unsaturated soil using NMR and TDR, *Cold Reg. Sci. Technol.*, 59, 34-41.
- Weishaupt, J. (1940), Nichtstationäres Verfahren zur bestimmung der Wärmeleitzahl von Flüssigkeiten (Non-stationary methods for determination of thermal conductivity of liquids), *ForschArb. IngWes.*, 11, 20.
- Williams, M. W. and J. M. Melack (1991), Solute chemistry of snowmelt and runoff in an Alpine Basin, Sierra Nevada, *Water Resour. Res.*, 27, 1575-1588.
- Winkelmann, V. A. (1875), Ueber die Wärmeleitung der Gase, *Ann. Phys. und Chem.*, 12, 497-531.
- Yong, R. N., C. H. Cheung, and D. E. Sheeran (1979), Prediction of salt influence on unfrozen water content in frozen soils, *Eng. Geol.*, 13, 137-155.
- Yoshikawa, K. and P. P. Overduin (2005), Comparing unfrozen water content measurements of frozen soil using recently developed commercial sensors, *Cold Reg. Sci. Technol.*, 42, 250-256.
- Zhang, T. (2005), Influence of the seasonal snow cover on the ground thermal regime: an overview, *Rev. Geophys.*, RG4002.
- Zhang, Y., M. Treberg, and S. K. Carey (2011), Evaluation of the heat pulse probe method for determining frozen soil moisture content, *Water Resour. Res.*, 47, W05544.
- Zhao, L., D. M. Gray, and D. H. Male (1997), Numerical analysis of simultaneous heat and mass transfer during infiltration into frozen ground, *J. Hydrol.*, 200, 345-363.

- Zhao, L. and D. M. Gray (1997a), A parametric expression for estimating infiltration into frozen soils, *Hydrol. Process.*, *11*, 1761-1775.
- Zhao, L. and D. M. Gray (1997b). Estimating snowmelt infiltration into medium and fine-textured frozen soils. In *Proc. Symposium on Physics, Chemistry and Ecology of Seasonally Frozen Soils, University of Alaska, Fairbanks* (pp. 287-293).
- Zhao, L. and D. M. Gray (1999), Estimating snowmelt infiltration into frozen soils, *Hydrol. Process.*, *13*, 1827-1842.
- Zuzel, J. F., R. R. Allmaras, and R. Greenwalt (1982), Runoff and soil erosion on frozen soils in northeastern Oregon, *J. Soil Water Conserv.*, *37*, 351-354.